New Li^+ ion conducting solid electrolytes based on the LISICON structure

By

Ludan Zhang

School of Biological and Chemical Sciences,

Queen Mary University of London,

September 2020

Submitted in fulfillment of the requirements of the Degree of Doctor of Philosophy

Declaration,

I hereby declare the Ph.D thesis titled 'New Li^+ ion conducting solid electrolytes based on the LISICON structure' is based on my own research work under the guidance from my supervisor, Dr Isaac Abrahams. Some results are conducted through collaboration with other facilities, which were properly acknowledged.

Ludan Zhang

09/2020

Acknowledgments

First, I would like to thank my supervisor Dr Isaac Abrahams for his patient guidance and tremendous help during my PhD studies. I have really learned so much from him, not only on the strengthening the knowledge about solid-state chemistry but also his attitude towards the scientific research. I would also like to thank my second supervisor Dr Haixue Yan, who really opens a different and new horizon about the ferroelectric materials, gives me the chances to work on this aspect. Whenever I need help, Dr Isaac Abrahams and Dr Haixue Yan are always there to support me and encourage me. I believe these valuable experiences will guide and accompany me all the time.

I would like to thank Queen Mary University of London and the Chinese Scholarship Council for providing financial support for my PhD. I am really grateful to Prof. Franciszek Krok and his research group at Warsaw University of Technology, Poland. I will never forget their hospitality and support during my two weeks' trip in their group. I thank Jan Jamroz's help in impedance test and Dr Marcin Malys in impedance analysis. I would like to thank Romio Martina and Dr Jahn Marcus in AIT, Austrian Institute of Technology GmbH, Vienna, Austria for their help in battery test. I would like to thank Dr Fu Song and Dr Devis Di Tommaso for their help in molecular dynamics simulation.

I am grateful to Dr Rory M Wilson and Dr Richard Whiteley for the help in XRD experiments, Dr Harold Toms in solid-state NMR, Dr Ron Smith in neutron scattering experiments. I also acknowledge the STFC for their financial support and technical help.

I would like to thank Mr. Maurizio Leo, Dr Theo Graves Saunders for their help when I was in the nano-force lab. I also want to thank the support from Hangfeng Zhang, Yajun Yue, Zhongna Yan and Tao Chen in our group and all my other friends.

Lastly, I would like to thank my family for their continuous support and encouragement during my PhD career.

Contents

Abstract

Three LISICON-based systems, Li_3PO_4-Li_4GeO_4, Li_2MoO_4-Li_4GeO_4 and Li_2WO_4-Li_4GeO_4, have been systematically investigated. Details of the phase behaviour, crystal structure and defect structure have been studied by powder X-ray and neutron diffraction and solid-state NMR, reverse Monte Carlo (RMC) modelling of neutron total scattering data and molecular dynamics simulations. Electrochemical impedance spectroscopy measurements have been used to characterise the electrical properties.

In the Li_3PO_4-Li_4GeO_4 system, a solid solution $Li_{3+x}Ge_xP_{1-x}O_4$, isostructural with the end member γ-Li_3PO_4 is found in the compositional range $0.00 \leq x \leq 0.90$. Two main types of defect are identified and clustering of these defects is proposed. Conductivity measurements show the $x = 0.75$ composition exhibits the best total conductivity ($\sigma_{250°C} = \sim 1.8 \times 10^{-2}$ S cm^{-1}) with a low activation energy of 0.42 eV.

In the $Li_{4-2x}Ge_{1-x}Mo_xO_4$ system, compositions in the range $0.1 \leq x \leq 0.5$, exhibit LISICON-type structures. Both the β and γ phase LISICON type polymorphs are observed in this system, the relative amounts of which vary with temperature. In this system, the highest conductivity ($\sigma_{250°C} = \sim 5.0 \times 10^{-3}$ S cm^{-1}) is obtained in the $x = 0.2$ composition with an activation energy of 0.67 eV.

In the Li_2WO_4-Li_4GeO_4 system, the solid solution only extends between $0.10 \leq x \leq 0.25$. Low activation energy and high electric conductivity are observed throughout this system. The highest elevated temperature conductivity values are seen in the $x = 0.15$ composition ($\sigma_{250°C} = \sim 3.12 \times 10^{-2}$ S cm^{-1}). Molecular dynamics simulations suggest an order of magnitude higher conductivity values could be achieved through reduction of grain boundary resistances.

Chapter 1 Introduction

1.1 Introduction to lithium ion batteries

Due to the energy crisis and environmental pollution caused by burning traditional fossil fuels such as coal, petrol and natural gas, there is a strong demand to develop clean and sustainable energy. The development of natural resources like wind, solar energy, waterpower and tidal energy can relieve the energy crisis to some extent, but they are restricted due to uncontrollable changes in weather and geographical conditions. Chemical energy storage is an effective method that matches well with the requirements of renewable energy and different life needs. The lithium ion battery is one example of such environmentally friendly energy storage systems and is characterised by high energy density and power density. In many areas such as portable electronics and vehicles, lithium ion batteries have been widely used. The lithium ion battery industry is strong both in terms of scale and competence. Over recent years, many big automobile manufacturers such as Porsche, General Motors, Toyota and Ford have devoted increasing resources into research and development of electrical vehicles, aiming to reduce the market percentage of petrol dependent vehicles, and eventually to replace them totally. Currently, it is mainly lithium batteries with liquid electrolytes that account for much of this type of research, including the development of anode materials, cathode materials and liquid electrolytes [1].

The history of the development of lithium ion batteries, can be traced back to the 1970s. In 1976, based on the known intercalation compounds of the transition metal layered di-sulfides, Whittingham reported a Li metal (Li°) || TiS_2 cell which showed reversable and rapid electrochemical intercalation of Li^+ ions into TiS_2 [2]. However, due to the high reactivity of Li metal with the electrolyte and the formation of lithium dendrites caused by the uneven deposition of Li on the surface of Li metal during the reversible process, there were significant safety problems associated with this type of battery. In the late 1970s, the use of two

intercalation electrodes with different potentials instead of the Li metal electrode was proposed and the concept of "rocking-chair" battery was born [3].

The main components of a lithium ion battery are the cathode, electrolyte and anode. The charge-discharge process is through a "rocking-chair" like mechanism illustrated in Fig. 1.1. When discharging, lithium ions leave the anode, diffuse into the electrolyte, cross the separator/electrolyte interface, then diffuse in the electrolyte towards the cathode, and finally enter unoccupied sites in the cathode structure. This ionic diffusion is charge compensated through electronic charge transfer in the external circuit. When charging, the mobile lithium ions and electrons move in the opposite direction. Taking the full battery with $LiCoO_2$ as the cathode and the graphite as the anode as an example, the charge-discharge process can be expressed as:

$$\text{Cathode reaction: } LiCoO_2 \underset{\text{discharging}}{\overset{\text{charging}}{\rightleftharpoons}} Li_{1-x}CoO_2 + x\,Li^+ + x\,e^- \tag{1.1}$$

$$\text{Anode reaction: } x\,Li^+ + x\,e^- + 6C \underset{\text{discharging}}{\overset{\text{charging}}{\rightleftharpoons}} Li_xC_6 \tag{1.2}$$

$$\text{Total reaction: } LiCoO_2 + 6C \underset{\text{discharging}}{\overset{\text{charging}}{\rightleftharpoons}} Li_{1-x}CoO_2 + Li_xC_6 \tag{1.3}$$

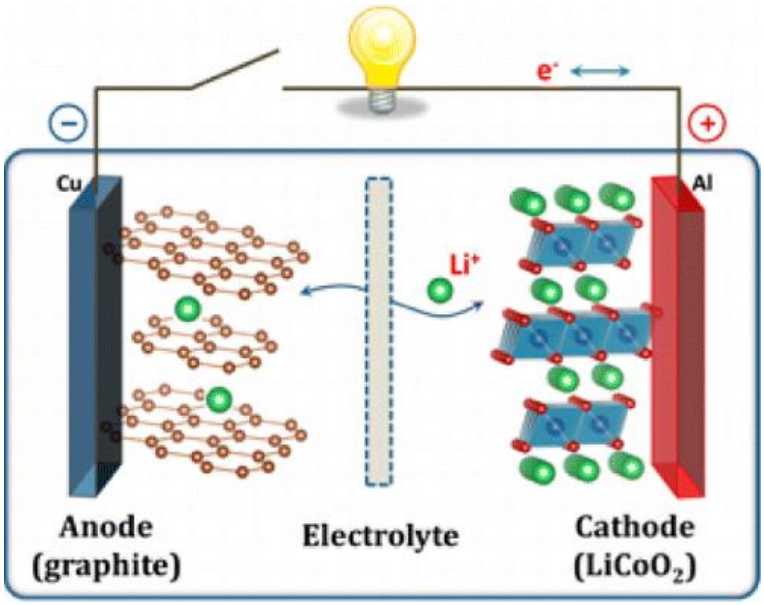

Figure 1.1 Schematic illustration of a lithium-ion battery [4]

For both the cathode and anode materials, candidates should have good electronic and ionic conductivity to facilitate rapid ion and electron transfer, thus ensuring small overpotential and high rate performance; the crystalline structure of electrode materials should have good reversibility during the continuous Li^+ intercalation/deintercalation processes, ensuring the whole battery has good cycling performance and power density; to have high energy density, the cathode should have a high redox potential (vs Li^+/Li) while the anode should have a low redox potential (vs Li^+/Li) to maximise the output voltage, and both should have high specific capacity. Additionally, good electrode materials should have good interface stability with the electrolyte to reduce the possibility of side reactions. At the same time, low cost, simple fabrication procedure and environmental benignancy are also critical for large-scale commercial production.

Fig. 1.2 shows common cathode and anode materials in lithium ion batteries. The cathode materials serve as a reservoir of mobile Li^+ ions and therefore they should possess a high concentration of these charge carriers. Currently, the cathode materials mainly include polyanionic compounds such as the olivine structured compounds $LiFePO_4$ [5] and $LiMnPO_4$ [6], NASICON structured compounds e.g. $Li_3V_2(PO_4)_3$ [7] and Li-based transition metal oxides (TMOs). TMOs exhibit a variety of crystal structures, the most important of which are spinels such as $LiMn_2O_4$ [8], $LiNi_{0.5}Mn_{1.5}O_4$ [9] and layered rocksalt-like structures such as $LiCoO_2$ [10], $LiNi_{0.5}Co_{0.5}O_2$ [11].

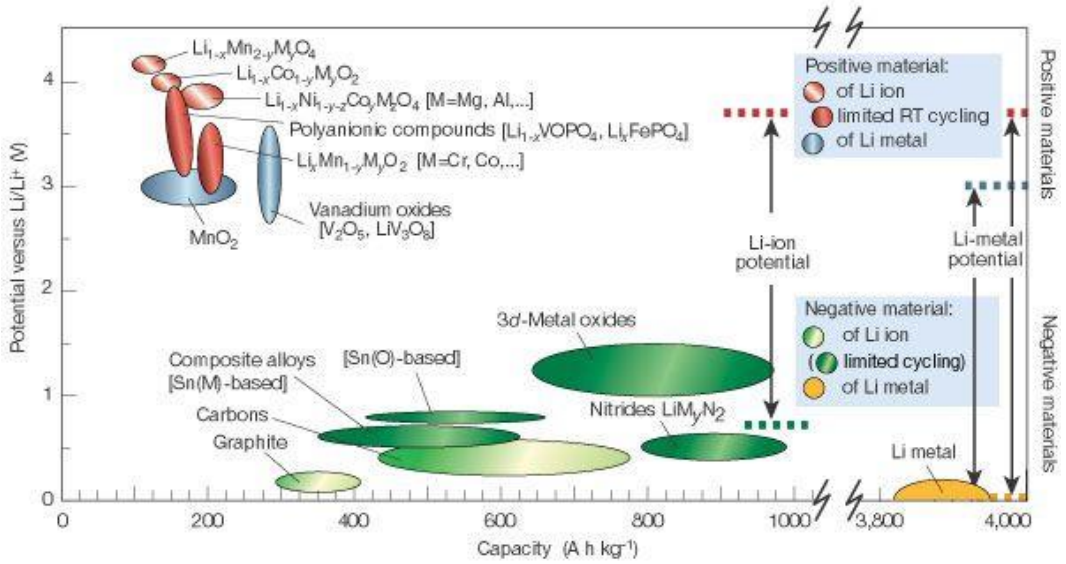

Figure 1.2 Voltage vs. specific capacity for electrode materials in lithium ion batteries [12]

Anode materials in lithium ion batteries can be generally divided into two major categories, carbons and non-carbons. Carbon-based anodes mainly include graphitized carbon like natural graphite, non-graphitized carbon like amorphous carbon, carbon nanotubes (CNTs) and graphene [13]. Since carbon-based anode materials have low Li^+ intercalation/deintercalation potentials (vs. Li^+/Li), are highly abundant and are low lost with high cycling efficiency, there has been much research on the application of these materials. Non-carbons mainly include transition metal oxides like SnO_2, which operate through a Li-alloy mechanism, TiO_2 through an insertion mechanism, Fe_2O_3 through a conversion mechanism, silicon-based and tin-based alloys and metal sulfides and nitrides [14].

Electrolytes are a crucial part of the lithium ion battery and act as a bridge for the lithium ion to shuttle between the cathode and anode. According to their phase states, electrolytes can be mainly divided into liquid electrolytes, solid electrolytes and gel polymer electrolytes. Currently, in commercial lithium ion batteries, it is mainly liquid electrolytes that are employed.

Liquid electrolytes are composed of two basic components, a lithium salt and an organic solvent. Liquid electrolytes should possess the following characteristics [15, 16]:

(1) They should have good chemical and electrochemical stability, including interface stability with the cathodes and the solid electrode/electrolyte interface (SEI) formed on the surface of anodes.

(2) They should have high ionic conductivity, usually around 1×10^{-3} to 2×10^{-2} S cm^{-1}, high dielectric constant, high solubility for lithium salts, low vapour pressure and low viscosity.

(3) They should have a high boiling point and low freezing point to keep the liquid state within a wide temperature range usually around –40 ~ 70 °C, suitable for the design of specialized batteries for use in extreme conditions.

(4) They should be non-toxic and non-flammable to ensure safe storage and flexible transport.

Tables 1.1 and 1.2 list common lithium salts and solvents, respectively, used in electrolytes for lithium batteries. Lithium salts include inorganic compounds such as $LiPF_6$, $LiAsF_6$, $LiBF_6$ and $LiClO_4$, as well as organic compounds like $Li(CF_3SO_3)$ and $Li(NCF_3SO_2)$. Usually a mixture of two or more organic solvents is used, because compared to pure solvents, the mixtures often exhibit better ionic conductivity and better physical properties. One solvent of the mixture is chosen to have weak volatilization and high dielectric constant, e.g. EC (ethylene carbonate) and PC (propylene carbonate), while another solvent is selected to have low viscosity and high volatility, e.g. DMC (dimethyl carbonate), DEC (diethyl carbonate), EMC (ethyl methyl carbonate) and THF (tetrahydrofuran). The resulting mixed electrolyte solvents have low viscosity, weak volatilization and high dielectric constant. The commonly used liquid electrolyte systems in lithium ion batteries include 1 M $LiPF_6$/PC: DEC (1 : 1), PC: DMC (1 : 1), PC : EMC (1 : 1) or 1 M $LiPF_6$/EC : DEC (1 : 1), EC : DMC (1 : 1) and EC : EMC (1 : 1).

Table 1.1 Common lithium salts in liquid electrolytes [16]

Salt	Structure	M. Wt	T_m/ °C	$T_{decomp.}$, / °C in solution	Al-corrosion	σ /mScm^{-1} (1.0 M, 25 ° C)	
						in PC	in EC/DMC
$LiBF_4$		93.9	293 (d)	> 100	N	3.4 [a]	4.9 [c]
$LiPF_6$		151.9	200 (d)	~ 80 (EC/DMC)	N	5.8 [a]	10.7 [d]
$LiAsF_6$	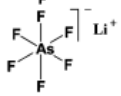	195.9	340	> 100	N	5.7 [a]	11.1 [c]
$LiClO_4$		106.4	236	>100	N	5.6 [a]	8.4 [d]
Li Triflate	$Li^+ CF_3SO_3^-$	155.9	>300	>100	Y	1.7 [a]	
Li Imide	$Li^+ [N(SO_2CF_3)_2]^-$	286.9	234 [b]	>100	Y	5.1 [a]	9.0 [e]
Li Beti	$Li^+ [N(SO_2CF_2CF_3)_2]^-$				N		

Table 1.2 Common organic carbonates and esters as solvents in liquid electrolytes [16]

Solvent	Structure	M. Wt	T_m/ °C	T_b/ °C	η/cP 25 °C	ε 25 °C	Dipole Moment/debye	T_f/ °C	d/gcm^{-3}, 25 °C
EC		88	36.4	248	1.90, (40 °C)	89.78	4.61	160	1.321
PC		102	-48.8	242	2.53	64.92	4.81	132	1.200
BC		116	-53	240	3.2	53			
γBL		86	-43.5	204	1.73	39	4.23	97	1.199
γVL		100	-31	208	2.0	34	4.29	81	1.057
NMO		101	15	270	2.5	78	4.52	110	1.17
DMC	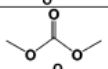	90	4.6	91	0.59 (20 °C)	3.107	0.76	18	1.063
DEC	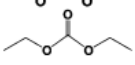	118	-74.3 [a]	126	0.75	2.805	0.96	31	0.969
EMC	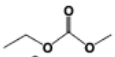	104	-53	110	0.65	2.958	0.89		1.006
EA		88	-84	77	0.45	6.02		-3	0.902
MB	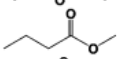	102	-84	102	0.6			11	0.898
EB	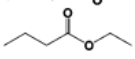	116	-93	120	0.71			19	0.878

There are several parameters used to assess the quality of a lithium ion battery. The energy density (W·h/kg or W·h/L) is the maximum energy the battery can deliver for a unit of mass or volume, while a battery's power density (W/kg or W/L) is the maximum power the battery

can deliver for a unit of mass or volume. The theoretical capacity, $Q_{\text{theoretical}}$, of a battery can be calculated according to Faraday's law (Eqn. 1.4)

$$Q_{\text{theoretical}} = (n\text{F}) / (3600 \times M_w) \text{ mA h/g} \quad (1.4)$$

where n is number of the apparent charge carriers per formula unit within the active material structure, F is the Faraday constant (F = 96485.3 C/mol) and M_w (g/mol) is the formula weight of the active material used in the electrode. The actual specific capacity Q_{actual} is calculated from the voltage-time curve from galvanostatic charge-discharge tests, as shown in Eqn. 1.5:

$$Q_{\text{actual}} = I \times A \times t / (3600 \times M_w) \text{ mA h/g} \quad (1.5)$$

where I is the current density (A/m^2 or A/g) used for charge-discharge, A is the electrode area (m^2) or the mass (g) of active material in the electrode and t is the time (s) taken to reach the cut-off voltage from the starting voltage.

Cycling performance is based on how the battery performance varies during repeated cycles, while rate performance describes how the battery performance varies when changing the charge/discharge current density which is usually expressed as a C-rate. A C-rate is an indication of the rate or speed at which the battery is discharged relative to its maximum capacity. A 1C discharge rate means the entire battery entirely discharges in 1 hour. Fig. 1.3 shows a typical galvanostatic charge-discharge curve and the rate performance for a $LiFePO_4$/Li battery. For a cathode material, the Coulombic efficiency of one cycle of charge-discharge is expressed in Eqn. 1.6, where $Q_{\text{discharge}}$ and Q_{charge} are the specific capacities during the discharge and the charge processes, respectively.

$$\eta = \frac{Q_{\text{discharge}}}{Q_{\text{charge}}} \quad (1.6)$$

For an anode material that employs lithium metal as the counter electrode, the Coulomb efficiency is expressed by Eqn. 1.7:

$$\eta = \frac{Q_{\text{charge}}}{Q_{\text{discharge}}} \quad (1.7)$$

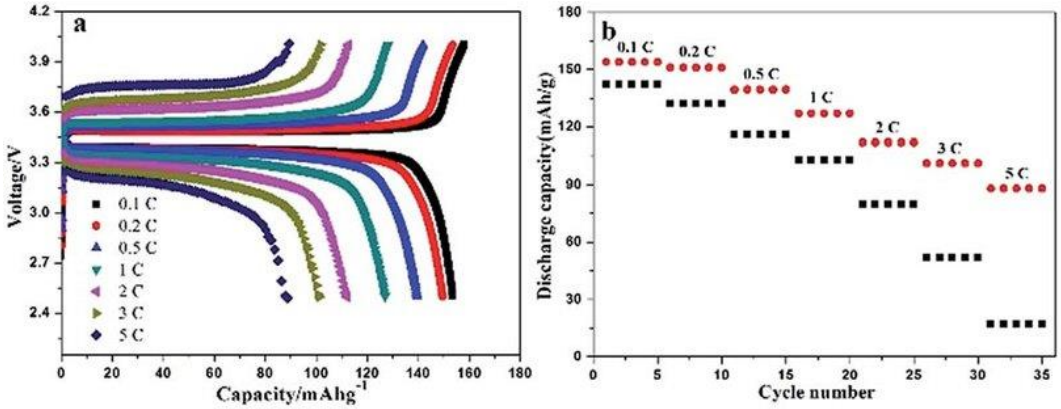

Figure 1.3 (a) Typical charge/discharge curves and (b) rate performance of a $LiFePO_4$/Li battery [17]

1.2 All solid-state lithium ion batteries

Though excellent performance can be achieved with systems based on liquid electrolytes, including high charging rates, cycling stability, power density and energy density, the disadvantage of liquid electrolytes cannot be ignored. For liquid electrolytes, such as DMC, DEC and PC, toxicity, flammability and air sensitivity, are all issues. There have been a number of well documented incidents in which fire has occurred. This could lead to catastrophic consequences for certain applications (e.g. in aircraft) [18]. Therefore, the safety of lithium ion batteries is a key problem that should be focused on. All solid-state lithium batteries are clean and safe systems that use solid electrolytes instead of a liquid one. Compared with the current commercial lithium ion batteries, all solid-state lithium batteries not only can solve the safety problem, but also have higher energy density and longer cycling life [19]. Additionally, the cost of packaging and monitoring is greatly reduced. There is a growing interest in next-generation lithium batteries to use as large energy storage devices and in electric vehicles. The related research is not only being carried out in academic research laboratories, but also attracts much effort in world-leading companies like Toyota and Seeo, as well as many others.

A schematic of an all solid-state lithium battery is illustrated in Fig.1.4. As can be seen, the electrolyte accounts for a critical component and plays the roles of ionic transporter and electrode separator. In the case of an all solid-state lithium battery, similar to the basic rocking chair mechanism for lithium ion batteries, when discharging, lithium ions are generated at the anode and cross the anode/ solid electrolyte interface, then diffuse in the solid electrolyte towards the cathode, then the mobile lithium ions cross the cathode/ solid electrolyte interface, and finally enter unoccupied sites in cathode structure together with electron transfer in the external circuit. When charging, the mobile lithium ions and electrons move in the opposite direction.

Figure 1.4 Schematic diagram of an all solid-state battery

The development of all solid-state lithium ion batteries is still at an early stage. One main reason that restricts the actual application of these systems is the lithium ion conducting solid electrolyte itself and the interfacial issues including the anode/electrolyte interface and the cathode/ electrolyte interface. For the desired application in lithium batteries, solid-state electrolytes should have the following characteristics:

(1) High ionic conductivity, typically about half that of a liquid electrolyte, in the order of 10^{-2} –10^{-3} S cm^{-1} or even higher at room temperature; at the same time, the electronic conductivity should be negligible.

(2) A wide electrochemical stabilised voltage window to maximise the output voltage.

(3) Favourable chemical and electrochemical compatibility with the anode and cathode materials [20].

Currently depending on the electrolytes, there are mainly three kinds of all solid-state lithium batteries, the first uses polymer films as the electrolyte, the second uses inorganic glasses, while the third utilises inorganic polycrystalline ceramics. Different systems have their own issues and problems related to the specific electrolyte. In general, the range of alternative solid electrolytes is still very limited. Though the ionic conductivity of a few solid-state electrolytes has achieved values in the order of 10^{-3} S cm^{-1} at room temperature, the electrode/electrolyte interface is still problematic and much more work is required to overcome the interface problem.

1.3 Lithium ion conducting solid electrolytes

As mentioned above, solid electrolytes can be mainly classified into three categories, namely polymers, inorganic glasses and inorganic crystalline solids. Each of them will be discussed below.

1.3.1 Solid polymer electrolytes

For the use of all solid-state lithium ion batteries, solid polymer electrolytes (SPEs) not only have the advantages of high safety, but also have the property of high flexibility, which is especially critical for the wearable devices.

Polymers, made up of many repeated subunits, are macromolecules with molecular weights varying from hundreds to millions g mol^{-1}. According to their structures, polymers can be either amorphous or semi-crystalline. As can be seen in Fig.1.5, when the temperature increases, both amorphous and semi-crystalline polymers go through a glass transition at temperature T_g, but with the further temperature increase, amorphous polymers (A) do not show any other phase

transitions, in contrast, semi-crystalline polymers (B) undergo crystallization followed by melting at temperatures T_c and T_m, respectively. At temperatures below T_g, molecular motion is restricted and the polymer itself is glassy and brittle, while above T_g, molecular motions are activated and the polymer becomes viscous and rubbery. In the case of semi-crystalline polymers, at the crystallization temperature, T_c, sufficient energy is available for the polymer to rearrange and crystallise.

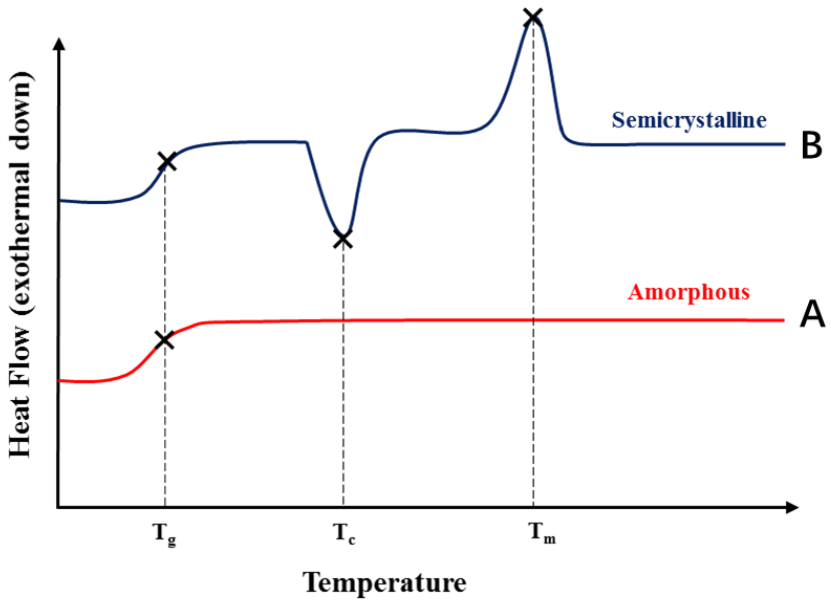

Figure 1.5 Heat flow for amorphous and semi-crystalline polymers based on differential scanning calorimetry (DSC)

SPEs are ion-conducting polymer-salt complexes formed through dissolution of an alkali metal salt into a solid polymer matrix, without the addition of an organic solvent. Within the polymer matrix, the lithium ions are bonded to electronegative atoms such as O atoms strongly through binding interactions [21]. Lithium ion transport happens through motion of the polymer chains allowing the Li^+ ions to move along the chains. Table 1.3 lists the lithium ion conductivity of some typical solid polymer electrolytes. Polyethylene oxide (PEO) is the most commonly used polymer in SPEs due to the combination of its flexible ethylene oxygen subunit, and ether oxygen atoms which act as strong donors and thus easily solvate Li^+ cations. Its T_g

and T_m are about -64 °C and 65 °C, which represents an ideal temperature range for most applications [22]. The most commonly used lithium salts in SPEs are $LiClO_4$, $LiPF_6$, $LiBF_4$, $LiAsF_6$, $LiCF_3SO_3$, $LiN(CF_3SO_2)_2$, etc, similar to liquid electrolytes.

Table 1.3 Lithium ion conductivity of some typical solid polymer electrolytes, adapted from [21]

Polymer electrolyte	Conductivity (S cm^{-1})	Temperature (ºC)
$P(EO)_{20}/LiBF_4$	6.32×10^{-7}	27
$P(EO)_{20}/LiClO_4$	2.78×10^{-7}	27
PEO/5 wt% $LiPF_6$	1.20×10^{-6}	25
PEO/11.1 wt% $LiAsF_6$	1.43×10^{-4}	25
$P(EO)_{20}/LiCF_3SO_3$	1.88×10^{-9}	27
$P(EO)_{24}/LiN(CF_3SO_2)_2$	3.84×10^{-4}	50
P(PO)/10 mol% $LiClO_4$	$> 10^{-4}$	50
MEEP/10 wt% $LiCF_3SO_3$	1.00×10^{-5}	25
MEEP/25 wt% $LiCF_3SO_3$	2.70×10^{-5}	30
$P(Si)_{32}/LiN(CF_3SO_2)_2$	4.50×10^{-4}	25

As can be seen in Table 1.3, SPEs still face the problem of low ionic conductivity. Research on overcoming this problem has included the addition plasticizers like succinonitrile (SN) [23] and polysquarate (PPS) [24], adding an ionic liquid like 1-ethyl-3-methylimidazolium (EMI) to weaken the interaction between the polymer chains and lithium ions [25] and adding inorganic compounds like Al_2O_3 [26] to weaken the crystallization of polymer and create a polymer-ceramic interface to enhance the conductivity.

If an organic liquid electrolyte is added to an SPE, a polymer gel can be formed. These gel polymer electrolytes (GPEs) show conduction mechanisms similar to organic liquid electrolytes, and higher conductivities are obtained while the mechanical strength may be

reduced in some cases such as PEO-based GPE where the PEO can become plasticized by the organic solvents [27].

1.3.2 Inorganic glass electrolytes

Inorganic glasses are an important class of solid electrolytes. Although the ionic conductivity in polycrystalline inorganic solid electrolytes is typically high, the total conductivity is reduced since the disordered interfacial region between individual grains leads to grain boundary resistance. In the process of vitrification for inorganic glasses, the individual crystallites are replaced by a continuous matrix and hence grain boundary resistances are eliminated. Additionally, the adjustable composition of inorganic glasses not only allows for the tailoring of electronic and ionic conduction, but also physical properties such as mechanical strength and thermal stability [28].

The principal strategy to develop glass electrolytes with high lithium ion conductivity is to increase the concentration and mobility of the ionic charge carriers. Currently there are mainly four types of glass electrolytes, oxide glasses, oxide glass ceramics, sulfide glasses and sulfide glass ceramics, all of which are commonly prepared by the melt-quenching method.

There are many definitions of what constitutes a glass but perhaps one of the most useful is that a glass is an amorphous solid that exhibits a glass transition temperature [29]. Only certain types of inorganic compounds can form glasses. In the case of oxide systems, the most common glass-formers are SiO_2, P_2O_5 and B_2O_3. Their structures are characterised by a covalent network of corner sharing tetrahedra or in the case of B_2O_3, tetrahedra and triangles. To these network formers, ionic network modifiers such as Li_2O, Na_2O and CaO can be added to break up the network through the introduction of non-bridging atoms, giving the network a negative charge. In the case of lithium ion conductors, the lithium ions become mobile through hopping along the anionic chains formed by the addition of network modifiers. A third type of component is

the network intermediate e.g. Al_2O_3, ZnO, MnO and FeO which can either act in a network forming or network modifying role. Glasses are typically characterised by two principal temperatures, The glass transition temperature, T_g, and the crystallisation temperature, T_c. When a melt of a glass forming system is cooled slowly it will typically crystallise at a certain temperature, roughly corresponding to the melting temperature on heating. However, if the melt is rapidly cooled it remains in a liquid-like state and bypasses crystallisation until it reaches the glass transition temperature, T_g, where the viscosity rapidly increases and the glass solidifies. In fact, the value of T_g can vary significantly depending on the cooling rate. Since the glass is metastable with respect to the crystalline phase, heating a glass above T_g results in exothermic crystallisation at T_c. At this point the system consists of crystallites within a residual glass matrix and is known as a glass ceramic.

Oxide glasses and oxide glass ceramics based on the lithium titanium phosphate system Li_2O:TiO_2:P_2O_5 are among the most promising oxide group due to their high lithium ion conductivity (around 1.3×10^{-3} S cm^{-1} at room temperature for glass ceramics) and high stability [30]. The well-known NASICON phase, $LiTi_2(PO_4)_3$, does not readily form glasses, but can be crystallised in more phosphate rich compositions. Based on the $50Li_2O - 10TiO_2 - 40P_2O_5$ parent composition, Al_2O_3 substitution for TiO_2 to introduce more Li_2O in the system of $(50 + x)Li_2O - xAl_2O_3 - (10 - 2x)TiO_2 - 40P_2O_5$ ($0 \leq x \leq 4.5$) was explored [31]. The highest conductivity ($\sigma = 2.0 \times 10^{-2}$ S cm^{-1} at 350 °C) and lowest activation energy (E_a = 0.50 eV) was exhibited for the x = 0.5 composition. This composition also exhibited the greatest thermal stability against crystallization with Tc – Tg = 146 °C. This research group later examined the different roles in glass structure of Sn and Ti in the closely related $50Li_2O - x\ SnO_2 - (10 - x)TiO_2 - 40P_2O_5$ ($0 \leq x \leq 10$) system [28]. They observed that increasing Sn content up x = 6.0 led to a decrease in d.c. (direct current) conductivity and attributed this to the different coordination environments of Sn and Ti, which were predominantly network forming, the

former being four coordinate and the latter five coordinate, leading to different availabilities for non-bridging oxygens and different trapping of the mobile Li^+ ions.

The Li_2S-based sulfide glasses, such as Li_2S - P_2S_5 and Li_2S - SiS_2 systems, exhibit higher ionic conductivities than oxide glasses. Table 1.4 lists the conductivity of some oxides and sulfides [32]. It can be seen that the ionic conductivity can be increased drastically by changing the matrix from oxide to sulfide. According to the "hard and soft acids and bases theory" by Pearson [33], the lithium ion is a "hard acid", and it would be more compatible to the sulfide ion which acts as a "soft base", thus increasing the mobility of Li^+ ions.

Table 1.4 Conductivity of oxide and sulfide solid electrolytes at 25 °C, adapted from [32]

Composition	Conductivity at 25℃ (S cm^{-1})	Classification
$La_{0.51}Li_{0.34}TiO_{2.94}$	1.4×10^{-3}	crystal (perovskite)
$Li_{1.3}Al_{0.3}Ti_{1.7}(PO_4)_3$	7×10^{-4}	crystal (NASICON)
$Li_7La_3Zr_2O_{12}$	3×10^{-4}	crystal (garnet)
$50Li_4SiO_4\cdot50Li_3BO_3$	4×10^{-6}	Glass
$Li_{2.9}PO_{3.3}N_{0.46}$	3.3×10^{-6}	amorphous (thin film)
$Li_{3.6}Si_{0.6}P_{0.4}O_4$	5.0×10^{-6}	amorphous (thin film)
$Li_{1.07}Al_{0.69}Ti_{1.46}(PO_4)_3$	1.3×10^{-3}	glass-ceramic
$Li_{1.5}Al_{0.5}Ge_{1.5}(PO_4)_3$	4.0×10^{-4}	glass-ceramic
$Li_{10}GeP_2S_{12}$	1.2×10^{-2}	Crystal
$Li_{3.25}Ge_{0.25}P_{0.25}S_4$	2.2×10^{-3}	Crystal
$30Li_2S\cdot26B_2S_3\cdot44LiI$	1.7×10^{-3}	Glass
$63Li_2S\cdot36SiS_2\cdot1Li_3PO_4$	1.5×10^{-3}	Glass
$57Li_2S\cdot38SiS_2\cdot5Li_4PO_4$	1.0×10^{-3}	Glass
$70Li_2S\cdot30P_2S_2$	1.6×10^{-4}	Glass
$50Li_2S\cdot50GeS_2$	4.0×10^{-5}	Glass
$Li_7P_3S_{11}$	5.4×10^{-3}	glass-ceramic
$Li_{3.25}P_{0.95}S_4$	1.3×10^{-3}	glass-ceramic

Other methods such as constructing glass – crystalline composites like $Li_{0.5}La_{0.5}TiO_3$ - silica-based glass [34] and polymer – glass composites like $(LiAlTiP)_xO_y$ glass - PEO-based polymer [35] have also been shown to be effective in increasing ionic conductivity.

Although sulfide glasses have better conductivity than oxide glasses, it is noteworthy that from the view of practical use, oxides have greater commercial potential since they are stable in air and easier to fabricate and handle while sulphides are hygroscopic in air and have special fabrication and storage requirements.

1.4 Inorganic crystalline solid electrolytes

In the category of inorganic crystalline solids, lithium-ion conductivity has been exploited in a large number of solid systems such as LISICONs (lithium superionic conductor), NASICON (sodium superionic conductor) structured lithium ion conductors, garnets, argyrodites, perovskites, lithium hydride, lithium halides etc. Within each family of crystal structures, a vast compositional space is included, with the lithium-ion conductivity varying greatly by up to 5-6 orders of magnitude. Lithium ionic conductivities of some representative inorganic crystalline solids are listed in Fig. 1.6 [36]. Some compositions of these structural families such as Li_6PS_5Br [37], $Li_{3.25}Ge_{0.25}P_{0.75}S_4$ and $Li_{10}GeP_2S_{12}$ [38] exhibit high lithium-ion conductivities in the range of 10^{-2} to 10^{-3} S cm^{-1} at room temperature.

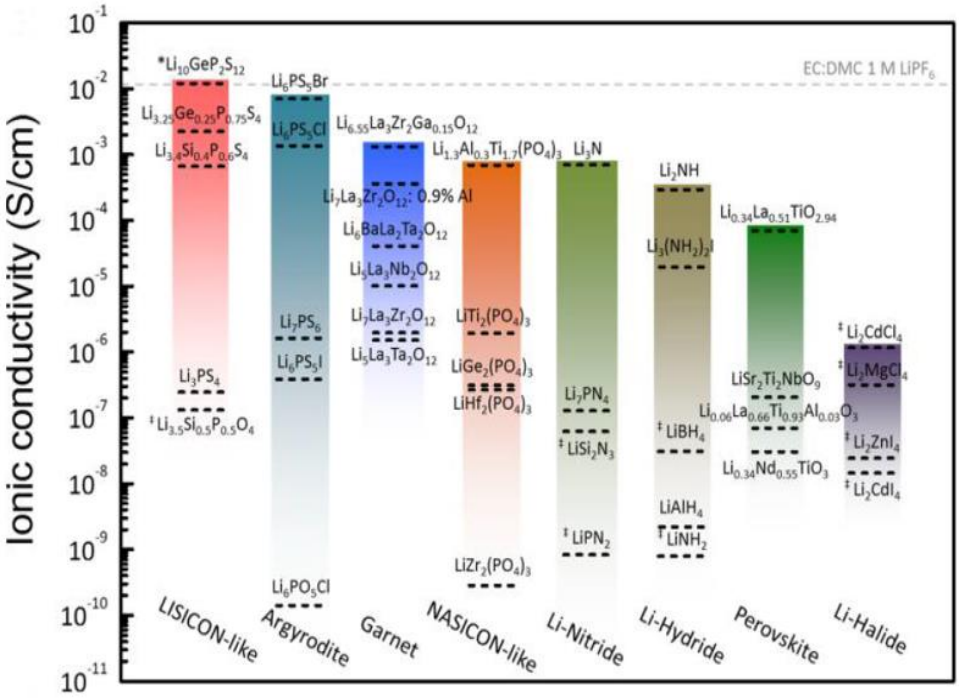

Figure 1.6 Reported ion conductivity of inorganic crystalline solid-state lithium-ion conductors at room temperature [36]

1.4.1 Ionic conductivity

For the inorganic crystalline lithium ion conducting solid electrolytes, lithium ion conduction is often due to the hopping of lithium ions between energetically favourable sites, with the activation energy for mobile ions to move through channels in the crystalline framework dictated by the motion of the surrounding ions [39].

In 1978, Hong proposed that for materials with a rigid cation-anion three-dimensional structure framework to be used as ionic conductors, some essential structural features need to be present. Firstly, the interstitial sites within the framework should be partially occupied by mobile Li^+ ions; secondly, since the ionic mobility is determined physically by the size of bottleneck between the adjacent mobile Li^+ interstitial sites and chemically by the chemical energy between the mobile Li^+ ion and the surrounding framework constituents, to favour Li^+ ion diffusion, the size of bottleneck should be twice the sum of the Li^+ and the framework anion radii and the bonding energy between the mobile lithium ion and the anion should be as weak

as possible and this can be achieved if the anion forms strong covalent bonds with the other cations that make the structure of the network.

Fig. 1.7a shows part of the NaCl structure including a Na^+ vacancy site. In order for ion migration to occur, the adjacent Na^+ ion has to pass through the cenral interstitial site of the cube. The face of this tetrahedral interstitial site is formed by the three Cl^- ions labelled 1-2-3 (Fig. 1.7b). To exit the interstitial site and enter the vacant octahedral site the ion must pass through a second face made up of Cl^- ions 1-2-4. These two faces of the interstitial sites make up the "bottleneck". The small bottleneck size raises the potential energy for Na^+ ion migration.

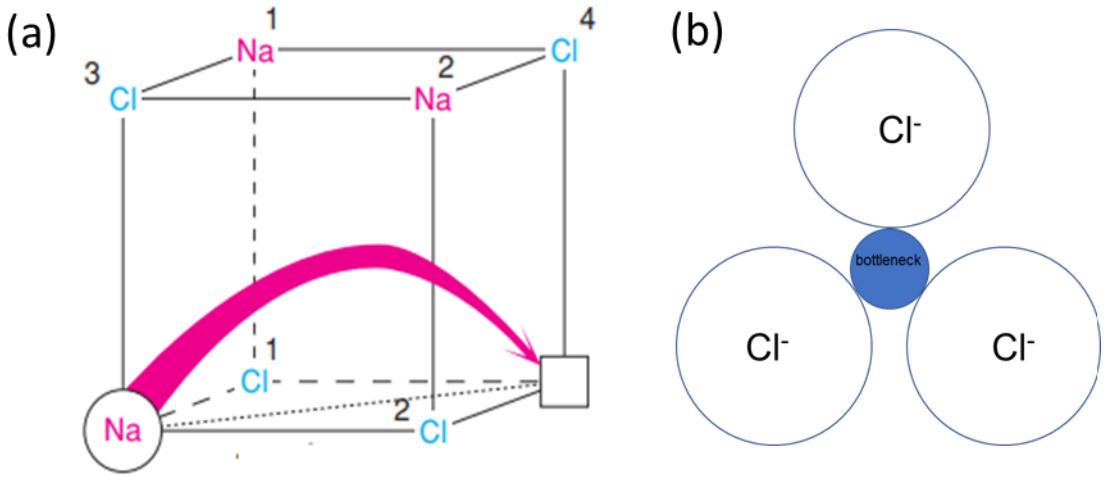

Figure 1.7 (a) Pathway for Na^+ migration in NaCl, (b) bottleneck formed by Cl^- through which a migrating Na^+ ion must pass in NaCl [40]

The specific conductivity (σ) of a conductor material is given by:

$$\sigma = nq\mu \tag{1.8}$$

where *n* is the number of charge carriers of (Li^+ ions in the case of Li+ ion conductors) per unit volume, *q* is the charge and μ is the mobility.

The conductivity can also be expressed through the related diffusion coefficient, *D*, through the Nernst−Einstein equation as in Eqn. 1.9, where k_B is the Boltzmann constant (k_B = 1.38 × 10^{-23} J/K) and *T* is the temperature in Kelvin.

$$\sigma = D \times \frac{nq^2}{k_B T} \tag{1.9}$$

Over a temperature range, the relationship between ionic conductivity σ and activation energy E_a is described in the Arrhenius equation, as expressed below:

$$\sigma = \left(\frac{A}{T}\right) e^{\frac{-E_a}{RT}} \tag{1.10}$$

where T is the temperature in Kelvin, A is a pre-exponential factor and R is the molar gas constant. As can be seen, lower activation energy and big pre-exponential factor lead to higher ionic conductivity. E_a contains two parts, one is the defect formation energy E_f and the other is the migration energy E_m. In a superionic phase, the temperature does not affect the number of mobile species and E_a can be identified with E_m.

From Eqn. 1.8 and 1.9, the ionic conductivity of lithium ion conducting crystalline solids is affected by the number of mobile Li^+ ions, and the concentration of mobile Li^+ ions is seen to be dependent on the type and amounts of interstitial Li^+ ions, vacancies, and partial occupancy on lattice sites which can be realised by partial substitution of aliovalent cations. However, high concentrations of Li^+ ions to some extent may not increase the lithium-ion conductivity, which might be suppressed by the strengthened interactions between Li^+ ions and the framework [41]. Therefore, lithium ion concentration will affect the mobility of lithium ions, μ, and the effective concentration of mobile Li^+ ions. Therefore, the coupling effect between the lithium ion mobility and lithium ion concentration should be considered when using the strategy of aliovalent substitution to enhance the ionic conductivity of lithium-ion conductors.

1.4.2 NASICON structure

Much early work on solid cationic conductors focused on sodium ion conductors such as sodium β-alumina and silver ion conductors such as rubidium silver iodide ($RbAg_4I_5$). In the 1960s, high Na^+ ion diffusion between adjacent alumina layers was observed in layered β-

Al_2O_3, indicating that β- Al_2O_3 is a two dimensional cation conductor [42]. In 1976, a 3D framework structure $Na_{1+x}Zr_2P_{3-x}Si_xO_{12}$ was prepared by Hong and Goodenough et al., in which Na^+ ions diffuse through three dimensional channels [43, 44]. $Na_{1+x}Zr_2P_{3-x}Si_xO_{12}$ was named the sodium super ionic conductor (NASICON). Subsequently other phosphate-based compounds were developed.

The general structural formula of NASICON can be described as $A_xM_2(BO_4)_3$ where A is an Na^+ ion, M is a trivalent (Cr^{3+}, Al^{3+}, Ga^{3+}, Sc^{3+}, Y^{3+}, In^{3+}, or La^{3+}) or tetravalent (Ti^{4+}, Ge^{4+}, Sn^{4+}, Hf^{4+}, or Zr^{4+}) cation and B is P or Si [45-48]. The NASICON structure consists of a rigid three-dimensional skeletal framework with PO_4/SiO_4 tetrahedra sharing oxygen corners with MO_6 octahedra. Generally NASICON crystals mainly exist in the form of a rhombohedral structure with space group $R\bar{3}c$, even though other phases are reported such as the triclinic $NaM_2(PO_4)_3$ (M^{4+}: Sn^{4+}, Hf^{4+} or Zr^{4+}) [49] . A small distortion of the $R\bar{3}c$ structure leads to a distorted monoclinic structure in space group $C2/c$. Correspondingly, the interstitial Na sites vary in these structures with changes in site-preference energy.

In the rhombohedral NASICON structure shown in Fig. 1.8, There are two kinds of interstitial Na sites located between the alternating MO_6 octahedral and PO_4/SiO_4 tetrahedral framework, Na1 (Wyckoff positions: 6b) and Na2 (Wyckoff positions: 18e). Na1 sites are located between two adjacent PO_4/SiO_4 - MO_6 units along the *c*-axis, surrounded by six oxygen atoms, in octahedral geometry. Na2 sites are again located between two PO_4/SiO_4 - MO_6 units, but this time are surrounded by ten oxygen atoms. The ionic conductivity is through the Na^+ ions diffusing between Na1 and Na2 sites through the interconnected bottlenecks. The size of bottlenecks is determined by the intrinsic nature of the skeletal ions and the concentration of mobile ions at interstitial sites.

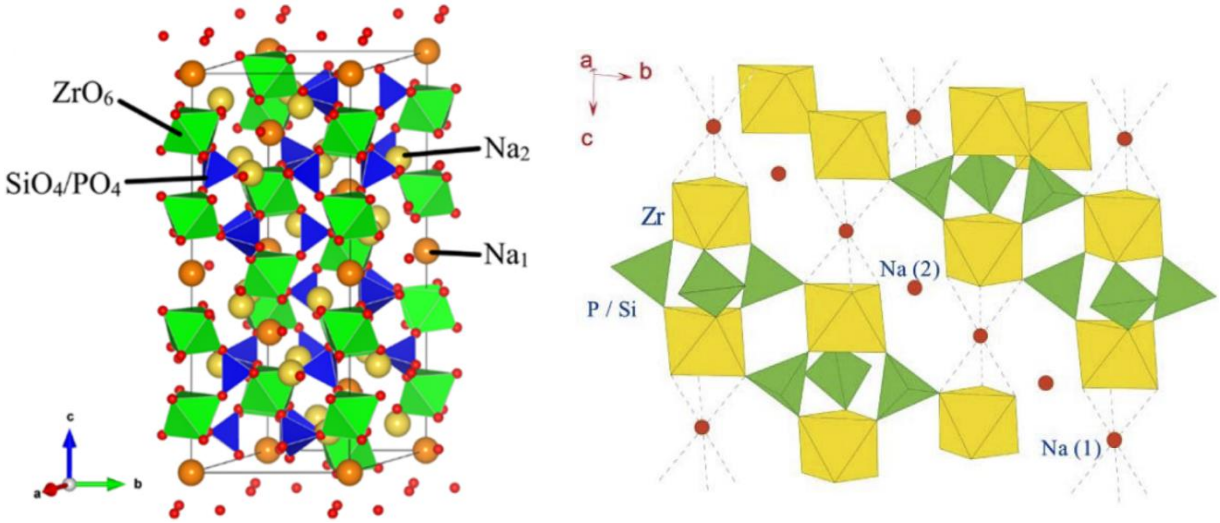

Figure 1.8 Crystal structure of rhombohedral NASICON $R\bar{3}c$ [50, 51]

Lithium ion conductors with the NASICION structure are realized by replacing the Na^+ ions with Li^+ ions. The ionic conductivity can vary a lot for the same composition with different phases. For example, $LiZr_2(PO_4)_3$ (LZP) shows complex polymorphism, depending on the synthesis conditions, LZP adopts the rhombohedral $R\bar{3}c$ structure when the calcination temperature is above 1100 °C, showing a conductivity of about 10^{-5} S cm^{-1} at 25 °C; when at low temperature (around 55 °C), phase transition occurs to a triclinic phase, showing a conductivity of about 10^{-9} S cm^{-1} at the same temperature [52].

Among the $LiM_2(PO_4)_3$ (M^{4+}: Ti^{4+}, Sn^{4+}, Hf^{4+}, Ge^{4+} or Zr^{4+}) phases, $LiTi_2(PO_4)_3$ (LTP) exhibits a relatively high conductivity of about 10^{-5} S cm^{-1} at 25 °C [53], making it attractive and promising for further optimization based on the end member $LiTi_2(PO_4)_3$. A great deal of work has been carried out based on LTP. Although altering the bulk microstructure through different synthetic methods such as wet or dry mixing, sintering techniques, etc. can make a big difference in the final conductivity, heteroatom doping is often used successfully as it can change the chemical nature of the crystal structure. Substitution of Ti^{4+} by sub-valent cations such as Al^{3+} and Sc^{3+}, with charge balance maintained by introduction of interstitial Li^+ ions yields materials with very high lithium ion conductivity at room temperature [54]. For example,

the Li^+ ion conductivity of $Li_{1.3}Sc_{0.3}Ti_{1.7}(PO_4)_3$ is 7×10^{-4} S cm^{-1} at room temperature [55, 56]. One of the highest Li^+ ion conductivities observed for this type of compound is for $Li_{1.3}Al_{0.3}Ti_{1.7}(PO_4)_3$ (LATP) with a value of 3×10^{-3} S cm^{-1} at room temperature. LATP can be easily fabricated without special control for moisture and air, which is very beneficial for large-scale production. However, several issues still exist, like the different volume expansion coefficients between electrode materials and LATP solid electrolytes, which can reduce the effective interfacial contact area and cause large interfacial impedance after long-term cycling [57]. Additionally, titanium-containing compounds are not stable in contact with lithium metal anodes and Ti^{4+} can be reduced to Ti^{3+} at low voltages [56].

1.4.3 Perovskite structure

The perovskite structure is no doubt one of the most important structural types in inorganic materials chemistry. Materials with this structure have wide applications in the area of energy, such as solar cells, photocatalytic water splitting, photo-electric catalysts in fuel batteries, etc. Perovskite structures refer to materials with the structure of $CaTiO_3$, which are generally expressed as the formula ABO_3, the A site and B site cations are 12-fold and 6-fold coordinated to the oxygen anions, respectively, as shown in Fig. 1.9. An ideal perovskite has a cubic structure in $Pm\bar{3}m$ space group as in $SrTiO_3$.

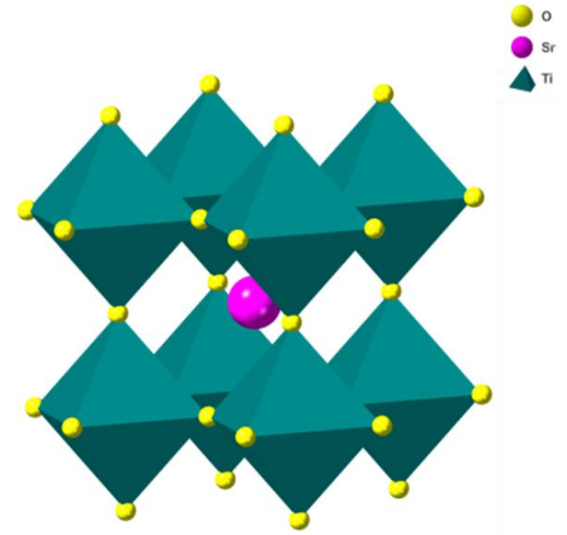

Figure 1.9 Ideal perovskite structure of $SrTiO_3$ (generated from the structural data in reference [58])

When researching the electrical properties of the perovskite type material $Li_{3x}La_{1/3-x}\square_{2/3-2x}TiO_3$ (where □ represents a vacancy) at high temperature, a large dielectric loss and dielectric relaxation were seen to occur, Belous et al. speculated that the system may have high lithium ion conductivity [59]. These authors concluded that the La^{3+} ions in $Li_{3x}La_{1/3-x}\square_{2/3-2x}TiO_3$ stabilize the perovskite structure, while some of the Li^+ ions are diffuse, resulting in high ionic conductivities. Depending on the *x*-value and synthesis conditions, the phase structure of $Li_{3x}La_{1/3-x}\square_{2/3-2x}TiO_3$ can be orthorhombic, tetragonal or cubic. It is considered that the high lithium ion conductivity of $Li_{3x}La_{1/3-x}\square_{2/3-2x}TiO_3$ occurs through a vacancy mechanism where lithium ions diffuse through the wide square planar bottlenecks between the A sites together with a large concentration of A-site vacancies. In addition, it is thought that TiO_6 octahedral tilting can also facilitate the lithium ion mobility in the perovskite structure [60]. However, similar to the LATP solid electrolyte, the easy reduction of Ti^{4+} to Ti^{3+} by metallic lithium anodes is an issue that restricts its commercial application. To date, the highest lithium-ion conductivity of a perovskite structured oxide has been found in the related compound $Li_{0.34}La_{0.56}\square_{0.1}TiO_3$ with a room temperature bulk ionic conductivity of 10^{-3} S cm^{-1} and a total lithium-ion

conductivity of 7×10^{-5} S cm^{-1} due to the high grain boundary resistance [61]. The mechanism of lithium ion conduction in this system is still not clearly understood.

Recently, a new class of materials with the lithium-rich anti-perovskite structure Li_3OX (X: Cl, Br) has been reported [62, 63]. As shown in Fig 1.10, the halogen anion occupies the A sites, while the B sites are occupied by O^{2-} anions, which form Li^+ corner-sharing OLi_6 octahedra with adjacent Li^+ ions. It has the highest lithium concentration among all the lithium-based solid-state electrolytes proposed so far.

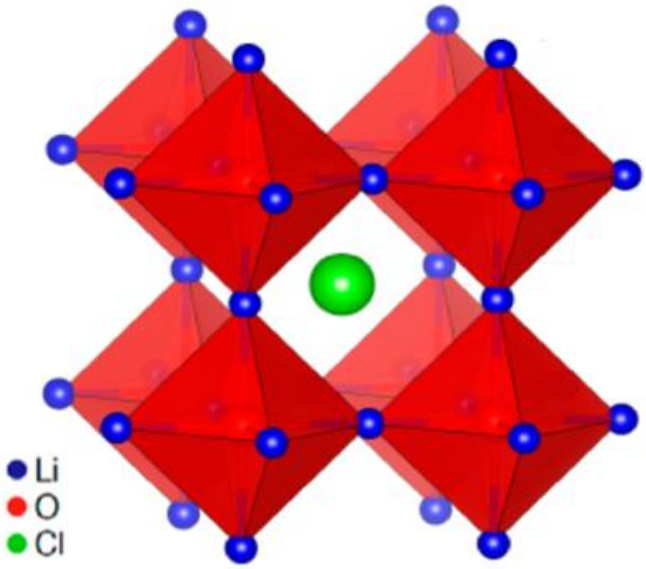

Figure 1.10 Crystal structure of lithium-rich anti-perovskite based on the structure reported in [62]

Correspondingly, Li_3OX (X: Cl, Br) compounds exhibit ionic conductivities of about 10^{-3} S cm^{-1} and activation energies of 0.2 – 0.3 eV at room temperature [63]. Large-scale molecular dynamics simulations were employed to assess the ionic transport at the grain boundaries in Li_3OCl. The calculated Li^+ ion migration activation energy at the grain boundaries was found to be around 0.40 – 0.56 eV, about two times higher than that of the bulk, which well explains the higher grain boundary resistance seen in these materials [62]. It has to be mentioned that in the presence of water, Li_3OX (X: Cl, Br) is decomposed immediately to lithium hydroxide and

lithium halides with low toxicity. This property necessitates careful synthesis conditions, but offers a possible solution to the recycling of Li_3OX compounds.

1.4.4 Garnet structure

In 2003, Weppner et al. first proposed the novel garnet $Li_5La_3M_2O_{12}$ (M = Ta, Nb) as a Li^+ ion conducting solid electrolyte. They proved that both $Li_5La_3Nb_2O_{12}$ and $Li_5La_3Ta_2O_{12}$ exhibit similar bulk ionic conductivities of around 10^{-6} S cm^{-1} at 25 °C, with activation energies of 0.43 and 0.56 eV, respectively [64]. Additionally, both are stable in contact with Li metal. Over the following years, Weppner and co-workers explored the Li^+ ion migration pathway in $Li_5La_3M_2O_{12}$ (M = Ta, Nb) [65] and several more garnet type lithium ion conductors like $Li_6ALa_2Nb_2O_{12}$ (A: Ca, Sr, Ba) and $Li_6ALa_2Ta_2O_{12}$ (A: Sr, Ba), all of which are isostructural with the cubic parent compounds $Li_5La_3M_2O_{12}$ (M = Ta, Nb) in space group $Ia\bar{3}d$. Of these, $Li_6BaLa_2Ta_2O_{12}$ exhibits the highest ionic conductivity, with a value of 4.0×10^{-5} S cm^{-1} and an activation energy of 0.40 eV at 22 °C, together with very low electronic conductivity and a wide electrochemical stability window (> 6 V/Li) [66-68].

The structures of the tetragonal and cubic phases of $Li_7La_3Zr_2O_{12}$ (LLZO) were determined by single-crystal X-ray analysis by Awaka et al. in 2009 and 2010 [69, 70]. Cubic $Li_7La_3Zr_2O_{12}$ adopts the same $Ia\bar{3}d$ space group as other cubic garnet structures. Its refined crystal parameters are summarised in Table 1.5 and the structure is shown in Fig. 1.11. The La^{3+} and Zr^{4+} cations are eight-fold and six-fold coordinated to oxygen anions, forming LaO_8 dodecahedra and ZrO_6 octahedra, respectively, which constitute the framework. There are two types of crystallographic sites for Li^+ ions in the structure, one is the tetrahedral 24d site for Li1 and the other one is the distorted octahedral 96h site for Li2. There are two equivalent Li2 sites in the distorted octahedron only one of which can be occupied at any one time.

Table 1.5 Refined structural parameters for cubic $Li_7La_3Zr_2O_{12}$ [69]

Atom	Site	*Occ.*	*x*	*y*	*z*	*U*/ Å^2
Li1	24*d*	0.94(7)	3/8	0	1/4	0.021(4)
Li2	96*h*	0.349	0.0959(15)	0.6922(14)	0.5731(15)	0.021
La	24*c*	1	1/8	0	1/4	0.0097(2)
Zr	16*a*	1	0	0	0	0.0064(2)
O	96*h*	1	-0.03163(18)	0.0538(2)	0.1501(2)	0.0107(7)

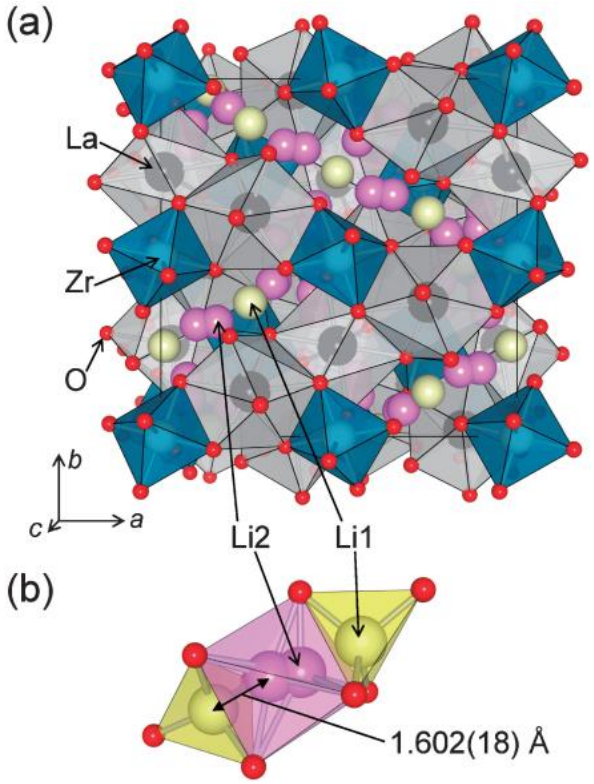

Figure 1.11 Crystal structure of cubic $Li_7La_3Zr_2O_{12}$ [69]

The tetragonal phase of $Li_7La_3Zr_2O_{12}$ adopts the $I4_1/acd$ space group, which is the maximal subgroup of $Ia\bar{3}d$ for the cubic garnet structure. The refined crystal parameters are given in Table 1.6, with structure shown in Fig. 1.12. There are three types of Li sites: one is a tetrahedral 8a site for Li1 and the other two are distorted octahedral 16f and 32g sites for Li2 and Li3.

Table 1.6 Refined structural parameters for tetragonal $Li_7La_3Zr_2O_{12}$ [70]

Atom	Site	*Occ.*	*x*	*y*	*z*	*U*/ Å^2
La (1)	8*b*	1	0	1/4	1/8	0.0059(2)
La (2)	16*e*	1	0.12716(5)	0	1/4	0.0057(2)
Zr	16*c*	1	0	0	0	0.0050(3)
Li (1)	8*a*	1	0	1/4	3/8	0.05(2)
Li (2)	16*f*	1	0.1813(13)	0.4313(3)	1/8	0.035(10)
Li (3)	32*g*	1	0.0796(12)	0.0863(11)	0.8099(12)	0.021(8)
O (1)	32*g*	1	-0.0335(3)	0.0546(3)	0.1528(3)	0.007(2)
O (2)	32*g*	1	0.0534(3)	0.8525(3)	0.5366(4)	0.008(2)
O (3)	32*g*	1	0.1499(3)	0.0273(3)	0.4454(3)	0.007(2)

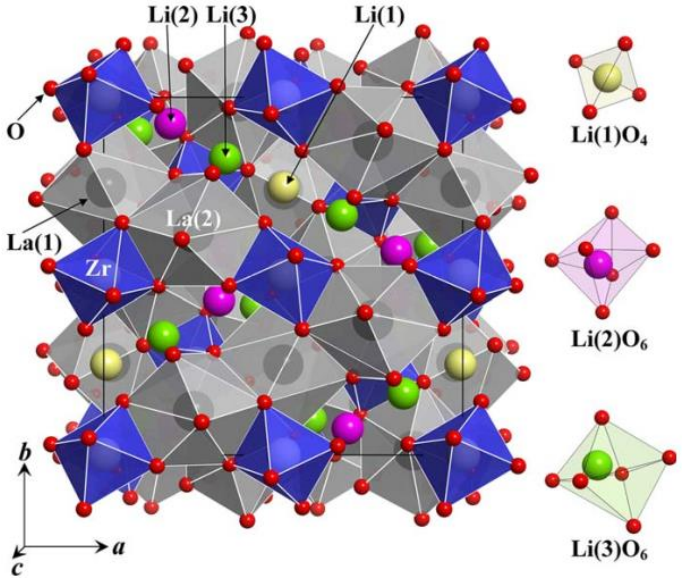

Figure 1.12 Crystal structure of tetragonal $Li_7La_3Zr_2O_{12}$ [70]

Through the combination of molecular dynamics and density functional theory, Chen et al. proposed that cubic LLZO exhibits 3-dimensional lithium ion diffusion, while tetragonal LLZO mainly exhibits diffusion in the *a* and *b* directions. The restricted *c*-direction diffusion is due to the blocking effect of thermodynamically stable 16f sites compared to the 8a and 32g

sites [71]. Generally, the cubic garnet structure has better ionic conductivity than the tetragonal structure.

Many kinds of garnets such as $Li_3Ln_3Te_2O_{12}$ (Ln = Y, Pr, Nd, Sm - Lu), $Li_5La_3M_2O_{12}$ (M = Nb, Ta, Sb), $Li_6ALa_2M_2O_{12}$ (A = Mg, Ca, Sr, Ba; M = Nb, Ta) and $Li_7La_3M_2O_{12}$ (M = Zr, Sn) have been investigated to explore the effect of Li^+ ion concentration and cation species on the conductivity [72]. Partial substitution of Li by Ga in LLZO was investigated [73]. $Li_{6.55}Ga_{0.15}La_3Zr_2O_{12}$ sintered in O_2 showed a high ionic conductivity of 1.3×10^{-3} S cm^{-1} at room temperature, the introduced Ga^{3+} cations are located in the tetrahedral Li1 sites in Fig. 1.12, promoting the random distribution of Li^+ ions and vacancies.

1.4.5 Non-oxide lithium ion conducting solid electrolytes

Non-oxide lithium ion conductors mainly include nitrides, halides, hydrides and sulfides. In 2008, Deiseroth et al. first reported new series of lithium argyrodites Li_6PS_5X (X: Cl, Br, I), of which the ion conductivity of Li_6PS_5Br approaches 10^{-2} S cm^{-1} at room temperature [37]. The crystal structure of Li_6PS_5I is shown in Fig. 1.13. The structure may be described as containing $(PS_4)^{3-}$ tetrahedra with additional S^{2-} and I^- ions making up a trigonal bipyramidal (double tetrahedron) coordination for the Li^+ ions which are disordered over two crystallographic sites Li1 and Li2, with two Li1 sites above and below the common face of the double tetrahedron and Li2 at the centre of the common face. However, since the lithium argyrodites are air-sensitive, their synthesis conditions require the use of inert atmosphere or a sealed environment, which could restrict their commercial application.

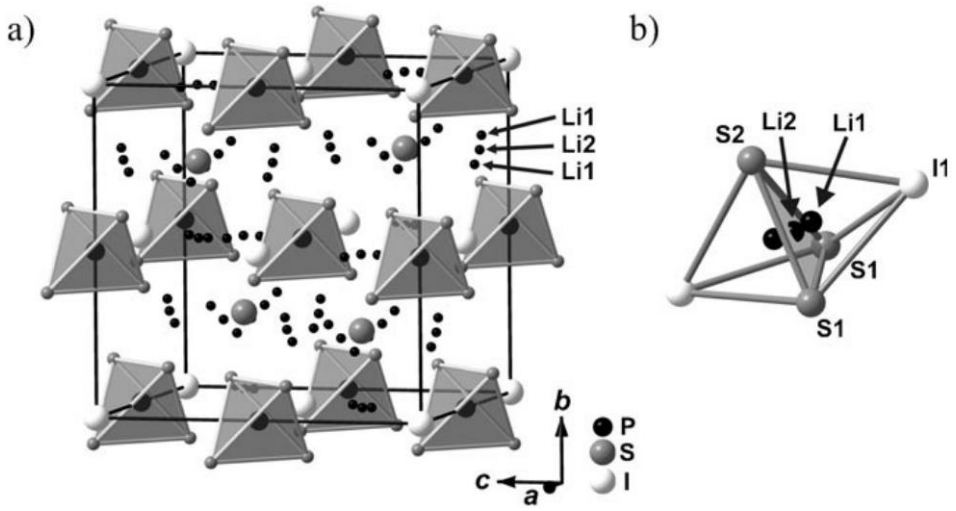

Figure 1.13 Crystal structure of Li_6PS_5I [37]. Li is distributed over Li1 and Li2 sites, which cannot be simultaneously occupied.

Li_3N exhibits a conductivity of 4×10^{-2} S cm^{-1} at room temperature [74]. It can be synthesised by heating Li rod in an atmosphere of N_2 at 800 °C. The structure of Li_3N consists of hexagonal close packed Li_2N layers, with adjacent layers connected by Li^+ ions to form N-Li-N bridges. Li^+ ions diffuse through the 2-dimensional layers [75]. Though the conductivity of Li_3N and related composite systems like Li_3N-LiCl is high, the electrochemical stability window is narrow, which is a barrier for their commercial application.

A new complex hydride $Li_3(NH_2)_2I$ shows a lithium ionic conductivity of 1×10^{-5} S cm^{-1} at 25 °C with a lithium ion transport number of almost unity [76]. This conductivity is much higher compared to those of the parent materials $Li(NH_2)$ (3×10^{-9} S cm^{-1}) and LiI (3×10^{-8} S cm^{-1}). $Li_3(NH_2)_2I$ adopts a double layer structure in the hexagonal space group $P6_3mc$.

Spinel-type halides Li_2MCl_4 (M = Mg, Mn, Fe and Cd) can also be used as lithium ion conductors, though their conductivity is still too low for commercial use [77].

Sulfides especially the thio-LISICONS have received much attention due to their excellent ionic conductivity values. Their structure and related performance are discussed in the next section.

1.5 LISICONs and thio-LISICONs

1.5.1 LISICONS

LISICON is the acronym for lithium superionic conductor and it was first proposed by Hong in 1978 to name $Li_{14}Zn(GeO_4)_4$ ($Li_{3.5}Zn_{0.25}GeO_4$), which is an intermediate composition in the Li_4GeO_4-Zn_2GeO_4 system (Fig. 1.14).

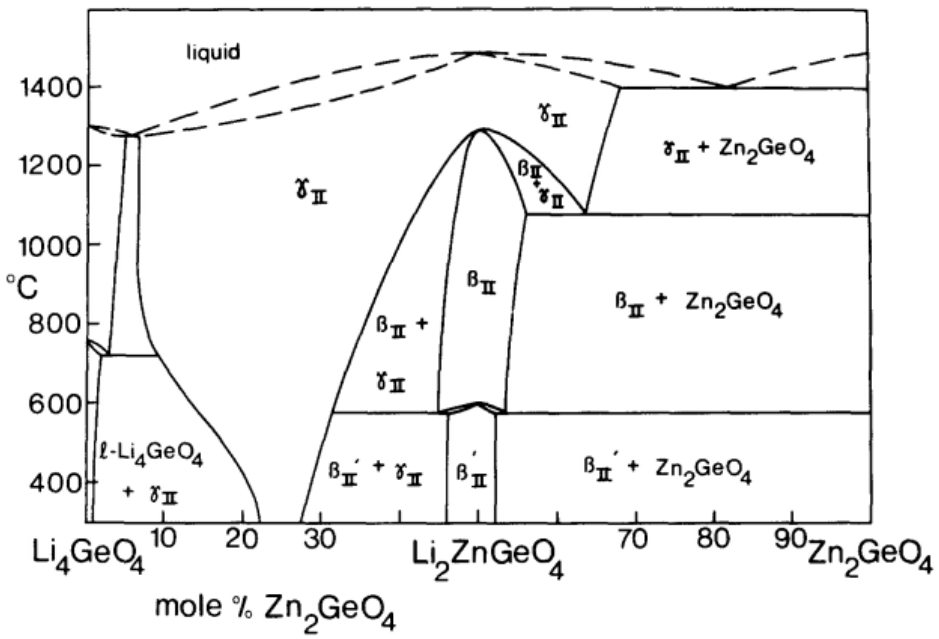

Figure 1.14 Phase diagram for the Li_4GeO_4-Zn_2GeO_4 system [78]

The structure of $Li_{3.5}Zn_{0.25}GeO_4$ is orthorhombic in space group *Pnma* (No. 62), with cell parameters of a = 10.828 Å, b = 6.251 Å and c = 5.14 Å [79]. The Li^+ ion conductivity of $Li_{3.5}Zn_{0.25}GeO_4$ was found to be 0.125 S cm^{-1} at 300 °C, but the room temperature conductivity was significantly lower ($\sigma_{25°C}$ = ~10^{-7} S cm^{-1}). The high dependency of the proposed interstitial conduction mechanism on temperature was attributed as the main reason accounting for the large difference in conductivity with temperature [79].

Using constant-wavelength powder neutron diffraction and later high-resolution time of flight powder neutron diffraction (HRPD), Abrahams et al. characterised the structural details of $Li_3Zn_{0.5}GeO_4$ in 1988 [80] and 1989 [81]. They proposed that $Li_{2+2x}Zn_{1-x}GeO_4$ is based on a

distorted hexagonal close packed (hcp) array of oxide ions with Li^+, Zn^{2+} and Ge^{4+} occupying half the tetrahedral sites and additional Li^+ ions located in the octahedral sites of the distorted hcp lattice. In fact the distorted hcp lattice in LISICON type systems has been described in terms of lying between ideal hcp and tetragonal packing [82], in which the anion packing distorts lowering the coordination number from 12 to 11 [83].

The structure of the end member of the solid solution, γ-Li_2ZnGeO_4 contains no Li^+ ions in octahedral sites and is built up of units of 3 edge sharing lithium oxide tetrahedra which corner share with a germanium oxide tetrahedron (Fig. 1.15a). These subunits corner share with each other to give a three-dimensional network structure (Fig. 1.15b).

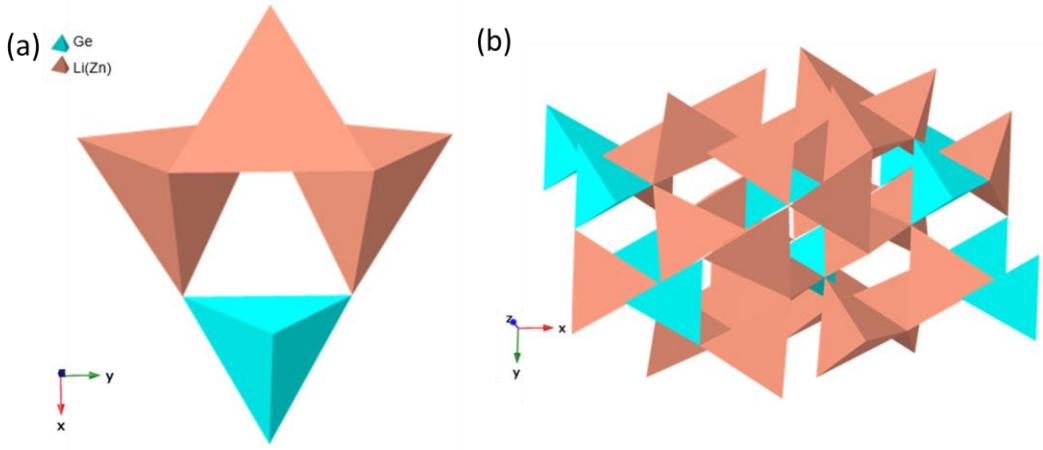

Figure 1.15 Structure of γ-Li_2ZnGeO_4 showing (a) lithium germanate subunits and (b) full structure

From the HRPD data, a detailed structure refinement of γ-$Li_3Zn_{0.5}GeO_4$ allowed for the accurate determination of Li^+ ion site occupancies (Table 1.7). Based on these results, two types of defect cluster, Type I and Type II, were proposed to accommodate the octahedral interstitial Li^+ ions in γ-$Li_3Zn_{0.5}GeO_4$ (Fig. 1.16a and b) at room temperature. Elevated temperature measurements at 300 °C and 500 °C revealed a third type of defect cluster, Type III (Fig. 1.16c) [84].

The type I defect cluster, shown in Fig. 1.16a, is made up of an octahedral Li3 site which shares two faces with the adjacent tetrahedral Li2 (Zn2) sites, the presence of Li3 promotes the displacement of one of the two neighbouring Li2 cations from its site into an interstitial tetrahedral Li2a site through the shared face. The displacement allows Li3 to move closer to the shared face with the empty Li2 site. Thus, unfavoured cation repulsion between Li3 and the two adjacent Li2(Zn2) sites is reduced. Since Li2a is quite close to the shared face with the unoccupied Li2 tetrahedra, it can be regarded as being in a distorted five coordinate site.

The type II defect cluster, shown in Fig. 1.16b, is made up of two Type I clusters which are linked through their empty Li2(Zn2) sites by a central octahedral Li4 site. The central octahedral Li4 site is surrounded by four face-sharing tetrahedral Li sites, two Li1(Zn1) and two Li2(Zn2); each of these tetrahedral sites shares one of its four faces with the central octahedral Li4 site. The type II defect cluster consists of three lithium ions in the octahedral sites, one Li4 site and two Li3 sites; the two Li1(Zn1) sites that surround Li4 are occupied by lithium ions whereas the corresponding Li2(Zn2) sites are unoccupied. Their lithium ions at Li2(Zn2) sites are displaced to positions located near the common face shared with the Li2a sites, but just inside the latter Li2a tetrahedra, as with the Type I defect cluster. Again, these displaced lithium ions can be regarded as occupying distorted five coordinate sites.

The type III defect cluster observed at elevated temperature, shown in Fig. 1.16c, is similar to the Type II defect cluster seen at room temperature but here the Li^+ ions in both the Li1(Zn1) sites which share faces with Li4 are now displaced to a position near the common face shared by each Li1(Zn1) site and its corresponding tetrahedral Li1a site. This displacement is similar to the lithium ion from Li2 to Li2a site, but here the displaced lithium ion remains inside the Li1(Zn1) tetrahedra, the new located position is designated as Lila.

In fact, in these three types of defect cluster, all the displaced lithium ions from the Li1 and Li2(Zn2) sites are sufficiently close to the common faces shared between the Lila and Li2a

tetrahedral sites, therefore all of them can be regarded as having the distorted five coordinate geometry.

Table 1.7 Refined unit cell parameters for $Li_3Zn_{0.5}GeO_4$ [81]

$a = 10{\cdot}8523\ (1),\ b = 6{\cdot}27431\ (7),\ c = 5{\cdot}15807\ (6)$ Å.

	Position	x	y	z	B(Å^2)	Occupancy
Ge	4(*c*)	0·4133 (6)	0·25	0·3335 (2)	—	1
O(1)	8(*d*)	0·3360 (1)	0·0230 (2)	0·2171 (2)	-	1
O(2)	4(*c*)	0·0875 (2)	0·75	0·1714 (3)	-	1
O(3)	4(*c*)	0·0652 (1)	0·25	0·2797 (3)	-	1
Li(1)	4(*c*)	0·4298 (8)	0·75	0·183 (2)	2·8 (3)	0·905 (6)
Zn(1)	4(*c*)	0·4298 (8)	0·75	0·183 (2)	2·8 (3)	0·095 (6)
Li(2)	8(*d*)	0·141 (2)	−0·039 (4)	0·356 (6)	2·7 (4)	0·647 (9)
Zn(2)	8(*d*)	0·141 (2)	−0·039 (4)	0·356 (6)	2·7 (4)	0·202 (3)
Li(2a)	8(*d*)	0·167 (2)	0·030 (3)	0·212 (5)	2·7 (4)	0·156 (9)
Li(3)	8(*d*)	0·204 (1)	0·206 (3)	−0·009 (3)	3·5 (3)	0·210 (4)
Li(4)	4(*b*)	0·0	0·0	0·5	3·5 (3)	0·081 (9)

Anisotropic thermal parameters (Å^2)

	B_{11}	B_{22}	B_{33}	B_{23}	B_{13}	B_{12}
Ge	0·89 (4)	1·17 (5)	0·96 (5)	—	0·05 (5)	—
O(1)	0·88 (4)	1·79 (5)	1·54 (5)	−0·49 (4)	0·02 (4)	−0·21 (4)
O(2)	1·10 (6)	1·11 (6)	0·79 (6)	-	0·15 (6)	—
O(3)	0·60 (6)	1·36 (6)	1·42 (7)	—	−0·05 (5)	-

(a)

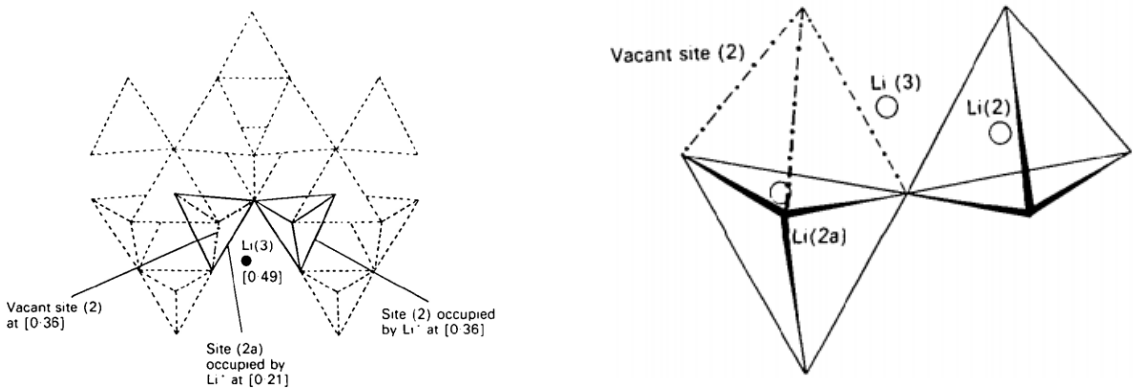

(b)

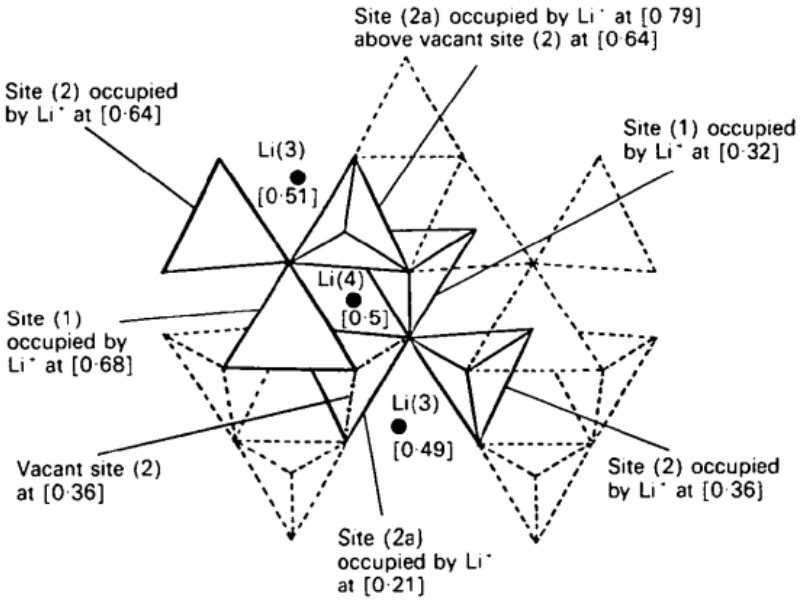

(c)

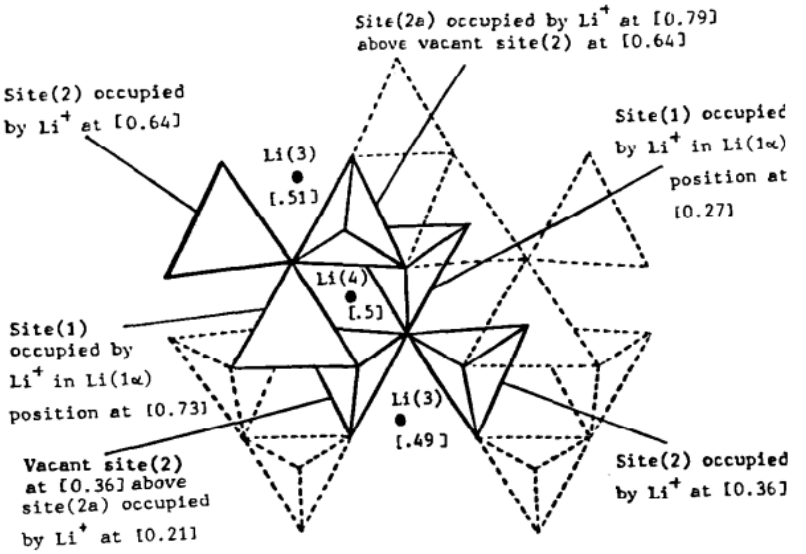

Figure 1.16 (a) type I, (b) type II and (c) type III defect clusters for $Li_3Zn_{0.5}GeO_4$ [81, 84]

Although a similar Li^+ ion distribution is seen in γ-$Li_{3.5}Ge_{0.5}V_{0.5}O_4$, distinct defect clusters were proposed to occur consisting of octahedrally coordinated interstitial Li^+ ions and displaced Li^+ ions arising from the face-sharing tetrahedral sites [85]. The specific lithium-rich defect clusters for γ-$Li_{3.5}Ge_{0.5}V_{0.5}O_4$ present at room temperature (Type Ia) and elevated temperature (Type IIa) are shown in Fig. 1.17.

The Type Ia cluster (Fig.1.17a) is made up of two basic moieties shown in Fig.1.18, one of which (Fig. 1.18a) is identical to the Type I cluster in $Li_3Zn_{0.5}GeO_4$ (Fig. 1.16a), here it should be noted that the exact site position of Li2a varies with temperature. The other basic moiety involves an interstitial octahedral Li4 ion, a non-displaced tetrahedral Li2 ion, a displaced Li2a ion and two tetrahedral Li1 ions (Fig. 1.18b). At room temperature, these two moieties are present in an approximate 1:1 ratio and it is proposed that they combine in pairs to form a larger cluster, the Type Ia defect cluster (Fig.1.17a). At elevated temperature, at least two defect clusters were proposed to exist in γ-$Li_{3.5}Ge_{0.5}V_{0.5}O_4$ according to the neutron data, Type Ia still exists, along with the basic moiety shown in Fig. 1.18b, which make up larger clusters.

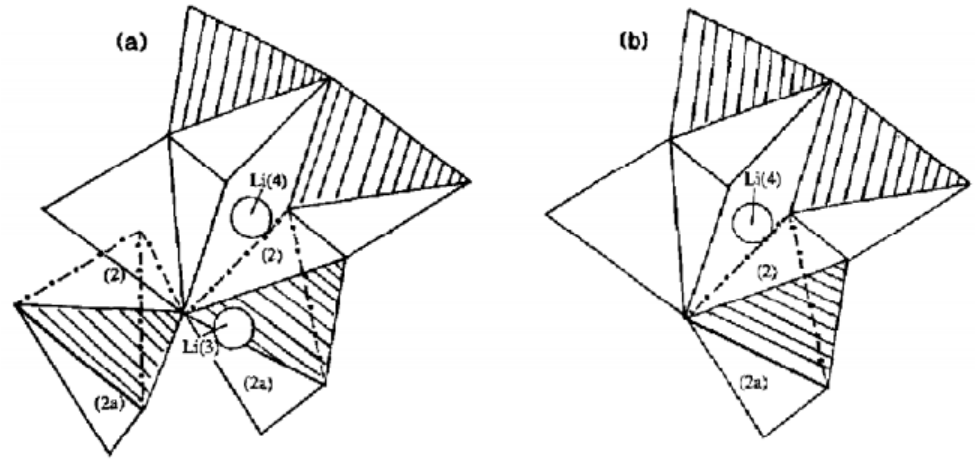

Figure 1.17 (a) Type Ia and (b) type IIa defect clusters in γ-$Li_{3.5}Ge_{0.5}V_{0.5}O_4$ [86]. Note in reference [86] these were referred as Types I and II and have been relabelled here to avoid confusion with the defect clusters in γ-$Li_3Zn_{0.5}GeO_4$.

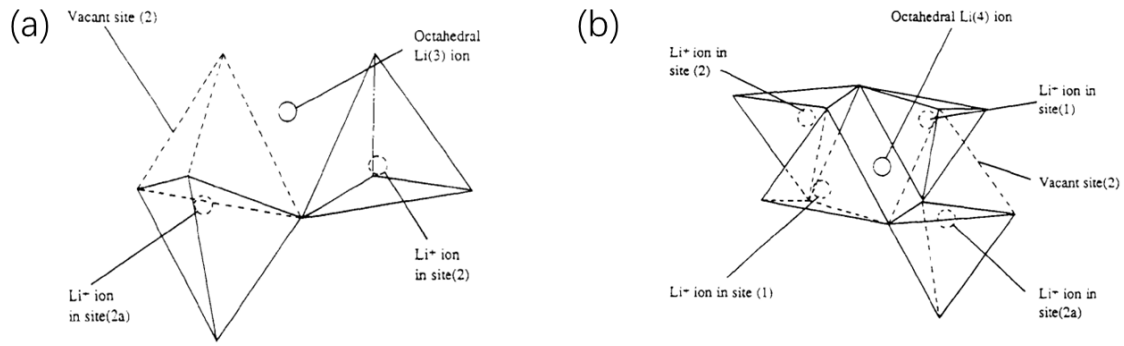

Figure 1.18 The two basic moieties that make up larger defect clusters in γ-$Li_{3.5}Ge_{0.5}V_{0.5}O_4$ [85]

In 1980, West et al. investigated the ionic conductivity in the Li_4GeO_4-Li_3VO_4 system, the $Li_{3.6}Ge_{0.6}V_{0.4}O_4$ composition had the highest ionic conductivity of 4×10^{-5} S cm^{-1} at 18 °C, with an activation energy of 0.44 eV. The high conductivity was attributed to the interstitial Li^+ ions produced by charge compensation due to the partial substitution V^{5+} with sub-valent Ge^{4+} [87]. Similar improvements in conductivity are found in the Li_4GeO_4-Li_3AsO_4 system [88, 89].

The improved conductivity in LISICON structure like $Li_3Zn_{0.5}GeO_4$, $Li_{3.5}Ge_{0.5}V_{0.5}O_4$ and $Li_{3.6}Ge_{0.6}V_{0.4}O_4$ is related to the interstitial Li^+ ions. The interstitial Li^+ ions are not randomly distributed over a set of atomic sites; they exist in the form of lithium-rich defect clusters as shown above. As a result, it is not likely that the ionic conduction is through the migrating of a few free Li^+ ions in a random manner in such a highly ordered structure. Abrahams et al. proposed that the entire lithium-rich defect cluster can migrate effectively through a concerted movement of the Li^+ ions within the cluster, during the process clusters can exchange places with a neighbouring stoichiometric skeleton region as the Li^+ ions migrate throughout the crystal. That is to say, the region initially with the structure of the cluster is converted to a stoichiometric skeleton region and vice versa. Thus, the lithium ion migration is not restricted to the interstitial Li^+ ions alone, but also involves the framework ions and may be described as an interstitialcy mechanism of ion transport. Fig. 1.19 shows the proposed cluster migration mechanism of Li^+ ion transport in $Li_3Zn_{0.5}GeO_4$ and $Li_{3.5}Ge_{0.5}V_{0.5}O_4$.

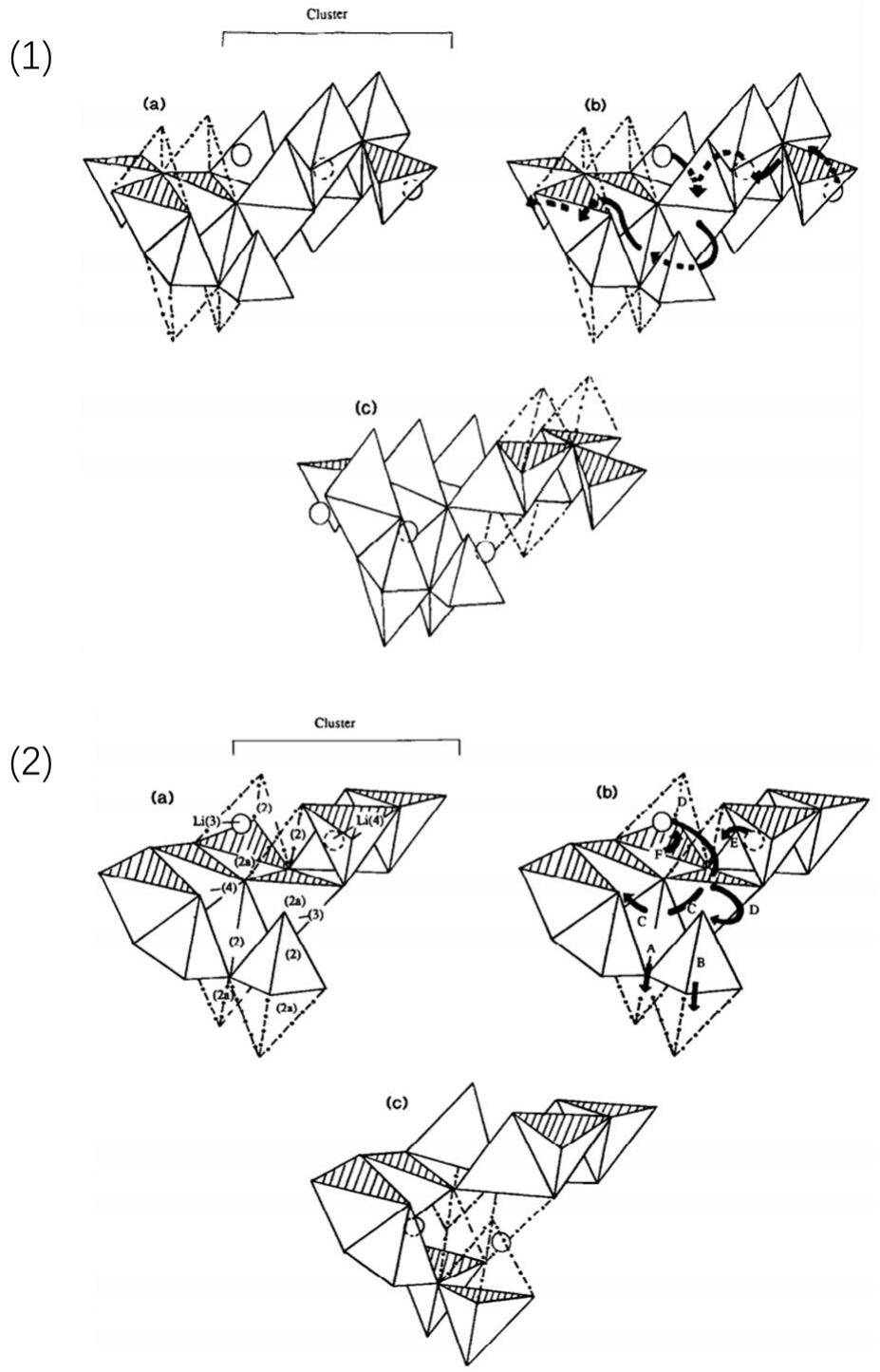

Figure 1.19 Mechanism of Li^+ ion transport by cluster migration in $Li_3Zn_{0.5}GeO_4$ (1) and $Li_{3.5}Ge_{0.5}V_{0.5}O_4$ (2), (a) before migration, (b) migration pathway (c) after migration [86]

The basic structure of LISICON in space group *Pnma* (No. 62) is also adopted by γ-Li_3PO_4 [90], which is the end member of the solid solution system $Li_{3+x}Ge_xP_{1-x}O_4$ investigated in this

thesis. In γ-Li_3PO_4, all the cations are tetrahedrally coordinated (Fig. 1.20) with no occupation of the octahedral sites.

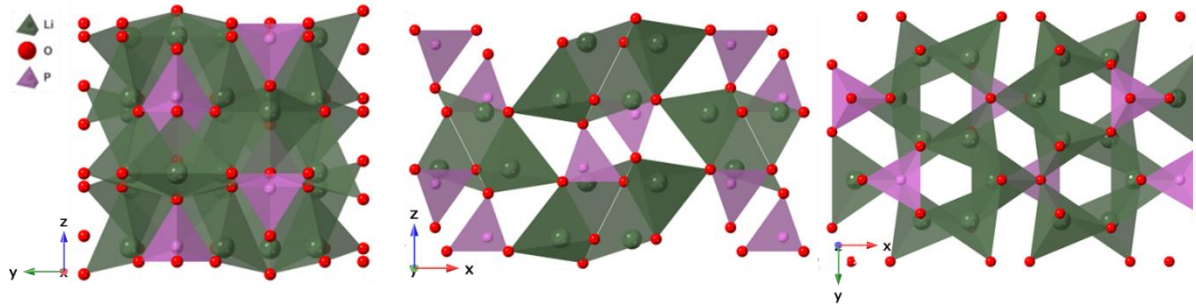

Figure 1.20 Crystal structure of γ–Li_3PO_4

Du et al. [91] employed first-principles modelling techniques and the nudged elastic band method to explore the possible Li^+ ion conduction mechanism in the idealized Li_3PO_4 structure. They concluded that the interstitial mechanism is much more efficient than vacancy transport processes. It is more possible that the lithium ions which are located in LiO_4 tetrahedra diffuse between these tetrahedra and interstitial sites to facilitate conductivity. Since all the Li^+ ions form chemical bonds with O^{2-} ion within the network structure, the mobility of Li^+ ions is very limited, thus the ionic conductivity of Li_3PO_4 is very low (10^{-9} - 10^{-10} S cm^{-1} at room temperature) [92]. Therefore, the creation of mobile lithium ions through substitution of pentavalent phosphorus with sub-valent cations should improve the ionic conductivity.

Lithium silicate, Li_4SiO_4, is also reported to have poor Li^+ ion conductivity even at elevated temperatures ($\sigma_{300\,°C} = 2 \times 10^{-5}$ S cm^{-1}) [93]. Ordered Li_4SiO_4 has a monoclinic structure in space group $P2_1m$ (No. 11), within the structure three types of Li-O polyhedral LiO_4, LiO_5 and LiO_6 connect to each other through the edge- and corner-sharing, the ordered nature results in the mentioned poor conductivity [94]. Since all the Li^+ ions are part of the framework structure, there are no spare mobile Li^+ ions, which causes an extremely low Li^+ ion conductivity.

Other binary lithium oxides, such as $LiMO_2$ (M = Al, Ga), Li_4MO_4 (M = Si, Ge, Ti), Li_3MO_4 (M = P, As, V) etc., also show relatively poor ionic conductivity at room temperature. Through

the introduction of interstitial Li^+ ions or vacancies by aliovalent substitution, improved Li^+ ion mobility can be expected through the formation of solid solutions.

In 1977 Hu et al. investigated the ionic conductivity in the Li_4SiO_4 - Li_3PO_4 system [95]. A complete solid solution is formed in the system $Li_{4-x}Si_{1-x}P_xO_4$ ($0 \leq x \leq 1$). Since the two end-members have different phase structures (monoclinic for Li_4SiO_4 and orthorhombic for Li_3PO_4), the structure changes at $x = 0.5$ in the solid solution. The ionic conductivity is improved through substitution of Si by P, with the highest ionic conductivities found for $Li_{3.5}Si_{0.5}P_{0.5}O_4$ and $Li_{3.4}Si_{0.4}P_{0.6}O_4$ in the order of 10^{-6} S cm^{-1} at room temperature, and a value of $\sigma = 1 \times 10^{-4}$ S cm^{-1} at 100 °C for the $x = 0.4$ composition [93].

Further work by Deng et al. [96] investigated more complex multi-cation systems. A wide range of compositions was studied including Li_4SiO_4, $Li_{3.75}Si_{0.75}P_{0.25}O_4$, $Li_{4.25}Si_{0.75}Al_{0.25}O_4$, $Li_4Al_{0.33}Si_{0.33}P_{0.33}O_4$ and $Li_4Al_{1/3}Si_{1/6}Ge_{1/6}P_{1/3}O_4$ using a combined theoretical and experimental approach. Molecular dynamics (MD) modelling calculated $Li_4Al_{1/3}Si_{1/6}Ge_{1/6}P_{1/3}O_4$ to exhibit the highest Li^+ ion conductivity with an activation energy of 0.28 eV ($\sigma_{27\,°C} = 9 \times 10^{-4}$ S cm^{-1}) due to the mixed polyanion effect. These authors proposed three temperature-dependent Li^+ ion conduction mechanisms: a local oscillation at low temperature, isolated hopping at intermediate temperature, and superionic flow motion at high temperature, as shown in Fig 1. 21.

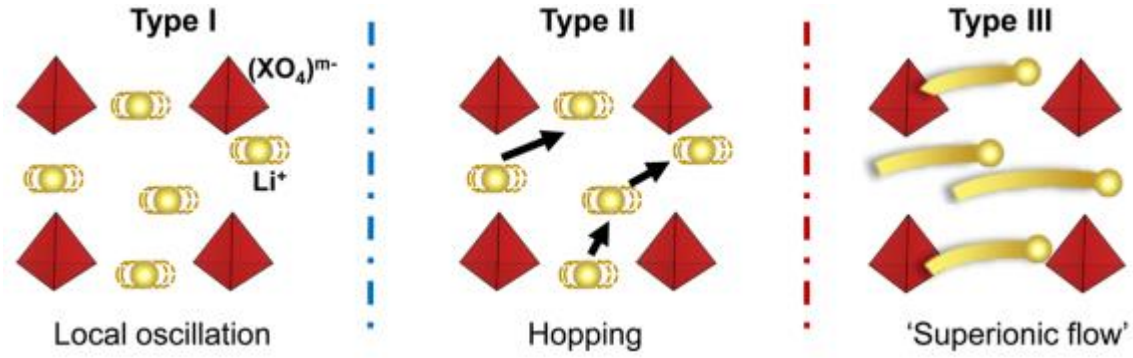

Figure 1.21 Three Li^+ ion conduction mechanisms in LISICON type structures proposed by Deng et al. Type I (low temperature), Type II (intermediate temperature) and Type III (high temperature) [96]

Interestingly, improvement in ionic conductivity is seen in isovalent substituted systems such as Li_4SiO_4-Li_4TiO_4, where a Li^+ ion conductivity of 5×10^{-4} S cm^{-1} at 300 °C is seen $Li_4Si_{0.6}Ti_{0.4}O_4$ [97], much higher than that of the end members. Similarly, improved conductivity is also seen in the Li_4SiO_4-Li_4GeO_4 system, in which the intermediate compositions showed better conductivity than the end members [98].

Due to the high stability of LISICON oxides to air and moisture, the synthesis process is very straightforward with low cost, which is a significant advantage for possible commercial production in the future. However, the current Li^+ ion conductivity for most LISICON compounds is still too low for commercial use and much effort is required to improve the conductivity.

1.5.2 Thio-LISICONs

In 2001, Kanno et al. first described the thio-LISICON system [99, 100]. In these systems the O^{2-} anion in the LISICON framework is replaced by the more polarizable S^{2-} anion which also has a larger ionic radius, thus improved lithium ionic conductivity is realized due to higher lithium ion mobility. For example, the room temperature ionic conductivity of $Li_{3.4}Si_{0.4}P_{0.6}S_4$ is 6.4×10^{-4} S cm^{-1}, two orders of magnitude higher than in its oxygen analogue $Li_{3.4}Si_{0.4}P_{0.6}O_4$

($\sigma_{25\,°C}$ = 4.0 ×10^{-6} S cm^{-1}) [100, 101]. Currently a record high ionic conductivity of 0.012 S cm^{-1} at room temperature has been observed in $Li_{10}GeP_2S_{12}$, which is even higher than commercial electrolytic liquids [38]. Its analogues $Li_{10}SnP_2S_{12}$ and $Li_{10}SiP_2S_{12}$ also have high conductivity [102, 103]. The high conductivity of $Li_{10}XP_2S_{12}$ (X= Ge, Sn, Si) can be attributed to the three-dimensional framework structure, allowing fast lithium ion diffusion. It should be noted here that these sulfide materials have to be prepared and processed in inert atmosphere, e.g. Ar, since they are highly air and moisture sensitive.

It can be seen that except for some non-oxides, no oxides have similar ionic conductivities to those of liquid electrolytes, such as 1 M $LiPF_6$ in EC: DMC mixture with an ionic conductivity around 10^{-2} S cm^{-1}. Therefore, there is still a significant gap to cross for air stable crystalline solid electrolytes to reach the levels required for commercial application. Compared with the LISICON structure-related sulfides, solid electrolyte oxides have the advantages of low cost and easy synthesis. Improving ionic conductivity in such materials would make their application much more commercially viable.

1.6 Aims

The main aims of the project are to develop new families of lithium ion conducting solid electrolytes that are based on the LISICION structure, to characterise their conductivities and defect structures using modern total neutron scattering methods and to establish models for the conduction mechanism. In the present work we explore the $Li_{3+x}Ge_xP_{1-x}O_4$, $Li_{4-2x}Ge_{1-x}Mo_xO_4$ and $Li_{4-2x}Ge_{1-x}W_xO_4$ systems. In the $Li_{3+x}Ge_xP_{1-x}O_4$ system, the sub-valent cation Ge^{4+} is used to partially substitute phosphorus in Li_3PO_4, with charge compensation through increased content of lithium cations in the interstitial sites. In the $Li_{4-2x}Ge_{1-x}Mo_xO_4$ and $Li_{4-2x}Ge_{1-x}W_xO_4$ systems, super-valent Mo^{6+} and W^{6+} are used to partially substitute Ge^{4+} in Li_4GeO_4, with the charge compensation through increased Li^+ ion vacancy content.

The work aims to investigate the structure-composition-conductivity relationships in these three systems. Neutron and X-ray powder diffraction is employed to confirm the average crystal structures and neutron total scattering is used to probe the local defect structure. The electrical conductivity of these systems is examined using a.c. impedance spectroscopy.

Chapter 2 Introduction to experimental techniques

2.1 Materials synthesis

For the synthesis of the LISICON structured compounds in this thesis, a classical method of solid-state synthesis is used. Unlike solvent based method like hydrothermal and sol-gel methods, both of which require relatively complex procedures with a long time. The preparation of the precursor mixtures is relatively easy here. The method generally consists of heating a dried mixture of precursors using a designed heating procedure.

The Gibbs function (Eqn. 2.1) is used to assess whether a reaction can happen or not, in which ΔG, ΔH and ΔS represent the changes in the state functions, Gibbs free energy, enthalpy and entropy, respectively, at absolute temperature T. For thermodynamically feasible reactions, the change in Gibbs free energy is less than zero. The temperature is critical in deciding the reaction rate. Increasing the temperature can accelerate the reaction rate, while lowering the temperature can slow down or stop the reaction.

$$\Delta G = \Delta H - T\Delta S \tag{2.1}$$

Phase transitions occur in a similar way. For example, if a compound exists in two stable polymorphs, one at high temperature and one at low temperature, then at high temperature the high temperature polymorph will have a lower value of Gibbs free energy than the low temperature polymorph and vice versa at low temperatures. On heating the transition from low temperature polymorph to the high temperature form will occur at a critical temperature when sufficient energy to allow the transition to take place has been provided. On cooling, the reverse transition will occur, usually at a slightly lower temperature (thermal hysteresis). However, depending on the kinetics of the process the high temperature phase may be preserved to lower temperatures provided the cooling rate is sufficiently high. This process is termed quenching and is usually facilitated by removal of a sample from a furnace at high temperature. In this case the preserved high temperature phase is said to be metastable with respect to the low

temperature phase which has a lower free energy. In some cases, the kinetics can drive other metastable phases to be formed.

Since the high temperature phases often have superior properties to the low temperature phases, research typically focuses on synthesising thermodynamically stable variants through solid solution formation. This may be in the form of aliovalent (super-valent or sub-valent) or isovalent substitution on the cation and/or the cation sublattices.

2.1.1 Sintering

Sintering is the process of compacting a powder or porous material to form a solid mass by heating without melting it, as is shown in Fig 2.1. For a single-phase polycrystalline material, sintering is achieved by heating the consolidated mass of powder particles, which are referred to as the powder compact or green body, to the so-called sintering temperature, which is located in the range between around 50% and 80% of the melting temperature [104]. Two methods of sintering are adopted in this thesis, one is the conventional solid-state sintering, the other method is spark plasma sintering.

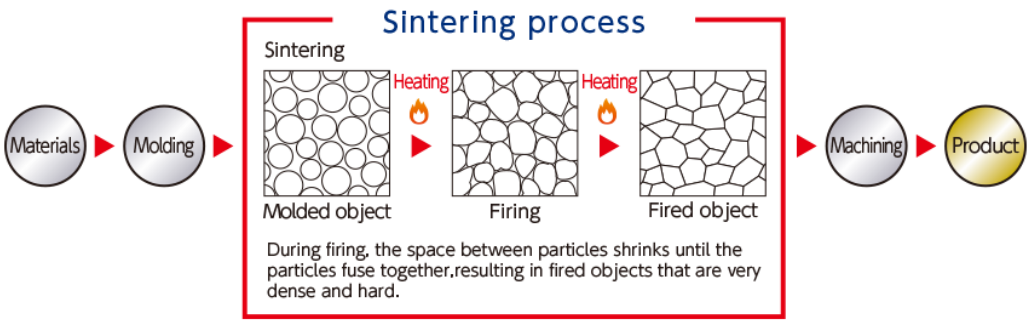

Figure 2.1 Schematic illustration of the sintering process [105]

Conventional solid-state sintering is the process by which dense pellets are prepared in a conventional high temperature oven or furnace. The calcined powder products are first shaped to a pellet under pressure, an aqueous binder such as 5% PVA (polyvinyl acetate) is often used

to facilitate the powder flowability to make consolidated pellets. A heating regime is then applied to yield the dense pellets. During the sintering process, grain growth typically occurs through ion diffusion, leading to a shrinkage of grain boundaries. This process can take several hours at high temperature to get dense pellets, and care needs to be taken not to overheat the pellets as phase decomposition may occur, especially in cases where volatile components are present. Two-step sintering can effectively suppress the grain boundary migration, whilst maintaining active grain boundary diffusion to obtain dense nanostructured ceramics[106], although optimised temperature setting takes time to figure out.

2.1.2 Spark Plasma Sintering

Spark plasma sintering (SPS) is a newly developed energy-saving sintering technique [107-109] and a schematic diagram of the SPS method is shown in Fig. 2.2. The characteristics of SPS are that it offers uniaxial pressing and the rapid heating and cooling simultaneously, reducing the required densification time and reaction time to the scale of several minutes. The maximum heating temperature is as high as 2500 °C, with heating and cooling rates of up to 600 °C/min and 150 °C/min, respectively. In the method the sample powder is wrapped in carbon foil and loaded into a graphite die. This is placed in a sealed chamber, allowing the selection of different atmospheres such as vacuum, nitrogen and argon. Through application of a small DC pulse of about 5 V on the two ends of graphite electrodes, a current of thousands of amperes is produced due to the ignorable electrical resistance of the graphite assembly. This generates a large amount of heat around the powder sample. Together with the applied high pressure, the particle and ionic diffusion is greatly accelerated with sufficient energy offered from the Joule heating. As a result, compared with traditional sintering of at least several hours in a furnace, the sintering time is greatly reduced through SPS. Additionally, due to the synergistic effect of

pressing and Joule heating, the required sintering temperatures in SPS are much lower (up to 100 °C) than traditional sintering methods.

The lower sintering temperature and minute-scale sintering time in SPS allow for the synthesis of different types of ceramics such as high density, nanostructure, metastable, textured, co-sintered etc. The SPS facility used in the thesis was a SPS (HPD 25/1 FCT (Germany) SPS furnace) located in the laboratories of Nano-force Technology Ltd (a QMUL spin out company).

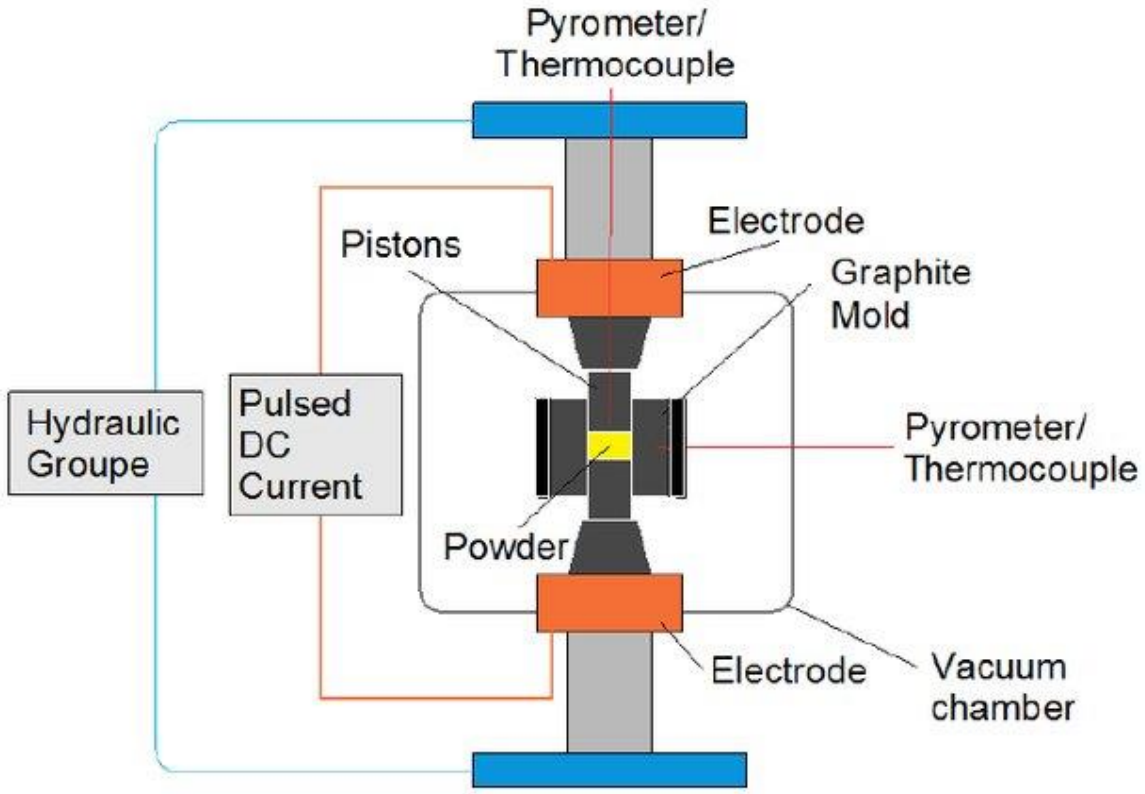

Figure 2.2 Schematic illustration of spark plasma sintering [110]

2.2 **Materials characterization**

2.2.1 Diffraction techniques

When waves come across some obstacles along their forward pathway, they can be scattered, and the scattered waves can interfere constructively or destructively, which can reflect how these obstacles are arranged in space. In the case of the crystals that have a periodic three-dimensional structure, when the incident wavelength of the radiation is comparable to the lattice spacings, constructive interference of the scattered waves can lead to the diffraction phenomenon. To analyse the crystal structure of crystalline materials, diffraction techniques are very widely used. X-rays, electrons and neutrons can act as the incident radiation though neutron sources are not easily accessible compared to the popular X-ray and electron sources.

2.2.1.1 X-ray powder diffraction

X-rays are part of the electromagnetic radiation spectrum as is shown in Fig 2.3. They have wavelengths (λ) in the range of 10 – 0.01 nm, corresponding to the frequency range from 3×10^{16} to 3×10^{19} Hz. Based on their properties of high energy and strong penetrability, X-ray related applications are quite popular in our daily life such as in security checks, hospital X-ray machines, dental imaging and so on.

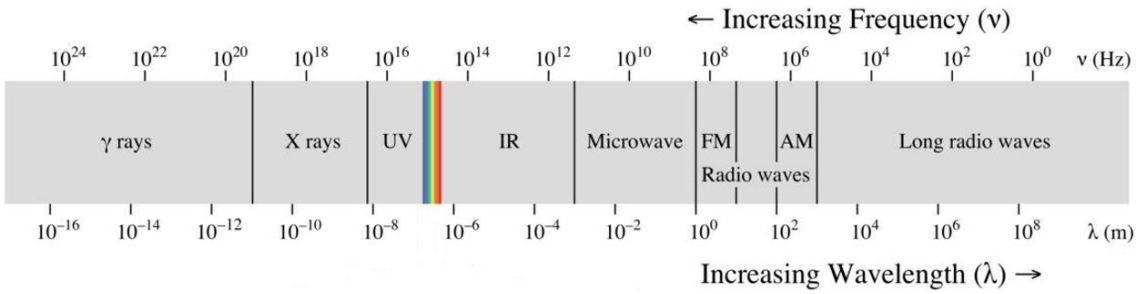

Figure 2.3 Electromagnetic radiation spectrum [111]

For crystalline diffraction, X-rays of wavelength, $\lambda \approx 1$ Å, are used, being similar to the lattice spacings in a crystal material. When X-rays interact with the surface of solid crystalline

powders, the X-rays are scattered by the electrons of atoms, the extent of scattering depends on the number of electrons, i.e. the atomic number; the higher the atomic number, the greater the scattering.

When parallel X-ray waves strike successive crystal planes in the crystal lattice, they travel different distances. If the two waves are in parallel prior to hitting the planes and the path difference is equal to an integral multiple of the wavelength λ after scattering, then constructive interference occurs (Fig. 2.4). This phenomenon known as diffraction will only occur at a specific angle θ for a specific set of planes separated by distance d.

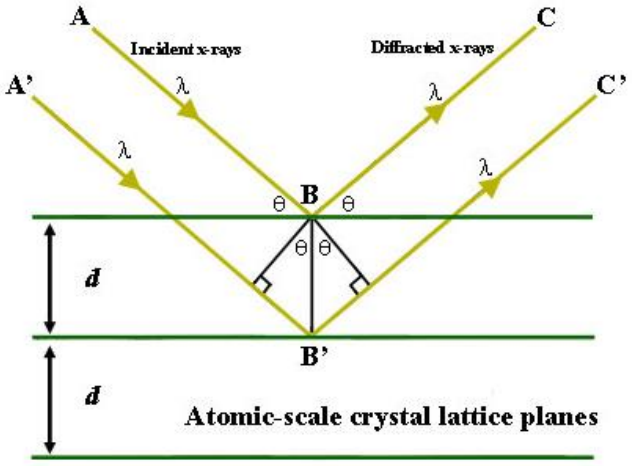

Figure 2.4 Schematic illustrating the diffraction of two parallel X-ray beams from successive crystal planes in a crystalline material [112]

The conditions for diffraction are expressed in Bragg's law (Eqn. 2.2), in which n is the order of diffraction.

$$n\,\lambda = 2d \sin\theta \tag{2.2}$$

In modern usage, the d-spacing and Bragg angle θ are qualified by the particular set of parallel planes that are defined by the Miller indices h, k and l and thus the diffraction order n is redundant, and Bragg's law is expressed as:

$$\lambda = 2\,d_{hkl} \sin\theta_{hkl} \tag{2.3}$$

The extent of scattering by an atom is also related to θ. Since the volume of an atom is in the same order of magnitude as the wavelength, λ, as θ increases, destructive interference of the scattered radiation increases, leading to a fall-off in scattering. The dependence of scattering on the atomic number and θ can be described by the scattering factor or atomic form factor, *f*, which describes the scattering amplitude of the scattered wave in terms of an isolated atom. It is defined such that the scattering of a single electron at $\theta = 0°$ is unity. Fig 2.5 shows the atomic scattering factor curves for selected atoms. It is noteworthy that when compared with other elements, the hydrogen atom (H) with one single electron scatters very little, especially with increasing incident angle θ. Therefore, hydrogen will be "difficult to see" when interacting with X-ray compared with heavy atoms.

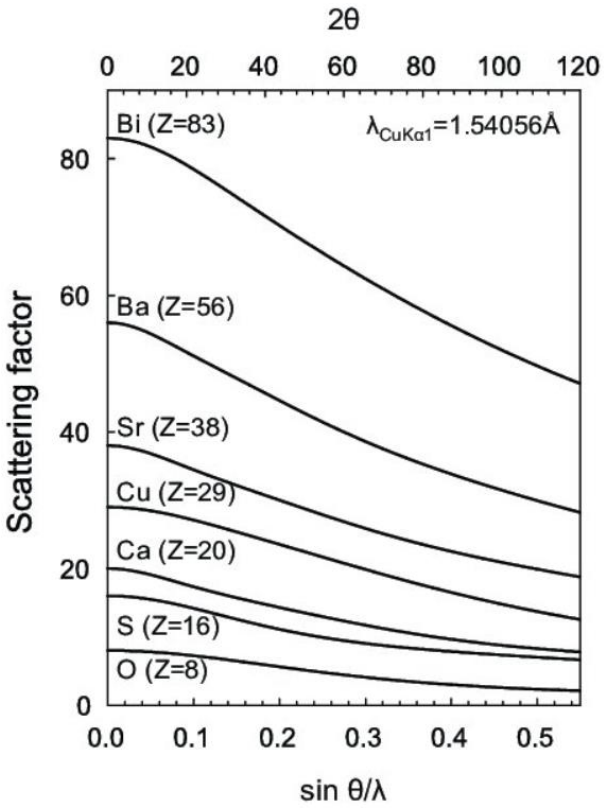

Figure 2.5 Examples of calculated atomic scattering factor for selected atoms [113]

In the case of diffraction by a single crystal, the crystal is rotated with respect to the X-ray beam in order to satisfy Bragg's law for each set of planes in the crystal. Powders contain many

randomly orientated crystallites and hence there is no need to rotate individual crystallites, since at any one time at least some of the crystallites will be correctly orientated to the beam so as to satisfy Bragg's law for all allowed reflections. In modern X-ray powder diffractometers, the sample is typically mounted on a flat plate (which may be rotated to maximise the randomness of the of the orientations) and the detector and/or X-ray tube are stepped through a θ arc to obtain a diffraction pattern, which is essentially a plot of radiation counts versus 2θ. Peaks in the pattern correspond to diffraction from allowed sets of *hkl* planes.

In the XRD pattern, the peak intensities of reflections are determined by many factors, like the scattering factor *f*, the diffractometer geometry related geometrical factors, texture-related preferred orientation and so on. The contribution resulting from the crystal itself is described by the structure factors. The equation to express the structure factor is shown in Eqn. 2.4.

$$F_{hkl} = \sum_{r=1}^{r=n} f_r[cos2\pi(hx_r + ky_r + lz_r) + isin2\pi(hx_r + ky_r + lz_r)] \qquad (2.4)$$

where F_{hkl} is the structure factor for a particular lattice plane defined by the Miller indices *h, k* and *l*; f_r is the scattering factor of atom *r* at θ corresponding to the particular lattice plane, *n* is the total number of atoms in the unit cell and x_r, y_r, and z_r are the fractional atomic coordinates of atom *r*. The observed intensity of reflections I_{hkl} is proportional to the square of the observed intensity magnitude of structure factor, as is shown in Eqn. 2.5.

$$I_{hkl} \propto (F_{hkl})^2 \qquad (2.5)$$

Therefore, from the observed intensity data, the magnitude of the structure factors can be obtained directly for the particular lattice plane, but not the phase. This is known as the phase problem of crystallography and is the reason why structures have to be solved and/or refined from diffraction data, rather than simply determined directly.

In this thesis, X-ray power diffraction data were collected on a PANalytical X'Pert Pro diffractometer equipped with an X'Celerator detector with Cu-Kα radiation (λ = 1.5418 Å). Data were collected over the 2θ range 5° to 70° for short identification scans or 5° to 120° for

detailed structural analysis. Short scans were collected in steps of 0.033°, with a count time of 50s per step, while longer scans were collected in steps of 0.0167°, with a count time of 50s per step. Variable temperature (VT) X-ray powder diffraction data were collected using Anton-Paar HTK 1200N and HTK-16 high temperature cameras.

2.2.1.2 Neutron powder diffraction

Except for ^{1}H, all atomic nuclei consist of neutrons and protons. Compared with protons which carry a positive charge, neutrons are subatomic particles with no net electric charge and a similar mass to protons. According to the de Broglie Equation (Eqn. 2.6) where *h* is Planck's constant, *m* is mass and *v* is velocity, neutrons with an appropriate velocity and wavelength can be used for the diffraction experiments.

$$\lambda = \frac{h}{mv} \tag{2.6}$$

Unlike X-rays which interact with the electrons surrounding atoms, neutrons interact with the atomic nuclei. The scattering power of an atom towards to the neutrons, which is called the scattering length, *b*, is very different from the atomic scattering factor, *f*, for X-rays. As shown in Fig. 2.6, unlike the X-ray scattering amplitude which has a positive correlation with atomic number, the value of scattering length, *b*, does not rely on the atomic number and for different nuclei, can be positive or negative. Additionally, the *b* values of lighter elements such as H, Li, O have values comparable to many other heavy elements, meaning that in systems that contain both light and heavy elements, the light elements make a greater contribution to the neutron scattering. Even for the same element, the *b* value is different for different isotopes, for example, ^{1}H and ^{2}D are two isotopes of hydrogen, ^{2}D has a positive scattering length and ^{1}H has a negative scattering length.

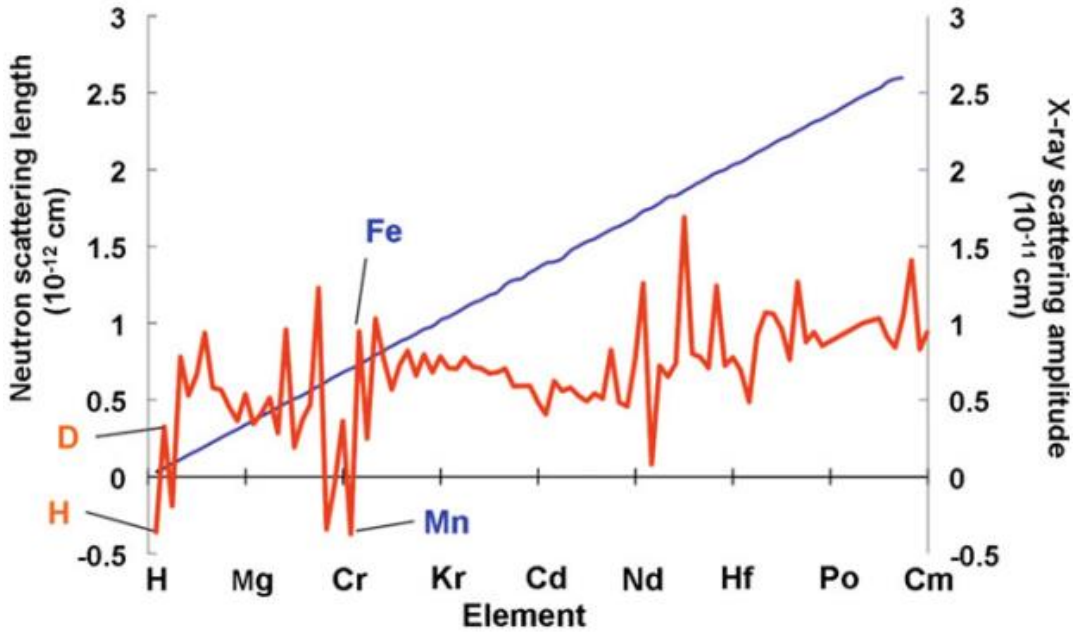

Figure 2.6 Neutron-scattering lengths, *b*, (red line) and X-ray scattering amplitudes (blue line) for various elements (*b* is based on naturally abundant isotopes unless specifically identified) [114]

Another difference between X-ray and neutron scattering is the scattering variation with the incident angle, θ. Within one atom, the size of the atomic nucleus, in the order of 10^{-15} m, is several orders of magnitude smaller than the size of the electron cloud surrounding an atom, which is in the order of 10^{-10} m. This means that while the electron cloud is of a comparable size to the X-ray wavelength, the atomic nucleus is effectively a point and thus exhibits no volume effect when interacting with neutron radiation. Fig. 2.7 shows the variation in neutron scattering length, *b*, and the atomic scattering factor, *f*, with wave vector $\boldsymbol{Q}$ (the absolute value of which is defined in Eqn. 2.7) for naturally abundant carbon. The neutron scattering length, *b* is constant and is independent of *Q*; however, for X-rays, the atomic scattering factor, *f* decreases with increasing *Q* due to the finite volume effect discussed in section 2.2.1.1. Therefore, higher signals can be obtained for neutron scattering at high *Q* or high θ, compared to those from X-ray scattering.

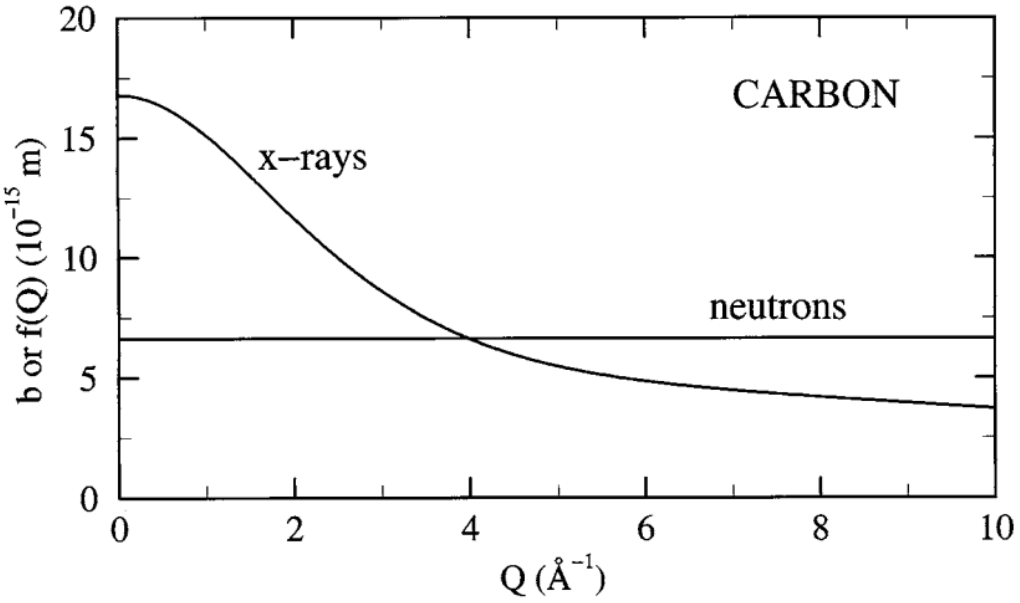

Figure 2.7 Variation of neutron scattering length, *b* and atomic scattering factor, *f*, with wave vector *Q* for naturally abundant carbon [115]

$$|\boldsymbol{Q}| = \frac{4\pi sin\theta}{\lambda} \tag{2.7}$$

Due to their different but complementary characteristics, data from X-ray and neutron scattering experiments are often combined. As mentioned above, X-rays are less sensitive to elements with low atomic number such as H, Li, O, while nuclei of these elements can show significant neutron scattering. Isotopic substitution can also be used as a tool to enhance or diminish scattering from a particular element, relying on the different neutron scattering lengths of different isotopes of the same element. For example by mixing ^{7}Li (*b* = -2.22 fm) and ^{6}Li (*b* = 2.00 fm) [116], a zero scattering length can be achieved making the lithium atoms invisible to neutrons. This can be important in systems where Li shares a site with other atoms allowing the coordination and distribution of the other atom to be distinguished [117].

Since X-ray facilities are much easier to access, it is usual to use X-ray powder diffraction before going on to study a system with neutron diffraction. Due to the intrinsic differences between neutrons, X-rays and electrons, such as carried energy and the matter nature of

neutrons and electrons, when they interact with a material, they will lose energy and penetrate the sample differently. Fig. 2.8 illustrates the penetration depths for X-rays, neutrons and electrons, for the elements of solid or liquid form. The depth is taken as the point when the beam energy is reduced by a factor of 1/e, which is around 37% of its original energy intensity. It can be concluded that neutrons have the highest penetration depth and electrons have the smallest. Table 2.1 summarizes the differences between the X-ray and neutron scattering.

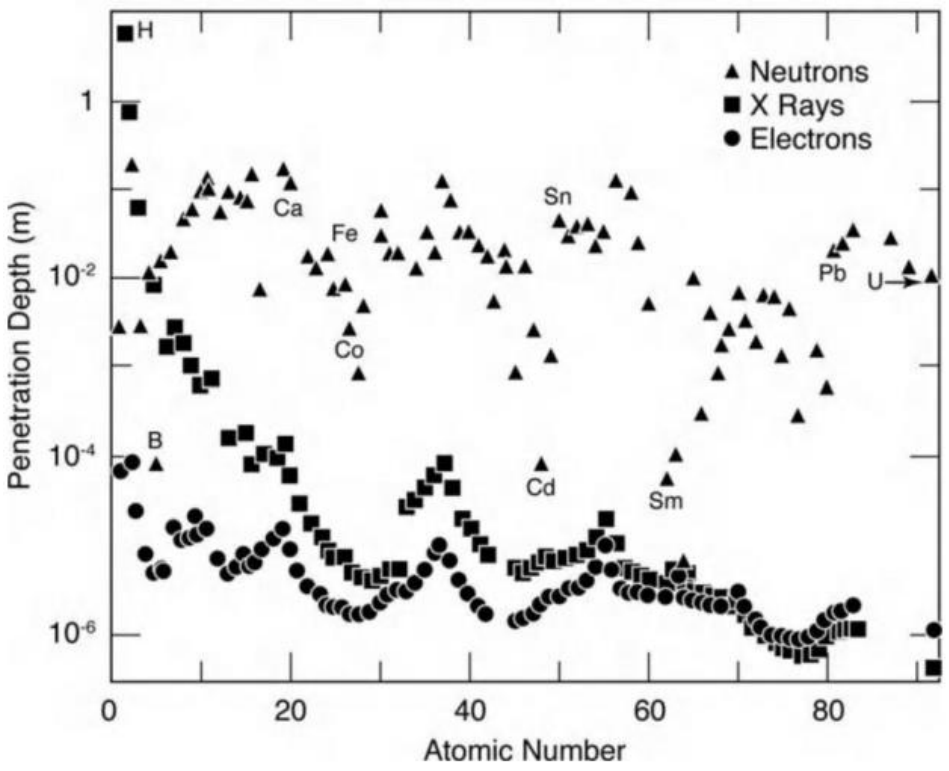

Figure 2.8 The penetration depths of neutrons, X-rays and electrons in the elements of solid or liquid form [118]

Table 2.1 Interaction properties of X-rays and neutrons with atoms

Property	X-ray	neutron
interaction	Electron cloud	Atomic nucleus
Atomic number dependence	Y	N
isotope dependence	N	Y
Scattering angle dependence	Y	N
Penetration depth	Deeper than electrons	Much deeper than X-rays

2.2.1.2.1 Neutron source

Currently, there are usually two available ways to produce high intensity neutron beams. One is through a nuclear reactor such as at the Institut Laue-Langevin (ILL), France, which is the most intense neutron source in the world. The neutrons are produced through fission in a compact-core fuel element like ^{235}U and are cooled using neutron moderators to achieve neutrons with suitable wavelengths. A typical nuclear fission reaction is shown in Fig 2.9.

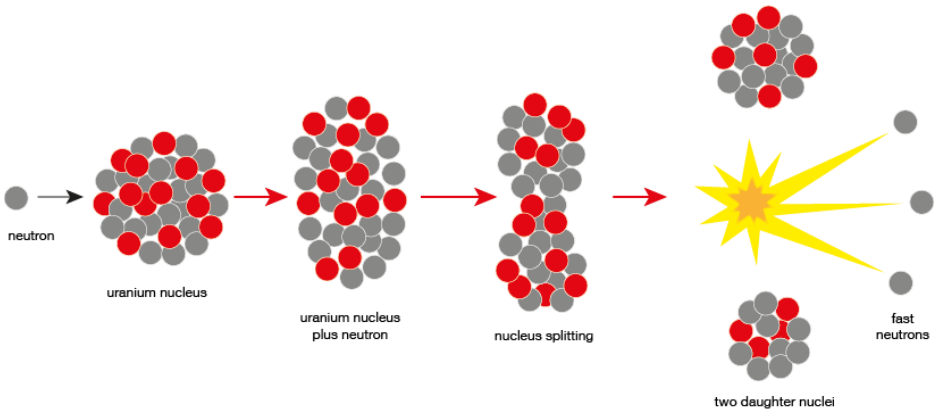

Figure 2.9 Typical nuclear fission reaction [119]

Another way to produce neutrons is through a pulsed source. This generates a pulsed neutron beam with multiple wavelengths. The ISIS neutron source at the Rutherford Appleton Laboratory, UK utilises proton spallation to achieve this. Two accelerators are first used to accelerate the H^- ions to 35% the speed of light. These H^- ions are then transferred to a synchrotron ring and stripped of their electrons by a thin foil when entering. When leaving the synchrotron ring, the H^+ ions are accelerated to a very high energy level of 800 MeV with 84% the speed of light. Before striking a heavy metal target, some of the H^+ ions are used to produce muons when going through a thin carbon target. On striking the primary target, tungsten, the H^+ ions make multiple collisions with nucleons in the tungsten nuclei, causing a spallation process to occur resulting in highly intense neutron beams. These neutrons are subsequently moderated and collimated prior to being channelled to interact with the samples being tested, as is shown in Fig. 2.10.

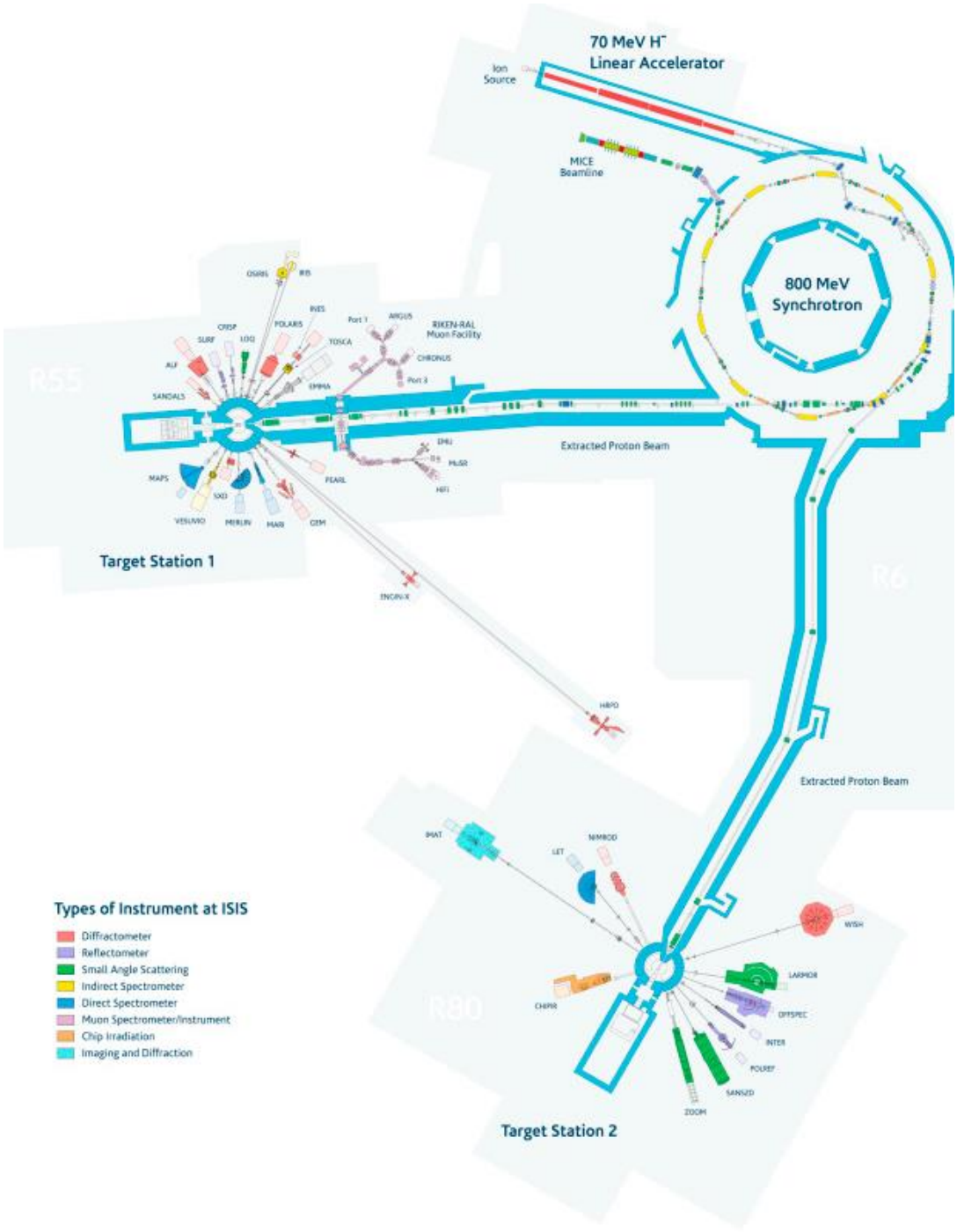

Figure 2.10 The Spallation Neutron Source at the ISIS Facility, UK

2.2.1.2.2 Time-of-flight method for neutron scattering

Diffraction experiments on spallation neutron sources, utilise variable neutron wavelengths and diffractometers with fixed incident angles to generate diffraction patterns, as illustrated in Fig. 2.11. Since the initial velocity for the pulsed neutrons is distributed over a wide range, after the same travelling distance to the detectors, they will arrive at different times. This is the so-called time-of-flight method.

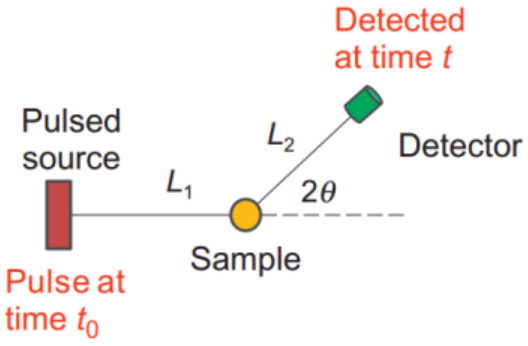

Figure 2.11 Time-of-flight setup for neutron scattering

As seen in Fig. 2.11, the distance between the pulsed source and the sample location can be defined as L_1, and the distance between the sample location and the detector as L_2. The detector is set at a fixed angle, 2θ, which corresponds to the change in the neutron wave vector shown in Fig. 2.12. $\boldsymbol{Q}$ is defined as the change in wave vector, expressed as $\boldsymbol{Q} = \boldsymbol{k}_{\mathbf{final}} - \boldsymbol{k}_{\mathbf{init}}$, with an absolute value $Q = |\boldsymbol{Q}| = 2k\sin\theta = 4\pi\sin\theta/\lambda$, where $k = |\boldsymbol{k}| = 2\pi/\lambda$.

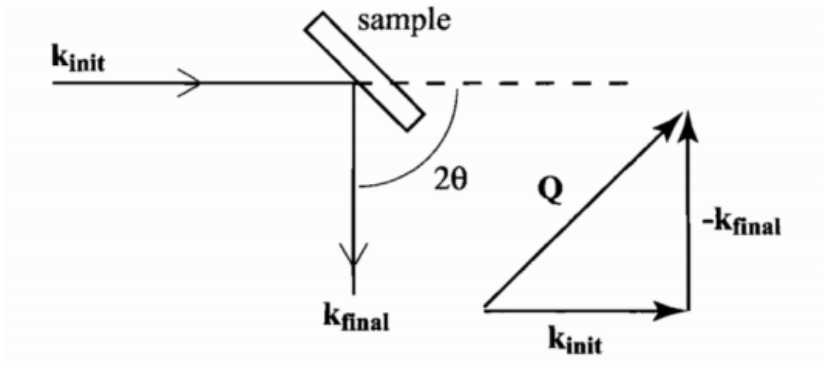

Figure 2.12 The geometry and definition of scattering wave vector *Q*

Assuming there is no energy loss during the neutron scattering process, based on the de Broglie Equation 2.6, the total flight time is shown in Eqn. 2.8 and since $v = \frac{L}{t}$ (where L is the total distance from source to detector and t is the time of flight), then:

$$t = \frac{L_1 + L_2}{v} = \frac{m}{h}(L_1 + L_2)\lambda = \frac{m}{\hbar}\frac{L}{k} \tag{2.8}$$

Since $Q = 2k\sin\theta$, Q can also be expressed as:

$$Q = \frac{2m}{\hbar}\frac{Lsin\theta}{t} \tag{2.9}$$

The overall resolution in Q, R, is defined in Eqn. 2.10, in which three independent variables, flight time t, flight path L and scattering angle θ contribute to it.

$$R = \frac{\Delta Q}{Q} = \left[\left(\frac{\Delta t}{t}\right)^2 + \left(\frac{\Delta L}{L}\right)^2 + (cot\theta\Delta\theta)^2\right]^{\frac{1}{2}} \tag{2.10}$$

For a properly designed time-of-flight diffractometer, the three variables t, L and θ all contribute equally to the resolution R, so Eqn. 2.11 can be simplified as:

$$R = \sqrt{3}\frac{\Delta t}{t} = \sqrt{3}\frac{\Delta\lambda}{\lambda} = \sqrt{3}\frac{\Delta L}{L} = \sqrt{3}cot\theta\Delta\theta \tag{2.11}$$

In this thesis, the neutron scattering experiments were carried out on the Polaris powder diffractometer at the ISIS pulsed neutron source. Polaris is a powder neutron diffractometer with medium resolution and high intensity (Fig. 2.13). It has a primary flight path of 14 m and five groups of detectors with the back-scattering detectors having the highest resolution as is summarised in Table 2.2. The resolution of the diffractometer is around 0.33%, based on the assumption that the distance uncertainty, ΔL, is the same as the effective thickness of the moderator ($\delta m \approx 28$ mm).

Table 2.2 Summary of detector banks for Polaris

Detector bank and 2θ range	Approx. *d*-spacing range
1. very low angle (~6 -14°, av. angle 10.4°)	0.3-48 Å
2. low-angle (~19 - 34°, av. angle 25.99°)	0.13-13.8 Å
3. intermediate-angle (~40 - 67°, av. angle 52.21°)	0.73-7.0 Å
4. 90 degree (~85 - 95°, av. angle 92.59°)	0.05-4.1 Å
5. back-scattering (~130 - 160°, av. angle 146.72°)	0.04-2.6 Å

For neutron scattering measurements, sample containers are typically made of vanadium, because this element has almost no coherent scattering (i.e. no strong Bragg peaks) although it does have appreciable incoherent scattering which contributes to the background signal. For Rietveld analysis, typically only data from the back-scattering and 90° detector banks are used, while for total scattering analysis, data from banks 2-5 are typically used, covering a wide *Q* range (between 0.3 to 31.4 $Å^{-1}$).

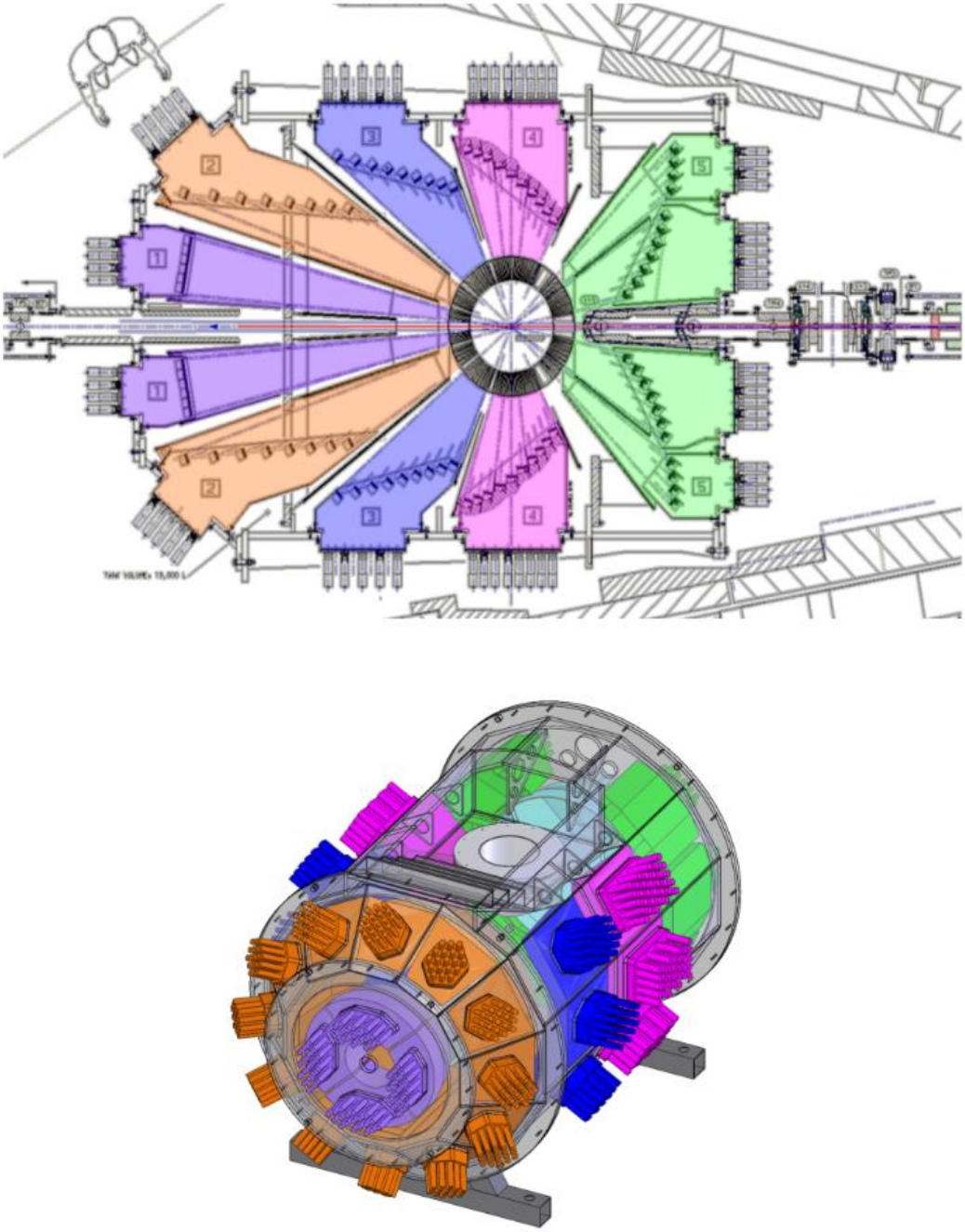

Figure 2.13 Schematic view of POLARIS neutron diffractometer, with detector banks 1–5 shaded with different colours [120]

2.2.1.3 Rietveld refinement

The Rietveld refinement method is a technique for crystalline structure refinement, which was initially proposed by Hugo Rietveld in 1969 to analyse complex diffraction patterns through the means of a curve-fitting procedure over the whole diffraction profile [121]. It can be used to refine the crystalline structure of polycrystalline powders from data collected on X-ray and neutron powder diffractometers. Various parameters including instrumental parameters, background parameters, crystal parameters, profile parameters and structural parameters such as atomic coordinates and thermal parameters etc. are used to calculate the intensity *y* of a given point *i* within the diffraction pattern profile, as expressed in Eqn. 2.12:

$$y\ (calc)_i = s \sum_{hkl} L_{hkl} |F_{hkl}|^2 \phi(2\theta_i - 2\theta_{hkl}) P_{hkl} A + I(b)_i \quad (2.12)$$

where *s* is the scale factor, L_{hkl} is a function which is associated with Lorentz, polarisation and multiplicity factors, F_{hkl} is the structure factor for the particular lattice plane ($h\ k\ l$), ϕ is the profile function of the peak shape whose calculated position is $2\theta_{hkl}$ at position $2\theta_i$ for a peak, P_{hkl} is the preferred orientation function, *A* is the absorption correction factor and $I(b)_i$ is the background intensity at point *i*. Eqn. 2.12 relates to data from fixed wavelength experiments. For time of flight data, the $\phi(2\theta_i - 2\theta_{hkl})$ peak shape function is replaced by one appropriate $\phi(x_i - x_{hkl})$ for these measurements.

In the process of Rietveld analysis, least squares refinement of the parameters described above is carried out until the best fit is obtained to the observed powder diffraction pattern. The least-squares refinement aims to minimise the difference between the calculated and observed profiles rather than several individual reflections. The quality of fitting can be indicated by several parameters, among which some important are given in Eqns. 2.13 to 2.17.

$$R_p = \frac{\sum_i^n |y(obs)_i - y(calc)_i|}{\sum_i^n y(obs)_i} \quad (2.13)$$

$$R_{wp} = \sqrt{\frac{\sum_i^n w_i |y(obs)_i - y(calc)_i|^2}{\sum_i^n w_i |y(obs)_i|^2}} \quad (2.14)$$

$$R_{exp} = \sqrt{\frac{N-P}{\sum_i^n w_i |y(obs)_i|^2}} \quad (2.15)$$

$$R_{F^2} = \frac{\sum_j^m |I(obs)_j - I(calc)_j|}{\sum_j^m I(obs)_j} \quad (2.16)$$

$$\chi^2 = \frac{\sum_i^n w_i |y(obs)_i - y(calc)_i|^2}{N-P} = \left(\frac{R_{wp}}{R_{exp}}\right)^2 \quad (2.17)$$

where R_p, R_{wp}, R_{exp} and R_{F^2} are the profile, weighted profile, expected and Bragg residuals, *n* is the total number of measured data points in the profile, w_i is the weight of an individual point *i* in the profile and it is derived from an error propagation scheme during the refinement process, *N* is the total numbers of observed points in the histograms, *P* is the total number of variables in the least squares refinement process, *m* is the total number of Bragg reflections, $I(obs)_j$ and $I(calc)_j$ are the observed and calculated integrated intensities of Bragg peak *j*, respectively.

In this thesis the Rietveld refinement was carried out by using the GSAS suite of programmes [122].

2.2.2 Total scattering and Reverse Monte Carlo (RMC) modelling

2.2.2.1 Total scattering

In the early 20th century, scientists found that not all the coherent scattering is Bragg scattering, some of it is diffuse scattering. Lovesey proposed the currently popular definition of the diffuse scattering shown in Eqn. 2.18, in which Ω is the solid angle and σ is the scattering cross-section of a nucleus defined in Eqn. 2.19.

$$\left(\frac{d\sigma}{d\Omega}\right)_{diff} = \left(\frac{d\sigma}{d\Omega}\right)_{total} - \left(\frac{d\sigma}{d\Omega}\right)_{Bragg} \quad (2.18)$$

$$\sigma = 4\pi b^2 \quad (2.19)$$

where *b* is the neutron scattering length. As is already known, Bragg scattering contains the average structure information, while diffuse scattering contains the structure deviation information from the average structure and it is related to the short-range atomic arrangement.

In the diffraction pattern of a crystalline system (Fig. 2.14), the diffuse scattering is extremely weak compared to the Bragg scattering and is considered as part of the background scattering. The amount of diffuse scattering is associated with the extent of the disorder. As disorder in a system increases, the intensity of the Bragg scattering decreases and the intensity of the diffuse scattering increases, until in amorphous systems only the diffuse scattering is observed.

According to Eqn. 2.18, total scattering can be considered as the summation of the Bragg scattering and diffuse scattering. For crystalline materials, total scattering not only includes Bragg scattering related information from the long-range average structure like the lattice parameters and the average atomic sites, but also includes the diffuse scattering related information from the shot-range structure (local disorder).

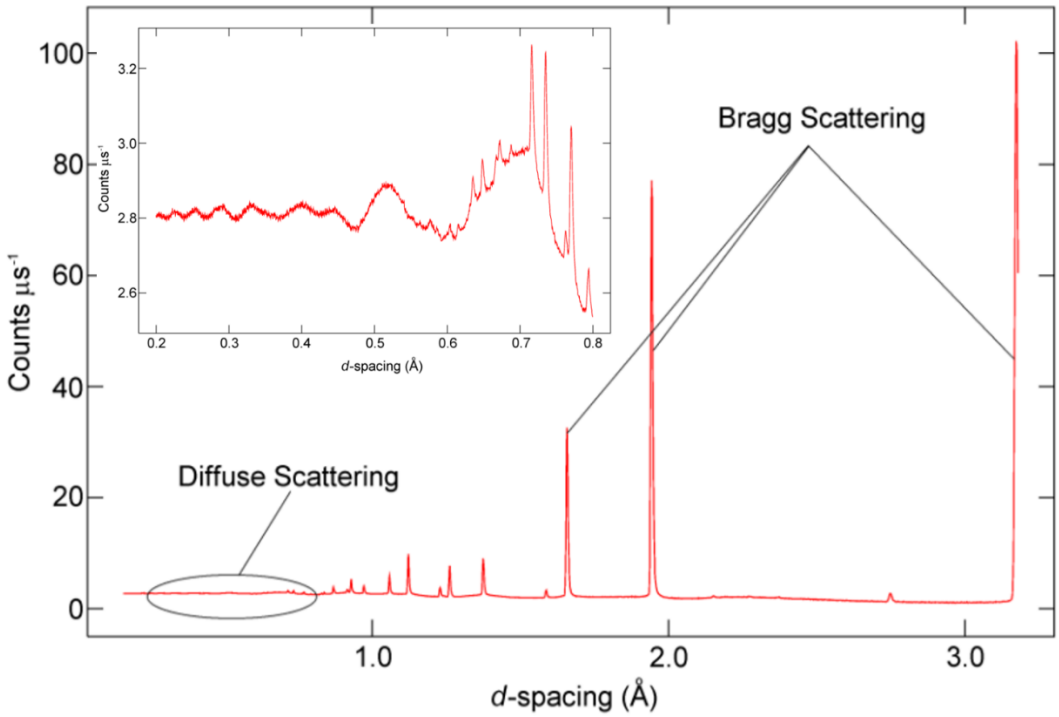

Figure 2.14 Comparison of the features of Bragg scattering and diffuse scattering [123]

The intensity of the total scattering is expressed in Eqn. 2.20, in which N is total number of atoms in the material, $F(Q)$ is the structure factor of the total scattering, c_j is the fraction of atom type j in all atoms and has the relationship shown in Eqn. 2.21,

$$\frac{1}{N}\frac{d\sigma}{d\Omega} = F(\mathrm{Q}) + \sum_{j=1}^{n} c_j \overline{b_j^2} \tag{2.20}$$

$$\sum_{j=1}^{n} c_j = 1 \tag{2.21}$$

2.2.2.2 Pair distribution function

In total scattering experiments, what is measured directly is the total scattering function, $S(\boldsymbol{Q})$, which is expressed in Eqn. 2.22, the $\boldsymbol{r}_{\mathrm{jk}} = \boldsymbol{r}_{\mathrm{j}} - \boldsymbol{r}_{\mathrm{k}}$.

$$S(\boldsymbol{Q}) = \frac{1}{N}|F(\mathbf{Q})|^2 = \frac{1}{N}\sum_{j,k} b_j\, b_k e^{i\boldsymbol{Q}\boldsymbol{r}_{jk}} \tag{2.22}$$

Averaging over time and orientation, the scattering function can be written as in Eqn. 2.23,

$$S(Q) = \frac{1}{N}\sum_{j,k} b_j\, b_k \frac{\sin(Qr_{jk})}{Qr_{jk}} \tag{2.23}$$

Eqn. 2.23 contains the self-scattering when $j = k$. When separating this term out, $S(Q)$ can be written as in Eqn. 2.24,

$$S(Q) = \frac{1}{N}\sum_{j} b_j^2 + \frac{1}{N}\sum_{j\neq k} b_j\, b_k \frac{\sin(Qr_{jk})}{Qr_{jk}} \tag{2.24}$$

Based on Eqn. 2.21, we can obtain:

$$\frac{1}{N}\sum_{j} b_j^2 = \sum_{j} c_j b_j^2 \tag{2.25}$$

The partial radial distribution functions or the partial pair distribution functions (PDFs), $g_{jk}(r)$, can be defined as in Eqn. 2.26, in which $n_{jk}(r)$ is the number of atoms of type k within the shell layer whose inner and outer distance from the atom j is r and $r + \mathrm{d}r$. If ρ_o is the average number density of the material, expressed as is $\rho_o = \frac{N}{V}$ (Å^{-3}), the average number density of all the atoms k in the material is written as $\rho_k = c_k\rho_o$. When r $\rightarrow \infty$, $g_{jk}(r) \rightarrow 1$.

$$g_{jk}(r) = \frac{n_{jk}(r)}{4\pi r^2 dr \rho_k} \tag{2.26}$$

The second term in Eqn. 2.24, is the sum over all atomic pairs, based on the partial radial distribution functions, $g_{jk}(r)$, then the pair sum, $i(Q)$, is given by:

$$i(Q) = \frac{1}{N}\sum_{j\neq k} b_j\, b_k \frac{\sin(Qr_{jk})}{Qr_{jk}} = 4\pi\rho_o \int \sum_{j,k} c_j\, c_k\, b_j\, b_k r^2 g_{jk}(r) \frac{\sin(Qr)}{Qr}\, dr \qquad (2.27)$$

The total radial distribution function, $G(r)$, is defined as in Eqn. 2.28. It is the summation of all the $g_{jk}(r)$ with proper weighting from the atomic scattering lengths and atom fractions.

$$G(r) = \sum_{j,k} c_j\, c_k\, b_j\, b_k \left[g_{jk}(r) - 1\right] \qquad (2.28)$$

The total radial distribution function $G(r)$ and the total scattering structure factor $F(Q)$ are related to each other through Fourier transformation as shown in Eqn. 2.29 and 2.30.

$$G(r) = \frac{1}{(2\pi)^3\rho_o} \int 4\pi Q^2 F(Q) \frac{\sin(Qr)}{Qr}\, dQ \qquad (2.29)$$

$$F(Q) = \rho_o \int 4\pi r^2 G\,(r) \frac{\sin(Qr)}{Qr}\, dr \qquad (2.30)$$

The differential correlation function, $D(r)$, is defined as:

$$D(r) = 4\pi\rho_o r G\,(r) = 4\pi\rho_o r \sum_{j,k} c_j\, c_k\, b_j\, b_k \left[g_{jk}(r) - 1\right] \qquad (2.31)$$

The number of atoms of type k between distances r_1 and r_2 ($r_1 < r_2$) from an atom of type j can be called the coordination number (CN) of atom j. It is can be determined from the partial radial distribution functions, $g_{jk}(r)$, as is shown in Eqn. 2.32,

$$CN = \int_{r_1}^{r_2} 4\pi r^2 \rho_k\, g_{jk}(r) dr \qquad (2.32)$$

According to the above description, the PDF reflects both the long-range and the local structural information. The PDF analysis is widely used to study the structural properties in materials, such as materials without long-range order like glasses and liquids, and polycrystalline materials with long-range order and short-range disorder. Both neutrons and high-energy X-rays can be used to produce the high-quality PDF data. Since different definitions of the above functions are used by different researchers, for clarity, the definitions and functions used in this thesis are based on Keen's work [124].

2.2.2.3 Gudrun corrections

Since the raw collected neutron radiation counts include signals from the adopted instrument and the sample containers, the sample cross section needs to be extracted relying on specialized software. Gudrun is such a programme which is aimed at correcting the raw neutron and X-ray total scattering data for the differential cross section and was developed by Alan Soper at ISIS [125].

There are two main data processing routines in the Gudrun package, Purge and Gudrun. Since most TOF diffractometers employ large arrays of detectors and part of them are bad detectors, Purge is the process of removing these bad detectors out of the data analysis, and it must be performed prior to any data processing. To correct the neutron radiation counts, the second Gudrun process normalises the data and sets them on an absolute scale.

After the Gudrun corrections, several kinds of sample related scattering functions can be produced like the $G(r)$, $D(r)$ in real space and $S(Q)$ and $i(Q)$ in reciprocal space. Fig 2.15 shows example plots of these scattering functions for $Li_{3.25}Ge_{0.25}P_{0.75}O_4$.

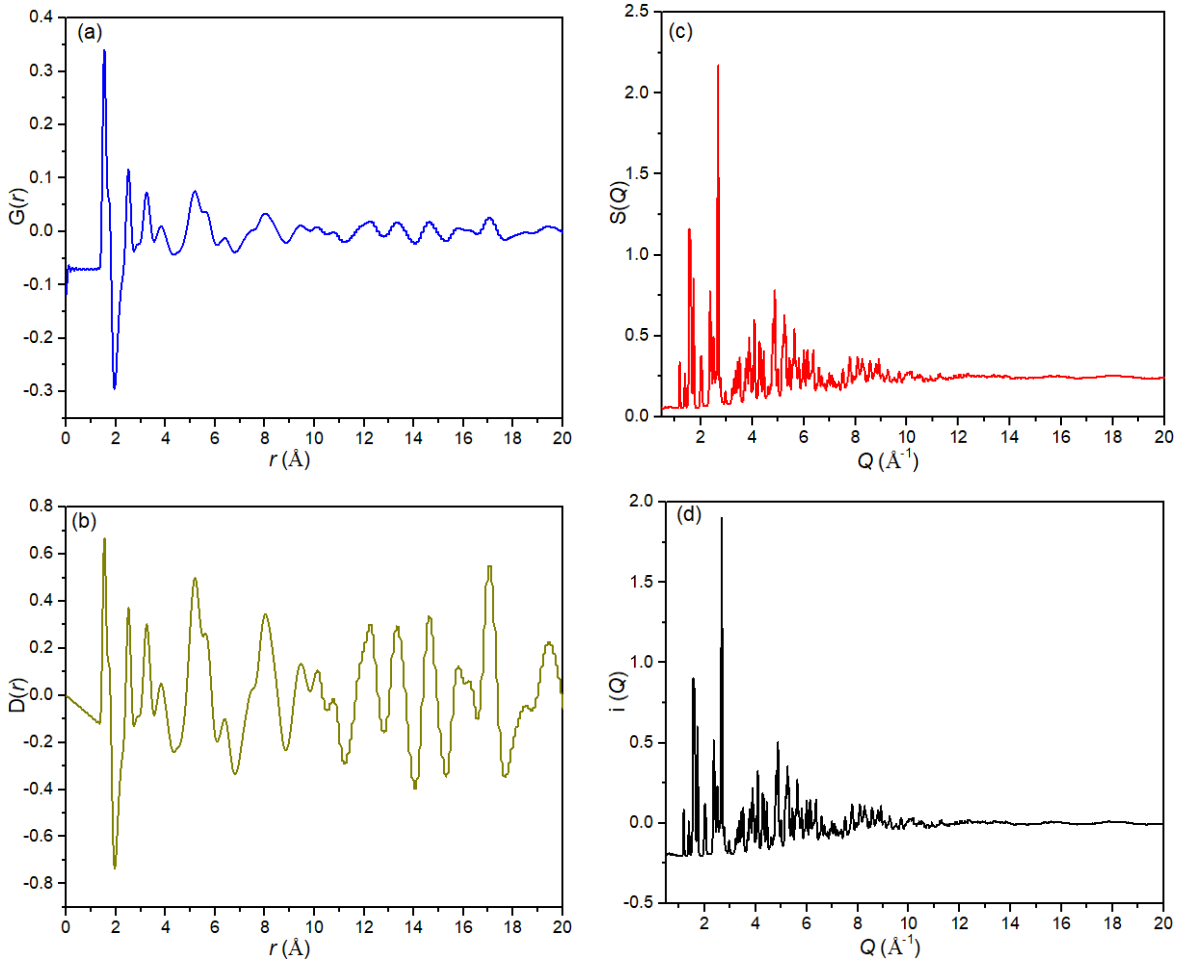

Figure 2.15 Scattering functions (a) *G*(*r*), (b) *D*(*r*), (c) *S*(*Q*) and (d) *i*(*Q*) for $Li_{3.25}Ge_{0.25}P_{0.75}O_4$

2.2.2.4 RMC modelling

The Reverse Monte Carlo (RMC) method was originally developed by McGreevy and Pusztai in 1988 [126] and was initially designed to produce three-dimensional structural models, consistent with experimentally collected structure data, for liquid and amorphous materials. Following developments, its application has expanded to crystalline materials with significant disorder.

Unlike other theoretical computational methods, like MD (molecular dynamics) and DFT (density function theory), which output the final calculation results mainly based on the input models and sets of constraints, RMC can give a unique understanding of the atomic structure within the studied material, directly based on the experimental data. For liquid and amorphous

materials and some crystalline materials, the inert structural disorder is a key parameter that might determine the physical and chemical properties and actual applications, while other probes can only reveal limited information. With data from neutron or X-ray total scattering experiments, RMC modelling can probe the structure disorder well, which is helpful in understanding the structure of disordered and partially disordered materials.

At the heart of the RMC method, is a process in which an initial atomic configuration is modified by hundreds of thousands of successive steps until the properties calculated from the last configuration are in best agreement with the experimental data. Since the focus of this thesis is on polycrystalline materials, the general RMC modelling procedures relating to these are introduced here.

2.2.2.4.1 RMC modelling procedures

1. Based on the crystal structure from a prior Rietveld refinement, an expanded supercell structural configuration that includes about 10^4 atoms (N atoms) is built. The big supercell is a three-dimensional box ($a \times b \times c$) and as such it can eliminate size and boundary effects rising from the finite unit cell size.
2. Within the set, constraints on the structure like bond length, bond angle, atoms swapping and bond valence sum constraints can be applied. A Monte Carlo algorithm is employed for the configuration optimization. For every move, one random atom from the N atoms (~10^4 atoms) is selected to move in a random direction for a random distance within the supercell. Thus, a new configuration is produced with its corresponding correlation functions, usually the calculated structure factor is used for comparison, If the difference between the new configuration and the experimental data is decreased, the move and new configuration will be accepted with a subsequent proposed random atomic move. χ^2 is used to describe the difference as is shown in Eqn. 2.33, in which y_j(exp) is the experimental

quantity, y_j(calc) is the corresponding calculated quantity and σ is the weighting factor that corresponds to the experimental uncertainty on y.

$$\chi^2 = \sum_j \frac{y_j(exp) - y_j(calc)}{\sigma_j^2} \tag{2.33}$$

χ^2 is based on a range of experimental data which can include $S(Q)$, $G(r)$, Bragg data (I_{hkl}) and polyhedral constraints (f_j) as seen in Eqn. 2.34. The polyhedral constraints can be applied to parameters such as bond lengths, bond angles and coordination numbers. σ_j is the weighting for a particular constraint that can be adjusted. By adjusting the weights of each component, the fit can be optimised so as not to weight a particular component unduly. The reason why a big range of experimental data are included in the RMC analysis is that the RMC method is a method based on statistical mechanics, the more data that are involved, the more effective the method is.

$$\chi^2 = \sum_j \frac{\left(S_{calc}(Q_j) - S_{exp}(Q_j)\right)^2}{\sigma_{Q_j}^2} + \sum_j \frac{\left(G_{calc}(r_j) - G_{exp}(r_j)\right)^2}{\sigma_{r_j}^2} + \sum_{hkl} \frac{\left(I_{calc}(hkl) - I_{exp}(hkl)\right)^2}{\sigma_{hkl}^2} + \sum_j \frac{\left(f_{j,RMC} - f_{j,exp}\right)^2}{\sigma_j^2} \tag{2.34}$$

As in Eqn. 2.34, if the difference in χ^2 between the new configuration and the experimental data is decreased, the move and the new configuration will be accepted with a subsequent proposed random atomic move. However, if the difference between the new configuration and the experimental data is increased, the move is not declined directly, a probability algorithm will be used to determine whether or not to accept or reject the proposed move, the probability is described in Eqn. 2.35. Through assessing the probability, the trapping in a local minimum of an idealised model can be avoided to make to allow for convergence to the global minimum.

$$P = e^{-\frac{\Delta\chi^2}{2}} \tag{2.35}$$

3. Thus, successive changes to the atomic configuration are proposed, followed by random atomic moves. Successive hundreds of thousands of moves are produced until the value of χ^2 reaches an equilibrium and cannot be decreased further. At this stage, the final configuration is taken as the corresponding structure configuration towards the experimental data.
4. The final supercell configuration can be averaged to the primitive unit cell. By examining the atomic distribution information, much information can be extracted to probe details of the local structure and local coordination environment.

2.2.2.4.2 Disadvantages of RMC modelling

RMC modelling is an iterative process, it evolves to increase the system entropy and maximise the amount of disorder within the structure configuration. In the end, RMC modelling outputs the most disordered atomic configuration which is consistent with the experimental data. However, there are a range of configurations that match the experimental data well with different degrees of disorder. This problem can only be minimised through enlarging the range of experimental data used in RMC simulation.

Although RMC can give a well-defined atomic configuration that matches the experimental data, it also has obvious disadvantages in comparison to MD or DFT simulations which can reveal the kinetic and the thermodynamic details of the studied system. RMC is a statistical mechanics-based method and can only provide static structural information and cannot give information on the kinetics and the thermodynamics of the studied system.

In this thesis the RMC method as implemented in the programme RMCProfile was used [127].

2.2.3 Scanning electron microscopy (SEM)

Electron microscopy uses an accelerated electron beam as an illumination source to get images of objects. Since the wavelength of the electron beam is more than a thousand times smaller than that of visible light, the image resolution can reach the micro-meter or even the nanoscale levels, reflecting the hyperfine structure of observed objects. According to their design and specialised function, electron microscopy can be divided into many different techniques, two of the most important being scanning electron microscopy (SEM) and transmission electron microscopy (TEM). In the present work only SEM has been used.

The basic construction of an SEM is shown in Fig. 2.16. The electron beam is produced by an electron gun, and is focused by a condenser lens. After interaction with the scan coil and objective lens, the focused electron beam hits the specimen.

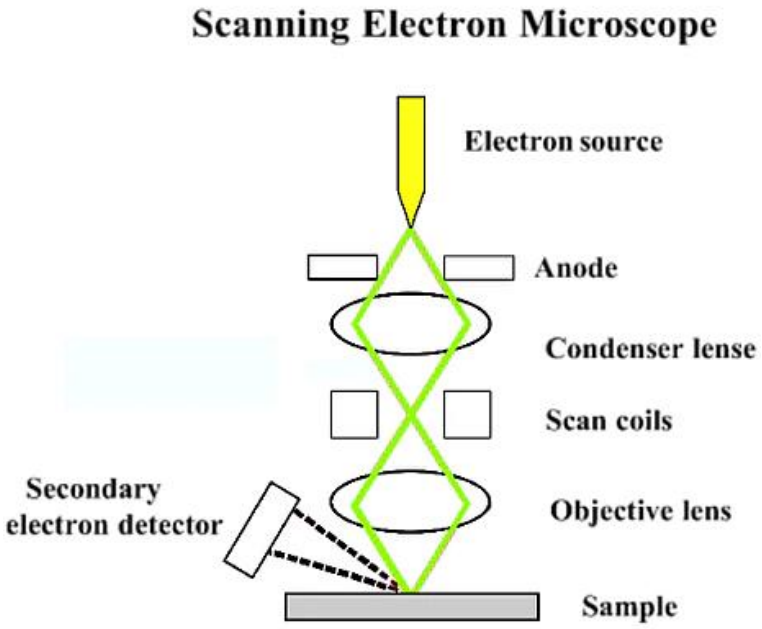

Figure 2.16 Basic components for an scanning electron microscopy (SEM) [128]

After the interaction with the specimen, the incident electron beams produce several kinds of signals including secondary electrons (SE), auger electrons, backscattered electrons (BSE) and cathode luminescence as shown in Fig. 2.17. In the case of the SEM, it is the backscattered

electrons and secondary electrons together that are used for the final 2D imaging. Backscattered electrons are part of the primary electron beam and are scattered backward after the elastic interactions with the sample. However, secondary electrons come from the atoms on the sample surface and have lower energy compared to the backscattered electrons. They are the result of inelastic interactions between the electron beam and the sample. Since backscattered electrons mainly come from the deeper regions of the sample whereas secondary electrons mainly come from the surface regions, they carry different types of sample information.

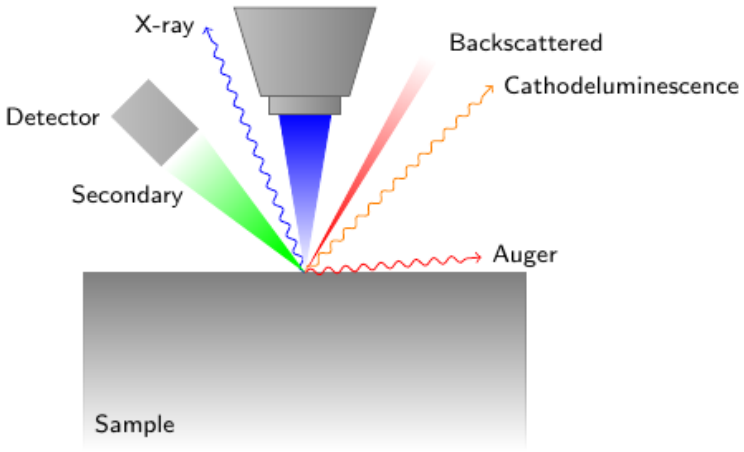

Figure 2.17 Incident electron beam-sample interactions in SEM [129]

Because the electron beam that hits the sample is of high energy, to avoid charge accumulation on the sample surface, the sample surface needs be conductive. For non-conductive specimens, coating with conductive carbon or gold is required.

Energy-dispersive X-ray spectroscopy (EDS) can be used to analyse the type and quantity of elements on the surface of a tested sample. It is based on the principle that every element has its unique electronic structure which generates a unique set of quantum energies in the emission spectrum. During the interaction between the incident electron beam and the sample, the ground state electron in an inner shell is ejected and at the same time an electron hole where

the electron was is created. An electron from an outer shell with higher energy fills the hole together with the release of an X-ray due to the energy difference between the two shells. Since the energy of the released X-ray is characteristic for every element, and the number of photons is proportional to the number of elements of a particular type, then the element types and quantities can be deduced.

The SEM used in this thesis was an FEI Inspect F (Hillsboro, OR) with energy-dispersive X-ray spectroscopy (EDS). Sample surfaces were sputtered with gold. The incident beam was generated at 5 or 10 kV for SEM image capture and at higher voltage for EDS.

2.2.4 Solid State NMR (NMR)

The phenomenon of the absorption of an electromagnetic radio wave with proper frequency by a nucleus located in an applied external magnetic field is called nuclear magnetic resonance (NMR). NMR can only happen for nuclei that have a non-zero spin quantum number, *I*, which occurs in nuclei where the numbers of protons and neutrons are not both even numbers. Table 2.3 lists some nuclei with the corresponding spin quantum number *I*. Nuclei with $I = 1/2$ are known as dipolar nuclei, Nuclei with $I > 1/2$ are known as quadrupolar nuclei [130, 131].

Table 2.3 Some examples of spin quantum numbers for different nuclei

No. of mass	No. of protons	No. of neutrons	*I*	Examples
Even	Even	Even	0	^{12}C, ^{16}O, ^{32}S
Odd	Even	Odd	1/2	^{13}C,
			5/2	^{17}O
Odd	Odd	Even	1/2	^{1}H, ^{19}F, ^{31}P
			3/2	^{7}Li, ^{11}B, ^{35}Cl, ^{79}Br
Even	Odd	Odd	1	^{2}H,^{6}Li,^{14}N

Since an atomic nucleus is positively charged and is spinning all the time, a magnetic field and spin angular momentum ***P*** are produced spontaneously. The nuclear magnetic moment, ***μ,*** is used to describe this magnetic property. The absolute value of ***P*** is determined by *I*, which is expressed in Eqn. 2.36, in which h is the Planck constant with a value of 6.626×10^{-34} J·s.

$$|P| = \frac{\mathrm{h}}{2\pi}\sqrt{I(I+1)} \tag{2.36}$$

The absolute value of ***μ*** is expressed as:

$$|\mu| = g.\frac{\mathrm{eh}}{4\pi m_p}\sqrt{I(I+1)} = g.\mu_{\mathrm{N}}\sqrt{I(I+1)} \tag{2.37}$$

where *g* is the Landé g-factor, its value varies with different nuclei; e is the electric charge of one electron or one proton, with the value of 1.60×10^{-19} C; m_p is the mass of one proton; *I* is the spin quantum number and μ_N is the nuclear magneton with a value of 5.05×10^{-27} J T^{-1}.

Both spin angular momentum *P* and ***μ*** are quantized. The projection value μ_z along the applied magnetic field direction *z* can only adopt discrete values:

$$\mu_z = g.\mu_N.m \tag{2.38}$$

where *m* is the magnetic quantum number, $m = I, I - 1, \ldots, -I + 1, -I$. The maximum value of μ_z is therefore $g \cdot \mu_N \cdot I$.

According to Eqns. 2.36 and 2.37, the ratio of nuclear magnetic moment μ and spin angular momentum *P* is a constant, and is expressed as,

$$\frac{\mu}{p} = \frac{g.\mu_N\sqrt{I(I+1)}}{\frac{h}{2\pi}\sqrt{I(I+1)}} = \frac{\frac{geh}{4\pi m_p}}{\frac{h}{2\pi}} = \frac{g.e}{2m_p} = \gamma \tag{2.39}$$

where γ is known as the magnetogyric ratio, which is a characteristic value for different nuclei.

2.2.4.1 Zeeman interaction

When an external magnetic field, B_0, is applied to a non-zero spin nucleus, it will remove the degeneracy of the energy states of the nucleus, making the energy states split into $2I + 1$ levels. This kind of interaction is called the Zeeman interaction. For example, for ^{1}H, $I = 1/2$,

and there are two orientations of m = -1/2 and m = +1/2, i.e. in the applied external magnetic field, the energy level of ^{1}H is split into two. According to the convention, Zeeman interactions take place along the direction of the field, setting the field direction as the z-axis while the electromagnetic radio frequency field is applied in the x-y plane. According to quantum mechanics, many types of electromagnetic interactions are contributors to the Hamiltonian, $\hat{H}$, which describes the different energy level states. The Zeeman interaction is the major contributor to the $\hat{H}$, other contributions come from the chemical shift interaction, dipole – dipole interaction, spin – spin coupling and quadrupolar interactions.

For Zeeman interactions, the corresponding Hamiltonian operator, $\hat{H}_z$, is given in Eqn. 2.40,

$$\hat{H}_Z = -\mu_Z \cdot B_0 \tag{2.40}$$

The energy produced by the Zeeman interaction is shown in Eqn. 2.41, in which $\hbar = h/2\pi$, B_{loc} is the local magnetic field the nucleus experiences, which is the sum of the external magnetic field, B_0, and internal magnetic field, B_{int}. B_{int} is much smaller than B_0 and is produced by the nucleus and its surrounding environment, as is shown in Eqn. 2.42.

$$E = -m\gamma\hbar B_{loc} \tag{2.41}$$

$$B_{loc} = B_0 + B_{int} \tag{2.42}$$

The Zeeman interaction determines the initial energy level splitting through removing the degeneracy of the energy states of the nucleus, and it also determines the resonant frequency ν. According to the selection law, transitions between the quantum energy levels can only happen whenr $\Delta m = \pm 1$, so only when the energy of the electromagnetic radio frequency field ($E = h\nu$) is the same as the energy difference ΔE, can NMR occur.

$$h\nu = 2\mu_Z B_{loc} = \frac{\gamma h}{2\pi} B_{loc} \tag{2.43}$$

$$\nu = \frac{\gamma}{2\pi} \cdot B_{loc} \tag{2.44}$$

From the above equations, it can be concluded that since the γ is different for different nuclei, the condition for NMR to happen is different. For a certain nucleus, ν is proportional to B_{loc},

since B_{int} is far smaller than B_0, it is the applied magnetic field B_0 that mainly determines the resonant frequency ν. However, it can also be seen that the exact value of ν is affected by B_{int}, i.e. various kinds of direct and indirect interactions between the tested nucleus and the surrounding environment (electrons and nuclei), and all these interactions indicate important local structural and dynamic information in both liquid and solid samples.

The NMR spectra of liquids and solids show significant differences. For solution NMR, due to the rapid random molecular tumbling, all the anisotropic NMR interactions are averaged to zero and make the NMR spectra show a series of very sharp transition peaks. In contrast, in solid-state NMR (SS-NMR), spectra are very broad, because of the effects from the direct and indirect interactions (anisotropic or orientation-dependent) are observed in the spectrum. There are mainly five kinds of interactions for the spin nucleus that cause broadening of the spectral line shapes in SSNMR spectra,

1) Zeeman interaction between the studied nucleus and the applied magnetic field

2) Chemical shifts caused by the magnetic shielding in the studied nucleus by the surrounding electrons

3) Direct dipole-dipole interactions between the studied nucleus and other nuclei

4) Spin-spin couplings between the studied nucleus and other nuclei

5) Quadrupolar interactions which occur when the nucleus has $I > 1/2$.

The total Hamiltonian, $\hat{H}$ for a studied nucleus of spin I in the solid state can be summarised as:

$$\hat{H} = \hat{H}_Z + \hat{H}_{CS} + \hat{H}_D + \hat{H}_{SC} + \hat{H}_Q \quad (2.45)$$

From the Zeeman interaction $\hat{H}_Z$ shown in Eqn. 2.40, there is no interaction between the studied nucleus and the surrounding environment and no local structural information can be inferred. Nevertheless, it is notable that all other interactions are based on the Zeeman interaction.

2.2.4.2 Chemical shift interaction

Electrons that move around the nucleus have a spin of ±1/2 and have a corresponding angular momentum, through which they contribute to the total interaction for the studied nucleus with a static (external) applied magnetic field B_0 and affect the final NMR spectrum. In response to the effect of B_0 on spinning electrons, electrons produce their own magnetic field through adjusting their rotation. As a result of the magnetic shielding from the surrounding electrons, the actual magnetic field the studied nucleus feel, B_{eff}, is smaller than B_0, and can be described by Eqn. 2.46, in which σ is the chemical shift tensor.

$$B_{eff} = B_0(1 - \sigma) \tag{2.46}$$

Thus, the resonant frequency v_0 is given by:

$$v_0 = \frac{\gamma}{2\pi} B_0(1 - \sigma) \tag{2.47}$$

Due to the magnetic shielding effect from electrons, for a certain applied magnetic field, a higher or lower resonant frequency v_0 is required for resonance to occur, depending on the extent of shielding. Shifts in the resonant lines for nuclei with differing degrees of shielding can be observed in the spectrum, and is known as the chemical shift. The expression for the chemical shift interaction Hamiltonian, $\hat{H}_{cs}$, can be expressed as:

$$\hat{H}_{CS} = \gamma\hbar\sigma B_0 \tag{2.48}$$

Chemical shift resulting from the electron cloud density is very sensitive to the local atomic environment such as the coordination number of the studied nucleus in inorganic solids and the bonding configuration in organic liquids. The chemical shift is usually expressed in the form of parts per million (ppm) instead of the Larmor frequency and a reference compound is used to calibrate it.

2.2.4.3 Dipole-dipole interaction

The dipole - dipole interaction results from the interaction between the nuclear spin and the magnetic field produced by another nuclear spin. It is a three-dimensional direct space interaction which depends on the radii γ of both nuclei and the distance r between them. The Hamiltonian of the dipole - dipole interaction can be expressed in Eqn. 2.49, in which $\widehat{\mathrm{D}}$ is the dipole coupling tensor.

$$\hat{\mathrm{H}}_D = \frac{\gamma^2\hbar^2}{r^3}\,\mathbf{I}_1\widehat{\mathrm{D}}\mathbf{I}_2 \tag{2.49}$$

The dipole - dipole interaction Hamiltonian can also be expressed as the sum of all nuclei pairs (nucleus i and nucleus j), seen in Eqn. 2.50, in which r_{ij} is the internuclear distance between i and j, θ_{ij} is the vector angle between r_{ij} and the applied magnetic field, B_0.

$$\hat{\mathrm{H}}_D = \sum\frac{1}{2}\gamma_i\gamma_j\hbar^2 r_{ij}^3\left(\mathbf{I}_i\cdot\mathbf{I}_j - 3\mathrm{I}_{ix}\mathrm{I}_{jx}\right)\left(3\cos^2\theta_{ij} - 1\right) \tag{2.50}$$

For liquid NMR, since the $\cos^2\theta_{ij}$ is 1/3, the dipole - dipole interaction is zero. However, for solid state NMR, since there are pairs of dipole interactions for every two nuclear spins, the dipole - dipole interaction is the main reason for the broadening of spectrum lines. For most solid materials, the relatively weak chemical shift interaction is usually hidden within the line broadening from dipole - dipole interaction, making the local chemical information almost totally lost.

2.2.4.4 Spin-spin coupling

Spin-spin coupling is the interaction between two nuclei through the coupling of their separate electronic spins and is an indirect dipole-dipole interaction. The Hamiltonian of this interaction is given in Eqn. 2.51, in which $\mathbf{J_{IS}}$ is the indirect coupling tensor.

$$\hat{\mathrm{H}}_{\mathrm{SC}} = h\mathbf{I}\cdot\mathbf{J_{IS}}\cdot\mathbf{S} \tag{2.51}$$

Spin-spin coupling is much smaller than other types of interactions, but it is also important for a complete understanding of an NMR spectrum.

2.2.4.5 Quadrupolar interactions

As mentioned above, nuclei with $I > 1/2$ such as ^{7}Li, ^{23}Na, ^{27}Al are known as quadrupolar nuclei. Unlike nuclei with $I = 1/2$, quadrupolar nuclei have a charge distribution with non-spherical symmetry. The Hamiltonian of this interaction is given in Eqn. 2.52, in which Q is nuclear quadrupolar moment.

$$\hat{H}_Q = \frac{e^2qQ}{4I(2I-1)}\left[3I_z{}^2 - I^2 + \eta\left(I_x{}^2 - I_y{}^2\right)\right] \quad (2.52)$$

For quadrupolar nuclei, the quadrupolar interaction is an important source of structural information on local symmetry and also contributes to the line broadening of the NMR spectrum.

2.2.4.6 Interaction frequency ranges

The energies of the various interactions described above are quite different and hence occur over different frequency ranges. Table 2.4 outlines the general frequency ranges for each of these interactions.

Table 2.4 Frequency ranges of five important NMR interactions

Zeeman interaction	~ 100 MHz
Quadrupolar interaction	~ 1-10 MHz
Dipole-dipole interaction	~ 100 kHz
Chemical shift interactions	~ 10 kHz
Scalar (J) interaction	~ 100 Hz

2.2.4.7 Conventions

There are many different descriptions to label the principal components of chemical shift tensors in the literature. Here we obey the Haeberlen convention [132-134]. For all conventions the absolute magnetic shielding, σ, and the chemical shift, δ, are defined in the same way [135]. σ in

ppm is the shielding difference resulting from the frequency difference of the bare nucleus, ν_b, and the studied nucleus of the same species, ν_s:

$$\sigma \text{ / ppm} = 1 \times 10^6 \times (\nu_b - \nu_s) / \nu_b \tag{2.53}$$

δ is the shielding difference between the studied nucleus in the species, σ_s, and that of a nucleus of the same kind in a reference compound, σ_{ref}.

$$\delta \text{ / ppm} = (\sigma_{ref} - \sigma_s) / (1 - \sigma_{ref}) \tag{2.54}$$

According to the Haeberlen convention [132], the principal components of the chemical shift tensor are labelled as δ_{xx}, δ_{yy} and δ_{zz} (or typically δ_{11}, δ_{22} and δ_{33}). Their order is given by:

$$|\delta_{33} - \delta_{iso}| \geq |\delta_{11} - \delta_{iso}| \geq |\delta_{22} - \delta_{iso}| \tag{2.55}$$

Fig. 2.18 illustrates this ordering.

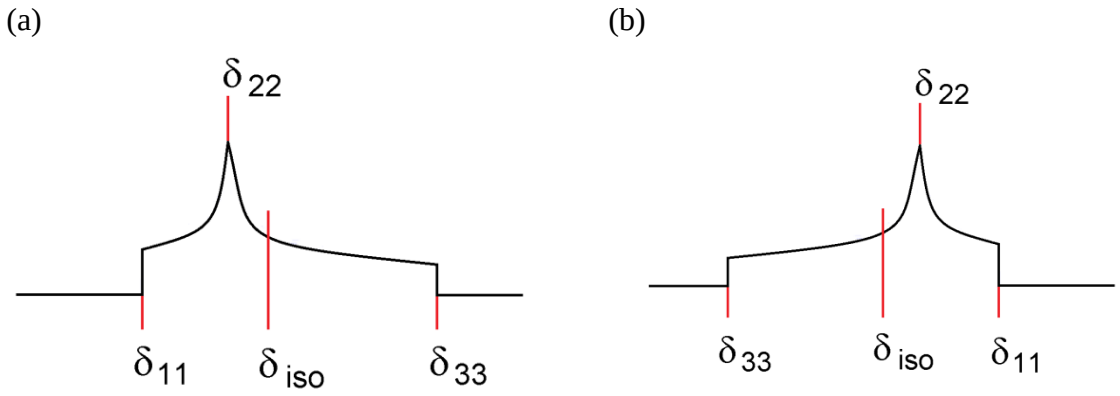

Figure 2.18 Ordering of principal components of the chemical shift tensor according to the Haeberlen convention (a) where the high frequency end is closer to δ_{iso} than the low frequency end and (b) where the low frequency end is closer to δ_{iso} than the high frequency end.

The isotropic shift δ_{iso}, is the average of the principal components:

$$\delta_{iso} = (\delta_{11} + \delta_{22} + \delta_{33})/3 \tag{2.56}$$

The chemical shift anisotropy $\Delta\delta$ is defined as:

$$\Delta\delta = \delta_{33} - \frac{1}{2}(\delta_{11} + \delta_{22}) \tag{2.57}$$

and the asymmetry η is given by:

$$\eta = \frac{\delta_{22}-\delta_{11}}{\delta_{33}-\delta_{iso}} \tag{2.58}$$

2.2.4.8 Magic angle spinning

In 1958 and 1959, E. R. Andrew and I. J. Lowe proposed that the anisotropic dipole interaction in solid state NMR could be supressed through introducing artificial motion to the tested solid samples [136, 137]. This technique involves rotating the sample at an angle of 54.74° relative to the direction of applied external magnetic field, which is known as magic angle spinning (MAS), as shown in Fig. 2.19. According to Eqn. 2.50, to eliminate the direct dipole-dipole interaction and first order quadrupolar interactions, the term $(3\cos^2\theta - 1)$ should be equal to zero, which occurs when $\theta = 54.74°$, which is known as the 'magic angle'.

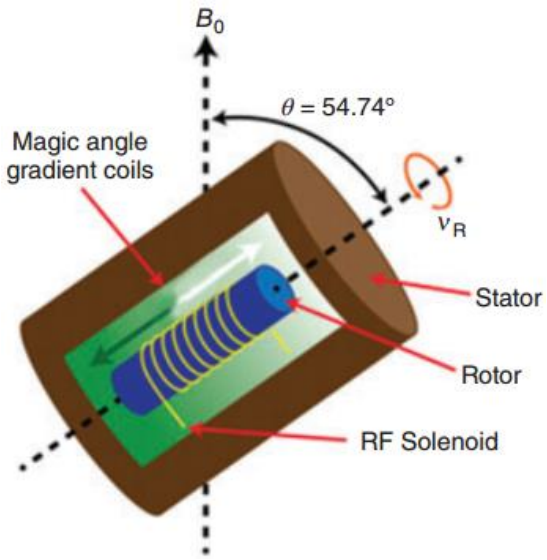

Figure 2.19 Schematic representation of MAS system [138]

Through MAS, both the homonuclear and heteronuclear dipole interactions are removed, leaving the isotropic chemical shift and weak spin-spin coupling visible in spectra. It is noteworthy that to make the MAS method work well, the spinning speed of the tested sample should be equal to or higher than the level of anisotropic dipole line width which is many kHz

wide. However, if the sample spinning speed is slower than the dipole line width, a manifold of spinning sidebands will become visible, which are separated by the spinning rate. The intensities of sidebands can be used to calculate the chemical shift tensor. If in the latter situation, key parameters like shielding anisotropy, $\Delta\delta$, and the shielding asymmetry factor, η, as defined in Eqns. 2.57 and 2.58 can be calculated.

Fig. 2.20 shows 81 MHz ^{31}P cross polarized MAS spectra of $NH_4H_2PO_4$ using high power proton decoupling at various spinning rates. When the sample is static, a broad NMR spectrum can be seen for the solid powder sample. As the spinning speed increases, a central band appears at the position of isotropic chemical shift with concomitant sidebands. When the spinning speed (at 4000 Hz) exceeds the span range of the chemical shift interaction, there is only one sharp isotropic central band with no visible sidebands and a final liquid-like NMR spectrum is obtained.

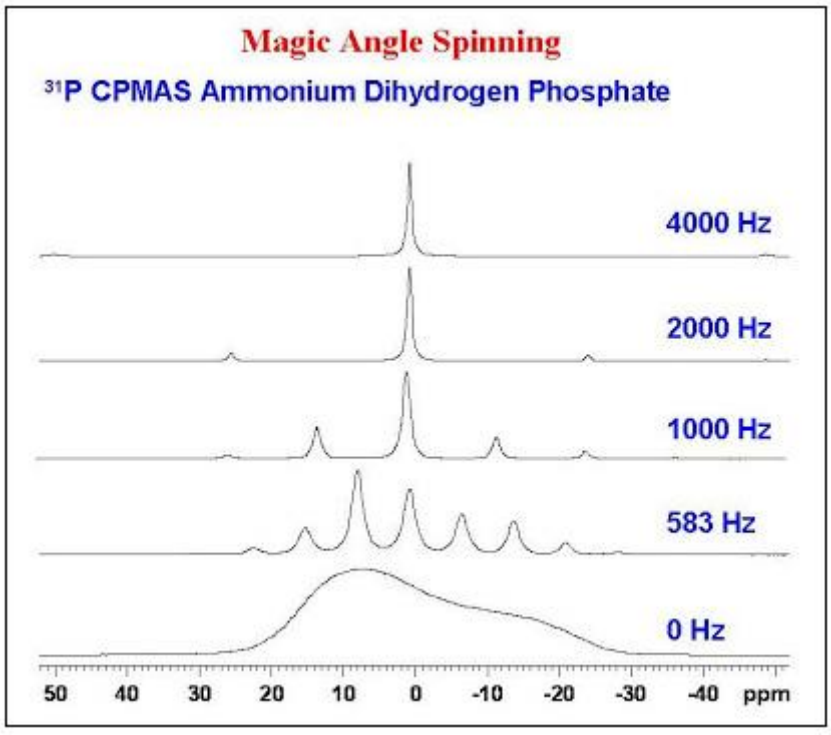

Figure 2.20 ^{31}P NMR in $NH_4H_2PO_4$ at different spinning speed [139]

2.2.5 Impedance spectroscopy

2.2.5.1 Fundamentals

Impedance spectroscopy (IS) is an important technique for assessing the electric behaviour of electro-ceramics such as solid electrolytes and electrode materials. For solids, the general two probe procedure involves application of an alternating voltage (AV) to the two parallel sides of a rectangular block or cylindrical pellet, which have previously been coated with a conductor such as gold or platinum. Through collecting the response current, the resistive and reactive components constituting the response can be identified. These measurements can be carried out over wide temperature ranges under different atmospheres such vacuum, N_2, Ar and mixed gases.

The value of applied alternating voltage is usually very small from 5 to 10 mV, while the frequency range is usually broad from 1 MHz to 0.1 Hz. When applying an AV, an alternating current (AC) is produced with a shift in phase angle θ ($\theta > 0$) from the voltage (Fig. 2.21). The phase difference is due to the delayed electrical response of the sample to the applied voltage. When $\theta = 0$, the tested sample exhibits purely resistive behaviour.

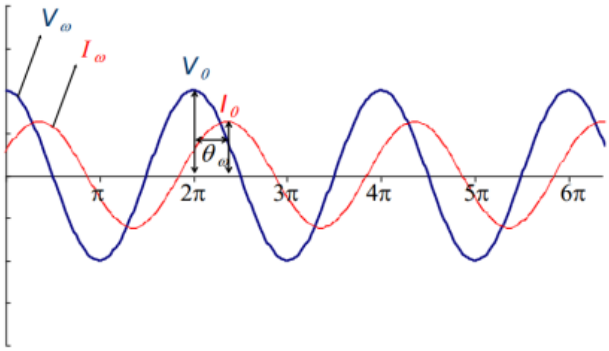

Figure 2.21 Schematic diagram of the waveforms of AV (V_ω) and current (I_ω) in impedance measurements, V_0 and I_0 are the amplitudes of voltage and current wave functions and θ is the phase shift.

In impedance spectroscopy, the impedance is defined as in Eqn. 2.59, in which ω is the radial frequency in radians s^{-1}, which is related to frequency (f) in Hz by $f = \frac{\omega}{2\pi}$.

$$\mathrm{Z}(\omega) = \frac{V_\omega}{I_\omega} = \frac{v\,(t)}{i\,(t)} = \frac{V_0 \sin(\omega \mathrm{t})}{I_0 \sin(\omega \mathrm{t} + \theta)} \tag{2.59}$$

where *t* represents time. The functions for V_ω and I_ω can be expressed in complex quantities in which real and imaginary components are included. Assuming that the response to the small applied AV is linear, their corresponding equations are in Eqn. 2.60 and Eqn. 2.61.

$$V(\omega, \mathrm{t}) = V_0\big(\cos(\omega \mathrm{t}) - i sin(\omega \mathrm{t})\big) = V_0 e^{i\omega t} \tag{2.60}$$

$$I(\omega, \mathrm{t}) = I_0\big(\cos(\omega \mathrm{t} + \theta) - i sin(\omega \mathrm{t} + \theta)\big) = I_0 e^{i\omega t + \theta} \tag{2.61}$$

Based on the complex exponential functions (Eqns. 2.60 and 2.61), in 1894 Heaviside expressed impedance in its complex form (Eqn. 2.62) to study electrical behaviour [140].

$$\mathrm{Z}(\omega) = \frac{U_\omega}{I_\omega} = |Z| e^{i\varphi} = Z' + iZ'' \tag{2.62}$$

in which $Z' = |Z|\cos\theta$ and $Z'' = |Z|\sin\theta$. When $\theta = 0$, $Z' = R$ where R represents a pure resistor which is independent of the frequency; when $\theta = \pi/2$, $Z'' = \frac{1}{\omega C}$ where C represents the capacitance.

Impedance spectra are typically presented in the form of a Nyquist plot -Z″ or Z″ versus Z′ as shown in Fig. 2.22.

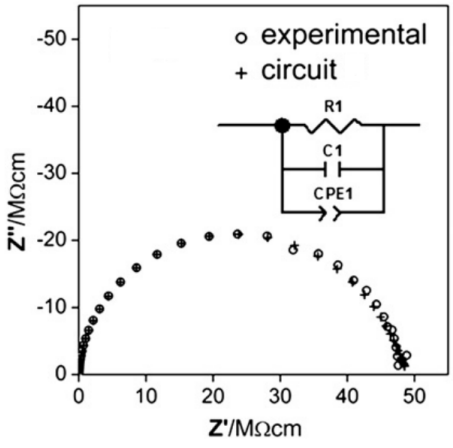

Figure 2.22 Experimental and fitted Nyquist plot with insert circuit (adapted from [141])

2.2.5.2 Electrical components

The impedance behaviour is dependent on the contribution of various resistive and reactive components in the system. These components are typically expressed in terms of equivalent electronic circuit elements. Fig. 2.23 summarises some basic electrical elements and their corresponding impedance spectra. In addition to resistors (R) and capacitors (C) mentioned in section 2.2.5.1, constant phase elements (CPE) are also critical in explaining the electrical response.

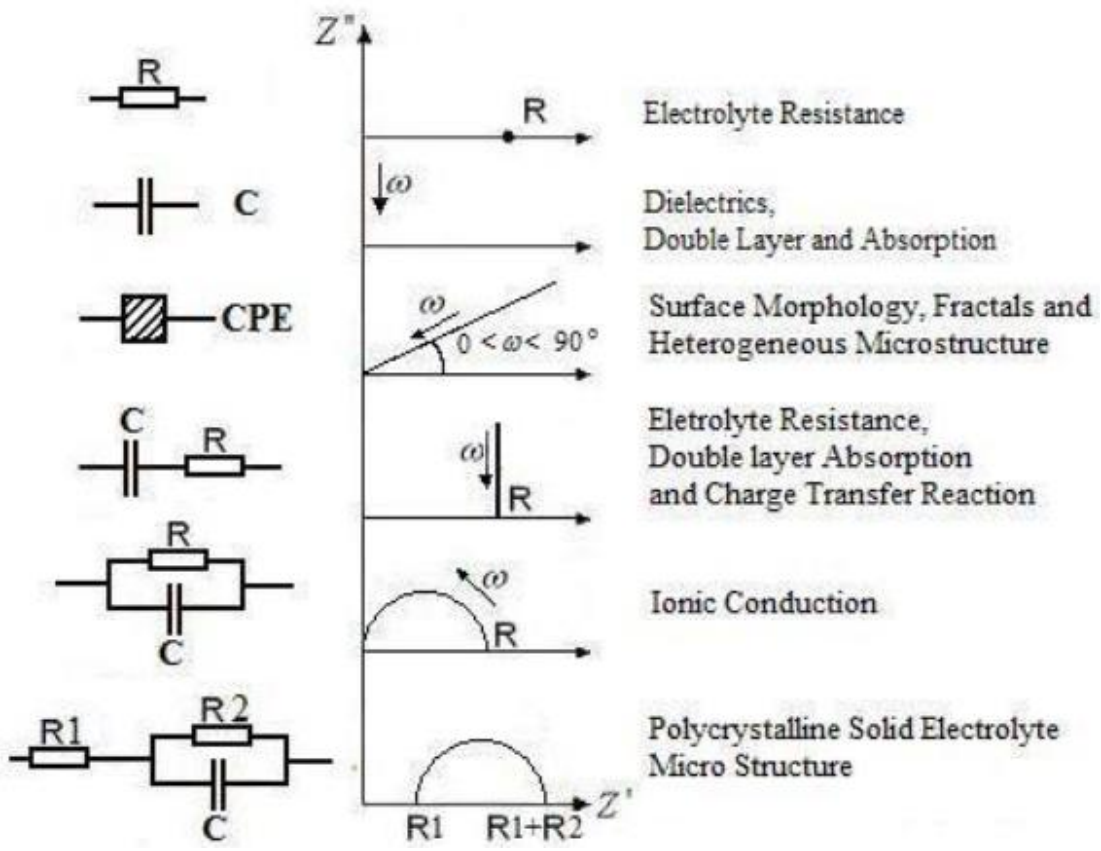

Figure 2.23 Electrical elements and their corresponding impedance spectra

According to Irvine et al., the magnitudes of capacitance values are usually representative of specialized electrical behaviour [142]. For example, small capacitance values in the order of 10^{-12} F are related to the large volume fraction i.e. the sample bulk, intermediate capacitance values in the order of 10^{-11} F are related to the small volume fraction i.e. grain boundaries and secondary phases, relatively large capacitance values around 10^{-7} F are related to the surface

layer and the sample surface–electrode interface, while large capacitance values in the order of 10^{-4} F are associated with electrochemical reactions. These are summarised in Table 2.5.

Table 2.5 Capacitance values and their possible responsible electrical phenomena [142]

Capacitance (F)	Phenomenon Responsible
10^{-12}	bulk
10^{-11}	minor, second phase
$10^{-11} – 10^{-8}$	grain boundary
$10^{-10} – 10^{-9}$	bulk ferroelectric near T_C (Curie Temperature)
$10^{-9} – 10^{-7}$	surface layer
$10^{-7} – 10^{-5}$	sample-electrode interface
10^{-4}	electrochemical reactions

2.2.5.3 Equivalent circuits

As explained in section 2.2.5.2, different electrical components and different combinations of these electrical components with sets of values can give rise to different kinds of impedance spectra. Correspondingly, equivalent electrical circuits, made up of different electrical components, combined in parallel or in series can be used to model the impedance spectrum. Fig. 2.24b shows an ideal impedance spectrum of a polycrystalline material pellet, which includes two adjacent distinct semicircles, with the left and right semicircles representing the electrical behaviour of the intra-grain (bulk) and the inter-grain (grain boundaries) regions, respectively. The equivalent electrical circuit shown in Fig. 2.24a can model the spectrum well and consists of two parallel RC units (i.e. a resistor and a capacitor connected in parallel) which are connected in series to each other. The total resistance of the sample, R_{tot}, corresponds to the low frequency (right side) intercept of the low frequency semicircle with the real axis. The bulk resistance, R_b, can be read off from the right-hand intercept of the high frequency (left) semicircle with the real axis, while the grain boundary resistance R_{gb} is the difference between

R_{tot} and R_b i.e. $R_{gb} = R_{tot} - R_b$. It is noteworthy that for the highest point in each semicircle, there is a relationship that $\omega RC = 1$, where R is the resistance associated with that semicircle and ω is the specific frequency at the top of the semicircle, allowing for the capacitance C associated with that process to be readily calculated.

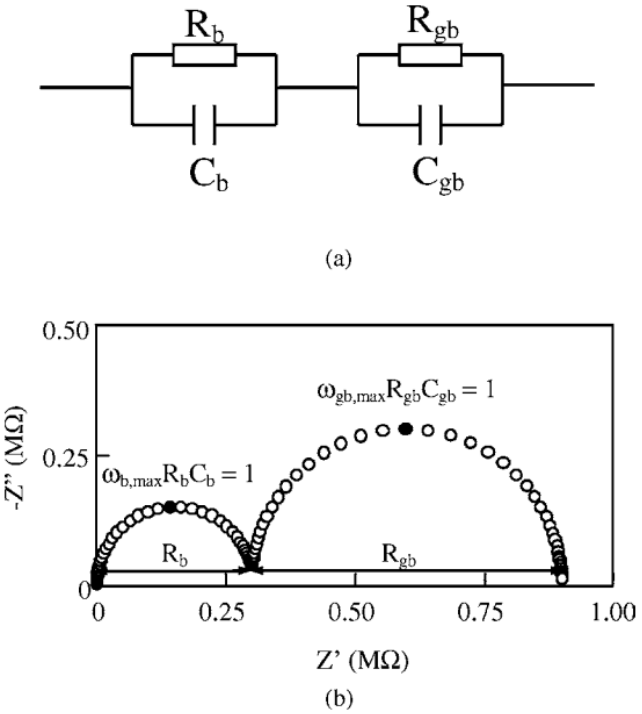

Figure 2.24 (a) An common equivalent electrical circuit used to model the impedance spectra of electro-ceramics, and (b) an ideal impedance spectrum of a polycrystalline material pellet [143]

Complicated impedance spectra can often be fitted using different equivalent circuit models. Therefore, it is an important point not only to obtain a good fit, but also to make sure that the equivalent circuit has some physical meaning with respect to the system under study.

2.2.5.4 Resistivity and conductivity

To allow comparison of electrical response values, the dimensions of the pellet need to be taken into account. This is done by converting resistance, R, from the impedance spectra to

resistivity, ρ and conductivity, σ, respectively as in Eqns. 2.63 and 2.64 where l and S are the pellet thickness and surface area, respectively.

$$\rho = \frac{R\,S}{l} \tag{2.63}$$

$$\sigma = \frac{1}{\rho} = \frac{l}{R\,S} \tag{2.64}$$

In this thesis for the impedance measurements, annealed ceramic pellets were first cut and polished into rectangles of ca. 4 × 4 mm of thickness around 2 mm. Gold electrodes were sputtered by cathodic discharge. Electrical characterisation was carried out by a.c. impedance spectroscopy using a fully automated system based on a Solartron 1255 frequency response analyser in conjunction with a bespoke automatic current/voltage converter. Impedance data were collected over the frequency range 0.1 Hz to 1 $\times 10^6$ Hz, in the approximate temperature range 50 to 300 °C or 50 to 400 °C.

Chapter 3 Structure and conductivity in the $Li_{3+x}Ge_xP_{1-x}O_4$ system

3.1 Introduction

Li_3PO_4 exhibits three known polymorphs, β, γ and α. The corresponding phase transition sequence is illustrated in Fig. 3.1 [144]. Both the low-temperature β and high-temperature γ phases are of orthorhombic structure. The β-phase possesses space group $Pmn2_1$ (No. 31) with unit cell parameters of a = 6.1150 Å, b = 5.2394 Å, c = 4.8554 Å, V = 156.87 Å^3 and Z = 2 [145]. The γ-phase crystallises in space group *Pnma* (No. 62) with unit cell parameters of a = 10.4612 Å $\approx 2b_\beta$, b_γ = 6.1113 Å $\approx a_\beta$, c_γ = 4.9208 Å $\approx c_\beta$, V_γ = 316.28Å^3 $\approx 2V_\beta$ and Z_γ = 4 [146]. Even though the low-temperature β phase is the thermodynamically stable under 500 °C, the high-temperature γ-phase can kinetically stabilize to room temperature during natural cooling.

$$\beta \xrightarrow{500\,^\circ C} \gamma \underset{}{\overset{1170\,^\circ C}{\rightleftharpoons}} \alpha \overset{1220\,^\circ C}{\rightleftharpoons} \text{liquid}$$

Figure 3.1 Phase transitions in Li_3PO_4

Fig.3.2 illustrates the crystal structures of β-Li_3PO_4 and γ-Li_3PO_4. Both of them consist of distorted hexagonal close packed (hcp) oxide ion sublattices with lithium and phosphorous occupying half the tetrahedral sites. The difference is that the occupied tetrahedral sites are different in the two polymorphs. In β- Li_3PO_4, all the tetrahedra have the same orientation and only corner-sharing exists for adjacent tetrahedra (Fig. 3.3a). In γ- Li_3PO_4, the orientation for some of the LiO_4 tetrahedra is not the same as for the PO_4 tetrahedra, resulting in both edge and corner sharing connections between adjacent LiO_4 tetrahedra and only corner-sharing between LiO_4 and PO_4 tetrahedra as indicated in Fig. 3.3b.

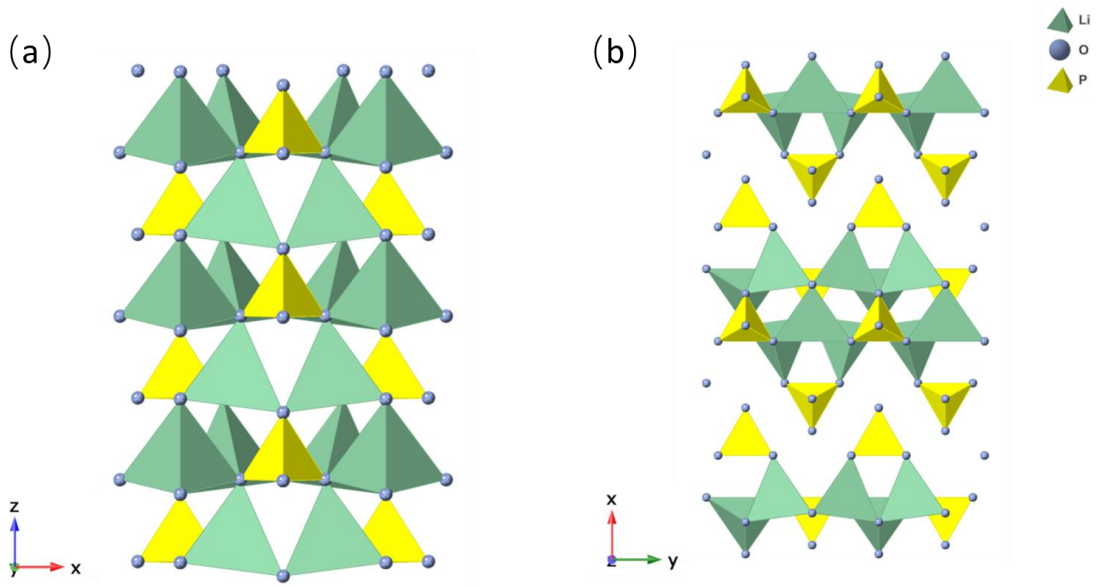

Figure 3.2 Structures of (a) *β*-Li_3PO_4 and (b) *γ*-Li_3PO_4

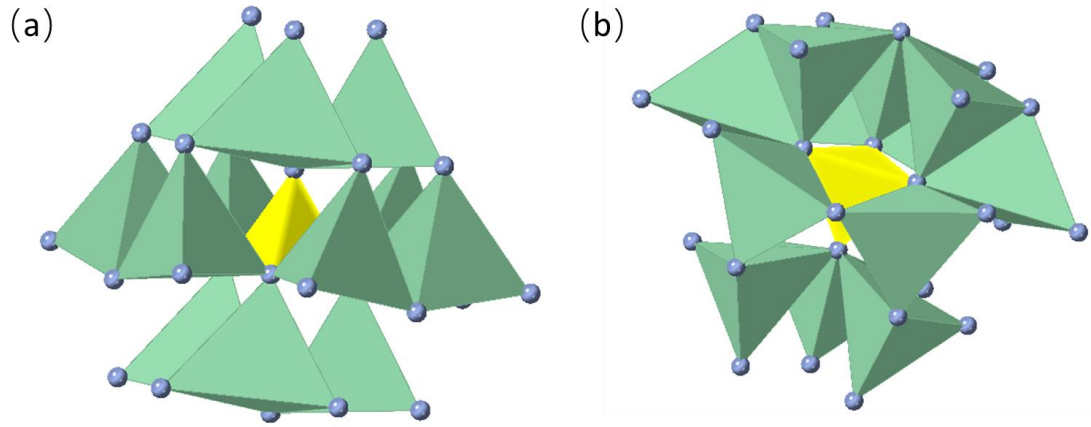

Figure 3.3 LiO_4 tetrahedral clusters around PO_4 tetrahedra in (a) *β*- Li_3PO_4 and (b) *γ*-Li_3PO_4

Li_4GeO_4, also exhibits a distorted hcp O^{2-} anion array with Ge^{4+} in tetrahedral sites. There are two crystallographically distinct sites for Li^+, both are tetrahedral. One of the sites (Li1) can be considered to occupy the normal tetrahedral sites in the close packed lattice. The other Li^+ (Li2) formally occupies an octahedral site but is shifted towards a corner of the octahedron to give distorted tetrahedral geometry. Li_4GeO_4 exhibits space group *Cmcm* (No. 63) with unit cell parameters of a = 7.766 Å, b = 7.357 Å, c = 6.049 Å, V = 345.61 Å^3 and Z = 4 [147]. As

shown in Fig. 3.4, there exists both corner-sharing and edge-sharing between the LiO_4 tetrahedra and only corner-sharing between LiO_4 and GeO_4 tetrahedra.

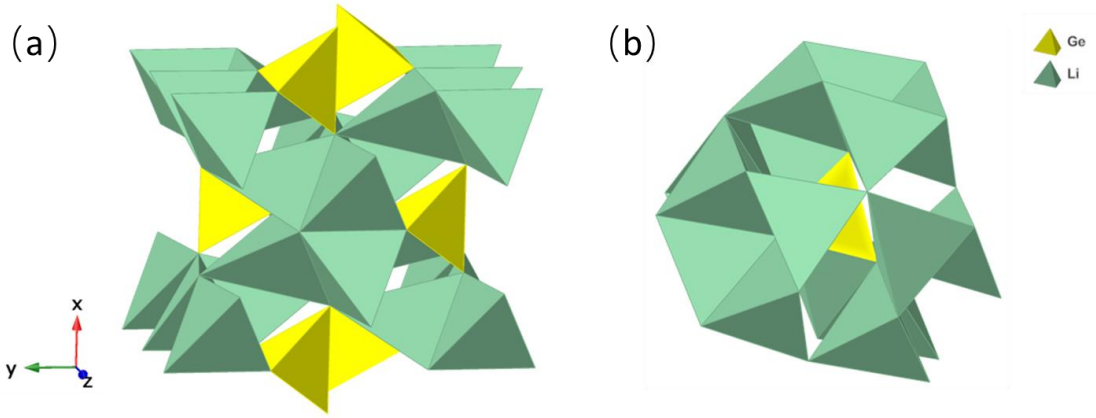

Figure 3.4 (a) Structure of Li_4GeO_4 with (b) detail of LiO_4 tetrahedral clusters around a GeO_4 tetrahedron

Similar to γ-Li_3PO_4, the LISICON (lithium superionic conductor) structure, originally defined based on the structure of $Li_{3.5}Zn_{0.25}GeO_4$, is also based on a distorted hexagonal close packed sublattice of oxygen atoms and has the same space group as γ-Li_3PO_4 (*Pnma*). It has a rigid three-dimensional framework of $[Li_{2.75}Zn_{0.25}GeO_4]^{0.75-}$ with the remaining Li^+ ions occupying the interstitial positions [79]. Partial substitution of P in γ-Li_3PO_4 with a sub-valent cation like $Si^{4+}$and Ge^{4+}, requires extra Li^+ ions for charge balance. Based on this strategy, a brief investigation along the $x$$Li_4GeO_4$-(1-$x$)$Li_3PO_4$ line was firstly carried out by Kamphorst and Hellstrom in 1980, proving that solid solution members at x = 0.33, 0.50, 0.60 and 0.75 can form and are structurally stable, with higher bulk ionic conductivities at 200 °C than in $Li_{3.5}Zn_{0.25}GeO_4$ and the Li_4SiO_4-Li_3PO_4 system [148]. In 1985, Rodger et al. found that in the $x$$Li_4GeO_4$-(1-$x$)$Li_3PO_4$ (x = 0.25, 050 and 0.75) system, similar activation energies occur in these compositions and that the highest conductivity was seen in the x = 0.75 composition which had the largest unit cell volume [149]. Later Ivanov-Shitz et al. grew single crystals of $Li_{3.34}Ge_{0.34}P_{0.66}O_4$ using a flux method and was able to identify the atomic structure. They proposed that an interstitialcy mechanism of lithium ion transport similar to that in

$Li_{3.5}Ge_{0.5}V_{0.5}O_4$ is energetically more favourable [86, 150, 151]. Recently, Muy et al reported that in the Li_3PO_4-Li_4GeO_4 system (x = 0.0, 0.2, 0.4, 0.6, 0.8 and 1.0), high bulk conductivity was observed in the intermediate compositions compared to the end-members and highest conductivity was observed in the x = 0.4 and 0.6 compositions with low activation energy. In contrast, they found one order of magnitude lower conductivity in the x = 0.8 composition with a high activation energy of 0.69 eV, which was hypothesized to be due to the inductive effect of the less positively charged Ge^{4+} compared to P^{5+} [152]. Through a co-doping strategy, Zhao et al. reported an improvement of the high conductivity in the x = 0.75 composition from 1.6×10^{-5} S cm^{-1} to 5.1×10^{-5} S cm^{-1} in $Li_{3.53}(Ge_{0.75}P_{0.25})_{0.7}V_{0.3}O_4$, with an activation energy of 0.43(2) eV at 25 °C. Table 3.1 summaries the reported conductivity data in $Li_{3+x}Ge_xP_{1-x}O_4$ system.

Table 3.1 Reported conductivity data in the $Li_{3+x}Ge_xP_{1-x}O_4$ system

x value	σ_b (S cm^{-1})	σ_{total} (S cm^{-1})	Ea (eV)	ref.
0.50	/	/	0.50	[148]
0.60	/	/	0.49	[148]
0.75	/	/	0.60	[148]
0.50	~ 1.8×10^{-6} (5 ºC)	/	0.51	[149]
0.75	~ 1.8×10^{-5} (25 ºC)	/	0.53	[149]
0.34	1.8×10^{-6} (40 ºC)	/	0.54	[150]
0.0	/	/	1.10	[152]
0.20	/	/	0.51	[152]
0.40	~ 1.0×10^{-5} (30 ºC)	/	0.50(2)	[152]
0.60	/	/	0.57(5)	[152]
0.80	~ 1.0×10^{-6} (30 ºC)	/	0.69(2)	[152]
1.0	/	/	0.95(3)	[152]
0.75	1.6×10^{-5} (25 ºC)	4.0×10^{-6} (25 ºC)	0.50	[153]

Based on the potential of the $Li_{3+x}Ge_xP_{1-x}O_4$ system as solid electrolytes from the perspective of low cost, good stability and relatively good conductivity, a study was carried out to determine the lithium ion distribution in this system and to probe the lithium ion diffusion pathway. In this chapter, the $Li_{3+x}Ge_xP_{1-x}O_4$ system has been systematically studied to establish

details of the lithium ion distribution and the defect structure and its relationship to ionic conductivity.

3.2 Experimental

3.2.1 Sample synthesis

Samples of composition $Li_{3+x}Ge_xP_{1-x}O_4$ ($0 \leq x \leq 1$), were prepared using a classical solid-state reaction. Stoichiometric amounts of Li_2CO_3 (99%, BDH Chemicals Ltd.) or for neutron diffraction studies $^7Li_2CO_3$ (99.99%, AEA technology), GeO_2 (99.999%, Aldrich Gold Ltd.) and $NH_4H_2PO_4$ (98%, May & Baker Ltd.) were ground thoroughly in an agate mortar to form a homogenous paste with methylated spirits. After drying the paste thoroughly at 80 °C, the mixture of precursors was then heated in a gold boat at 300 °C for 1 h, 650 °C for 1 h and 900 °C for 24 h, followed by quenching in air to room temperature. In some cases, an excess amount of Li_2CO_3 (or $^7Li_2CO_3$) was needed to account for the volatility of lithium during the high temperature synthesis as detailed in Table 3.2. Ball milling of the as prepared samples using a planetary ball mill in a nylon jar with zirconia balls was required for some samples with further heating to complete the reaction. Various conditions were tried to optimise the purity of the different compositions with specific details of those used to prepare the final compositions summarised in Table 3.2.

Table 3.2 Summary of preparation conditions used to prepare $Li_{3+x}Ge_xP_{1-x}O_4$ samples

x	Conditions
$x = 0.00$	2 mol% extra Li_2CO_3, 300 °C for 1 h, 650 °C for 1 h and 900 °C for 24 h, followed by natural cooling to RT in furnace
$x = 0.10$	300 °C for 1 h, 650 °C for 1 h and 900 °C for 24 h followed by quenching to RT in air.

Table 3.2 continued on next page

x = 0.20	2 mol% extra Li_2CO_3, 300 °C for 1 h, 650 °C for 1 h and 900 °C for 24 h followed by quenching to RT in air.
x = 0.25	12 mol% extra Li_2CO_3, 300 °C for 1 h, 650 °C for 1 h and 950 °C for 6 h followed by quenching to RT in air; ball milling the as-prepared samples for 4 h, then heated at 950 °C for 2 h followed by quenching to RT in air.
x = 0.30	300 °C for 1 h, 650 °C for 1 h and 900 °C for 24 h with followed quenching, reground and reheated at 950 ºC for 24 h followed by quenching to RT in air.
x = 0.40	2 mol% extra Li_2CO_3, 300 °C for 1 h, 650 °C for 1 h and 900 °C for 24 h followed by quenching to RT in air.
x = 0.50	1 mol% extra Li_2CO_3, 300 °C for 1 h, 650 °C for 1 h and 950 °C for 19 h followed by quenching to RT in air; ball milling the as-prepared samples for 4.5 h, then heated at 950 °C for 12 h followed by quenching to RT in air; 0.3 mol% extra Li_2CO_3, heated at 950 °C for 4 h followed by quenching to RT in air; regrinding and reheating the as-prepared samples at 950 °C for 5 h followed by quenching to RT in air.
x = 0.60	2 mol% extra Li_2CO_3, 300 °C for 1 h, 650 °C for 1 h and 900 °C for 24 h followed by quenching to RT in air.
x = 0.70	300 °C for 1 h, 650 °C for 1 h and 900 °C for 24 h followed by quenching to RT in air.
x = 0.75	2 mol% extra Li_2CO_3, 300 °C for 1 h, 650 °C for 1 h and 900 °C for 24 h followed by quenching to RT in air; add 3 mol% extra Li_2CO_3, ball milling the as-prepared samples for 8 h, heat at 920 ºC for 12 h; 10 mol% extra Li_2CO_3, heat at 950 °C for 5 h followed by quenching to RT in air.
x = 0.80	2 mol% extra Li_2CO_3, 300 °C for 1 h, 650 °C for 1 h and 900 °C for 24 h followed by quenching to RT in air.
x = 0.90	300 °C for 1 h, 650 °C for 1 h and 900 °C for 24 h followed by quenching to RT in air; reground and reheated at 900 ºC for 24 h followed by quenching to RT in air.
x = 1.0	300 °C for 1 h, 650 °C for 24 h; reground and reheated at 650 ºC for 4 h followed by natural cooling to RT in furnace.

The as-prepared powders (x = 0.0, 0.25, 0.50, 0.75 and 1.0) were uniaxially pressed at a pressure of 150 MPa into pellets of 10 mm diameter and approximate thickness 2 mm. The

pellets were sintered at temperatures between 640 and 1050 °C for 9 to 25 h, depending on composition (Table 3.3). For preparation of high-density pellets, spark plasma sintering (SPS) (HPD 25/1, FCT, Rauenstein, Germany) was used. Samples were pressed in a graphite die with 10 mm diameter surrounded by carbon foil. The resulting powder was then sintered between 800 and 1050 °C for 5 min at a uniaxial pressure of 60 MPa under vacuum. SPS processed samples were subsequently annealed to remove residual carbon arising from the carbon foil. Table 3.3 summarises the sintering conditions used for each composition.

Table 3.3 Summary of sintering conditions used to prepare $Li_{3+x}Ge_xP_{1-x}O_4$ pellets

x	Sintering conditions	density%
x = 0.00	900 ºC for 9 h	< 85%
x = 0.00	900 ºC for 9 h and reheat at 900 ºC for 24 h	93.7% - 94.8%
x = 0.00	SPS: 1000 ºC for 5 min, anneal at 800 ºC for 20 h	99.7%
x = 0.25	1050 ºC for 12 h with x = 0.25 powders covered	89.4% - 89.9%
x = 0.25	1000 ºC for 10 h	91.8% - 92.7%
x = 0.25	800 ºC for 25 h with x = 0.25 powders covered	90.5%
x = 0.25	900 ºC for 9 h with x = 0.25 powders covered	< 85%
x = 0.25	900 ºC for 9 h with x = 0.25 powders covered and reheat at 800 ºC for 25 h	95.4%
x = 0.25	SPS: 1050 ºC for 6 min, anneal at 1000 ºC for 11 h	99.8% (crash into fragments)
x = 0.25	SPS: 1100 ºC for 6 min	crash into fragments
x = 0.50	800 ºC for 25 h with x = 0.50 powders covered	87.1% - 88.2%
x = 0.50	950 ºC for 10 h	89.7% - 92.4%
x = 0.50	SPS: 1050 ºC for 5 min, anneal at 800 ºC for 24 h	99.1%
x = 0.75	800 ºC for 25 h with x = 0.75 powders covered	fail
x = 0.75	900 ºC for 25 h with x = 0.75 powders covered	95.8%
x = 0.75	SPS: 1050 ºC for 5 min, anneal at 800 ºC for 24 h	95.2%
x = 1.00	640 ºC for 10 h	85.7% - 86.1%
x = 1.00	650 ºC for 10 h	90.2% - 90.4%
x = 1.00	SPS: 800 ºC for 5min, anneal at 590 ºC for 20 h	95.7% - 96.8%

3.2.2 Characterization

The density of ceramics pellets was measured based on the classical Archimedes method by displacement of water. X-ray powder diffraction (XRD) was used to characterize the crystallographic structure of samples. The XRD data were collected on a PANAlytical X'Pert Pro diffractometer, equipped with an X'Celerator detector, in θ/θ geometry using Ni-filtered Cu-Kα radiation (λ = 1.5418 Å), over the 2θ range 5° to 120° in steps of 0.0334° per step, with an effective count time of 200 s per step. Elevated temperature measurements were performed using an Anton-Paar HTK 1200 high temperature camera. Data were collected in flat plate θ/θ geometry on a Pt coated sample holder. Calibration was carried out with an external LaB_6 standard. Diffraction patterns were acquired at room temperature and at 50 °C intervals from 50 °C to 700 °C, over the 2θ range 5–120° in steps of 0.033° per step, with an effective scan time of 50 s per step. The XRD data were analysed using the Rietveld method through the GSAS suite of programs [122]. The starting models were based on the structures of $Li_{3.5}Zn_{0.5}GeO_4$ [84], Li_3PO_4 [154] and Li_4GeO_4 [147]. The microstructure of the ceramic pellets was examined through scanning electron microscope (SEM), using an FEI Inspect F (Hillsboro, OR).

Magic angle spinning solid-state nuclear magnetic resonance (MAS-NMR) spectra were acquired on a Bruker AVANCE NEO 600 spectrometer using a 4 mm MAS broadband probe. ^7Li and ^{31}P data were recorded at spinning speeds of 12 kHz with a relaxation delay of 5s and 60s, respectively. Chemical shifts were referenced to external $H_3{}^{31}PO_4$ and ^7LiCl, respectively. Dmfit [155] was used for deconvolution and preliminary fitting of the centre band region. Whole spectrum fitting was carried out using the program NMRLSS for ^{31}P [156], in addition to the peak parameters, the spinning speed and a polynomial baseline were refined. Integrated intensities for all spinning sidebands were analysed for chemical shift anisotropy using the Herzfeld–Berger method [133], with the program HBA [157] yielding the principal components of the chemical shift tensor (δ_{11}, δ_{22}, δ_{33}), chemical shift anisotropy ($\Delta\delta$) and asymmetry (η)

parameters. The principal components of the chemical shift tensor were ordered according to the Haeberlen convention [158].

Neutron total scattering data at room temperature were collected on the Polaris diffractometer at the ISIS Facility, Rutherford Appleton Laboratory, on back-scattering (average angle 146.72°), 90° (average angle 92.59°), intermediate-angle (average angle 52.21°), low-angle (average angle 25.99°) and very low angle (average angle 10.40°) detectors, corresponding to the approximate d-spacing ranges 0.04–2.6 Å, 0.05–4.1 Å, 0.73–7.0 Å, and 0.13–13.8 Å and 0.3–48 Å, respectively. In each case, the sample was loaded into an 11 mm diameter thin walled vanadium can, located in front of the back-scattering detectors. Collections corresponding to proton beam charges of ca. 1000 μA h were made to allow for total scattering analysis. For total scattering data correction, diffraction data were collected on an empty 11 mm diameter thin walled (0.05 mm wall thickness) vanadium can for ca. 600 μA h at room temperature. Data were summed, normalised and corrected using Gudrun [125]. The total pair correlation function $G(r)$ and the normalised total scattering structure factors $S(Q)$ were fitted by reverse Monte Carlo modelling using the program RMCProfile [127]. In each case, supercell configurations, in $P1$ symmetry, generated from the refined structures were used as starting models. For x = 0.0, 0.25, 0.50 and 0.75, a 5 × 8 × 10 supercell was used, while for x = 1.0 the supercell was 6 × 6 × 7. For the x = 0.25, 0.50 and 0.75 compositions, which showed disordered structures, full occupancies were assumed for Li1 and Li2, with Li1a and Li2a omitted. In all cases, 10 sets of parallel calculations were performed under periodic boundary conditions to yield satisfactory statistics on the radial distribution functions and allow for the calculation of standard deviations. The Bragg scattering data were used as a constraint on the long-range crystallinity. Pseudo-potential constraints were used for P-O, Ge-O and O-O as well as other long-range correlations in some cases. For the x = 0.25, 0.50 and 0.75 compositions, a modified Li-Li distribution based on the MD simulation of $Li_{3.7}Ge_{0.85}W_{0.15}O_4$ (Chapter 5) was

used to constrain the low *r*-value tail of the Li-Li distribution. A soft bond valence sum constraint was applied.

For the impedance measurements, annealed ceramic pellets were first cut and polished into blocks of ca. 4 mm × 4 mm × 2 mm. Gold electrodes were sputtered by cathodic discharge. Electrical characterisation was carried out by a.c. impedance spectroscopy using a fully automated system based on a Solartron 1255 frequency response analyser in conjunction with a bespoke automatic current/voltage converter. Impedance data were collected over the frequency range 0.1 Hz to 1×10^6 Hz, in the approximate temperature range of 50 to 400 °C over two cycles of heating and cooling. Fitting of impedance data was carried out using the program WFIRDARMM [159, 160].

3.3 Results and discussion

3.3.1 Solid solution formation

The XRD patterns of the optimised samples for compositions in the system $Li_{3+x}Ge_xP_{1-x}O_4$ are shown in Fig. 3.5. It can be seen that in the compositional range $0.00 \leq x \leq 0.90$, a solid solution isostructural with the end member γ-Li_3PO_4 in space group *Pnma* (No. 62) is evident. Only the end member Li_4GeO_4 exhibits a different but related structure in space group *Cmcm* (No. 63). It should be noted that the crystallinity of the samples in the range $0.7 \leq x \leq 0.9$ was poorer than those at lower levels of substitution and is reflected in the broadening of peaks in the XRD patterns.

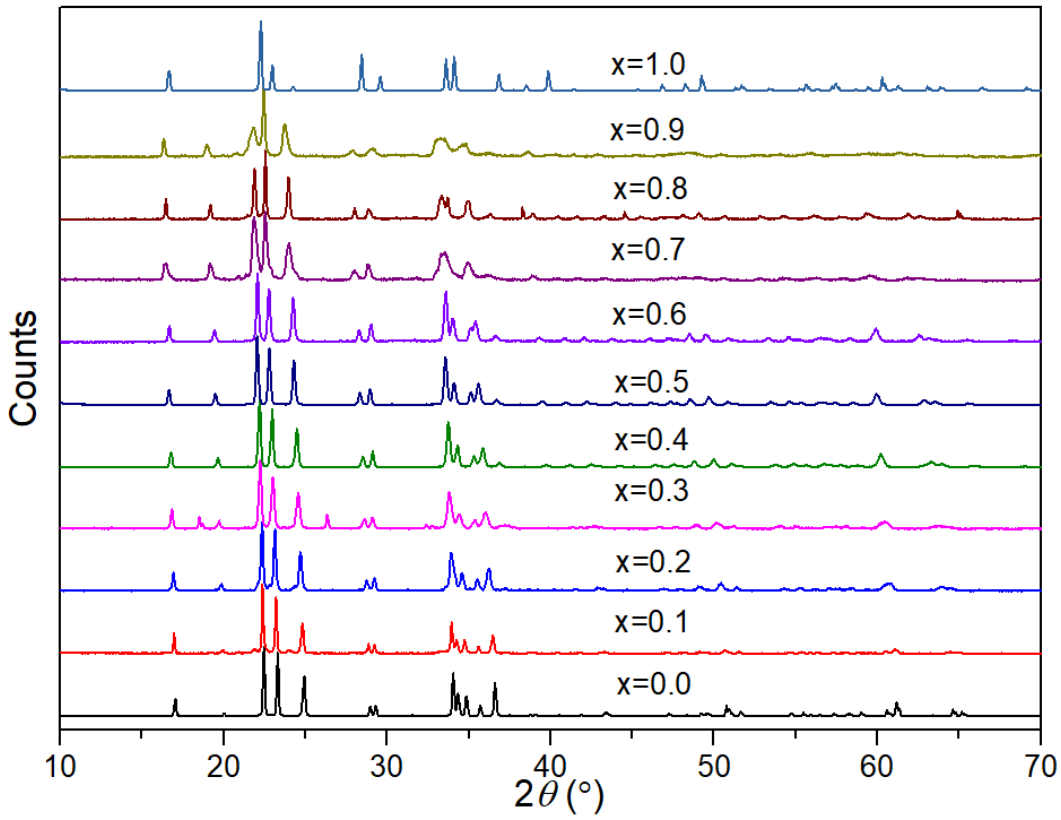

Figure 3.5 XRD patterns for compositions in the $Li_{3+x}Ge_xP_{1-x}O_4$ system

The refined unit cell parameters for the $Li_{3+x}Ge_xP_{1-x}O_4$ system are listed in Table 3.4, with the corresponding plots in Fig. 3.6. The unit cell volume in the $Li_{3+x}Ge_xP_{1-x}O_4$ series shows a general increase with increasing *x*-value, with the unit cell volume of composition $Li_{3.9}Ge_{0.9}P_{0.1}O_4$ (x = 0.90) reaching 347.9(8) $Å^3$ compared to 315.62(2) $Å^3$ for Li_3PO_4 (x = 0.0), an increase of around 10%. This can be mainly attributed to the ionic radius of Ge^{4+} (0.39 Å) which is bigger than that of P in Pentavalent state (0.17 Å) when both of them are 4-coordinated [161]. This trend is reflected in the compositional variation of the lattice parameters, with a slight decrease in the *b*-axis parameter at x = 0.90. In the $Li_{3+x}Ge_xP_{1-x}O_4$ system, to maintain charge balance, with increased Ge content in the $(Li_3Ge_xP_{1-x}O_4)^{x-}$ skeleton, interstitial lithium ions are introduced to compensate for the loss of positive charge. Therefore, it can be concluded that a solid solution can be formed in the $Li_{3+x}Ge_xP_{1-x}O_4$ system up to around x = 0.90, and that all the

intermediate compositions exhibit a structure based on that of the end member γ-Li_3PO_4, with extra interstitial sites.

Table 3.4 Refined unit cell parameters for compositions in the $Li_{3+x}Ge_xP_{1-x}O_4$ system. Estimated standard deviations are given in parentheses

Composition	*a* (Å)	*b* (Å)	*c* (Å)	unit cell volume (Å^3)
Li_3PO_4 (*x* = 0.0)	10.4761(2)	6.1187(1)	4.9238(1)	315.62(2)
$Li_{3.1}Ge_{0.1}P_{0.9}O_4$ (*x* = 0.1)	10.483(1)	6.1221(5)	4.9347(4)	316.70(7)
$Li_{3.2}Ge_{0.2}P_{0.8}O_4$ (*x* = 0.2)	10.557(1)	6.1386(5)	4.9783(4)	322.63(7)
$Li_{3.3}Ge_{0.3}P_{0.7}O_4$ (*x* = 0.3)	10.595(2)	6.1532(9)	4.9999(7)	325.9(1)
$Li_{3.4}Ge_{0.4}P_{0.6}O_4$ (*x* = 0.4)	10.6571(9)	6.1638(4)	5.0292(3)	330.37(5)
$Li_{3.5}Ge_{0.5}P_{0.5}O_4$ (*x* = 0.5)	10.6881(5)	6.1787(3)	5.05412(2)	333.77(3)
$Li_{3.6}Ge_{0.4}P_{0.4}O_4$ (*x* = 0.6)	10.728(1)	6.1841(7)	5.0896(5)	337.65(8)
$Li_{3.7}Ge_{0.7}P_{0.3}O_4$ (*x* = 0.7)	10.818(3)	6.198(1)	5.134(1)	344.2(2)
$Li_{3.8}Ge_{0.8}P_{0.2}O_4$ (*x* = 0.8)	10.818(5)	6.196(2)	5.140(2)	344.6(4)
$Li_{3.9}Ge_{0.9}P_{0.1}O_4$ (*x* = 0.9)	10.87(1)	6.175(4)	5.185(4)	347.9(8)
Li_4GeO_4 (*x* = 1.0)	7.7737(1)	7.3714(1)	6.05931(9)	347.22(1)

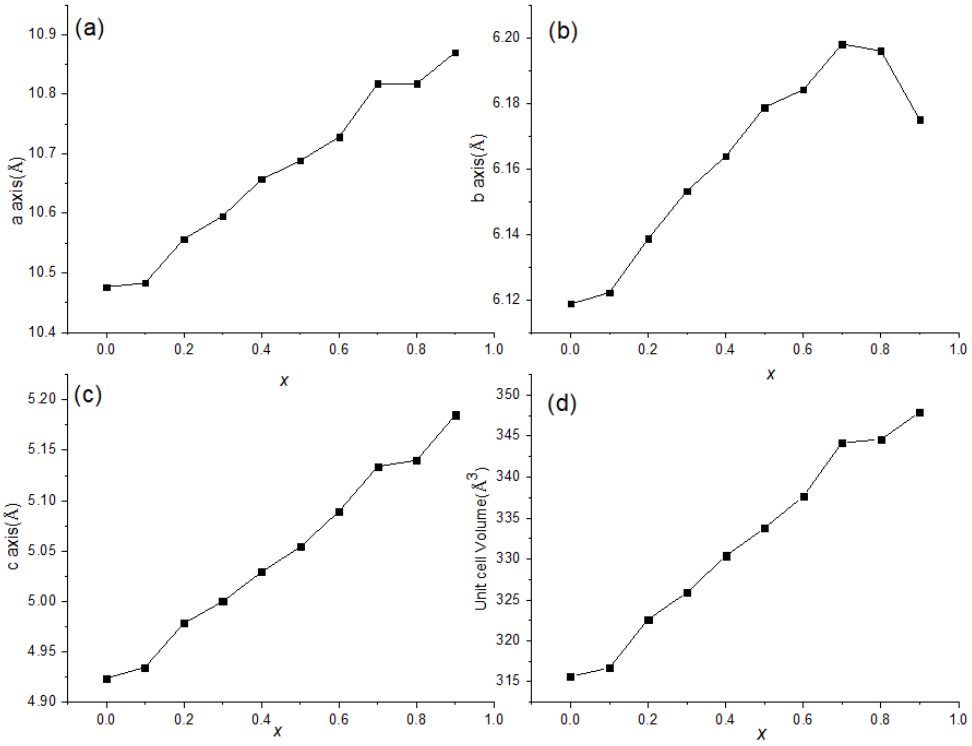

Figure 3.6 Variation of unit cell parameters (a) *a*, (b) *b*, (c) *c* and (d) unit cell volume with composition in the $Li_{3+x}Ge_xP_{1-x}O_4$ system. Error bars are smaller than the symbols used.

3.3.2 Thermal variation of structure

To investigate the structural stability, a variable temperature (VT) XRD study was performed on the intermediate compositions, x = 0.25, 0.50 and 0.75, as shown in Fig. 3.7. As can be seen, for all of these compositions, no significant and obvious changes in XRD patterns are seen up to 700 °C, indicating that the system exhibits the γ-phase structure in space group *Pnma* throughout the studied temperature range during heating and cooling. It is also noted that the Bragg peaks are seen to move to lower 2θ values on heating and move to higher 2θ values on cooling, corresponding to the thermal expansion and contraction of the unit cell, respectively. These are reflected in the variation of unit cell parameters shown in Fig. 3.8. For x = 0.25, the composition exhibits reversible thermal expansion and contraction of the unit cell parameters and two linear regions are seen with one at low temperature range and one at high temperature

range with a transition at around 250 °C. For x = 0.50 and 0.75 compositions, reversible thermal expansion and contraction of the unit cell parameters are still seen above 300 °C with some hysteresis evident in x = 0.50 below 300 °C. This difference is even more significant in x = 0.75 below 250 °C. In the patterns for the x = 0.75 composition a weak additional peak at around 21 ° 2θ is evident on heating between 300 and 700 °C, but is much weaker on cooling and is absent at room temperature. The peak remains unidentified, but might suggest some disproportionation at intermediate temperatures for this composition, which might account for the difference in cell volume on heating and cooling. The transition seen at around 250 °C in all compositions is not accompanied by a significant change in average structure. It has previously been suggested in related LISICON systems that this change is associated with a change in defect structure [84].

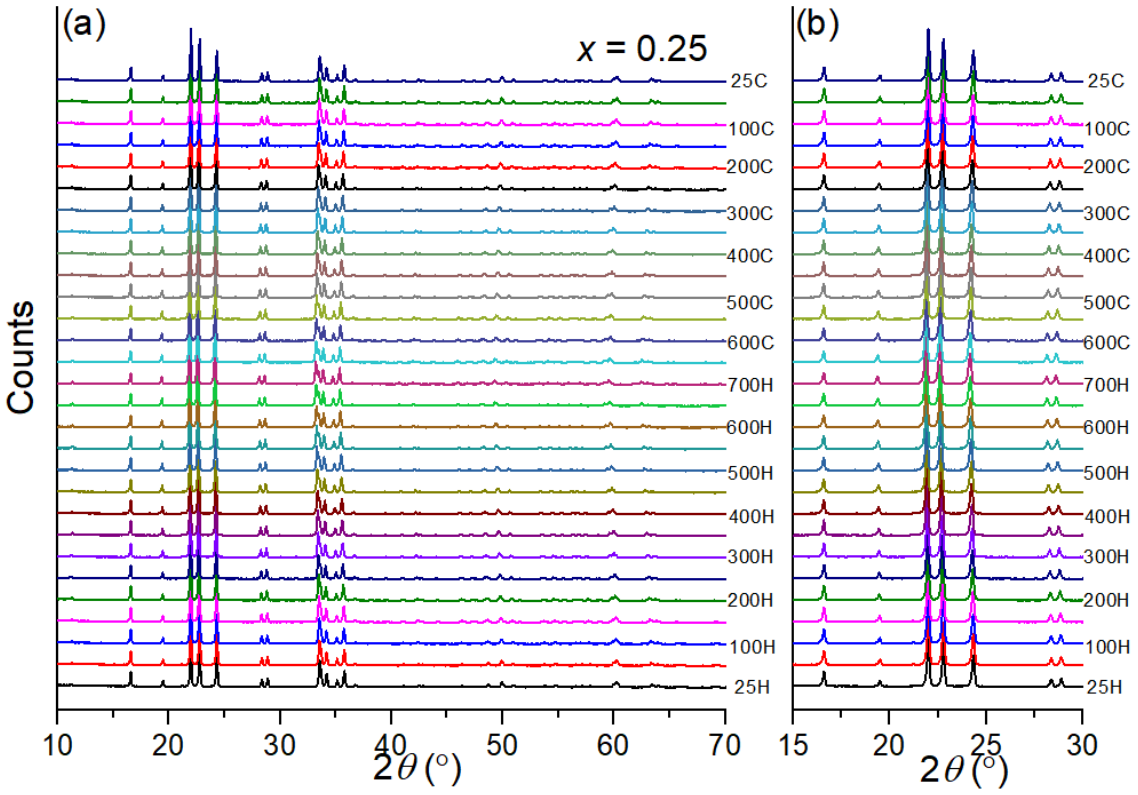

Figure 3.7 continued on next page

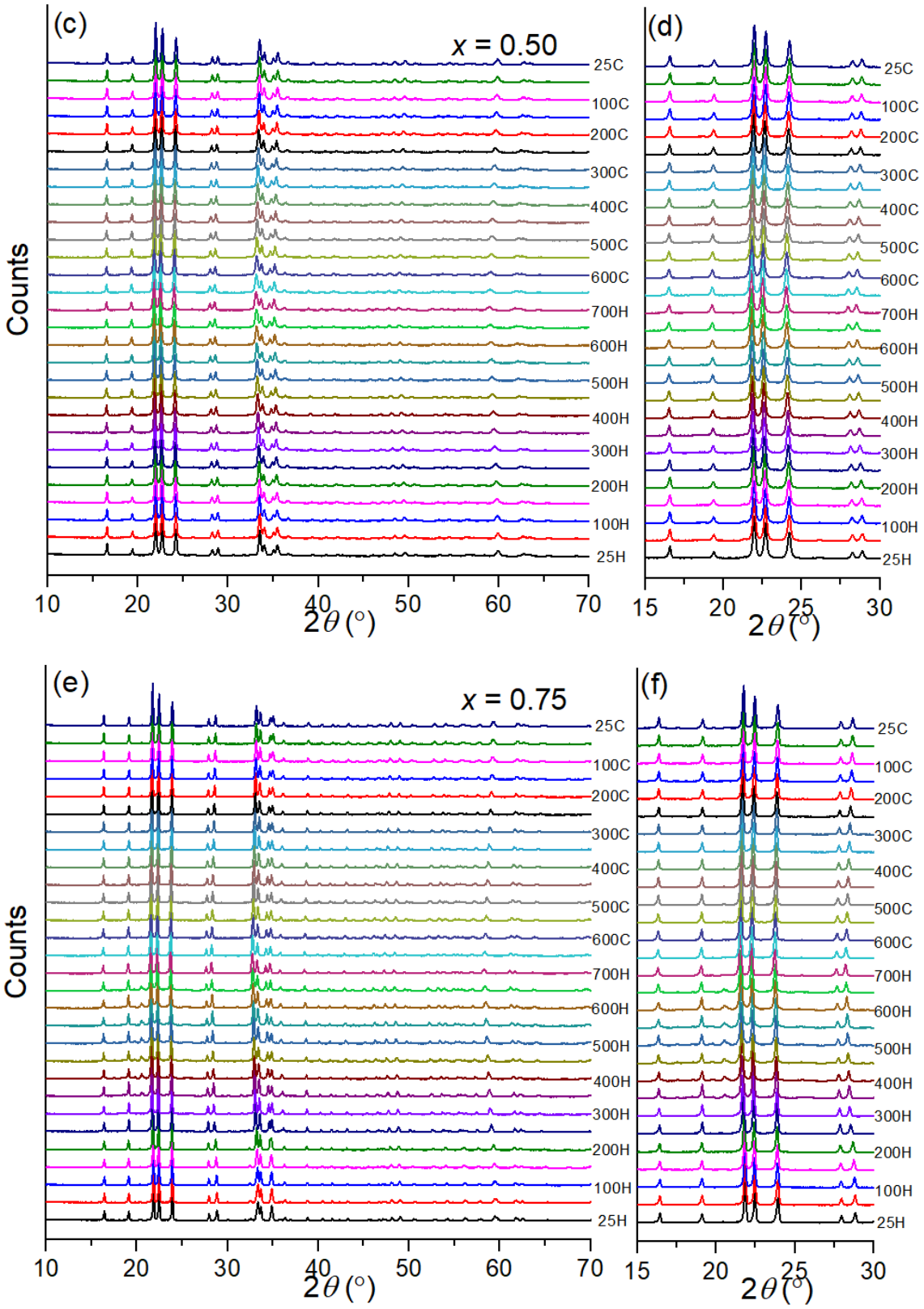

Figure 3.7 VT-XRD patterns for (a) x = 0.25, (c) x = 0.50 and (e) x = 0.75 over RT to 700 ºC during heating and cooling in the $Li_{3+x}Ge_xP_{1-x}O_4$ system with details shown in (b)(d)(f)

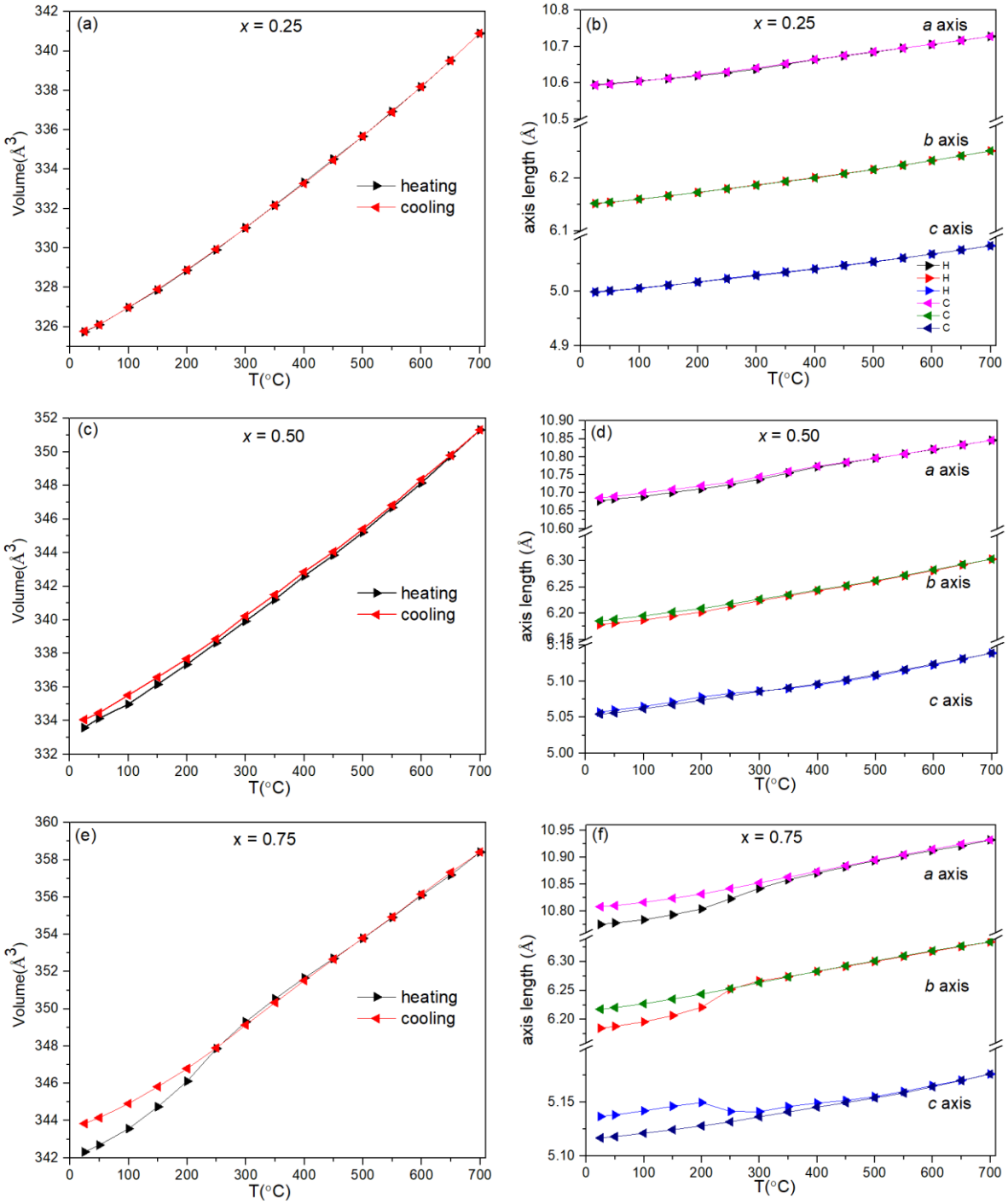

Figure 3.8 Refined unit cell parameters for (a) and (b) *x* = 0.25, (c) and (d) 0.50 and (e) and (f) 0.75 from RT to 700 ºC during heating and cooling in the $Li_{3+x}Ge_xP_{1-x}O_4$ system

3.3.3 Pellet morphology and electrical behaviour

In preparation for impedance analysis measurements, two methods of sintering, conventional sintering (CS) and SPS, were employed to obtain pellets of optimum density. In both cases pellets were sintered from as-prepared powders. Table 3.3 summaries the different conditions used and the relative densities achieved as a percentage of theoretical density. As can be seen in Table 3.3, the best sintering conditions varied for different compositions. In conventional sintering, sintering at too high or too low a temperature led to low relative densities (< 90%) especially at low temperatures. Compared to conventional sintering, SPS allows for fast sintering and high pellet densities of above 95%, with some pellets achieving densities higher than 99%.

Fig. 3.9 shows SEM images of cross-sections of pellets of the $x = 0.25$ composition prepared under different conventional sintering conditions. Comparing Fig. 3.9 (c) and (d) with Fig. 3.9 (a) and (b) at the same scale, increased grain size and densification is evident at the lower sintering temperature of 1000 °C. Fig. 3.10 shows the SEM images for $x = 0.0$, 0.25, 0.50, 0.75 and 1.0 pellets prepared using the SPS method. Good densification is confirmed for all of these compositions. Interestingly, the $x = 0.75$ pellet prepared by SPS shows a slightly different morphology with the presence of flakes and rods evident on the bulk matrix. These rod-like crystals are also evident in the image for the $x = 1.0$ SPS pellet (Fig. 3.10i).

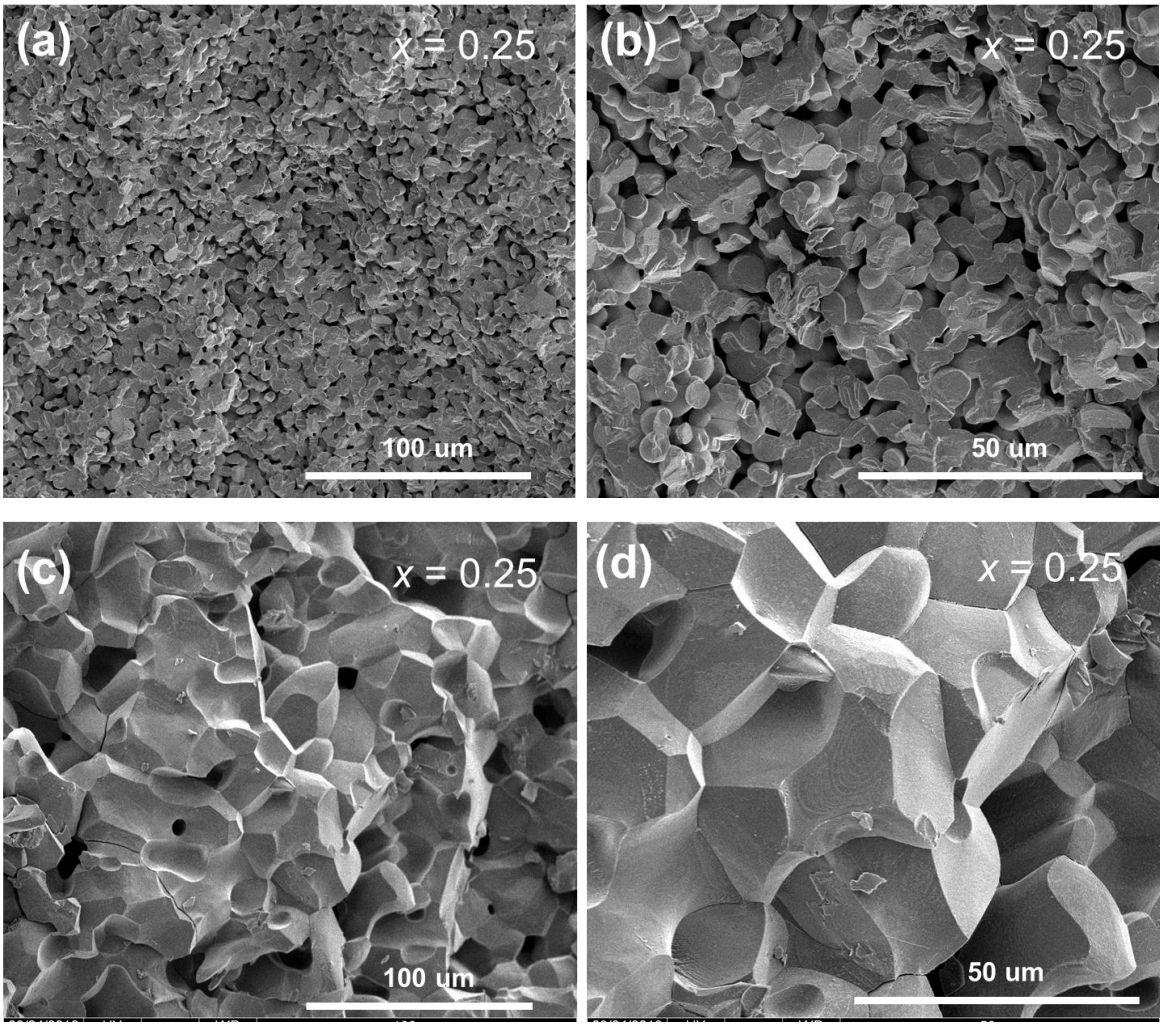

Figure 3.9 SEM cross-section images for x = 0.25 pellets prepared using different conventional sintering conditions: (a) and (b) 1050 ºC for 12 h buried in powder of the same composition, (c) and (d) 1000 ºC for 10 h.

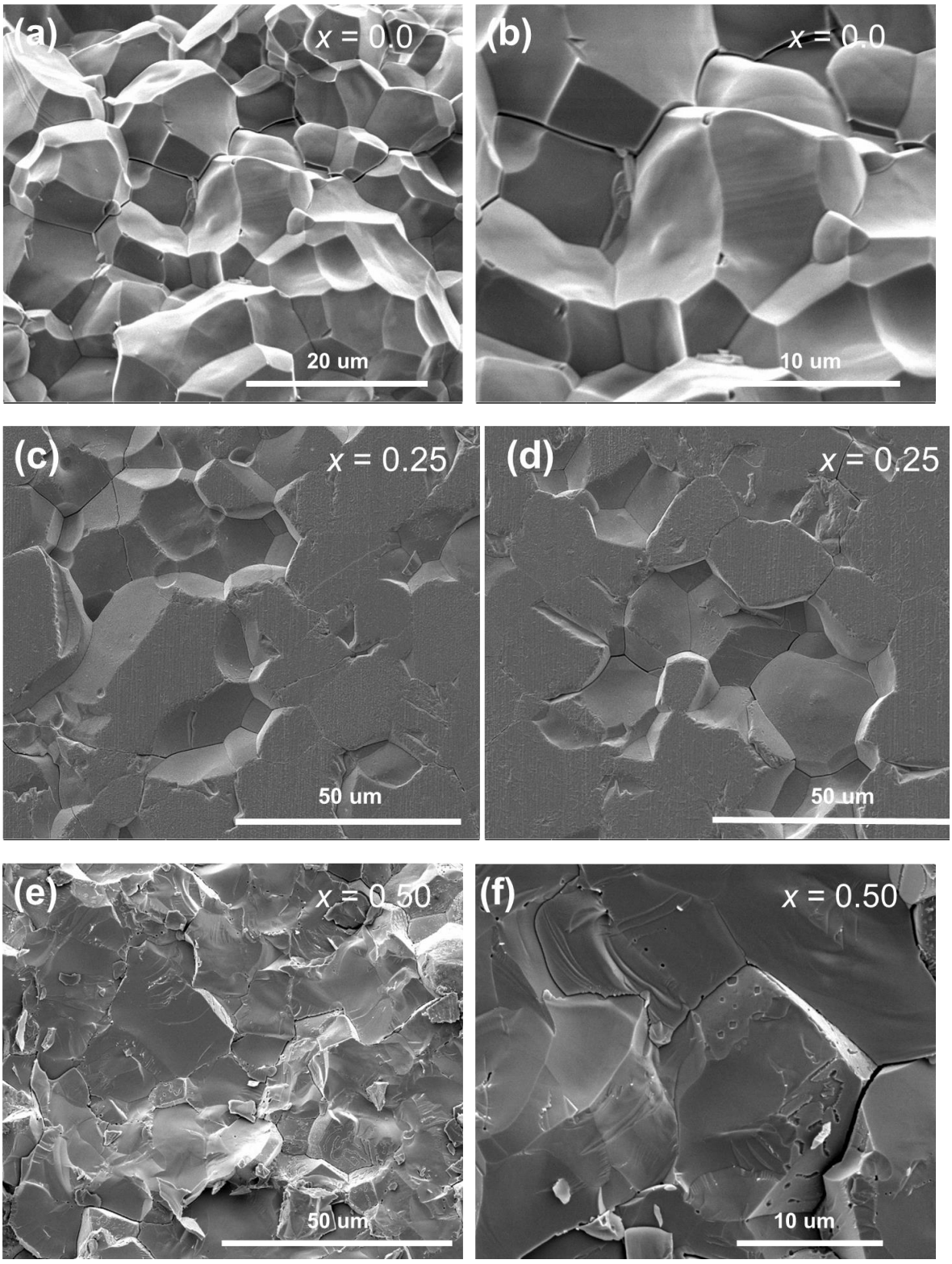

Figure 3.10 continued on next page

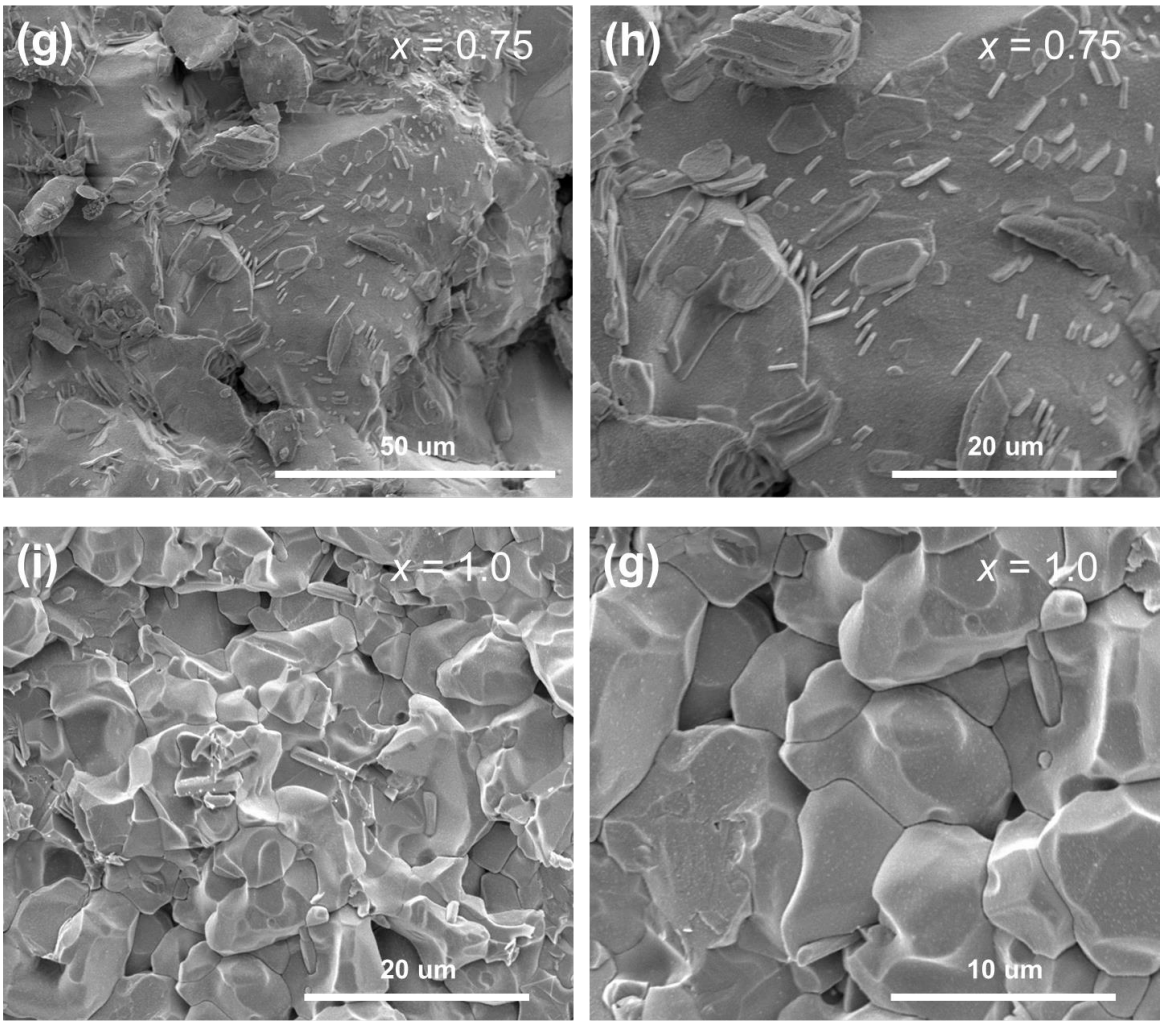

Figure 3.10 SEM images for (a) and (b) x = 0.0, (c) and (d) x = 0.25, (e) and (f) x = 0.50, (g) and (h) x = 0.75, (i) and (g) x = 1.0 pellets prepared using SPS

XRD patterns of the selected pellets (SPS-pellets of x = 0.0, 0.25, 0.50, 0.75 and 1.0 and CS-pellet x = 0.25) in the $Li_{3+x}Ge_xP_{1-x}O_4$ system are shown in Fig. 3.11. All the intermediate compositions maintain strong LISICION diffraction peaks with good crystallinity, consistent with the pristine calcined powders (Fig. 3.5), though there is some texture in the SPS-sintered pellets. It is also noticeable that the XRD patterns of x = 0.75 and x = 1.0 SPS pellets show small amounts of secondary phases, identified as Li_2CO_3 for x = 0.75 and Li_2GeO_3 for x = 1.0. These impurities are consistent with the SEM images of these two compositions, which appeared to show the presence of crystals of different morphology. These impurities arise due

to the fast sintering process used in SPS, especially in the case of Li_4GeO_4, which easily transforms to Li_2GeO_3 at higher temperatures.

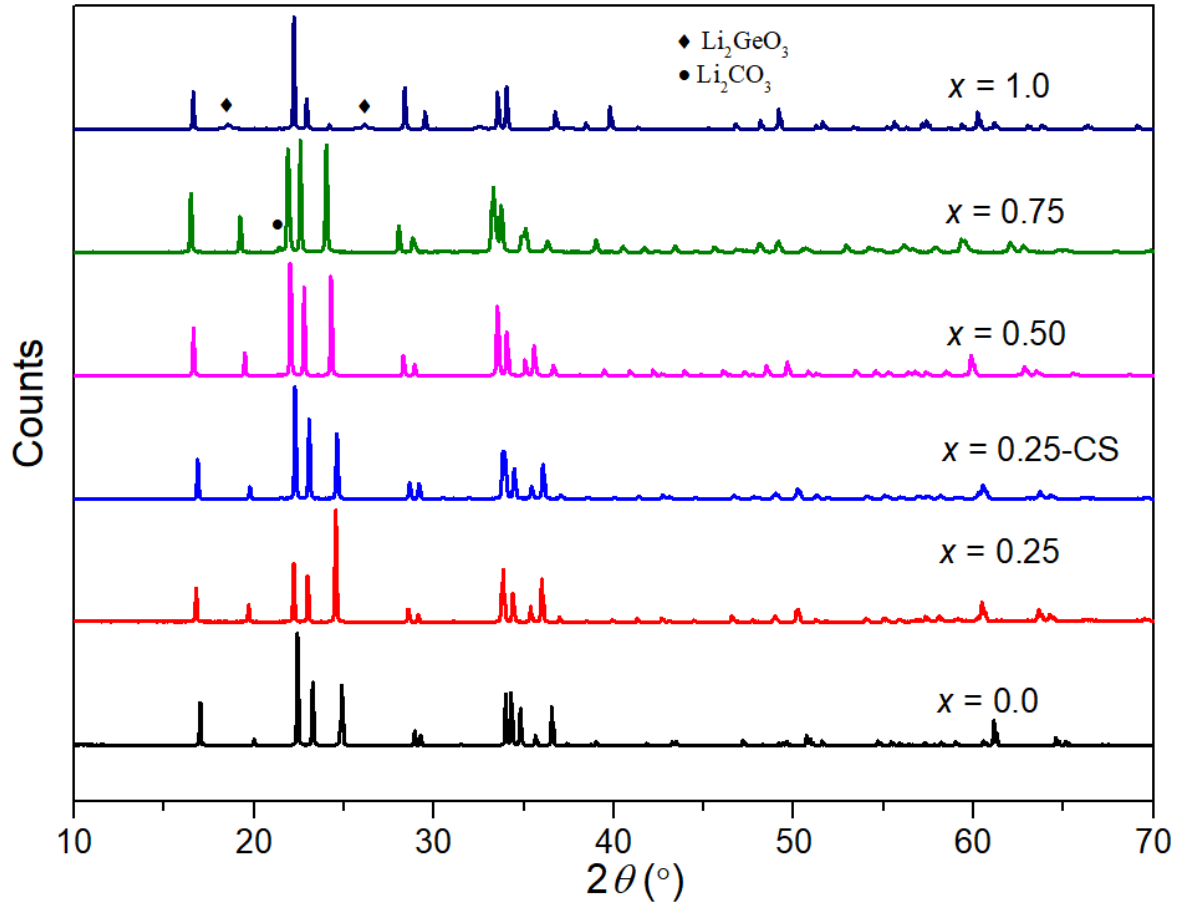

Figure 3.11 XRD patterns for SPS-prepared pellets of compositions x = 0.0, 0.25, 0.50, 0.75 and 1.0 and that for x = 0.25 conventionally sintered (0.25-CS) in the $Li_{3+x}Ge_xP_{1-x}O_4$ system

Electrochemical impedance measurements were employed to study the electrical response of the studied compositions in the $Li_{3+x}Ge_xP_{1-x}O_4$ system. Fig. 3.12 shows the Nyquist plots for $Li_{3.75}Ge_{0.75}P_{0.25}O_4$ at selected temperatures during the 1st heating run. As can be seen, the spectra at low temperatures show a capacitive quasi-semicircle, with an extrapolated non-zero high frequency intercept with the real axis. When at low frequencies, an inclined capacitive spike is observed. With increased temperature, the semicircle gets smaller and moves out of

the frequency window and only the tail is observed as shown in the spectra at 150 ºC. Interestingly for ca. 113 ºC, this semicircle appears to broaden and increase in radius in the second heating run but less visible during the subsequent 1st cooling and 2nd cooling runs (Fig. 3.13).

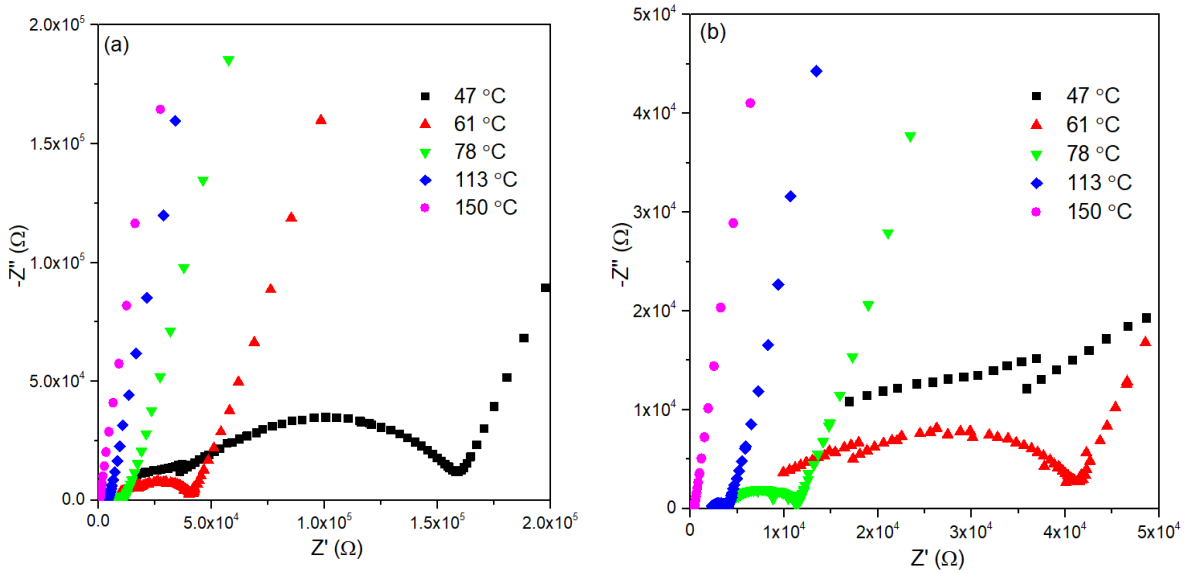

Figure 3.12 (a) Nyquist plots at selected temperatures for $Li_{3.75}Ge_{0.75}P_{0.25}O_4$ SPS pellet with an enlargement at the high frequency end shown in (b). Data correspond to the 1st heating run

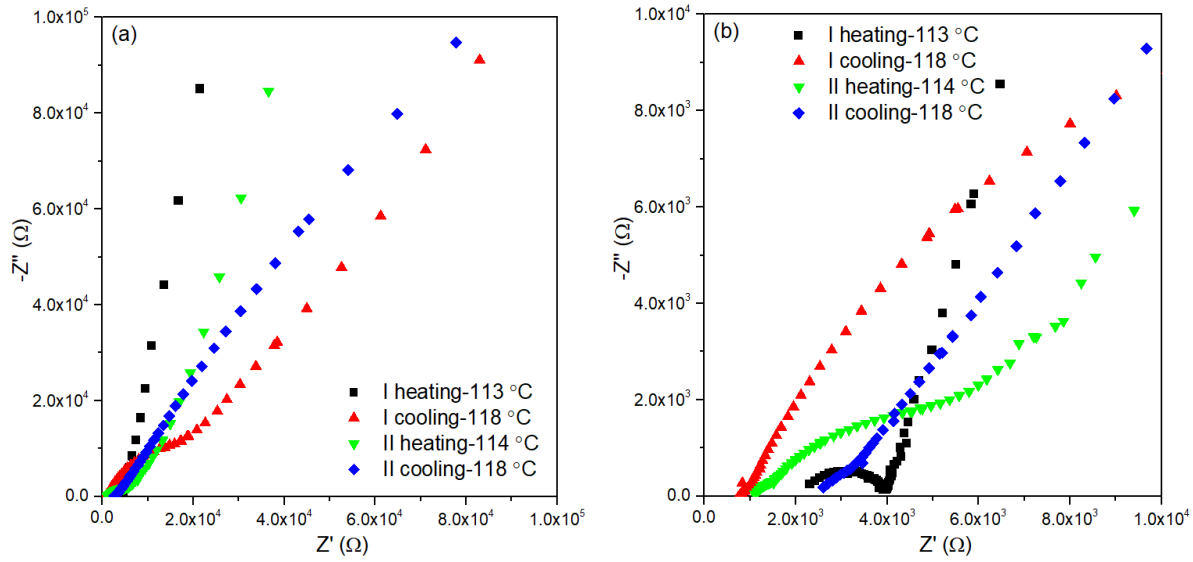

Figure 3.13 (a) Nyquist plots for $Li_{3.75}Ge_{0.75}P_{0.25}O_4$ at ca.113 ºC with the amplification near the origin in (b) over the two heating and cooling runs

From Fig. 3.13, it is clear that the impedance spectra evolve with time and thermal history. The spectra of the 1st and 2nd heating around the same temperature of 113 ºC were selected for further analysis. Figs. 3.14 and 3.15 show the equivalent circuits used for fitting and the fitted Nyquist plots with fitted equivalent circuit parameters summarised in Table 3.5. As can be seen, good fitting can be obtained based on the selected equivalent circuits over the whole frequency range. Here L represents the inductance of connections and cables of the experimental set-up. According to Table 3.5, the estimated capacitance of the first semicircle is in range of 10^{-8} F, which should correspond to resistances and capacitances of electrode-electrolyte processes based on the empirical capacitance values and the responsible electrical phenomena [142]. In 2nd heating, the semicircle enlarges together with an additional semicircle. A larger capacitance value is obtained 10^{-7} F, indicative of an electrode process response. The errors on the values of R_1, P_2, n_2 and R_2, are small and the quality of the fit in the high frequency region is good, indicating the model gives a good description of the bulk sample. R_1 therefore represents the total resistance of the $Li_{3.75}Ge_{0.75}P_{0.25}O_4$ sample. Considering the complex processes like diffusion-controlled adsorption or reaction at the electrode, especially designed experiments would be required to properly understand the electrode and electrode-electrolyte interfacial processes.

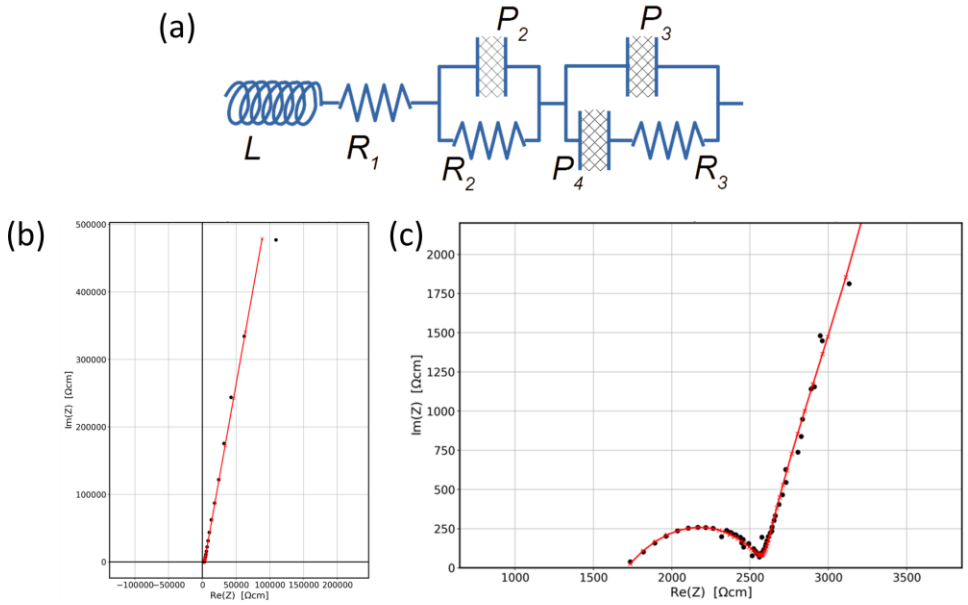

Figure 3.14 (a) equivalent circuit, (b) Experimental and simulated Nyquist plot with the amplification near the origin in (c) for the $Li_{3.75}Ge_{0.75}P_{0.25}O_4$ composition at ca. 113 ºC on 1st heating

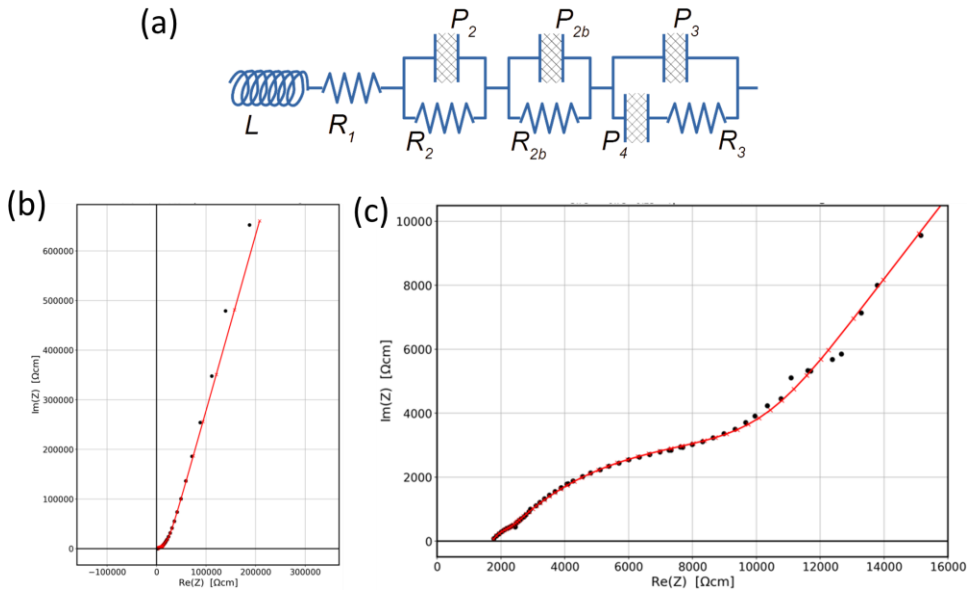

Figure 3.15 (a) equivalent circuit, (b) Experimental and simulated Nyquist plot with the amplification near the origin in (c) for the $Li_{3.75}Ge_{0.75}P_{0.25}O_4$ composition at ca. 114 ºC on 2nd heating

Table 3.5 Equivalent circuit parameters for the $Li_{3.75}Ge_{0.75}P_{0.25}O_4$ composition at ca. 113 ºC for 1st and 2nd heating runs

parameters	I heating-113 ºC		II heating-114 ºC	
	Value	Conf%	value	Conf%
L (H)	5.4×10^{-5}	9.2	5.0×10^{-5}	16.6
R_1 (Ω)	356	5.0	771	19.6
R_2 (Ω)	1253	14.2	5979	5.5
P_2 (F)	1.8×10^{-8}	15.2	9.3×10^{-7}	10.9
n_2	0.33	5.5	0.43	2.6
R_{2b} (Ω)	/	/	475	36.4
P_{2b} (F)	/	/	3.4×10^{-10}	83.8
n_{2b}	/	/	0.0	-0.1
P_3 (F)	3.5×10^{-6}	7.0	1.5×10^{-6}	28.4
n_3	0.12	7.0	0.17	28.6
P_4 (F)	7.2×10^{-7}	33.9	1.4×10^{-6}	31.5
n_4	0.09	46.4	0.18	23.1
R_3 (Ω)	7.5×10^{3}	29.3	2.8×10^{4}	32.1

Fig. 3.16 shows the Arrhenius plots of total conductivity for compositions of $0.0 \leq x \leq 1.0$ in $Li_{3+x}Ge_xP_{1-x}O_4$ system over two cycles of heating and cooling from room temperature to 400 ºC. It should be noted that for these measurements, the tested pellet for $x = 0.25$ was prepared by conventional sintering, while the spectra for the other compositions were acquired on SPS prepared pellets. It can be observed that, in some cases the data for the first heating run differ from those in subsequent cooling and heating runs and may be associated with some moisture being present in the first run. Additionally, for the $x = 0.75$ composition, the values of conductivity appear to drop significantly. This might be due to the disproportionation identified in the variable temperature XRD data and in the SEM images, but since this was not seen in the first cooling run, it is more likely due to electrode degradation over the course of the experiment. Therefore, for subsequent discussion the data of the first cooling and second heating run are used.

For the two end-members γ-Li_3PO_4 and Li_4GeO_4, a linear Arrhenius plot is seen over the entire studied temperature range. Similarly, for the $x = 0.25$ and 0.50 compositions, again only

a single linear region is seen over the studied temperature range. Only for the x = 0.75 is a transition evident at around 180 °C, consistent with the variable temperature X-ray data.

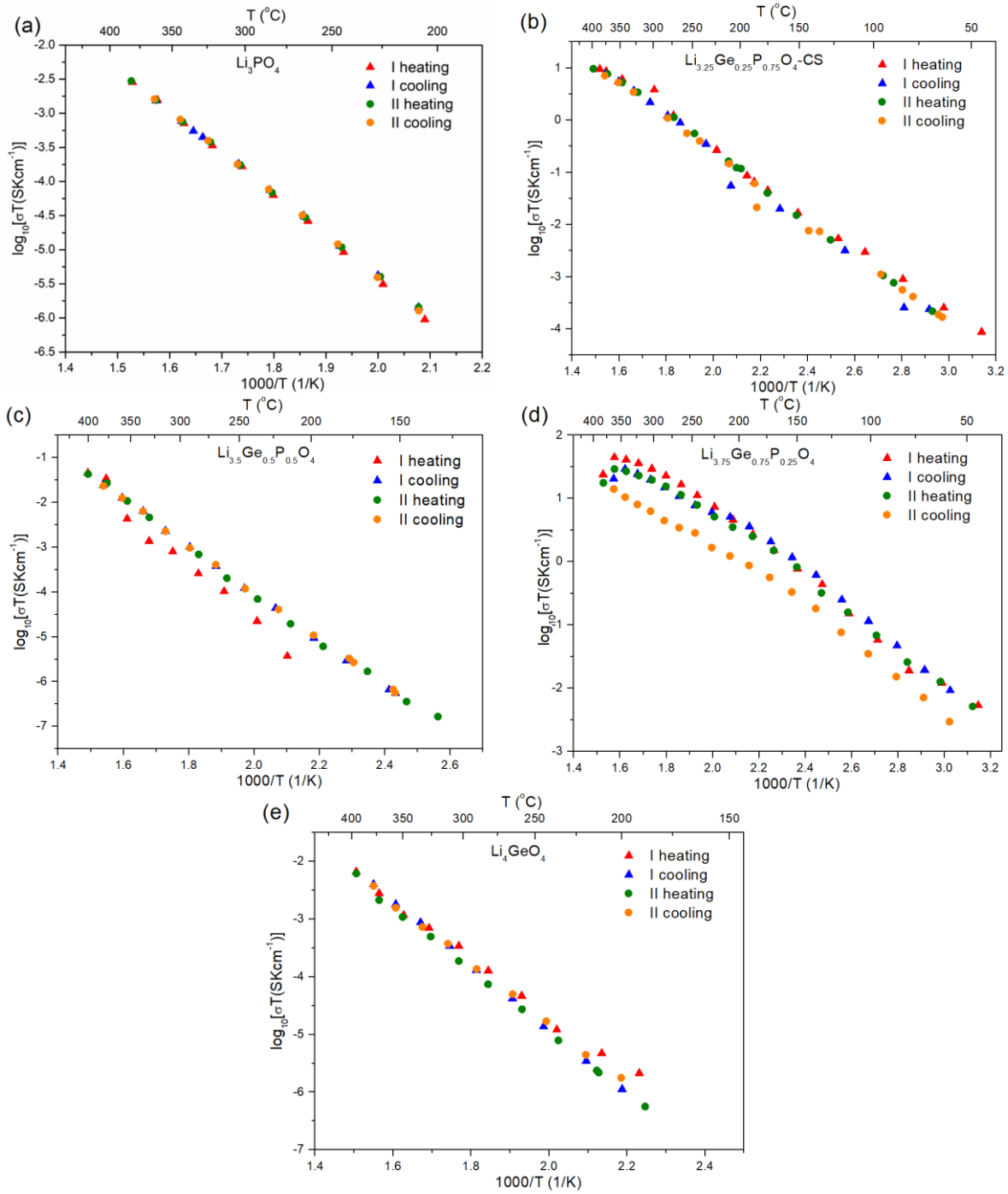

Figure 3.16 Arrhenius plots of total conductivity for x = 0.0, 0.25, 0.50, 0.75 and 1.0 compositions in the $Li_{3+x}Ge_xP_{1-x}O_4$ system

Table 3.6 summarises the conductivities at selected temperatures along with activation energies for the first cooling and second heating runs (for x = 0.75 activation energies in the

low (ΔE_{LT}) and high temperature (ΔE_{HT}) regions are included). High activation energies (> 1 eV) and low conductivities are seen for the two end members γ-Li_3PO_4 and Li_4GeO_4. Similarly, the x = 0.5 composition shows significantly lower conductivity and higher activation energies than the x = 0.25 and 0.75 compositions. The highest conductivity and lowest activation energy are shown by the x = 0.75 composition with a value of conductivity at 250 °C of 1.83×10^{-2} S cm^{-1}.

Table 3.6 Activation energies ΔE_{LT} and ΔE_{HT} and conductivities ($\sigma_{temp°C}$) at selected temperatures for x = 0.00, 0.25, 0.50, 0.75 and 1.00 compositions in the $Li_{3+x}Ge_xP_{1-x}O_4$ system. Data correspond to the first cooling and second heating run. Estimated errors are ±4%. Values at 25°C were obtained through extrapolation.

x	ΔE_{LT} (eV)	ΔE_{HT} (eV)	$\sigma_{25°C}$ (S cm^{-1})	$\sigma_{100°C}$ (S cm^{-1})	$\sigma_{150°C}$ (S cm^{-1})	$\sigma_{250°C}$ (S cm^{-1})
0.00	1.209		/	/	/	2.64×10^{-8}
0.25	0.659		2.76×10^{-8}	3.83×10^{-6}	3.80×10^{-5}	9.74×10^{-4}
0.50	1.030		2.99×10^{-14}	7.54×10^{-11}	2.93×10^{-9}	5.24×10^{-7}
0.75	0.579	0.423	3.36×10^{-6}	2.49×10^{-4}	1.85×10^{-3}	1.83×10^{-2}
1.00	1.045		/	/	/	8.08×10^{-8}

3.3.4 Structural characterisation

3.3.4.1 Solid state NMR

To investigate the compositional variation of lithium and phosphorus environments, ^{7}Li and ^{31}P MAS-NMR were employed. ^{7}Li MAS-NMR spectra for compositions in the $Li_{3+x}Ge_xP_{1-x}O_4$ system are shown in Fig. 3.17. The spectra reveal an apparent single ^{7}Li NMR signal centred

at around 0 ppm flanked by spinning sidebands due to chemical shift anisotropy. Close examination of the centre band resonance (Fig. 3.17b) reveals an increasing chemical shift with increasing *x*-value indicating higher deshielding.

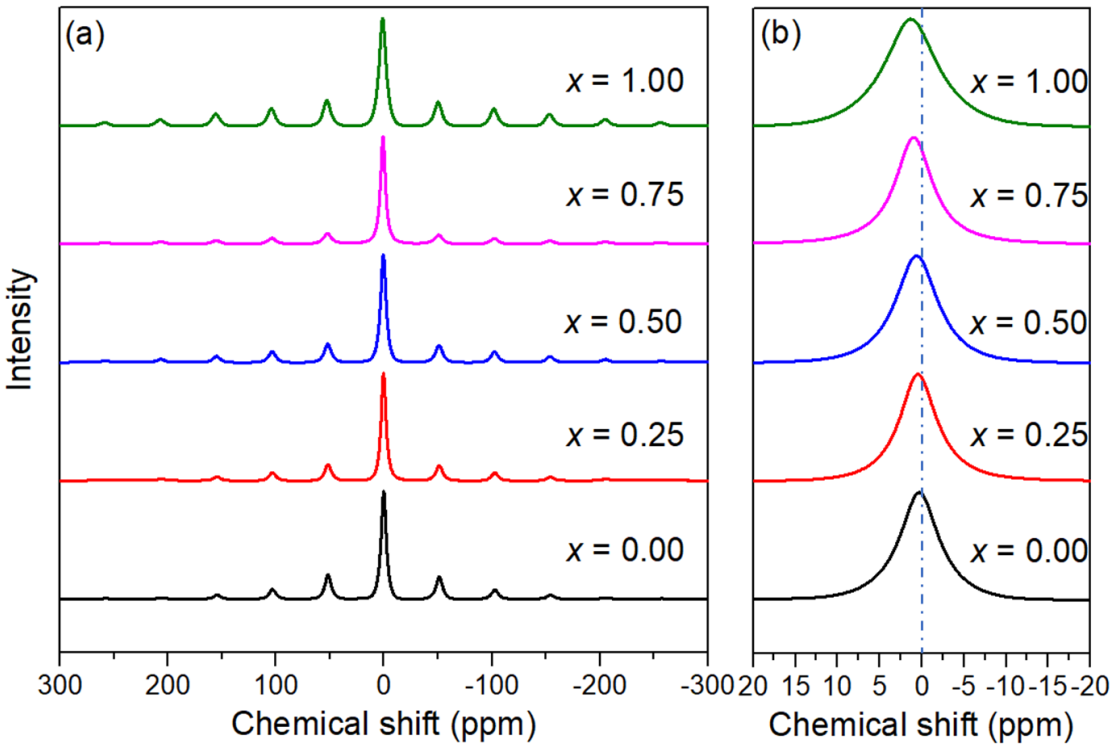

Figure 3.17 (a) ^{7}Li NMR spectra for *x* = 0.0, 0.25, 0.50, 0.75 and 1.0 compositions in the $Li_{3+x}Ge_xP_{1-x}O_4$ system at 12 kHz MAS speed at 298 K with (b) magnification of centre band resonance

The central resonances in the ^{7}Li spectra were fitted using a simple Czjzek distribution in DMfit [155]. In order to examine the chemical shift anisotropy, the spinning sidebands were fitted separately at their calculated positions using the same parameters as the isotropic resonances with only the amplitude varying. The final chemical shift anisotropy parameters were calculated using the program HBA [157]. Modelling of the centre band resonance revealed that it was actually made up of two separate resonances in each case. The fitted central band resonances are shown in Fig. 3.18 with the derived spectral parameters given in Table 3.7.

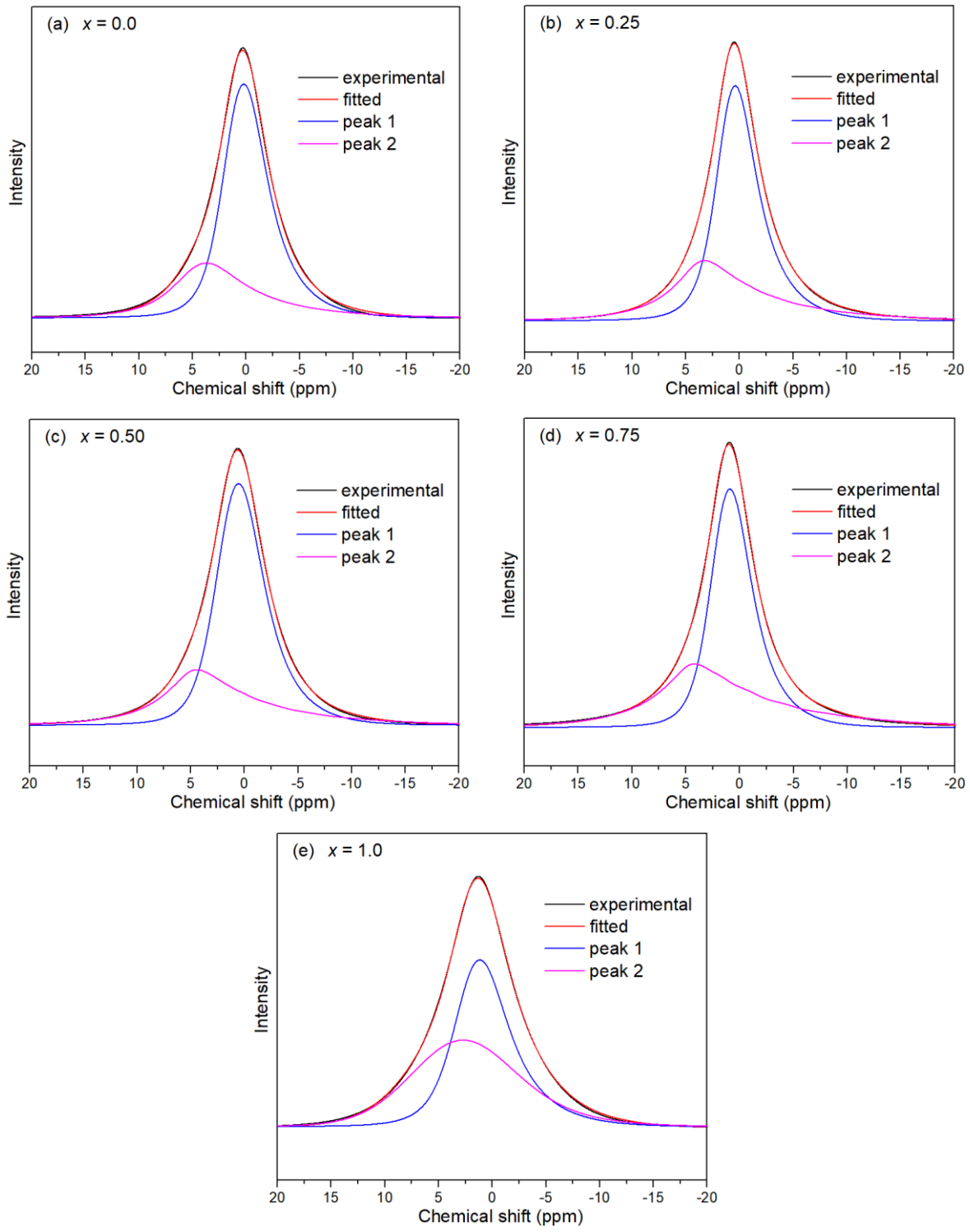

Figure 3.18 Fitted ^{7}Li NMR central band resonances for (a) x = 0, (b) x = 0.25, (c) x = 0.50, (d) x = 0.75 and (e) x = 1.0 compositions in $Li_{3+x}Ge_xP_{1-x}O_4$ system

Table 3.7 Derived ^{7}Li NMR parameters for $Li_{3+x}Ge_xP_{1-x}O_4$ system

x	δ_{iso}/ppm	NuQ/kHz	δ_{11}/ppm	δ_{22}/ppm	δ_{33}/ppm	$\Delta\delta$/ppm	η	%
0.00	0.65(5)	696.4(2)	812(19)	17(9)	-827(17)	-1241(26)	0.96(3)	70.75
	4.33(5)	1025.0(5)	978(21)	-1(11)	-964(18)	1461(32)	0.99(3)	29.25
0.25	0.79(5)	694.7(2)	705(22)	26(9)	-729(20)	-1094(30)	0.93(4)	65.72
	3.72(5)	1140.9(5)	928(36)	17(17)	-933(32)	-1405(48)	0.97(5)	34.28
0.50	1.01(5)	697.1(2)	789(32)	21(14)	-807(29)	-1212(43)	0.95(6)	69.79
	4.91(5)	1159.7(5)	1000(47)	14(23)	-999(41)	-1506(62)	0.98(7)	30.21
0.75	1.31(5)	661.6(2)	563(21)	53(8)	-613(20)	-921(30)	0.83(5)	60.55
	4.64(5)	1261.1(5)	873(39)	3(18)	-862(35)	1302(58)	1.00(6)	39.45
1.00	1.69(5)	776.8(2)	942(51)	19(24)	-956(45)	-1436(67)	0.96(7)	51.59
	3.74(5)	873.4(2)	1009(56)	15(27)	-1013(49)	-1525(73)	0.98(8)	48.41

Based on the crystal structures of compositions in the $Li_{3+x}Ge_xP_{1-x}O_4$ system (See Tables 3.10 to 3.14 in section 3.3.4.2), there are two crystallographic positions for Li (Li1 and Li2) in Li_3PO_4 and Li_4GeO_4 and six crystallographic positions (Li1, Li2, Li1a, Li2a, Li3 and Li4) in x = 0.25, 0.50 and 0.75. The ^{7}Li results for Li_3PO_4 show two resonances in the ratio of 71:29, which is reasonably close to the expected ratio of 2:1 for Li2:Li1. Therefore, the resonance at 0.65 ppm can be assigned to Li2 with the second resonance at 4.33 ppm assigned to Li1. In the case of Li_4GeO_4, the observed ratio of the two Li resonances is approximately 1:1 in agreement with the two 8-fold crystallographic sites in the structure of Li_4GeO_4. In the cases of the intermediate compositions of x = 0.25, 0.50 and 0.75, the least shifted resonance is still attributed predominantly to Li2/Li2a, but the additional octahedral Li cannot be resolved separately and appear to contribute mainly to the second resonance and may account for the fluctuation in the chemical shift of this peak. All resonances show asymmetry values close to 1 indicating fairly asymmetric environments. The compositional variation of the ^{7}Li chemical shifts is plotted in Fig. 3.19. A clear increasing trend with increasing x-value is confirmed for the lower field resonance. The trend for the higher field resonance is less clear, but as discussed above this resonance also contains significant contributions from the octahedral Li^+ ions.

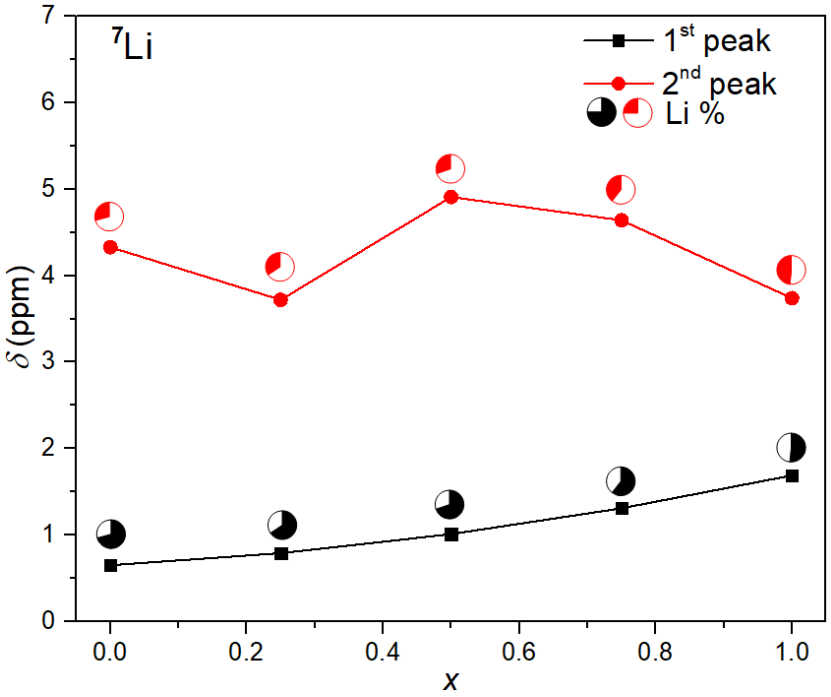

Figure 3.19 Compositional variation of ^{7}Li δ_{iso} in the $Li_{3+x}Ge_xP_{1-x}O_4$ system

The ^{31}P MAS-NMR spectra for the studied compositions are shown in Fig. 3.20. In each case, an isotropic resonance is seen at around 10 ppm corresponding to the phosphate tetrahedra accompanied by weak spinning sidebands. Similar to the ^{7}Li MAS spectra, the isotropic peak is seen to increase its chemical shift with increasing *x*-value. The chemical shift is in the range typical for Q^0 phosphate species [162] and a similar phenomenon is observed in the Li_4SiO_4-Li_3PO_4 solid solution system, where higher chemical shift is seen in the compositions of $Li_{3.75}Si_{0.75}P_{0.25}O_4$, $Li_{3.5}Si_{0.5}P_{0.5}O_4$ and $Li_{3.25}Si_{0.25}P_{0.75}O_4$ compared to the end-member Li_3PO_4 [93]. It is also noteworthy that a significantly increased broadening of the line shapes occurs with increasing *x*-value. This suggests a diversity of chemical environments, arising not only from the introduction of interstitial Li^+ ions but also from the disorder caused by the mixed occupancy of the Ge/P site. Despite there being only one crystallographic site for P, this asymmetric peak broadening in the intermediate compositions, especially in $x = 0.75$, is an indication that unlike the end member Li_3PO_4, the local atomic ordering for the intermediate

compositions is more complex than the spatially averaged picture derived from the X-ray and neutron diffraction.

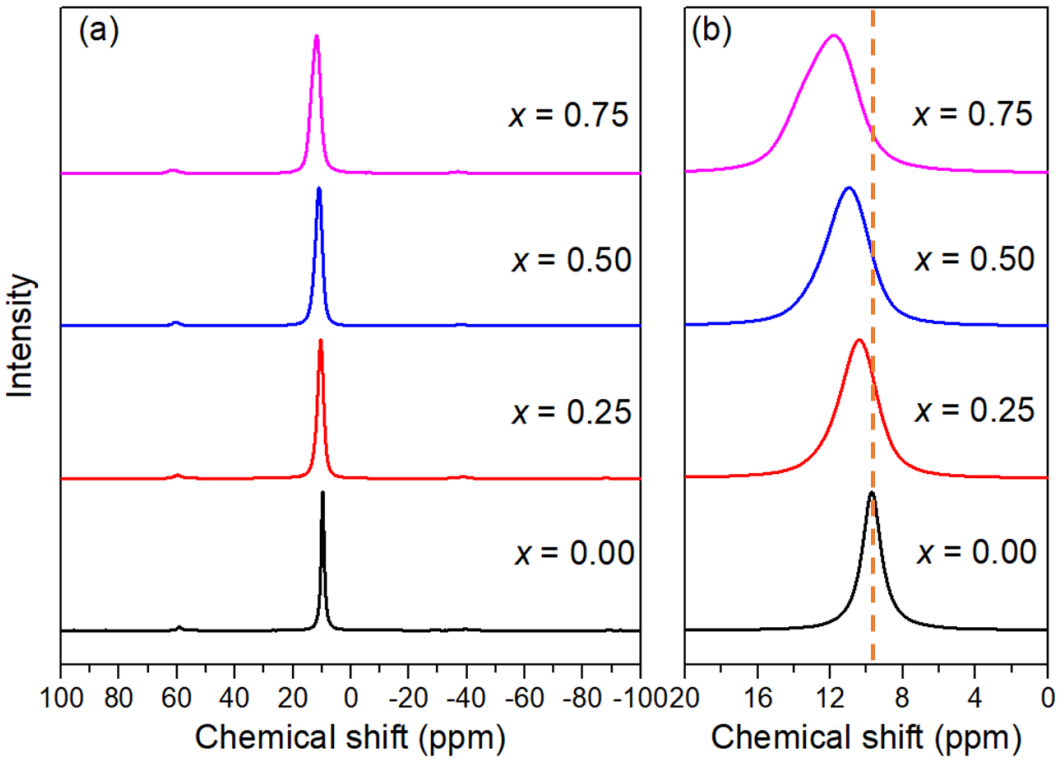

Figure 3.20 (a) ^{31}P NMR spectra for x = 0, 0.25, 0.5, and 0.75 in the $Li_{3+x}Ge_xP_{1-x}O_4$ system at 12 kHz MAS speed at 298 K with (b) magnification of the central resonance

As with the ^{7}Li spectra, the ^{31}P spectra were fitted, in this case using a Gaussian-Lorentzian peak shape in DMfit [155] and the spinning sidebands were fitted separately using the program NMRLSS [156]. The fitted central band resonances are shown in Fig. 3.21 and the fitted spectra are shown in Fig. 3.22. The derived spectral and chemical shift anisotropy parameters (obtained using HBA [157]), with the derived spectral parameters are given in Table 3.8.

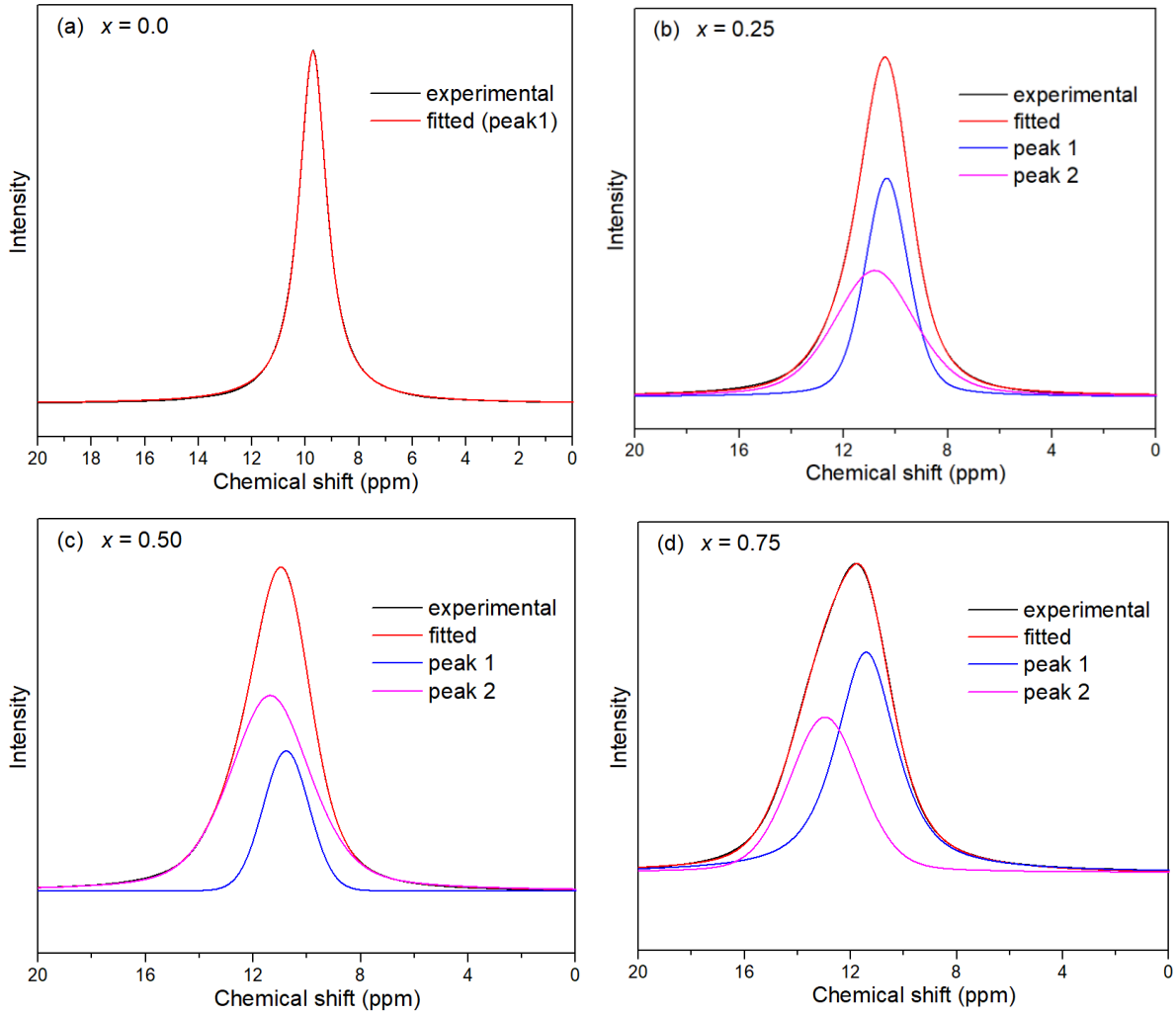

Figure 3.21 Fitted ^{31}P NMR central band resonances for (a) x = 0.0, (b) x = 0.25, (c) x = 0.50 and (d) x = 0.75 compositions in the $Li_{3+x}Ge_xP_{1-x}O_4$ system

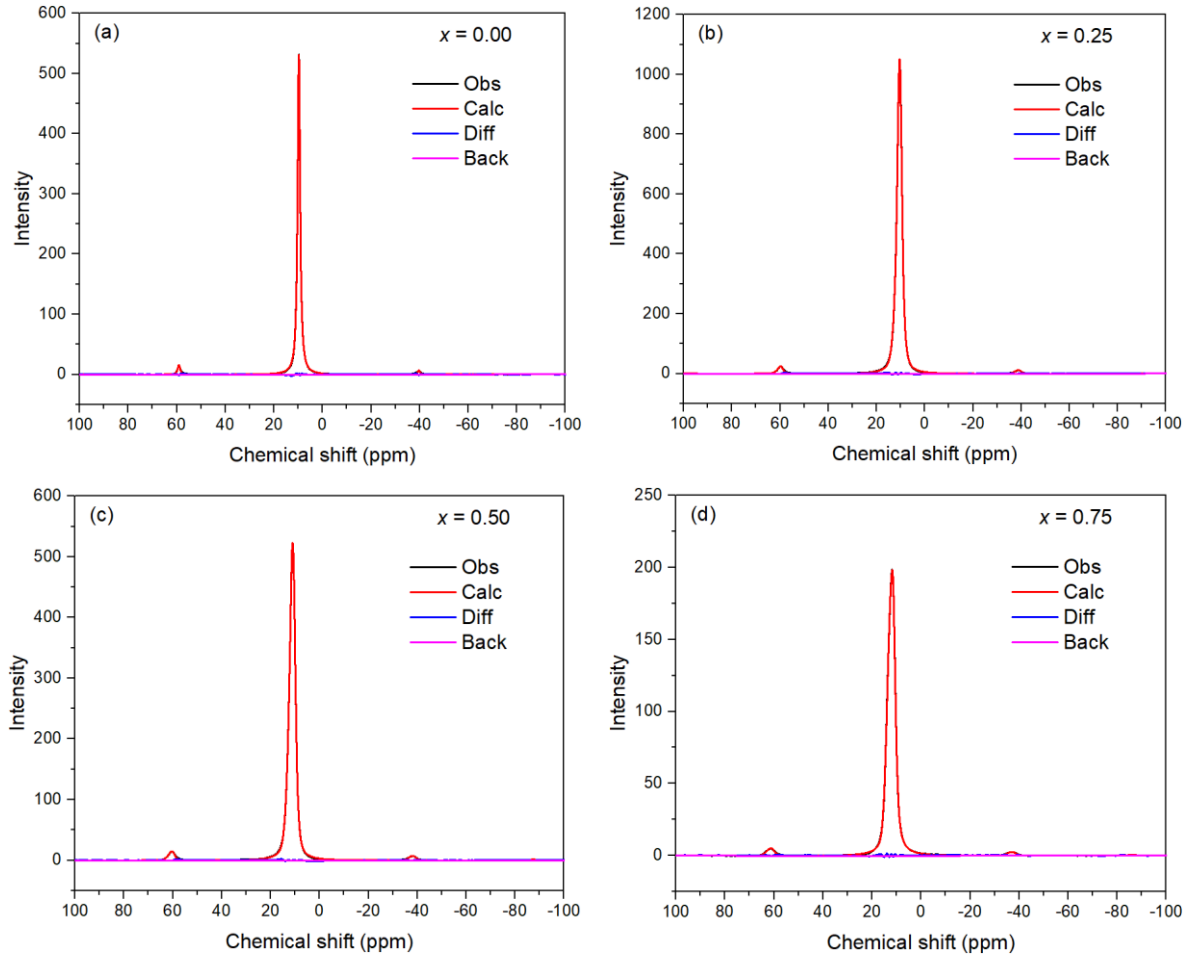

Figure 3.22 Fitted ^{31}P NMR whole spectra for x = 0, 0.25, 0.5, and 0.75 in the $Li_{3+x}Ge_xP_{1-x}O_4$ system

Table 3.8 Derived ^{31}P NMR parameters for the $Li_{3+x}Ge_xP_{1-x}O_4$ system

x	δ_{iso}/ppm	δ_{11}/ppm	δ_{22}/ppm	δ_{33}/ppm	$\Delta\delta$/ppm	η	%
0.00	9.72	200(5)	83(2)	-254(5)	-396(7)	0.45(2)	100
0.25	10.34	206(15)	34(4)	-209(14)	-329(21)	0.78(9)	46.43
	10.80	176(3)	157(2)	-301(2)	-468(3)	0.06(1)	53.57
0.50	10.77	1734(12)	-71(6)	-71(11)	245(18)	0.00(7)	24.60
	11.36	175(2)	166(2)	-307(2)	-477(3)	0.03(1)	75.40
0.75	11.41	187(6)	82(2)	-235(6)	-369(9)	0.43(3)	57.71
	12.96	212(3)	77(2)	-251(2)	-396(4)	0.51(1)	42.29

For Li_3PO_4 (x = 0.0), the data were modeled on a single resonance with a chemical shift of 9.72 ppm. For the other compositions two isotropic resonances were needed to describe the

central band. Fig. 3.23 shows the compositional variation of ^{31}P chemical shifts for the two isotropic resonances. In both cases a general increasing trend is seen with increasing *x*-value. As seen in the ^{7}Li data, this indicates a general deshielding trend with increasing *x*-value.

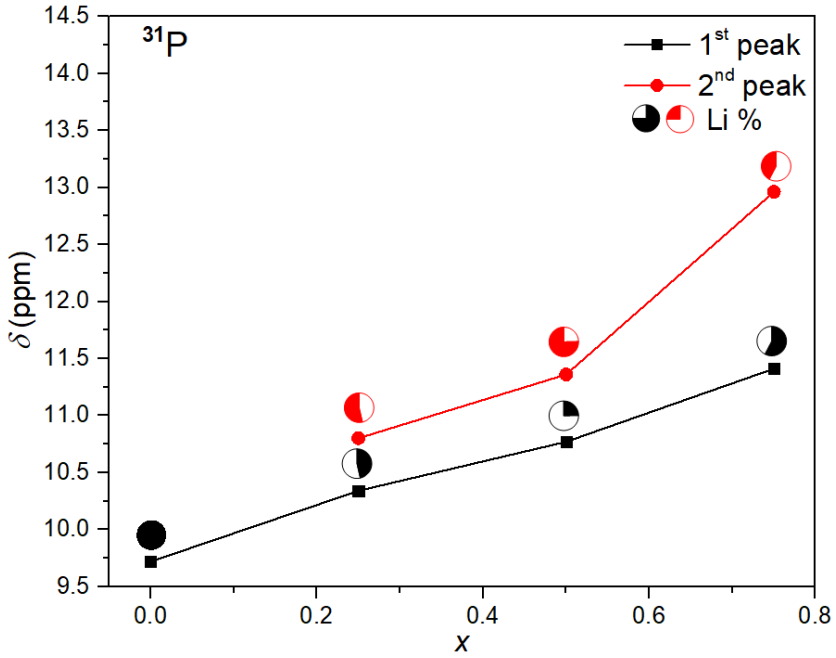

Figure 3.23 Compositional variation of ^{31}P δ_{iso} in $Li_{3+x}Ge_xP_{1-x}O_4$ system

3.3.4.2 Average structure analysis

To examine the lithium ion distribution and local defect structures, which determine the lithium ion conductivity in the $Li_{3+x}Ge_xP_{1-x}O_4$ system, the intermediate compositions x = 0.25, 0.50 and 0.75 and the two end-members γ-Li_3PO_4 and Li_4GeO_4 were selected for neutron total scattering. A combined neutron and X-ray approach was used for the Rietveld analysis for these compositions. The fitted diffraction profiles are shown in Figs. 3.24 to 3.28, with crystal and refinement parameters given in Table 3.9, refined structural parameters in Tables 3.10 to 3.14, and significant contacts and angles in Table 3.15-3.16. Table 3.17 includes short Li…Li contacts that preclude the simultaneous occupancy of the sites.

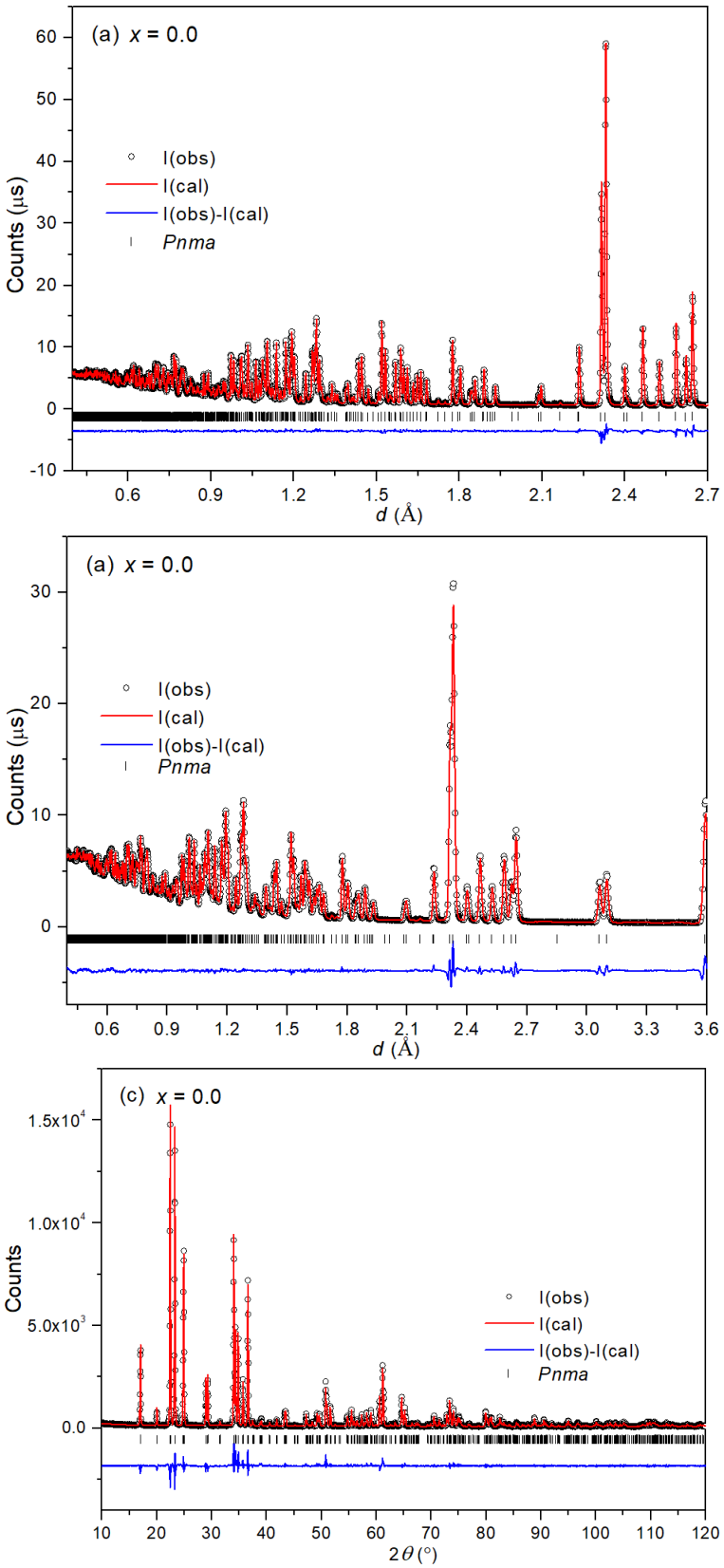

Figure 3.24 Diffraction profiles for Li_3PO_4 (x = 0.0) showing (a) neutron back scattering (b) neutron 90° and (c) X-ray data, fitted by conventional Rietveld analysis. Observed (crosses), calculated (line) and difference (lower) profiles are shown, with reflection positions indicated by markers

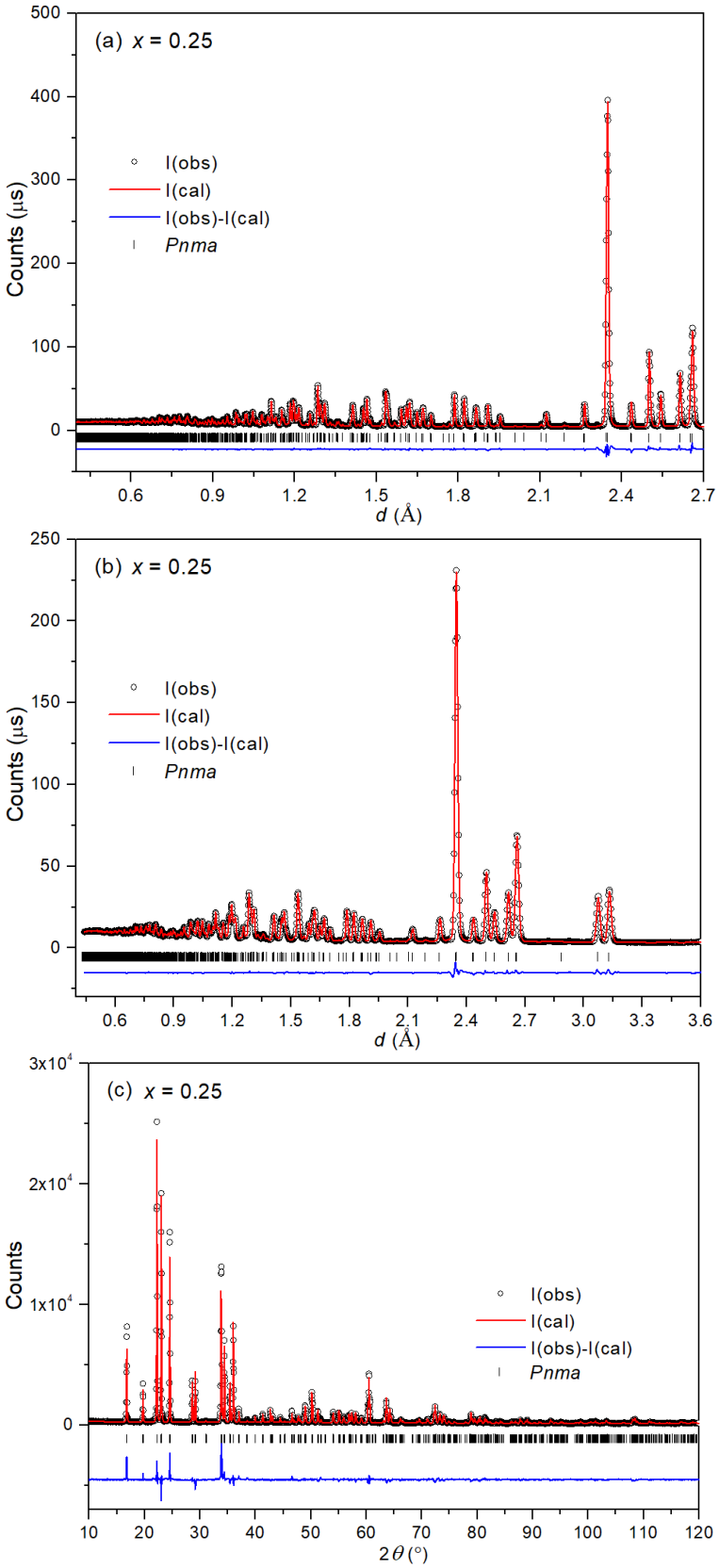

Figure 3.25 Diffraction profiles for $Li_{3.25}Ge_{0.25}P_{0.75}O_4$ (x = 0.25) showing (a) neutron back scattering (b) neutron 90° and (c) X-ray data, fitted by conventional Rietveld analysis. Observed (crosses), calculated (line) and difference (lower) profiles are shown, with reflection positions indicated by markers

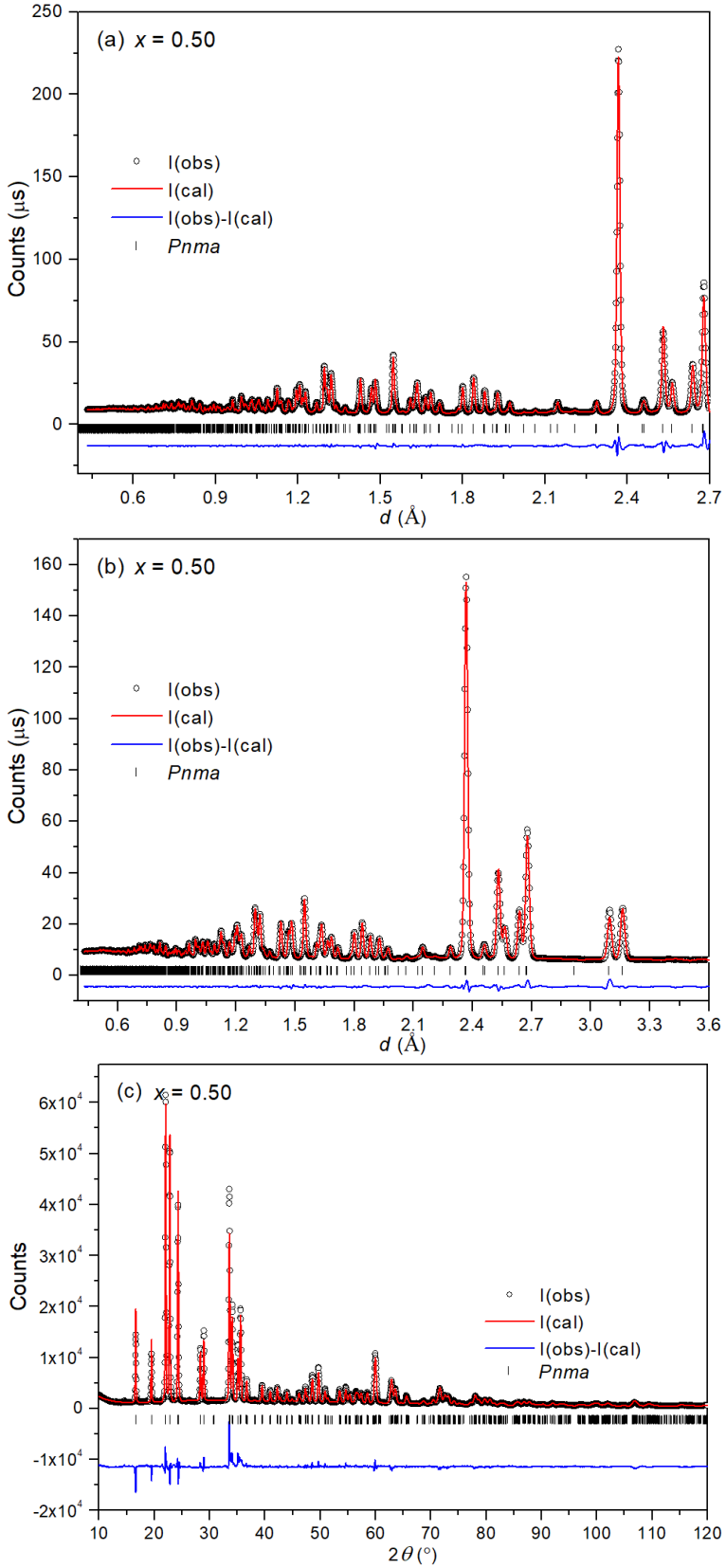

Figure 3.26 Diffraction profiles for $Li_{3.50}Ge_{0.50}P_{0.50}O_4$ (x = 0.50) showing (a) neutron back scattering (b) neutron 90° and (c) X-ray data, fitted by conventional Rietveld analysis. Observed (crosses), calculated (line) and difference (lower) profiles are shown, with reflection positions indicated by markers

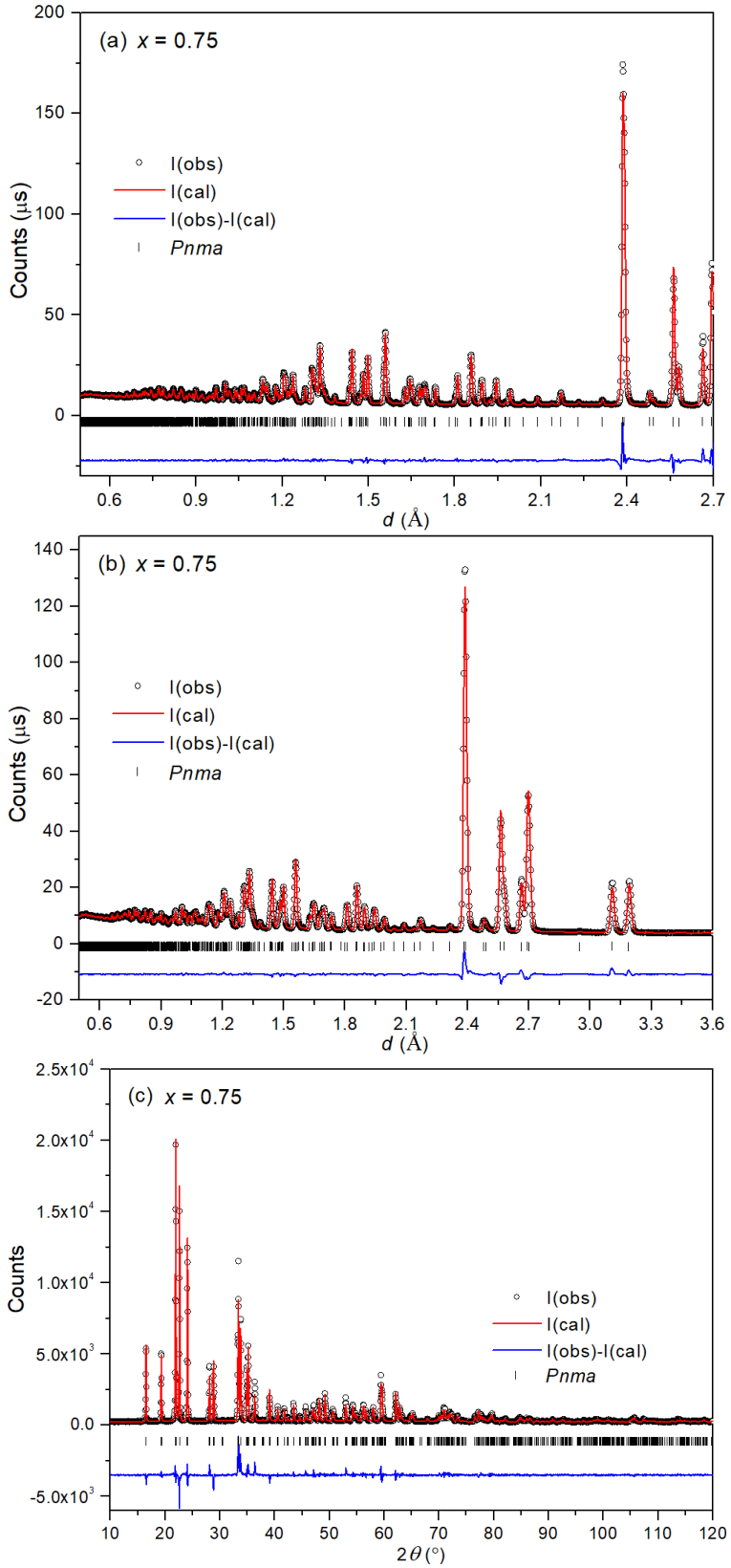

Figure 3.27 Diffraction profiles for $Li_{3.75}Ge_{0.75}P_{0.25}O_4$ (x = 0.75) showing (a) neutron back scattering (b) neutron 90° and (c) X-ray data, fitted by conventional Rietveld analysis. Observed (crosses), calculated (line) and difference (lower) profiles are shown, with reflection positions indicated by markers

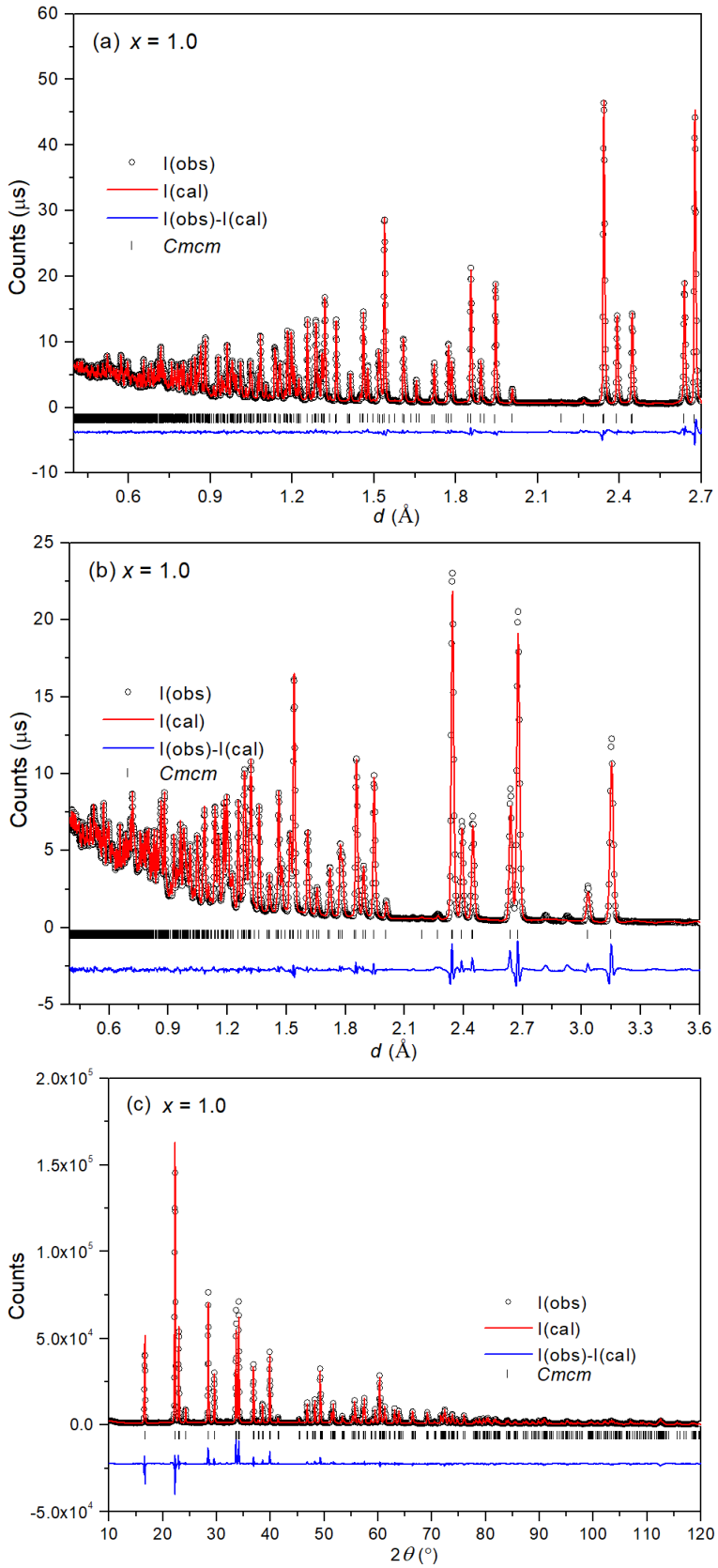

Figure 3.28 Diffraction profiles for Li_4GeO_4 (x = 1.0) showing (a) neutron back scattering (b) neutron 90° and (c) X-ray data, fitted by conventional Rietveld analysis. Observed (crosses), calculated (line) and difference (lower) profiles are shown, with reflection positions indicated by markers

Table 3.9 Crystal and refinement parameters at room temperature for compositions in the $Li_{3+x}Ge_xP_{1-x}O_4$ system.

x	$x = 0.00$	$x = 0.25$	$x = 0.50$	$x = 0.75$	$x = 1.00$
Chemical formula	Li_3PO_4	$Li_{3.25}Ge_{0.25}P_{0.75}O_4$	$Li_{3.5}Ge_{0.5}P_{0.5}O_4$	$Li_{3.75}Ge_{0.75}P_{0.25}O_4$	Li_4GeO_4
M_r (g mol^{-1})	115.79	127.94	140.08	152.23	164.37
Space group	*Pnma*	*Pnma*	*Pnma*	*Pnma*	*Cmcm*
Unit cell dimensions (Å)	$a = 10.4800(3)$ $b = 6.1214(1)$ $c = 4.9263(1)$	$a = 10.6034(3)$ $b = 6.1438(2)$ $c = 4.9981(2)$	$a = 10.6916(4)$ $b = 6.1846(2)$ $c = 5.0567(2)$	$a = 10.8060(4)$ $b = 6.2119(2)$ $c = 5.1197(2)$	$a = 7.77330(9)$ $b = 7.37177(9)$ $c = 6.05917(7)$
Volume （Å^3）	316.04(2)	325.60(3)	334.37(4)	343.66(4)	347.21(1)
Z	4	4	4	4	4
Density (calculated)	2.434 g/cm^3	2.615 g/cm^3	2.788 g/cm^3	2.942 g/cm^3	3.144 g/cm^3
R-factors (neutron back scattering)	$R_{wp} = 0.0153$ $R_p = 0.0230$ $R_{ex} = 0.0050$ $R_F^2 = 0.0215$	$R_{wp} = 0.0158$ $R_p = 0.0246$ $R_{ex} = 0.0033$ $R_F^2 = 0.0352$	$R_{wp} = 0.0139$ $R_p = 0.0252$ $R_{ex} = 0.0032$ $R_F^2 = 0.0253$	$R_{wp} = 0.0150$ $R_p = 0.0265$ $R_{ex} = 0.0037$ $R_F^2 = 0.0351$	$R_{wp} = 0.0166$ $R_p = 0.0245$ $R_{ex} = 0.0043$ $R_F^2 = 0.0528$
R-factors (neutron 90º)	$R_{wp} = 0.0188$ $R_p = 0.0279$ $R_{ex} = 0.0031$ $R_F^2 = 0.0798$	$R_{wp} = 0.0142$ $R_p = 0.0208$ $R_{ex} = 0.0021$ $R_F^2 = 0.0328$	$R_{wp} = 0.0129$ $R_p = 0.0186$ $R_{ex} = 0.0020$ $R_F^2 = 0.0392$	$R_{wp} = 0.0142$ $R_p = 0.0230$ $R_{ex} = 0.0023$ $R_F^2 = 0.0398$	$R_{wp} = 0.0202$ $R_p = 0.0335$ $R_{ex} = 0.0031$ $R_F^2 = 0.0290$
R-factors (X-ray)	$R_{wp} = 0.1169$ $R_p = 0.0918$ $R_{ex} = 0.0582$ $R_F^2 = 0.0794$	$R_{wp} = 0.1186$ $R_p = 0.0938$ $R_{ex} = 0.0484$ $R_F^2 = 0.1448$	$R_{wp} = 0.0982$ $R_p = 0.0749$ $R_{ex} = 0.0226$ $R_F^2 = 0.1130$	$R_{wp} = 0.1099$ $R_p = 0.0848$ $R_{ex} = 0.0441$ $R_F^2 = 0.1080$	$R_{wp} = 0.1226$ $R_p = 0.0908$ $R_{ex} = 0.0195$ $R_F^2 = 0.1170$
Total R-factors	$R_{wp} = 0.0184$ $R_p = 0.0856$	$R_{wp} = 0.0157$ $R_p = 0.0782$	$R_{wp} = 0.0156$ $R_p = 0.0718$	$R_{wp} = 0.0156$ $R_p = 0.0752$	$R_{wp} = 0.0245$ $R_p = 0.0901$
χ^2	14.86	22.82	25.02	18.08	29.36
No. of variables	122	133	135	133	116
No. of profile points neutron back scattering	3819	3818	3660	3415	4508
neutron 90º	2406	2126	2148	2038	2252
X-ray	3290	3290	3290	3290	3290

Table 3.10 Refined structural parameters for Li_3PO_4.

Atom	Site	*x*	*y*	*z*	U_{iso} (Å^2)	Occ.
Li1	4*c*	0.4240(1)	0.75	0.2069(3)	0.0141(2)	1.0
Li2	8*d*	0.16386(9)	0.5019(1)	0.3010 (2)	0.0121(2)	1.0
P	4*c*	0.41143(4)	0.25	0.30873(9)	0.00534(7)	1.0
O1	8*d*	0. 34183(3)	0. 04416(5)	0. 20587(6)	0.00872(6)	1.0
O2	4*c*	0. 04985(4)	0.25	0. 29293(9)	0.00890(8)	1.0
O3	4*c*	0.08974(4)	0.75	0.12194(8)	0.00783(7)	1.0

Table 3.11 Refined structural parameters for Li_4GeO_4.

Atom	Position	*x*	*y*	*z*	U_{iso} (Å^2)	Occ.
Li1	8*e*	0.1620(1)	0.0	0.0	0.0102(2)	1.0
Li2	8*g*	0.3529(1)	0.2264(1)	0.25	0.0129(2)	1.0
Ge	4*c*	0.0	0.33896(4)	0.25	0.00536(6)	1.0
O1	8*f*	0.0	0.20370(4)	0.00905(6)	0.00753(6)	1.0
O2	8*g*	0.19338(5)	0.46255(5)	0.25	0.00782(6)	1.0

Table 3.12 Refined structural parameters for $Li_3Ge_{0.25}P_{0.75}O_4$.

Atom	Site	*x*	*y*	*z*	U_{iso} (Å^2)	Occ.
Li1	4*c*	0.462(2)	0.75	0.130(5)	0.0247(4)	0.10(1)
Li1a	4*c*	0.4259(3)	0.75	0.1963(6)	0.0247(4)	0.90(1)
Li2	8*d*	0.1631(5)	-0.0045(7)	0.353(2)	0.0169(2)	0.31(2)
Li2a	8*d*	0.1634(2)	-0.0002(3)	0.2912(9)	0.0169(2)	0.69(2)
Li3	4*c*	0.223(2)	0.25	-0.075(4)	0.105(5)	0.167(5)
Li4	4*c*	0	0	0.5	0.105(5)	0.083(5)
Ge	4*c*	0.41203(5)	0.25	0.32116(8)	0.00933(9)	0.25
P	4*c*	0.41203(5)	0.25	0.32116(8)	0.00933(9)	0.75
O1	8*d*	0.34027(3)	0.03890(5)	0.21408(7)	0.01573(8)	1.0
O2	4*c*	0.08969(6)	0.75	0.13811(9)	0.0151(1)	1.0
O3	4*c*	0.05295(5)	0.25	0.28499(9)	0.0148(1)	1.0

Table 3.13 Refined structural parameters for $Li_{3.5}Ge_{0.5}P_{0.5}O_4$.

Atom	Position	*x*	*y*	*z*	U_{iso} (Å^2)	Occ.
Li1	4*c*	0.433(2)	0.75	0.12(1)	0.0317(9)	0.22(5)
Li1a	4*c*	0.4269(5)	0.75	0.190(2)	0.0317(9)	0.78(5)
Li2	8*d*	0.1621(2)	0.0016(3)	0.3161(4)	0.0231(4)	0.853(4)
Li2a	8*d*	0.156(1)	0.030(2)	0.155(2)	0.0231(4)	0.147(4)
Li3	4*c*	0.184(1)	0.25	-0.028(3)	0.117(5)	0.342(7)
Li4	4*c*	0	0	0.5	0.117(5)	0.158(7)
Ge	4*c*	0.41270(8)	0.25	0.3294(1)	0.0127(1)	0.5
P	4*c*	0.41270(8)	0.25	0.3294(1)	0.0127(1)	0.5
O1	8*d*	0.33854(6)	0.03187(9)	0.2200(1)	0.0186(1)	1.0
O2	4*c*	0.08866(9)	0.75	0.1530(1)	0.0194(2)	1.0
O3	4*c*	0.05622(8)	0.25	0.2815(2)	0.0172(2)	1.0

Table 3.14 Refined structural parameters for $Li_{3.75}Ge_{0.75}P_{0.25}O_4$.

Atom	Position	*x*	*y*	*z*	U_{iso} (Å^2)	Occ.
Li1	4*c*	0.4361(9)	0.75	0.124(4)	0.0177(7)	0.39(3)
Li1a	4*c*	0.4269(6)	0.75	0.193(2)	0.0177(7)	0.61(3)
Li2	8*d*	0.1617(2)	-0.0001(3)	0.3234(3)	0.0167(4)	0.851(4)
Li2a	8*d*	0.164(1)	0.040(2)	0.129(2)	0.0167(4)	0.149(4)
Li3	4*c*	0.202(1)	0.25	-0.036(2)	0.085(2)	0.421(7)
Li4	4*c*	0	0	0.5	0.085(2)	0.329(7)
Ge	4*c*	0.41255(7)	0.25	0.3389(1)	0.0124(1)	0.75
P	4*c*	0.41255(7)	0.25	0.3389(1)	0.0124(1)	0.25
O1	8*d*	0.33723(6)	0.02567(8)	0.2252(1)	0.0177(1)	1.0
O2	4*c*	0.08779(8)	0.75	0.1686(1)	0.0184(2)	1.0
O3	4*c*	0.05967(7)	0.25	0.2759(2)	0.0169(2)	1.0

Table 3.15 Significant bond lengths (Å) in the $Li_{3+x}Ge_xP_{1-x}O_4$ system from conventional Rietveld analysis.

bond	x = 0.0	x = 0.25	x = 0.50	x = 0.75	x = 1.0
Ge/P-O1	1.5416(4) × 2	1.5961(4) × 2	1.6598(7) × 2	1.7155(6) × 2	1.7681(4) × 2
Ge/P -O2	1.5347(6)	1.5842(6)	1.6362(9)	1.6879(8)	1.7579(4) × 2
Ge/P -O3	1.5430(6)	1.5857(8)	1.6337(13)	1.6951(11)	/
Li1-O1	1.9960(6) × 2	2.232(18) × 2	2.079(16) × 2	2.084(8) × 2	1.9609(7) × 2
Li1-O2	2.0576(16)	1.787(17)	2.026(28)	1.953(10)	1.9059(7) × 2
Li1-O3	1.9310(14)	1.730(23)	1.71(5)	1.783(18)	/
Li1a-O1	/	1.9958(17) × 2	1.990(4) × 2	1.974(4) × 2	/
Li1a-O2	/	1.9238(24)	1.906(6)	1.877(5)	/
Li1a-O3	/	2.0677(32)	2.063(13)	2.141(12)	/
Li2-O1	2.0119(10)	2.021(6)	1.9573(25)	1.9687(21)	2.0092(8) × 2
Li2-O1′	1.9437(10)	1.817(10)	2.0529(20)	2.0631(19)	
Li2-O2	1.9512(9)	2.009(6)	1.9281(23)	1.9177(21)	2.1372(12)
Li2-O3	1.9205(10)	1.981(5)	1.9161(21)	1.9204(20)	1.9779(12)
Li2a-O1	/	1.9300(26)	1.977(12)	1.940(11)	/
Li2a-O1′	/	2.127(4)	2.238(12)	2.109(11)	/
Li2a-O2	/	1.8844(22)	1.874(12)	1.991(11)	/
Li2a-O3	/	1.9325(22)	1.845(12)	1.878(11)	/
Li3-O1	/	2.307(18)	2.475(13)	2.421(9)	/
Li3-O1′	/	2.170(12)	2.172(10)	2.147(7)	/
Li3-O1″	/	2.307(18)	2.475(13)	2.421(9)	/
Li3-O1‴	/	2.170(12)	2.172(10)	2.147(7)	/
Li3-O2	/	2.449(21)	/	2.726(12)	/
Li3-O3	/	2.548(20)	2.078(17)	2.219(12)	/
Li4-O1	/	2.01755(33) × 2	2.0631(6) × 2	2.1092(6) × 2	/
Li4-O2	/	2.5564(4) × 2	2.5237(6) × 2	2.4882(6) × 2	/
Li4-O3	/	1.95683(30) × 2	1.9931(5) × 2	2.0355(6) × 2	/
Mean Ge/P-O	1.540(4)	1.591(6)	1.647(14)	1.704(14)	1.763(6)
Mean Li-O	1.970	2.009	2.022	2.060	1.983

Table 3.16 Significant bond angles (°) in the $Li_{3+x}Ge_xP_{1-x}O_4$ system from conventional Rietveld analysis

	x = 0.0	x = 0.25	x = 0.50	x = 0.75	x = 1.0
O1-Ge/P-O1	109.643(32)	108.700(33)	108.74(5)	108.65(5)	111.335(31)
O1-Ge/P-O2	109.876(20)	109.260(24)	109.21(4)	109.767(35)	106.995(9)
O1-Ge/P-O3	108.962(21)	109.696(22)	109.532(34)	109.106(29)	/
O1-Ge/P-O2	109.876(20)	109.260(24)	109.21(4)		
O1-Ge/P-O3	108.962(21)	109.696(22)	109.532(34)		
O2-Ge/P-O3	109.50(4)	110.20(4)	110.59(6)		
O1-Li1-O1	128.89(7)	105.4(12)	113.9(14)	110.5(6)	100.04(5)
O1-Li1-O2	93.15(5)	108.4(7)	105.0(13)	107.2(5)	117.867(15)
O1-Li1-O3	112.90(4)	97.9(6)	106.2(12)	105.2(4)	/
O1-Li1-O2	93.15(5)	108.4(7)	105.0(13)	107.2(5)	
O1-Li1-O3	112.90(4)	97.9(6)	106.2(12)	105.2(4)	
O2-Li1-O3	108.24(7)	135.6(19)	120.9(15)	121.5(7)	
O1-Li1a-O1	/	125.58(18)	122.3(4)	120.3(4)	/
O1-Li1a-O2	/	113.05(5)	113.38(26)	115.04(22)	/
O1-Li1a-O3	/	95.38(7)	97.0(4)	96.66(33)	/
O1-Li1a-O2		113.05(5)	113.38(26)	115.04(22)	
O1-Li1a-O3		95.38(7)	97.0(4)	96.66(33)	
O2-Li1a-O3		109.27(19)	110.0(5)	108.3(5)	
O1-Li2-O1	106.63(5)	112.01(33)	105.05(10)	104.81(9)	102.73(5)
O1-Li2-O2	95.96(5)	105.98(35)	111.31(11)	111.19(9)	96.96(4)
O1-Li2-O3	109.98(4)	112.63(31)	118.03(11)	117.08(11)	/
O1-Li2-O2	117.91(4)	115.87(31)	110.06(10)	110.62(9)	
O1-Li2-O3	113.08(5)	104.54(34)	99.77(9)	101.06(9)	
O2-Li2-O3	111.58(5)	105.82(32)	111.57(12)	111.31(11)	
O1-Li2a-O1	/	103.29(16)	97.9(5)	104.1(5)	/
O1-Li2a-O2	/	115.04(14)	112.8(6)	109.3(5)	/
O1-Li2a-O3	/	119.12(12)	120.6(6)	120.6(6)	/
O1-Li2a-O2		107.75(15)	81.1(4)	85.5(4)	
O1-Li2a-O3		95.39(14)	118.7(6)	121.6(6)	
O2-Li2a-O3		112.96(15)	117.5(7)	110.0(6)	

Table 3.17 Li…Li inter-site contact distances (Å) in the $Li_{3+x}Ge_xP_{1-x}O_4$ system from conventional Rietveld analysis

	$x = 0.25$	$x = 0.50$	$x = 0.75$
Li1..Li1a	0.503(28)	0.357(35)	0.367(11)
Li1..Li3	2.45(4)	2.18(4)	2.294(20)
Li1..Li4	1.716(14)	1.806(18)	1.814(8)
Li1a..Li3	1.948(23)	1.863(19)	1.967(16)
Li1a..Li4	1.9845(25)	1.975(8)	2.004(7)
Li2..Li2a	0.310(7)	0.831(11)	1.025(11)
Li2..Li3	2.726(18)	2.333(13)	2.448(10)
Li2..Li3′	1.966(15)	2.398(13)	2.256(9)
Li2..Li4	1.879(6)	1.9666(23)	1.967(2)
Li2a..Li3	2.473(15)	1.677(16)	1.609(12)
Li2a..Li3′	2.062(15)	2.910(17)	2.878(14)
Li2a..Li4	2.0223(31)	2.418(13)	2.607(11)

According to the refined structural parameters in Tables 3.10-3.14, the end-members γ-Li_3PO_4 and Li_4GeO_4 only show full occupancy of their respective Li tetrahedral sites (Li1 and Li2) in their structures with no occupation of interstitial tetrahedral or octahedral sites. The refined structure of Li_4GeO_4 is in good agreement with that determined from single crystal X-ray data presented by Hoffman and Hoppe [147]. In the present case, the use of neutron diffraction has enabled greater accuracy in the Li positions. Similarly, there is good agreement between the refined structural parameters for γ-Li_3PO_4 and those presented by Wang et al. [146], also from neutron diffraction data. Interestingly, attempts to model the splitting of the Li3 and Li4 sites as found Rabadanov et al. [151] were unsuccessful and always resulted in refinement onto their respective special positions.

All the structures of the intermediate compositions $x = 0.25$, 0.50 and 0.75 show disorder in the Li^+ ion sublattice. There is partial occupancy of the Li1 and Li2 sites, with some ions displaced in the *c*-axis direction towards the neighbouring interstitial tetrahedral sites. The displaced ions are labelled as Li1a for Li1 and Li2a for Li2. As seen in Fig. 3.29 and Table 3.17, Li1a remains very close to Li1 within the same tetrahedron throughout the compositional

range. Similarly, at x = 0.25, the Li2a position is close to that of Li2 and sits in the same tetrahedral site. However, the Li2-Li2a distance increases with increasing x-value, such that at x = 0.50 and 0.75, the Li2a ions reside in the neighbouring tetrahedral site. It is noteworthy that the thermal parameters of Li3 and Li4 in these three compositions are several times higher than those for Li1/Li1a and Li2/Li2a pairs, indicating significant positional disorder in these octahedral interstitial sites. However, attempts at resolving this disorder through splitting of sites was unsuccessful. Throughout the studied compositional range, all the compositions contain more occupied Li3 than Li4 sites, and both the Li3 and Li4 sites increase their occupancy with increasing x-value at roughly the same rate.

The displacement of the tetrahedral Li ions towards the interstitial sites is a result of the repulsive forces between Li^+ ions in the Li3 and Li4 sites and the Li^+ ions in the Li2 sites, and to a certain extent, Li1 sites. Table 3.17 includes short Li…Li contacts that preclude the simultaneous occupancy of the sites. Whilst the structures of the x = 0.25, 0.50 and 0.75 compositions have been refined with the splitting of the Li1 site into Li1 and Li1a sites, the structures can be equally well described using a single site with a larger thermal parameter and in this way are similar to the structures described for γ-$Li_3Zn_{0.5}GeO_4$ at room temperature [81] and γ-$Li_{3.5}Ge_{0.5}V_{0.5}O_4$ at room temperature and elevated temperature [85], which were reported with fully occupied Li1 sites.

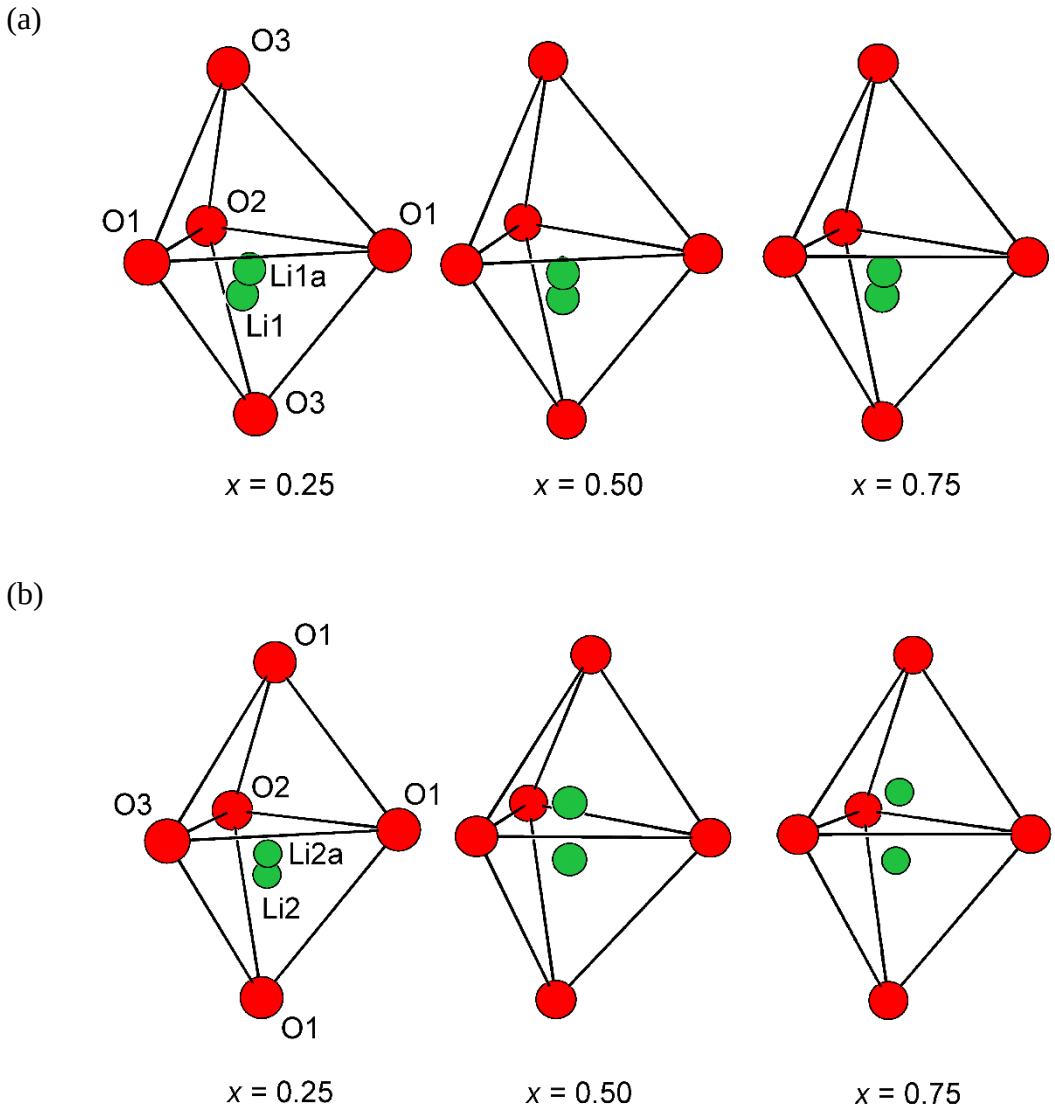

Figure 3.29 Compositional variation of Li^+ ion positions in tetrahedral Li sites in the $Li_{3+x}Ge_xP_{1-x}O_4$ system

Based on the structural data it is possible to propose individual defects in the $Li_{3+x}Ge_xP_{1-x}O_4$ system. The simplest of these involves Li^+ ions in the Li3 site which displace Li from a neighbouring Li2 site towards an empty tetrahedral site (Li2a) as seen in Fig. 3.30a. A small displacement of a neighbouring Li1 to the Li1a position also occurs but is omitted from Fig. 3.30a for clarity. This type of defect was previously identified as the Type I defect in $Li_3Zn_{0.5}GeO_4$ [81] and $Li_{3.5}Ge_{0.5}V_{0.5}O_4$ [85]. A second type of defect can be identified involving in the Li4 ions. Li4 ions in the octahedral site share faces with two Li1 tetrahedra and two Li2

tetrahedra (Fig. 3.30b). The Li1-Li4 distance is very short and it is likely that the presence of Li^+ ions on the Li4 site displace Li1 to the Li1a position, lengthening the Li-Li distance for example from 1.8 to 2.0 Å in the case of $x = 0.75$. While this is still short for an Li…Li contact, the high thermal parameter of Li4 suggests considerable positional disorder and it is likely that the Li-Li distance lengthens further through displacement of the Li4 position away from the site centre. Similarly, Li^+ ions on the Li4 site minimise the Li4-Li2 repulsion by displacement of Li2 into the Li2a site. Thus, the second type of defect consists of Li^+ in the Li4 site with a Li1 ion displaced into Li1a and a Li2 ion displaced into Li2a (Fig. 3.30b). This type of defect is similar to those previously identified in the $Li_3Zn_{0.5}GeO_4$ and $Li_{3.5}Ge_{0.5}V_{0.5}O_4$ systems, but differs somewhat in the fact that it includes displacement of the Li1 ions. It is arguable that it is the presence of a neighbouring Li3 ion that makes the Li4 site more favourable by displacing the Li2 ion into the Li2a position that lies between Li3 and Li4. In this case the individual Type I and Type II defects would be clustered. Indeed, the Li3:Li4 ratio is ca. 2:1 for $x = 0.25$ and 0.50, but lowers for $x = 0.75$. This might suggest a larger defect cluster (Type III) involving three interstitial octahedral ions (2 × Li3 and 1 × Li4) as proposed in other LISICON system [84] (Fig. 3.30c).

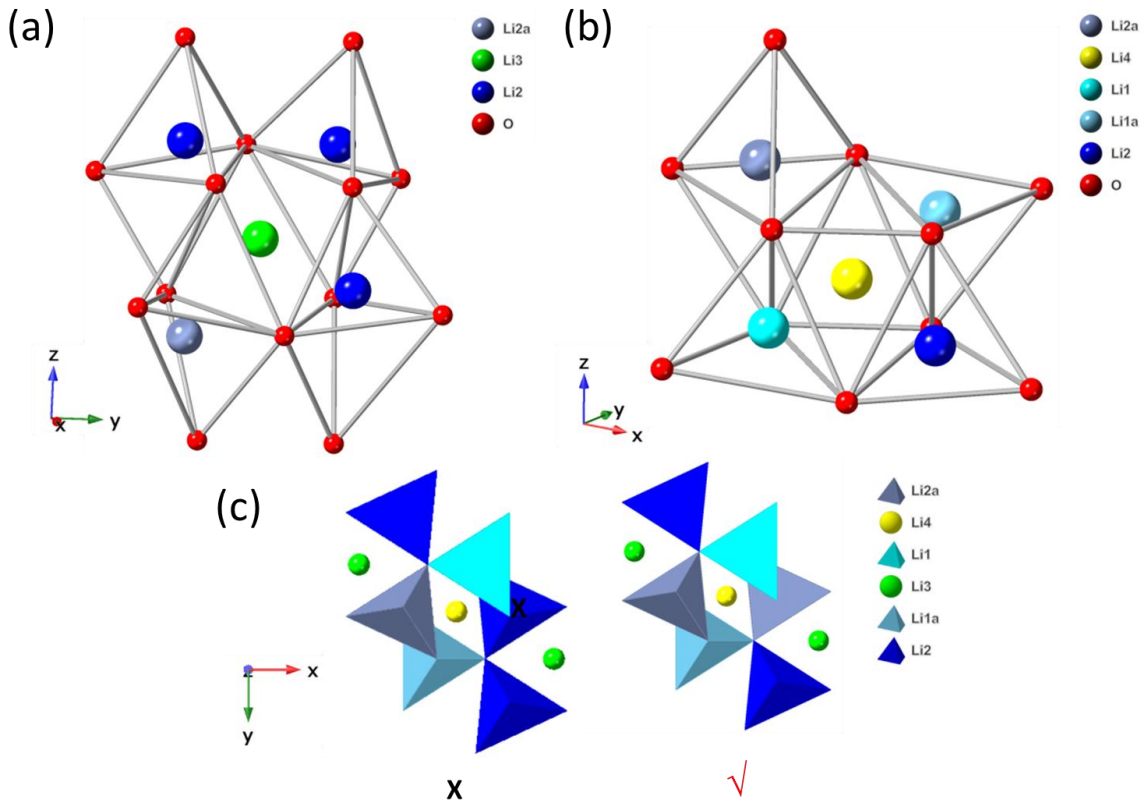

Figure 3.30 Three types of proposed defect clusters in the $Li_{3+x}Ge_xP_{1-x}O_4$ system: (a) Type I, (b) Type II and (c) Type III.

3.3.4.3 Neutron total scattering analysis

Although the average structure of the intermediate compositions x = 0.25, 0.50 and 0.75 and the two end-members γ-Li_3PO_4 and Li_4GeO_4 can be well identified through Rietveld analysis of a combination of the XRD and neutron diffraction data, the exact nature of the defects and in particular the defect clusters remain somewhat speculative. Further information on the local structure can be obtained from analysis of total neutron scattering data through RMC simulation. Simulations were carried out to fit the Bragg scattering as well as the functions $S(Q)$ and $G(r)$.

Fig.3.31 shows the total pair correlation functions $G(r)$ for the studied compositions along with calculated patterns derived from the initial configurations based on the refined structures, but excluding Li1a and Li2a. These calculated profiles were obtained through 40 cycles of smoothing of the corresponding individual pair correlations of the primary idealised

configuration and summing them based on the neutron scattering coefficients. Since the primary idealised configuration-derived $G(r)$ represents the highly ordered crystalline structure and the experimental $G(r)$ illustrates the actual structure including the short-rang and long-range order, the difference between the primary model-derived $G(r)$ and experimental $G(r)$ is a measure of the disorder of the system.

As can be seen in Fig.3.31, for the experimental $G(r)$, similar overall distributions can be observed for $0.0 \leq x \leq 0.75$, while for $x = 1.0$, the experimental $G(r)$ is noticeably different, reflecting the change in structure for Li_4GeO_4. The primary idealised configuration-derived $G(r)$ exhibits good accordance with the experimental $G(r)$ for $x = 0.0$ and 1.0 both over the short range (Fig. 3.31b) and the long range (Fig. 3.31a), in accordance with their highly ordered crystalline structures (Tables 3.10 and 3.11). For the intermediate compositions $x = 0.25$, 0.50 and 0.75, the primary idealised configuration-derived $G(r)$ exhibits good agreement with the experimental data over the long range (3.75 Å and beyond); for the short range of 1.3-3.75 Å, the deviation from the experimental $G(r)$ is lowest in $x = 0.25$ and highest in $x = 0.75$, indicating the increased local disorder from $x = 0.25$ to $x = 0.75$.

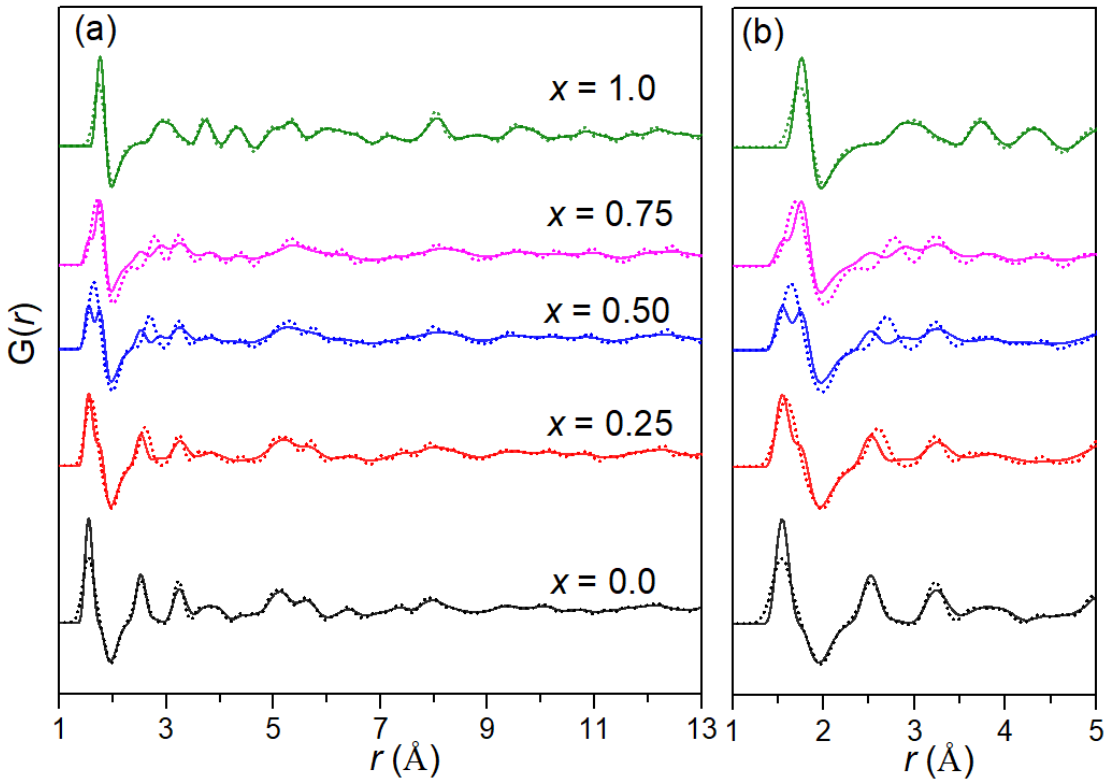

Figure 3.31 (a) Experimental (solid line) and primary idealised configuration-derived (dotted line) G(*r*) profiles for compositions in the $Li_{3+x}Ge_xP_{1-x}O_4$ system with short range correlations shown in (b).

In each case, 10 parallel sets of RMC calculations were performed to ensure sufficient statistics in the individual pair correlations, with calculations carried over 7 days to ensure the residual differences between observed and calculated profiles were as small as possible. In the case of the intermediate compositions x = 0.25, 0.50 and 0.75, 10 different initial configurations were used each with a random distribution of Li3 and Li4 sites and Ge and P randomly distributed on their shared site. Calculations were also performed for Li_3PO_4 and Li_4GeO_4, for comparison. In these cases, where there was no randomness in the initial configuration, a single configuration was used for each of the 10 parallel calculations, but each calculation started at a different time to ensure different random seeds were used. For the intermediate compositions it was necessary to include a simulated *g*Li-Li(*r*) distribution as a constraint to model the low *r*-range of the Li-Li pair correlation in order to prevent short Li…Li contacts. These simulated

data were based on the molecular dynamics simulation of the related $Li_{3.7}Ge_{0.85}W_{0.15}O_4$ (see Chapter 5). Fig. 3.32 to Fig. 3.36 show the final fitted $G(r)$ and $S(Q)$ profiles for these calculations. Good fits were obtained, indicating the produced configurations model the observed scattering data well.

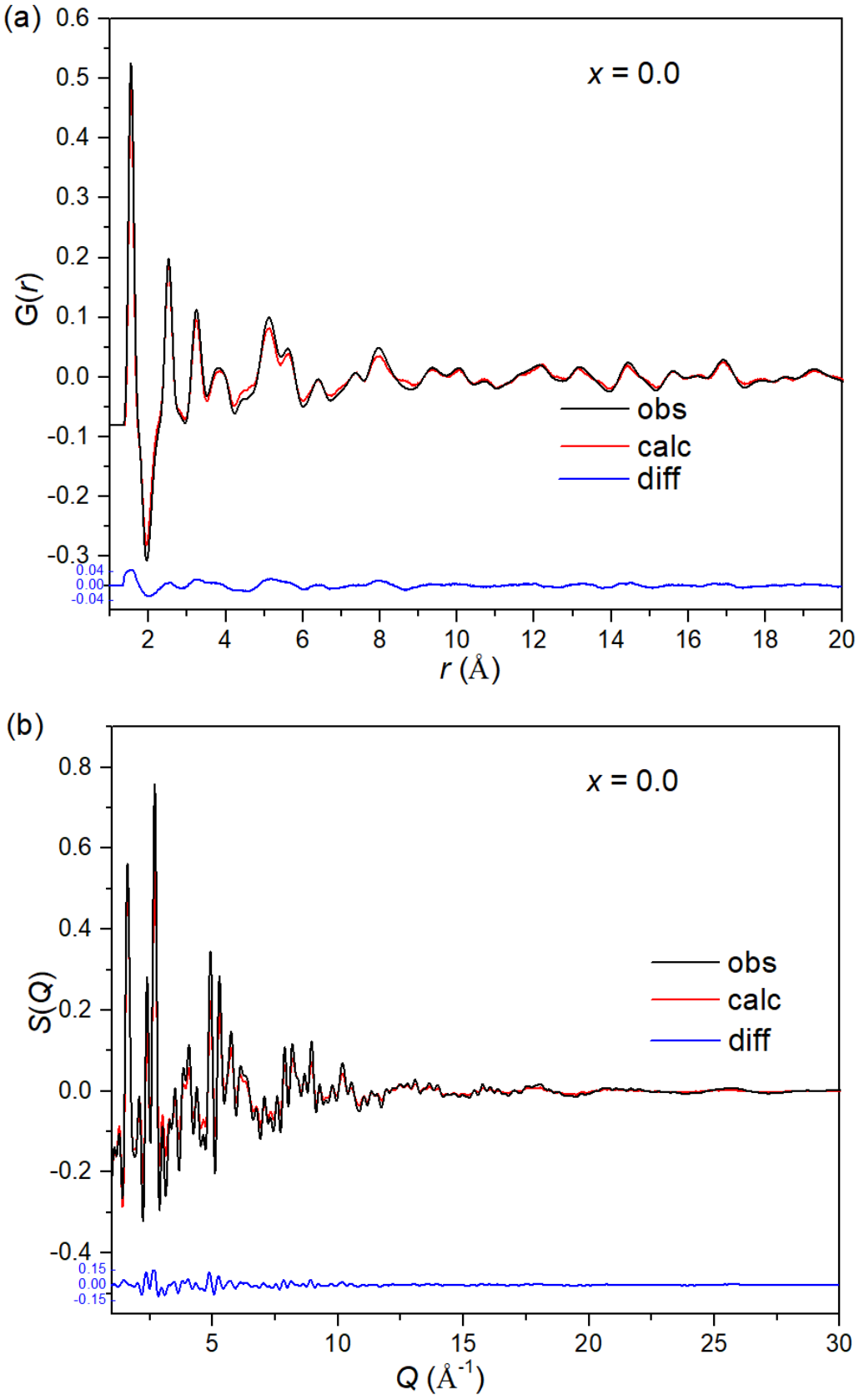

Figure 3.32 (a) Fitted total pair correlation functions, *G*(*r*) and (b) fitted normalised total scattering structure factor, *S*(*Q*) for Li_3PO_4 (*x* = 0.0).

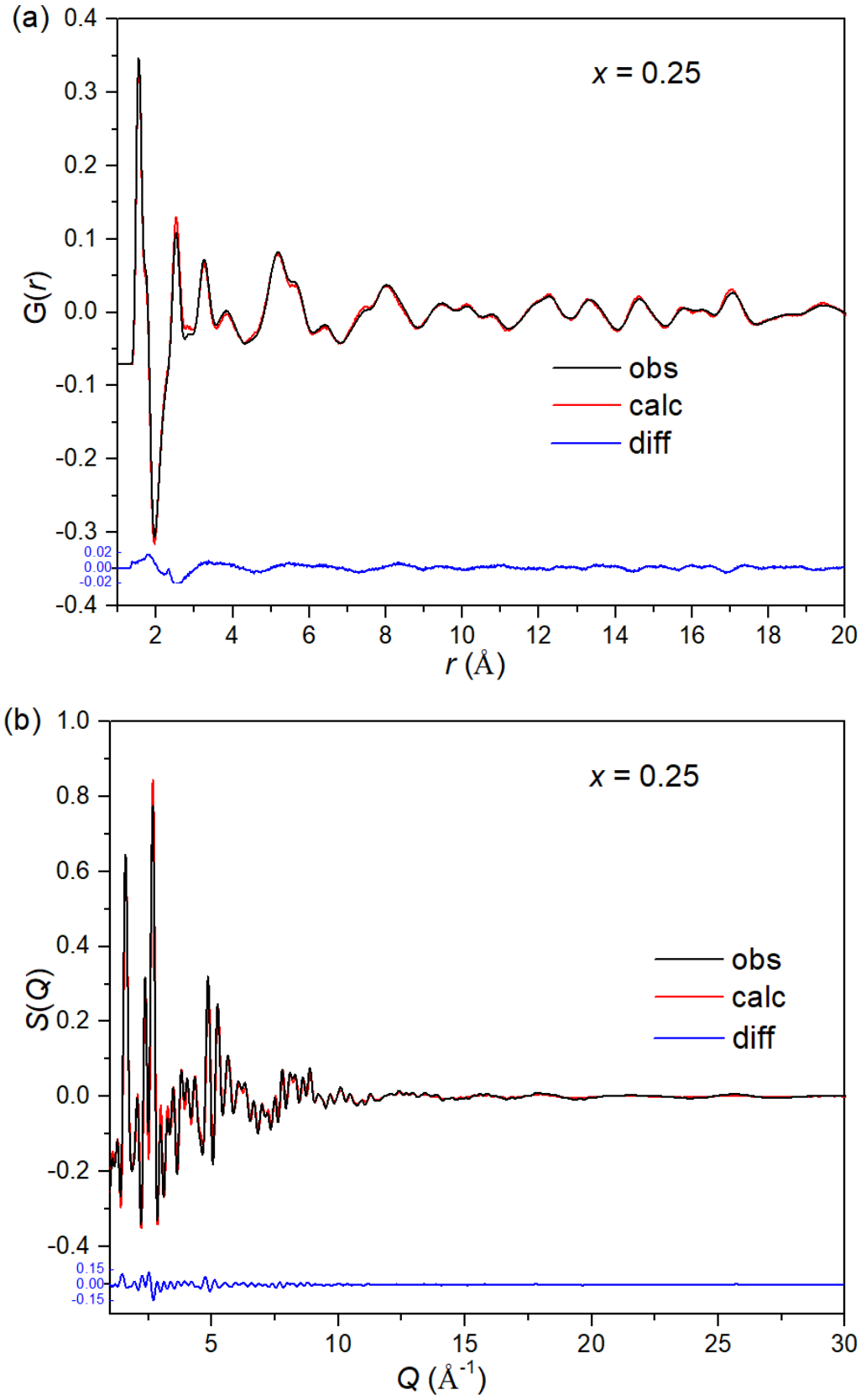

Figure 3.33 (a) Fitted total pair correlation functions, *G*(*r*) and (b) fitted normalised total scattering structure factor, *S*(*Q*) for $Li_{3.25}Ge_{0.25}P_{0.75}O_4$ (*x* = 0.25) in the $Li_{3+x}Ge_xP_{1-x}O_4$ system

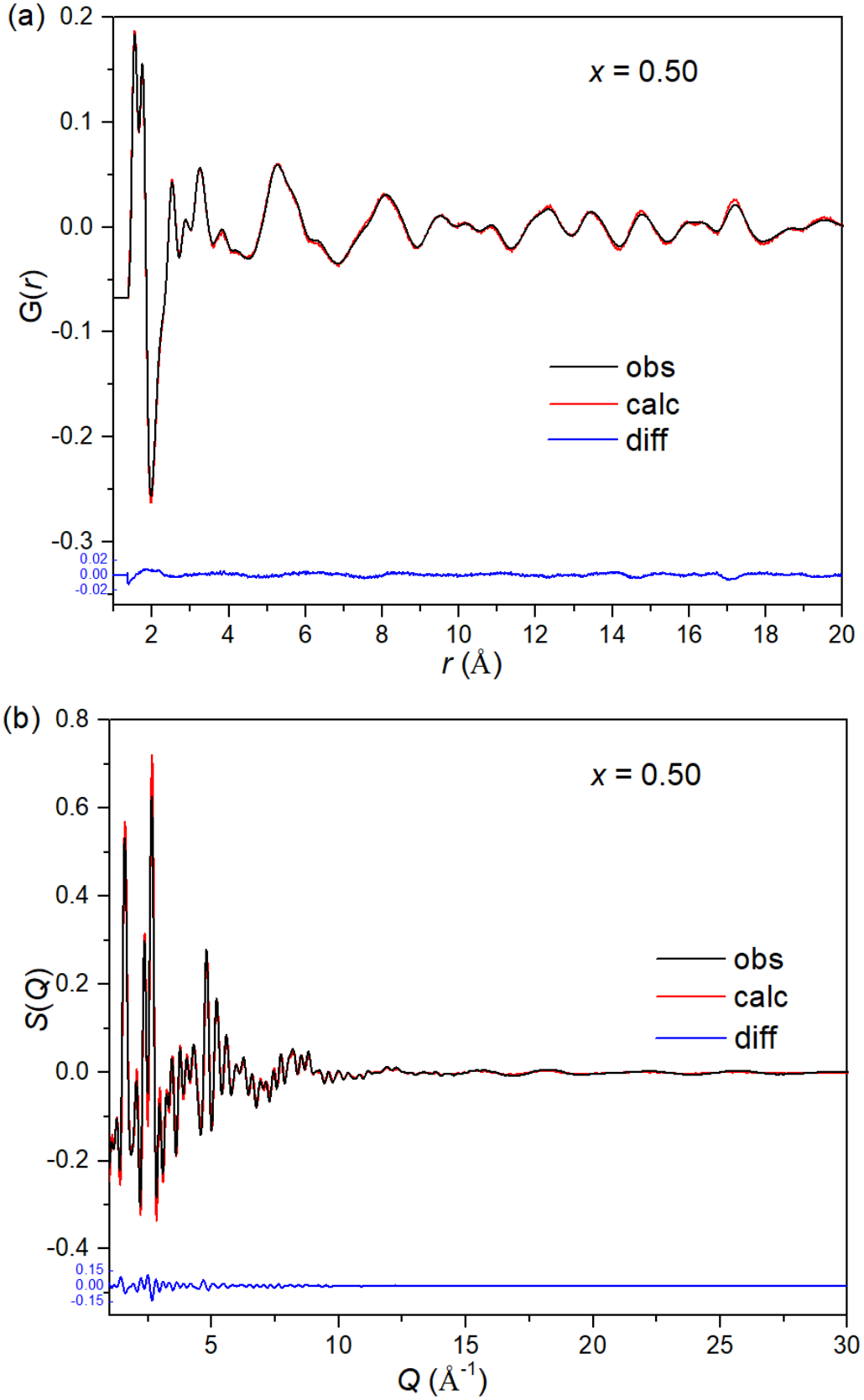

Figure 3.34 (a) Fitted total pair correlation functions, *G*(*r*) and (b) fitted normalised total scattering structure factor, *S*(*Q*) for $Li_{3.5}Ge_{0.5}P_{0.5}O_4$ (*x* = 0.50) in the $Li_{3+x}Ge_xP_{1-x}O_4$ system

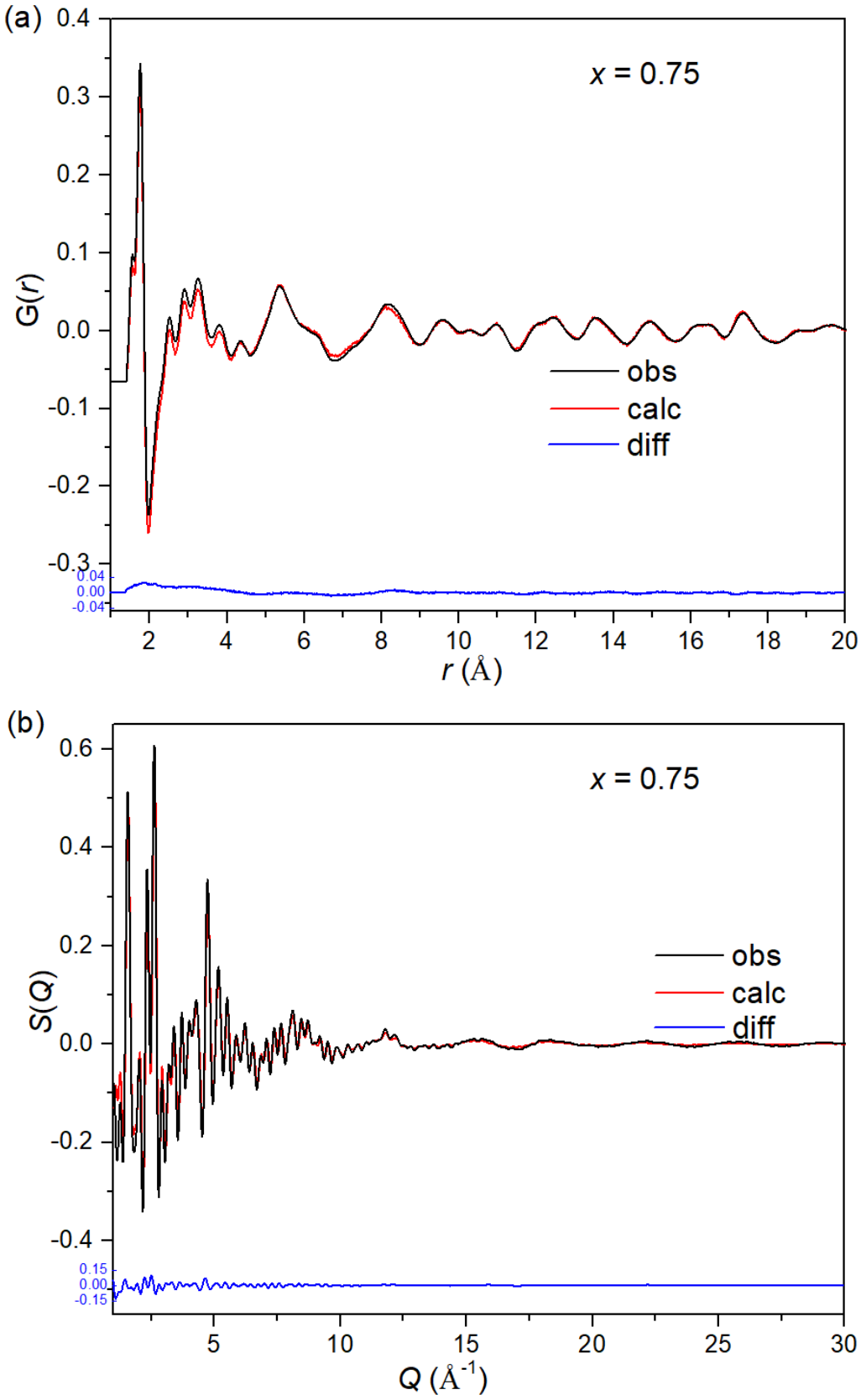

Figure 3.35 (a) Fitted total pair correlation functions, *G*(*r*) and (b) fitted normalised total scattering structure factor, *S*(*Q*) for $Li_{3.75}Ge_{0.75}P_{0.25}O_4$ (*x* = 0.75) in the $Li_{3+x}Ge_xP_{1-x}O_4$ system

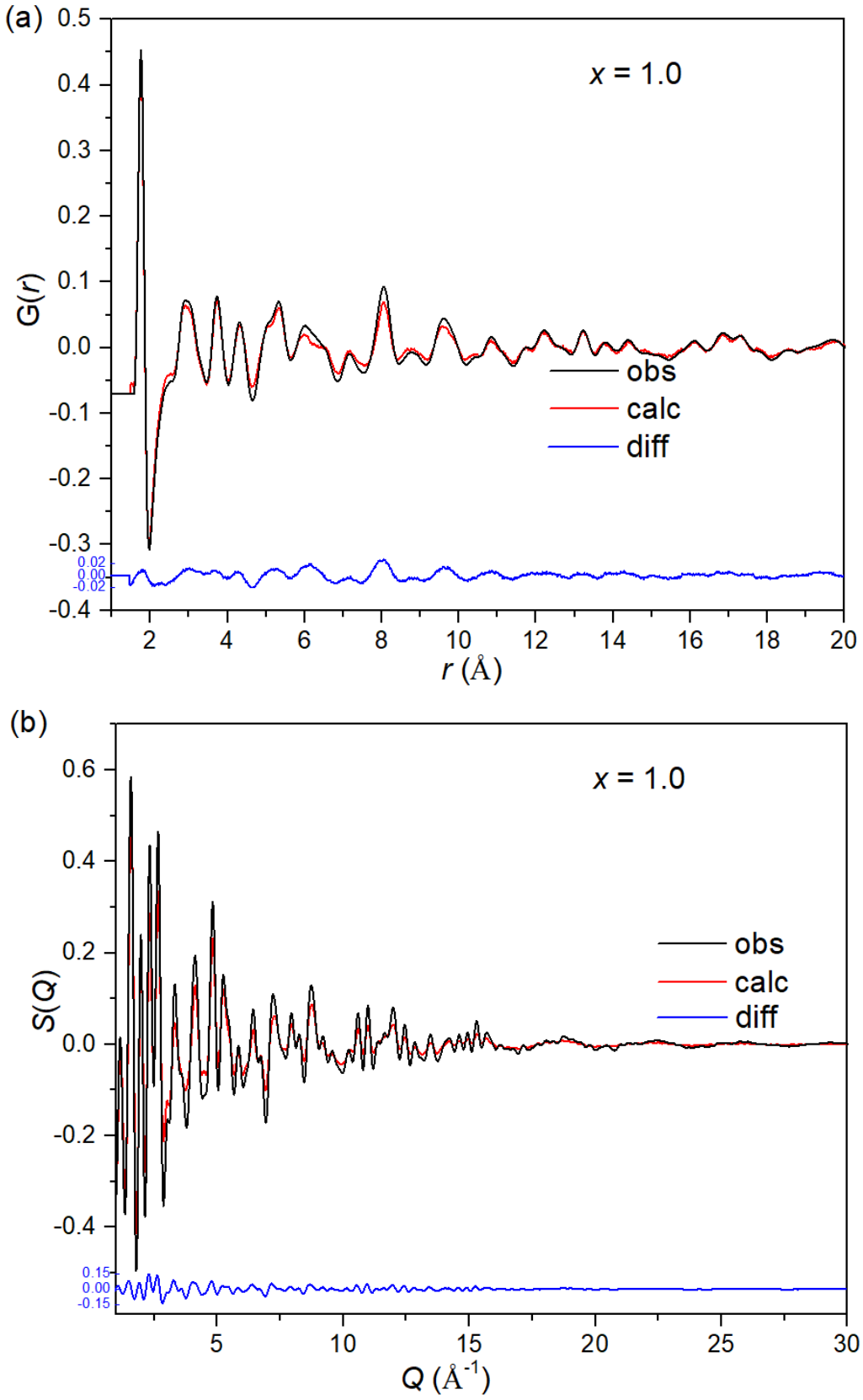

Figure 3.36 (a) Fitted total pair correlation functions, *G*(*r*) and (b) fitted normalised total scattering structure factor, *S*(*Q*) for Li_4GeO_4 (*x* = 1.0) in the $Li_{3+x}Ge_xP_{1-x}O_4$ system

Fig. 3.37 shows the projections of one of the final RMC supercell configurations for $x = 0.25$, 0.50 and 0.75 compositions in the $Li_{3+x}Ge_xP_{1-x}O_4$ system. As seen from the projections on the *x*-*y* plane, there is an irregular distribution of Li^+ ions, some of which are clustered together. As the *x*-value increases, the Li^+ density increases and the clusters grow in size.

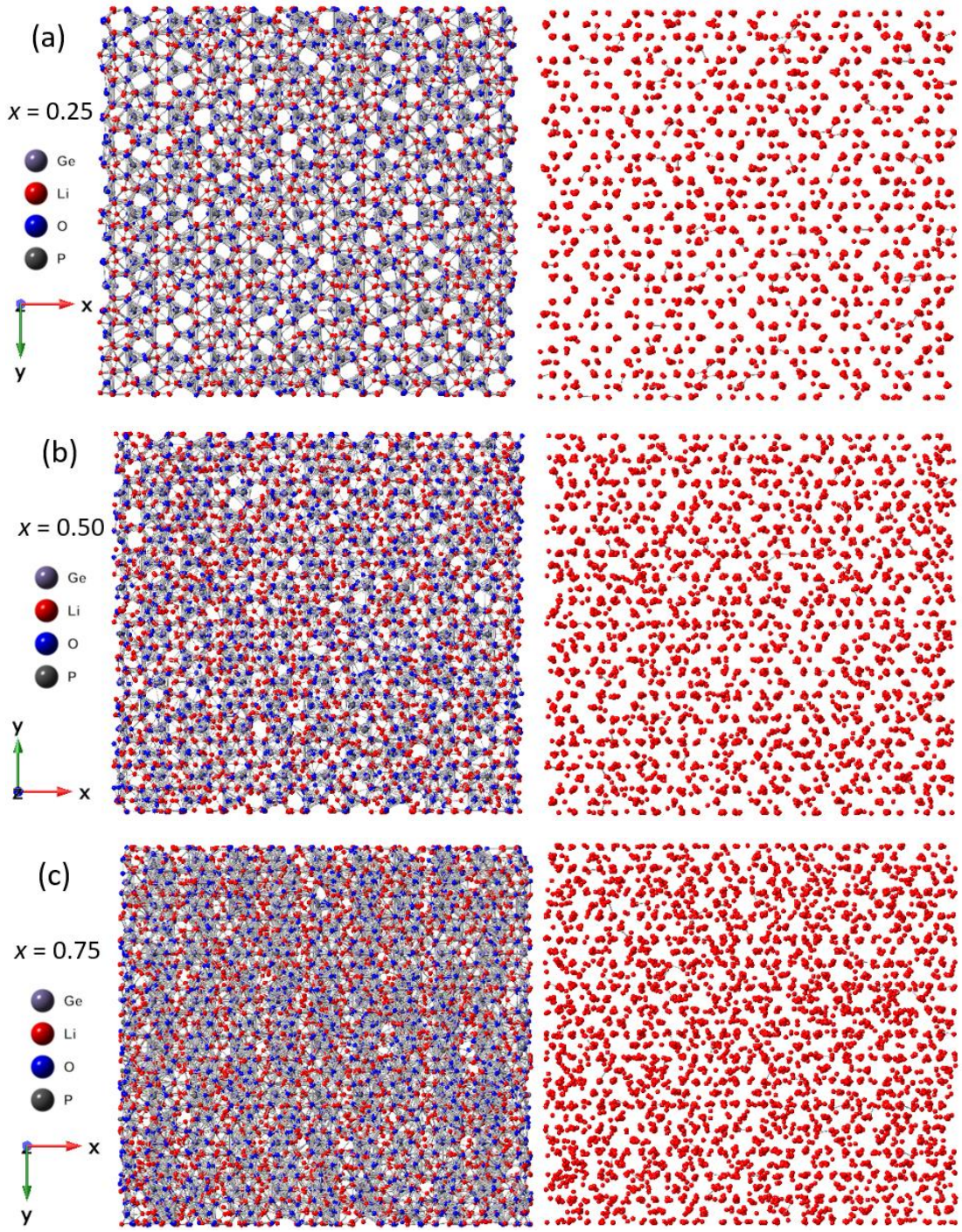

Figure 3.37 Projections down *c*-axis of final supercell configurations for (a) $x = 0.25$, (b) $x = 0.50$ and (c) $x = 0.75$ compositions in the $Li_{3+x}Ge_xP_{1-x}O_4$ system, showing (left) full configuration and (right) Li only.

Fig. 3.38 shows the individual pair correlations $g_{ij}(r)$ derived from the RMC configurations. The individual pair correlations easily distinguish between P-O, Ge-O and Li-O correlations, with respective modal distances of approximately 1.5 Å, 1.8 Å and 1.9 Å. Table 3.18 summarises the coordination numbers (CN), modal distances and mean distances for the individual pair correlations. The coordination numbers for Ge and P approximate to 4, consistent with the tetrahedral geometry for these atoms. The averages of the mean Li-O distances of 2.002, 2.040 and 2.072 Å are in good agreement with the corresponding weighted average values from the Rietveld analysis of 2.009, 2.022 and 2.060 Å, for the x = 0.25, 0.50 and 0.75 compositions, respectively. In contrast, the weighted average of the mean Ge/P-O distances of 1.613, 1.668 and 1.713 Å for the x = 0.25, 0.50 and 0.75 compositions, respectively, are slightly longer than the corresponding values of 1.591, 1.647 and 1.704 Å derived from the Rietveld analysis. The Li coordination number to oxygen is slightly greater than 4 and increases with increasing x-value. This is consistent with the Rietveld analysis where the high thermal parameters for Li3 and Li4 suggest significant positional disorder for the interstitial octahedral sites. It is therefore expected that Li ions in these sites minimise their coordination number through displacement away from the centre of the site.

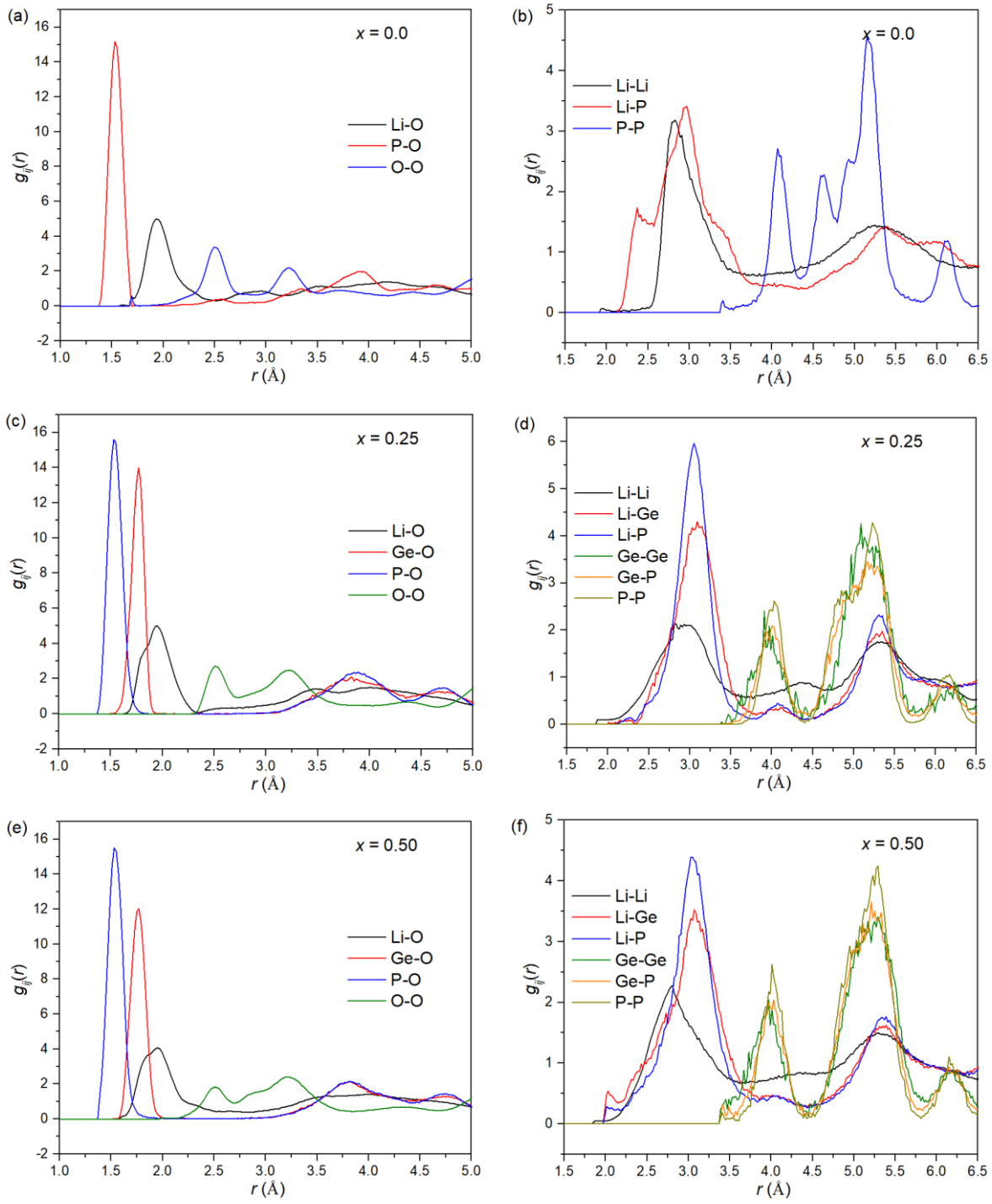

Figure 3.38 continued on next page

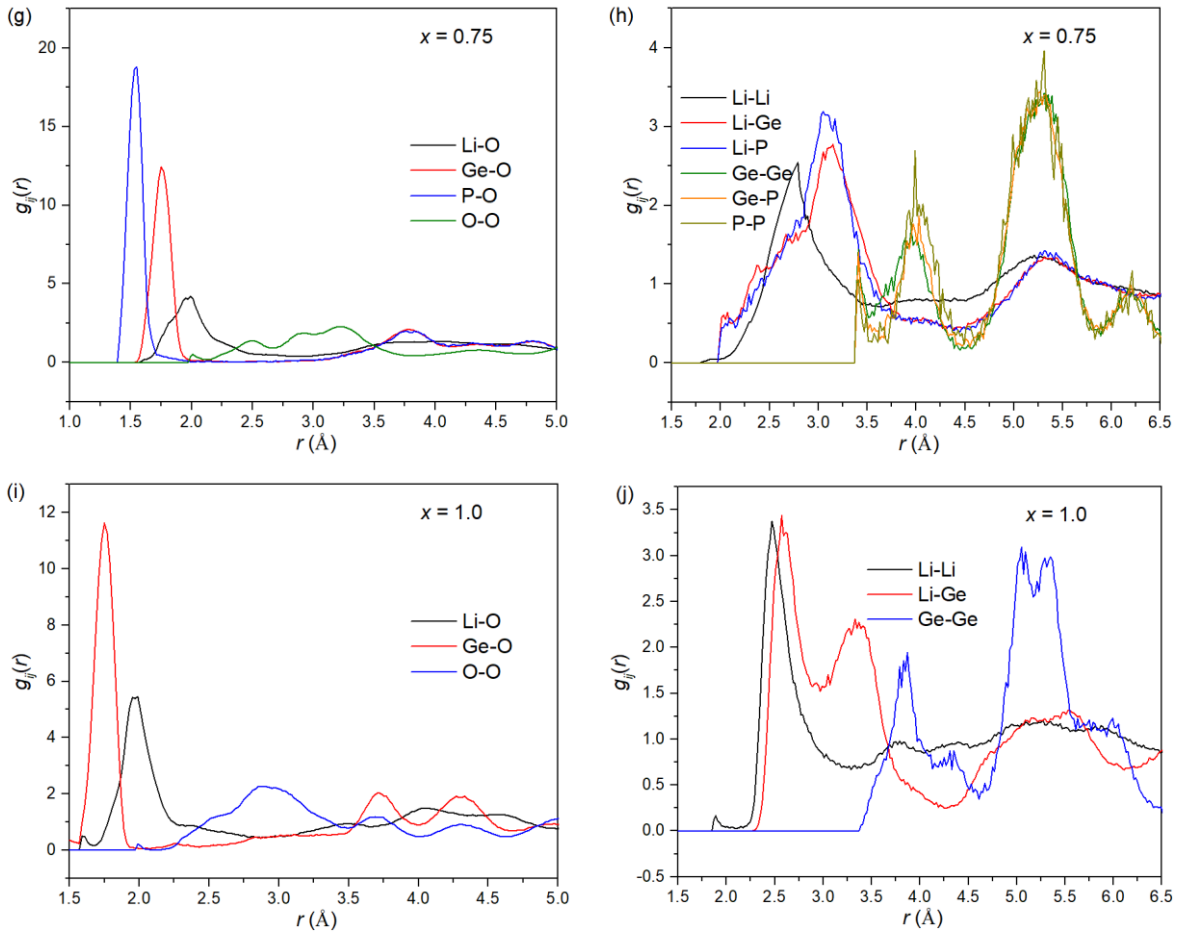

Figure 3.38 (left) $g_{MO}(r)$ and $g_{OO}(r)$, (right) $g_{MM}(r)$ pair correlation functions for (a, b) x = 0, (c, d) x = 0.25, (e, f) x = 0.50, (g, h)x = 0.75 and (i, j) x = 1.0 compositions in the $Li_{3+x}Ge_xP_{1-x}O_4$ system

Table 3.18 Summary of coordination numbers (CN) and modal and mean bond distances from the RMC analysis of x = 0.25, 0.50 and 0.75 compositions in $Li_{3+x}Ge_xP_{1-x}O_4$ system. Estimated standard deviations between the 10 parallel calculations are given in parentheses.

central atom	bonded atom	CN			Modal distance			Mean distance			Cut off (Å)
		x = 0.25	x = 0.50	x = 0.75	x = 0.25	x = 0.50	x = 0.75	x = 0.25	x = 0.50	x = 0.75	
Li	Li	8.985(11)	9.467(23)	9.934(20)	2.935(70)	2.777(15)	2.755(10)	2.76(95)	3.0455(18)	3.0280(14)	3.80
Li	Ge	1.0987(16)	2.2737(55)	3.4060(50)	3.116(45)	3.087(24)	3.124(14)	3.2007(27)	3.2418(25)	3.2914(8)	4.50
Li	P	3.3459(23)	2.2629(30)	1.1396(67)	3.065(6)	3.069(16)	3.120(36)	3.1604(9)	3.2292(27)	3.2839(44)	4.50
Li	O	4.1143(56)	4.1438(57)	4.1772(55)	1.943(3)	1.932(3)	1.975(3)	2.0024(8)	2.0397(7)	2.0721(7)	2.60
Ge	Li	14.282(20)	15.917(38)	17.030(24)	3.116(45)	3.087(24)	3.124(14)	3.2136(34)	3.2536(26)	3.3087(30)	4.50
Ge	Ge	0.550(20)	1.145(23)	1.690(17)	5.1(2.3)	3.972(49)	4.22(77)	3.988(19)	3.9628(90)	3.9173(58)	4.50
Ge	P	1.603(16)	1.055(15)	0.530(13)	3.997(39)	4.015(29)	4.007(44)	4.0246(60)	4.0076(57)	3.9646(82)	4.50
Ge	O	3.9812(57)	4.0310(71)	4.1574(70)	1.823(5)	1.814(2)	1.783(2)	1.7700(12)	1.7758(6)	1.7655(4)	2.00
P	Li	14.499(10)	15.839(21)	17.09(10)	3.065(6)	3.069(16)	3.120(36)	3.1736(9)	3.2376(35)	3.2916(52)	4.50
P	Ge	0.5342(56)	1.055(15)	1.590(38)	3.997(39)	4.015(29)	4.007(44)	4.0255(75)	4.0055(63)	3.9654(88)	4.50
P	P	1.5956(68)	1.077(13)	0.638(36)	4.017(14)	4.025(53)	4.00(79)	4.0364(32)	4.027(11)	4.019(24)	4.50
P	O	4.0000(5)	4.0274(44)	4.094(14)	1.548(2)	1.535(3)	1.509(5)	1.5610(2)	1.5601(5)	1.5574(13)	2.00
O	Li	3.3429(46)	3.6260(52)	3.9161(53)	1.943(3)	1.932(3)	1.975(3)	1.9974(9)	2.0349(7)	2.0692(7)	2.60
O	Ge	0.2488(4)	0.5039(9)	0.7795(14)	1.823(5)	1.814(2)	1.783(2)	1.7702(11)	1.7758(6)	1.7648(3)	2.00
O	P	0.7500(1)	0.5035(7)	0.2558(11)	1.548(2)	1.535(3)	1.509(5)	1.5610(2)	1.5606(6)	1.5590(17)	2.00
O	O	12.477(10)	12.1747(80)	11.7924(94)	2.474(2)	3.243(5)	3.264(7)	3.1106(8)	3.1199(7)	3.0988(6)	3.83

Fig. 3.39 shows plots of the O-M-O (M = Li, Ge, P) angular distribution functions (ADFs) and the average O-M-O ADF for the x = 0.25, 0.50 and 0.75 compositions in the $Li_{3+x}Ge_xP_{1-x}O_4$ system. For all three compositions, the ADFs exhibit distributions centred around ca 109º, consistent with predominantly tetrahedral geometry. Furthermore, the distribution ranges of O-Li-O are the widest and O-P-O are the narrowest, indicating that the LiO_4 tetrahedra have the largest degree of distortion and the PO_4 tetrahedra have the smallest degree of distortion, consistent with the smaller asymmetry values in the ^{31}P MAS-NMR spectra compared to those of ^{7}Li. It is also noteworthy that there is secondary O-Li-O distribution centred around 65º, which is discussed below. The broadness and asymmetry of O-Ge-O distribution compared to that for O-P-O confirms the non-identical nature of the coordination environment for Ge and P despite sharing the same crystallographic site.

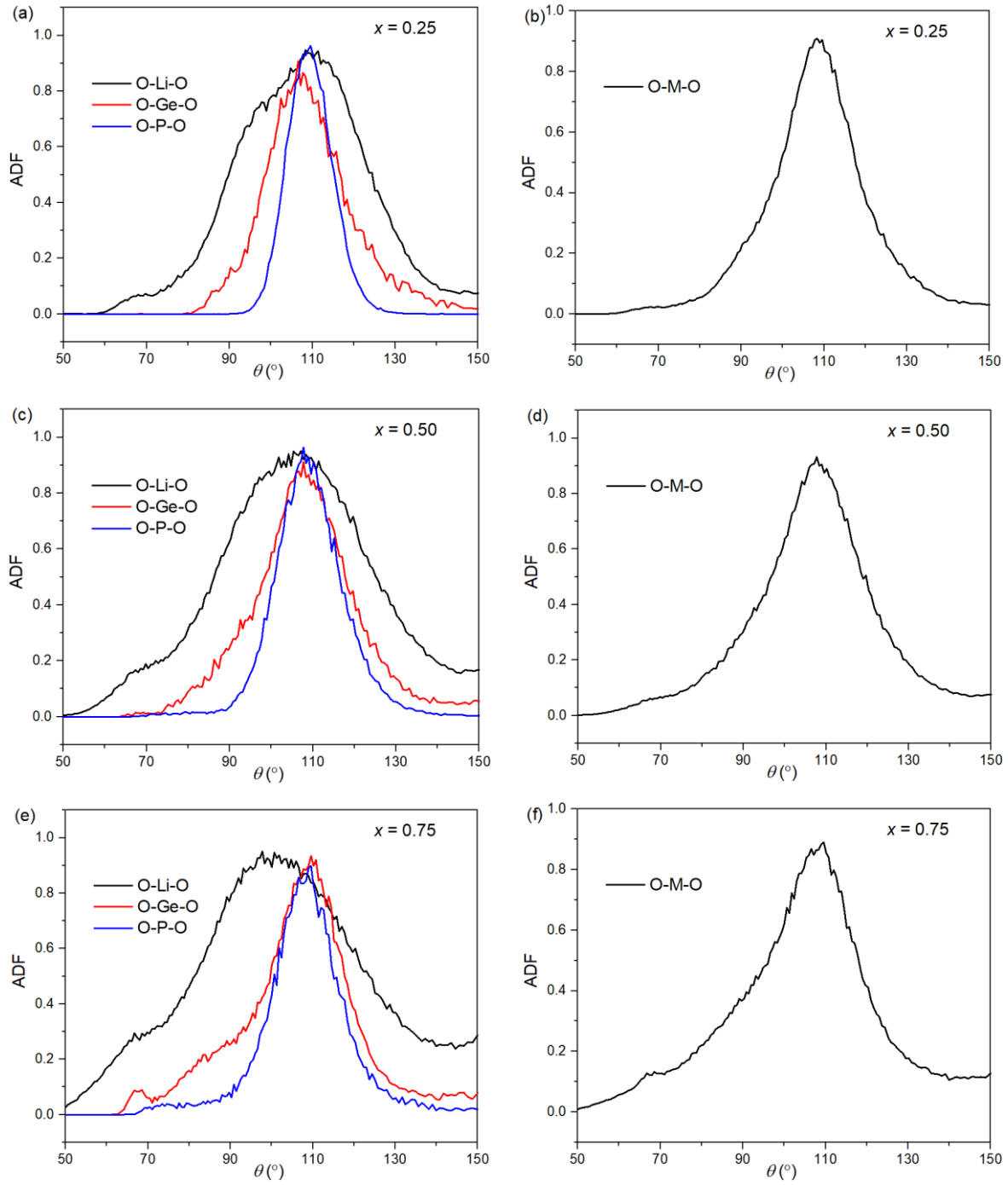

Figure 3.39 (left) O-M-O ADF, (right) averaged O-M-O AFD for (a, b) x = 0.25, (c, d) x = 0.50 and (e, f) x = 0.75 compositions in $Li_{3+x}Ge_xP_{1-x}O_4$

Within the distorted hexagonal close packed (hcp) array of oxide ions that make up the LISICON structure, there are 8 crystallographically distinct tetrahedral sites and 4 octahedral sites per four O^{2-} unit. Following the above description, these 8 tetrahedral sites are labelled as Li1, Li1a, Li2, Li2a, Li (Ge) and Li (Ge1a). Li1, Li1a, Li (Ge) and Li (Ge1a) have 4-fold

multiplicity (4c sites), while Li2 and Li2a have 8-fold multiplicity (8d sites). The octahedral sites are labelled as Li3, Li4, Li5 and Li6, all of which have 4-fold multiplicity. Table 3.19 summarises these sites in their ideal positions.

Table 3.19 Ideal positions of tetrahedral and octahedral sites in unit cell of the LISICON structure

tetrahedral sites					octahedral sites				
Atom	*x*	*y*	*z*	Site	Atom	*x*	*y*	*z*	Site
Li1	0.0707	0.25	0.6437	4*c*	Li3	0.2439	0.25	-0.0368	4*c*
Li1a	0.0707	0.25	0.8937	4*c*	Li4	0.0	0.0	0.50	4*c*
Li2	0.1606	0.0	0.3378	8*d*	Li5	0.0	0.0	0.0	4*c*
Li2a	0.1606	0.0	0.0878	8*d*	Li6	0.7561	0.75	0.5368	4*c*
Li (Ge)	0.4110	0.25	0.3203	4*c*	/				
Li (Ge1a)	0.4110	0.25	0.0703	4*c*					

Based on the ideal positions listed in Table 3.19, the Li atoms in each configuration were assigned to one of these sites based on their proximity to the nearest ideal position. Table 3.20 summarises the assigned tetrahedral and octahedral Li sites. Where no Li atom was found to be located in Li1 or Li2 sites, these were considered as tetrahedral vacancies Vac (Li1) and Vac (Li2), respectively. Table 3.21 summarises the numbers of Li1, Vac (Li1), Li2 and Vac (Li2) sites from the configurations. Figs. 3.40 and 3.41 show the percentage distributions of Li sites and vacancies derived from the data in Tables 3.20 and 3.21. As can be seen from the standard deviations, there is generally a consistent assignment of Li atoms to sites between the parallel configurations of the same composition. It can be seen that with increasing *x*-value in $Li_{3+x}Ge_xP_{1-x}O_4$, the occupancy of Li1 and Li2 sites decreases while the occupancy of Li1a, Li2a, Li3 and Li4 sites increases. Correspondingly, the number of tetrahedral vacancies Vac (Li1) and Vac (Li2) sites increases with increasing *x*-value, indicating the correlation between these vacancies and the introduced Li in the octahedral sites. In agreement with the Rietveld analysis, the numbers of Li3 and Li4 sites increase with increasing *x*-value. Interestingly, for $x = 0.50$

and 0.75 compositions, there is a small degree of occupation of the Li5 and Li6 octahedral sites. These sites are considered less energetically favoured due to their close proximity to the Ge/P-O4 tetrahedron. The occupation of the other tetrahedral sites Li (Ge) (i.e. substituting for Ge/P) and Li (Ge1a) (i.e. face sharing with the Ge/PO_4 tetrahedron) in all compositions is negligible.

Table 3.20 Summary of assigned tetrahedral and octahedral Li sites for compositions in the $Li_{3+x}Ge_xP_{1-x}O_4$ system. Values are averages over 10 parallel configurations. Estimated standard deviations between configurations are shown in parentheses.

atom	x = 0.25		x = 0.50		x = 0.75	
	No.	Li%	No.	Li%	No.	Li%
Li1	1465(7)	28.18(13)	1190(10)	21.28(18)	946(14)	15.89(23)
Li2	3132(6)	60.25(11)	2724(13)	48.74(24)	2337(26)	39.23(44)
Li1a	141(8)	2.70(14)	427(18)	7.64(32)	576(7)	9.68(12)
Li2a	77(5)	1.48(10)	485(15)	8.67(27)	656(24)	11.02(40)
Li3	233(3)	4.49(6)	377(9)	6.75(16)	481(13)	8.08(21)
Li4	150(2)	2.89(3)	286(9)	5.12(16)	598(14)	10.04(24)
Li5	0	0.00(0)	45(7)	0.80(12)	109(6)	1.83(11)
Li6	0.10(1)	0.00(1)	17(6)	0.30(11)	165(9)	2.77(16)
Li (Ge)	0.30(1)	0.01(1)	32(7)	0.57(12)	58(7)	0.98(11)
Li (Ge1a)	0	0.00(0)	8(2)	0.13(4)	29(5)	0.48(8)
Total Li	5198(1)	100	5589(4)	100	5955(6)	100

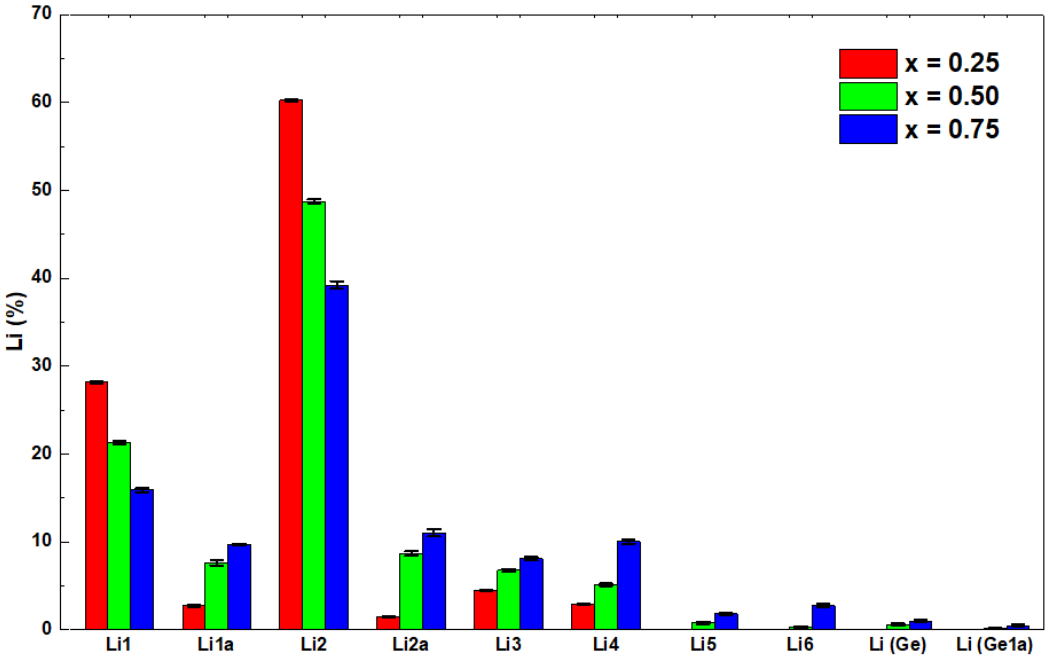

Figure 3.40 %Li distribution in octahedral and tetrahedral sites from RMC calculations for the $Li_{3+x}Ge_xP_{1-x}O_4$ compositions. Error bars indicate standard deviations between parallel configurations.

Table 3.21 Average numbers of occupied (Li1, Li2) and vacant (Vac (Li1), Vac (Li2)) framework Li tetrahedral sites in $Li_{3+x}Ge_xP_{1-x}O_4$ compositions. Values derived from RMC calculations on 10 parallel configurations.

atom	x = 0.25		x = 0.50		x = 0.75	
	No.	Li%	No.	Li%	No.	Li%
Li1	1465(7)	91.54(44)	1190(10)	74.34(64)	946(14)	59.15(85)
Vac (Li1)	135(7)	8.46(44)	411(10)	25.66(64)	654(14)	40.85(85)
Li2	3132(6)	97.87(18)	2724(13)	85.12(42)	2337(26)	73.01(81)
Vac (Li2)	68(6)	2.13(18)	476(13)	14.88(42)	864(26)	26.99(81)

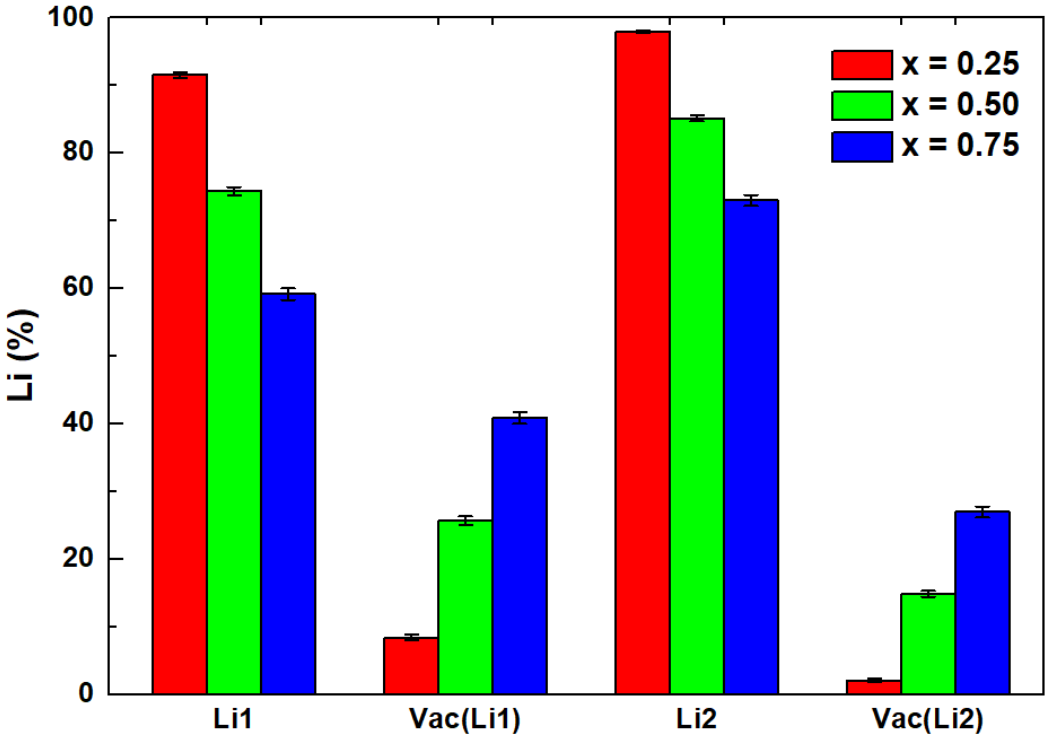

Figure 3.41 Percentages of occupied (Li1, Li2) and vacant (Vac (Li1), Vac (Li2)) framework Li tetrahedral sites in $Li_{3+x}Ge_xP_{1-x}O_4$ compositions. Error bars derived from RMC calculations on 10 parallel configurations.

A summary of coordination numbers and modal distances is given in Table 3.22 with the Li-O pair correlations for individual Li sites shown in Fig. 3.42. It is evident that that while Li1 and Li2 have coordination numbers near 4, Li1a and Li2a coordination numbers are always higher. In the case of $x = 0.25$, these are close to 5, indicating that the displaced Li in these sites is close to the shared face between two tetrahedra resulting in 5-coordination, a peculiar feature of hexagonal close packed structures. The coordination numbers of Li1a and Li2a decrease with increasing x-value, consistent with increased displacement into the interstitial sites as seen in the Rietveld analysis. This feature is also evident in an increase in the Li-O modal distance with increasing x-value for Li1a and Li2a. All the Li3, Li4, Li5 and Li6 show coordination numbers around 6, consistent with octahedral geometry.

Table 3.22 Summary of selected coordination numbers (CN) and modal contact distances (Å) for Li-O pairs in x = 0.25, 0.50 and 0.75 compositions of $Li_{3+x}Ge_xP_{1-x}O_4$ derived from RMC calculations.

centre	Bonded atom	CN			Peak			cutoff (Å)
		x = 0.25	x = 0.50	x = 0.75	x = 0.25	x = 0.50	x = 0.75	
Li1	O	4.34(1)	4.40(2)	4.50(2)	1.94(0)	1.92(0)	1.93(0)	2.75
Li2	O	4.28(1)	4.32(1)	4.24(1)	1.92(0)	1.91(0)	1.92(0)	2.74
Li1a	O	5.07(3)	4.80(3)	4.64(2)	1.84(1)	1.90(2)	1.93(0)	2.86
Li2a	O	5.04(7)	4.70(4)	4.51(3)	1.85(1)	1.86(0)	1.92(0)	2.84
Li3	O	6.39(4)	6.21(4)	6.03(3)	2.02(1)	1.92(1)	2.00(2)	3.05
Li4	O	6.11(3)	6.07(4)	6.06(5)	1.92(0)	1.95(1)	2.01(1)	3.06
Li5	O	/	6.14(8)	5.97(6)	/	1.94(1)	1.98(4)	3.05
Li6	O	/	6.10(13)	6.05(10)	/	1.97(5)	1.99(3)	3.13

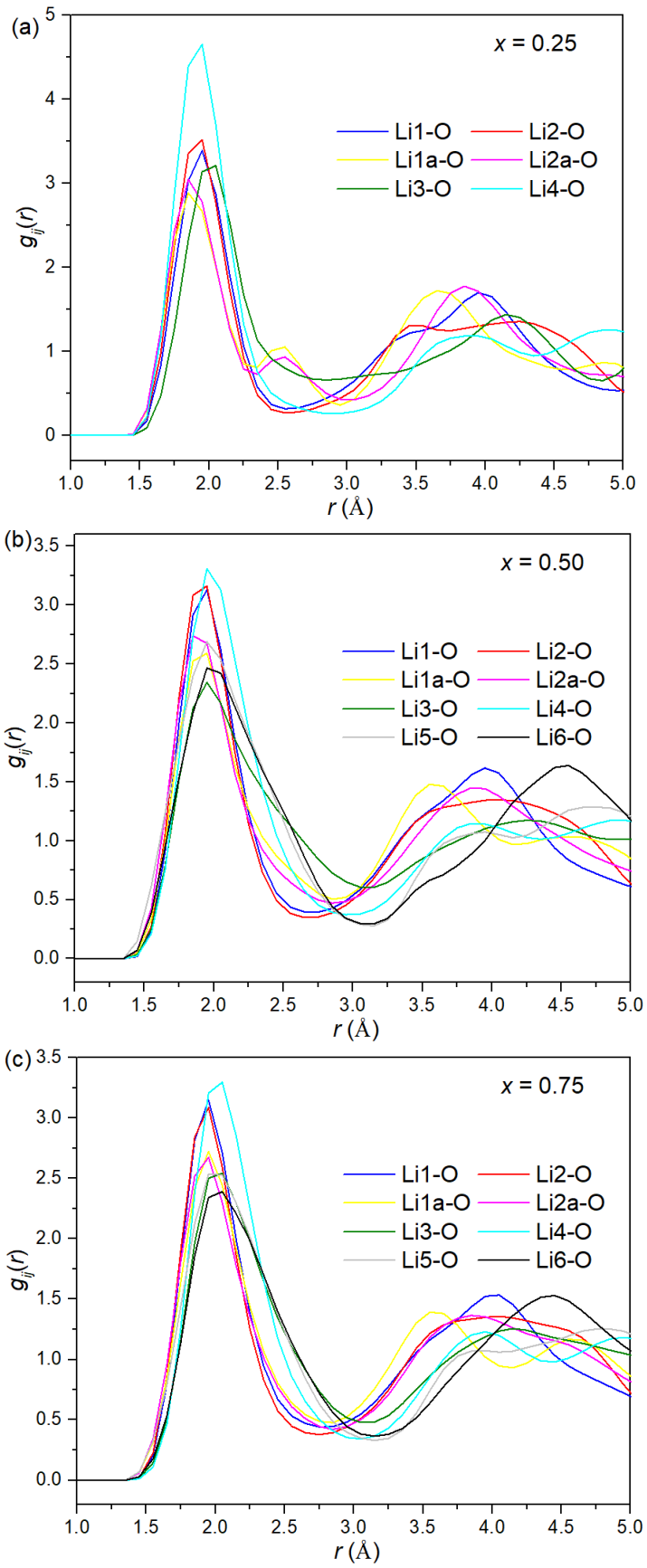

Figure 3.42 $g_{LiO}(r)$ pair correlation functions for (a) x = 0.25, (b) x = 0.50 and (c) x = 0.75 compositions in the $Li_{3+x}Ge_xP_{1-x}O_4$ system

The O-Li-O ADFs for the individual Li sites in the x = 0.25, 0.50 and 0.75 compositions are shown in Fig. 3.43. For the Li1, Li2, Li1a and Li2a atoms, a strong peak around 109° is observed, consistent with predominantly tetrahedral geometry. Interestingly, further distributions at around 90° and 70° are seen. The 90°peak is more prominent in the displaced sites Li1a and Li2a and is consistent with 5 coordinate geometry. The peak at around 65°, which is clearly visible in the plots for Li1 and Li2 can be attributed to the O atom furthest away in the neighbouring Li1a and Li2a sites. This also accounts for the slightly high coordination numbers for Li1 and Li2. For the six coordinate Li3, Li4, Li5 and Li6 sites, the distributions are all centred around 90°, consistent with octahedral geometry.

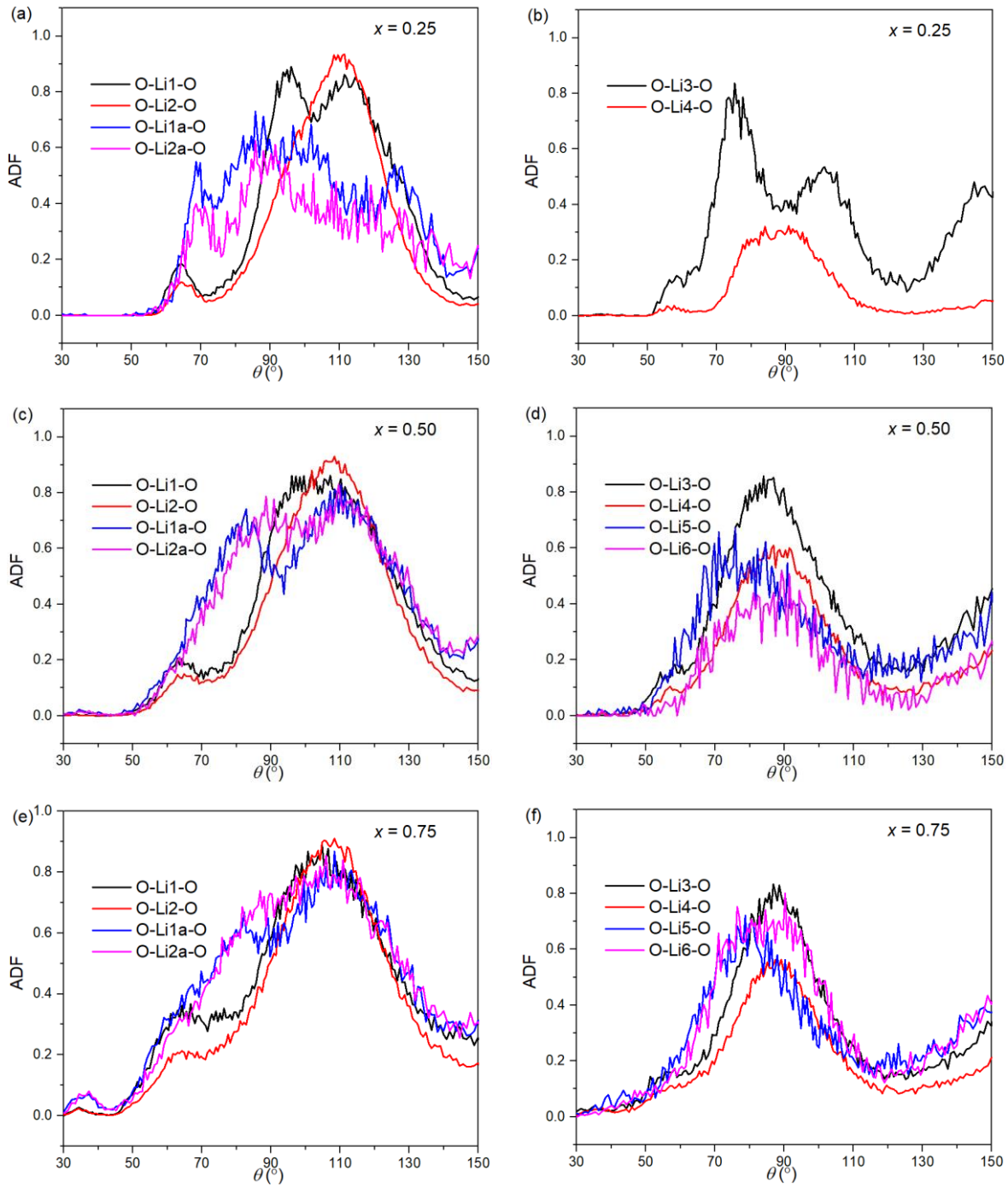

Figure 3.43 O-Li-O ADFs for (a) (b) x = 0.25, (c) (d) x = 0.50 and (e) (f) x = 0.75 compositions in the $Li_{3+x}Ge_xP_{1-x}O_4$ system

In order to examine the configurations for defects and defect clusters, it is helpful to look at the Li-Li pair correlations. Fig. 3.44 shows selected $g_{Li3\text{-}Li}(r)$ and $g_{Li4\text{-}Li}(r)$ pair correlation functions for the x = 0.25, 0.50 and 0.75 compositions in the $Li_{3+x}Ge_xP_{1-x}O_4$ system. A strong short correlation (ca. 1.9 to 2.0 Å) is seen between Li3 and Vac (Li2) with no such short

correlations between Li3 and Li2. Indeed, all contacts between Li3 and occupied Li sites (Li2, Li2a and Li1) are around 2.5 Å. Li4 shows strong correlations to both Vac (Li1) and Vac (Li2) at around 1.7 Å. For $x = 0.25$, there are short correlations at around 2.3 Å from Li4 to Li1a and Li2a as well as some occupied Li1 and Li2 sites. As x increases, these correlations lengthen to around 2.5 Å. This suggests that Li atoms in the Li4 sites are always associated with Li1 and Li2 vacancies, as well as some occupied Li1 and Li2 sites, suggesting that of the 2 Li1 and 2 Li2 tetrahedra that surround the Li4 sites, and at least some of each type are vacant. Table 3.23 summarises selected Li site occupancy ratios derived from the RMC calculations. It can be seen that the Li4:Li1a and Li4:Li2a ratios vary somewhat with composition, although at $x = 0.75$ the ratios suggest equal numbers of Li4, Li2a and Li1a. Thus, the RMC calculations are consistent with the Rietveld analysis in predicting the Type I and Type II defects.

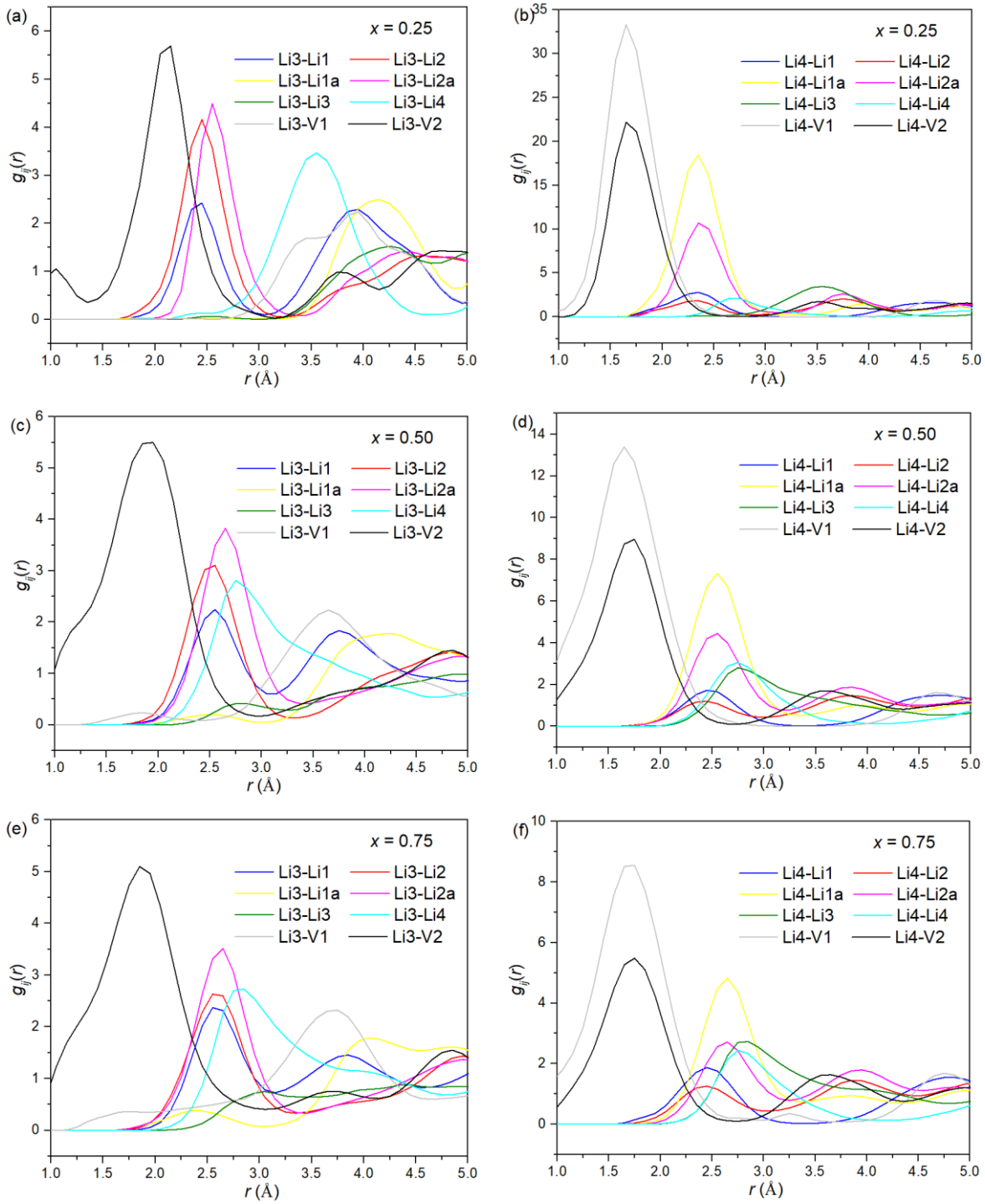

Figure 3.44 Selected (left) $g_{Li3Li}(r)$ and (right) $g_{Li4Li}(r)$ pair correlation functions for (a, b) x = 0.25, (c, d) x = 0.50 and (e, f) x = 0.75 compositions in the $Li_{3+x}Ge_xP_{1-x}O_4$ system

Table 3.23 Summary of selected Li site occupancy ratios derived from the RMC calculations in x = 0.25, 0.50 and 0.75 compositions in $Li_{3+x}Ge_xP_{1-x}O_4$ system

Ratios	x = 0.25	x = 0.50	x = 0.75
Li3:Li1a	1.65	0.88	0.84
Li3:Li2a	3.03	0.78	0.73
Li4:Li1a	1.06	0.67	1.04
Li4:Li2a	1.95	0.59	0.91
Li3:LI4	1.55	1.32	0.80

Interestingly, at x = 0.25, the main Li3-Li4 correlation appears at around 3.5 Å, but at x = 0.50 and 0.75 shifts considerably to around 2.7 Å. This suggests that at low levels of substitution, the Type I and Type II defects are independent, but as x-increases they form a larger defect cluster. As x increases, the proportion of available octahedral sites occupied increases such that at x = 0.75, 30% of the Li3 sites and 37% of the Li4 sites contain Li atoms. This means that there is a high likelihood of adjacent Li3 and Li4 sites being coupled in a larger cluster. The effect of this would lower the Li3:Li2a and Li4:Li2a ratios since ions in the 2a site would be shared between Li3 and Li4. This is indeed observed in Table 3.24. The approximate 1:1 ratio of Li3:Li4 at x = 0.75 suggests roughly equal numbers of these ions in the cluster and the simplest arrangement would involve 1 each of Li3, Li4, Li2a and Li1a (Fig. 3.45). This type of cluster we designate here as Type Ia and is similar to the cluster identified in $Li_{3.5}Ge_{0.5}V_{0.5}O_4$ (see ref [86] and Chapter 1).

Table 3.24 Summary of the selected coordination numbers (CN) and peaks for Li3 and Li4 atoms in x = 0.25, 0.50 and 0.75 compositions in $Li_{3+x}Ge_xP_{1-x}O_4$ system

centre	Bonded atom	CN			peak			cutoff (Å)
		x = 0.25	x = 0.50	x = 0.75	x = 0.25	x = 0.50	x = 0.75	
Li3	Li1	1.01(1)	1.08(3)	0.93(3)	2.43(1)	2.54(1)	2.57(2)	3.13
Li3	Li2	3.90(1)	3.15(3)	2.59(5)	2.44(0)	2.53(2)	2.60(4)	3.22
Li3	Li1a	0.00(0)	0.03(1)	0.09(2)	3.30(91)	2.50(16)	2.43(13)	2.94
Li3	Li2a	0.10(1)	0.80(4)	0.98(4)	2.54(3)	2.65(1)	2.64(3)	3.40
Li3	Li3	0.01(1)	0.10(2)	0.22(2)	3.29(78)	2.80(12)	2.98(11)	3.33
Li3	Li4	0.46(3)	0.71(5)	1.44(6)	3.54(11)	2.74(8)	2.79(3)	3.82
Li3	V1	0.00(0)	0.02(1)	0.12(2)	3.38(61)	1.83(16)	3.22(3.28)	2.50
Li3	V2	0.10(1)	0.85(3)	1.47(6)	2.13(7)	1.89(10)	1.88(4)	3.20
Li4	Li1	1.27(5)	0.76(3)	0.66(3)	2.35(1)	2.47(4)	2.46(2)	3.49
Li4	Li2	2.06(4)	1.50(3)	1.31(4)	2.34(2)	2.41(6)	2.44(1)	3.15
Li4	Li1a	0.74(5)	1.21(5)	1.17(2)	2.34(3)	2.55(1)	2.65(1)	3.20
Li4	Li2a	0.24(3)	0.89(5)	0.80(4)	2.37(3)	2.53(3)	2.64(2)	3.22
Li4	Li3	0.71(5)	0.93(6)	1.16(4)	3.54(11)	2.74(8)	2.79(3)	3.82
Li4	Li4	0.16(1)	0.52(4)	0.92(4)	2.66(7)	2.72(9)	2.74(3)	3.94
Li4	V1	0.73(5)	1.20(3)	1.41(7)	1.21(66)	1.64(4)	0.93(70)	3.52
Li4	V2	0.24(2)	0.87(3)	1.01(2)	1.67(5)	1.72(5)	1.73(5)	2.77

Figure 3.45 Proposed Type Ia defect for x = 0.75 in the $Li_{3+x}Ge_xP_{1-x}O_4$ system

3.4 Conclusions

A solid solution, isostructural with the end member γ-Li_3PO_4 in space group *Pnma* (No. 62), can be formed in the compositional range of $0.00 \leq x \leq 0.90$ in the $Li_{3+x}Ge_xP_{1-x}O_4$ system. The unit cell parameters exhibit a general increase due to the larger ionic radius of Ge^{4+} (0.39 Å) compared to that of P in the pentavalent state (0.17 Å). The solid solution mechanism involves substitution of pentavalent P by tetravalent Ge on a shared tetrahedral site, with charge balance maintained by additional Li^+ occupying predominantly two interstitial octahedral sites to the γ-Li_3PO_4 structure.

^{7}Li MAS-NMR spectra reveal two resonances that become increasingly deshielded with increasing level of substitution. Both show high asymmetry, |with the least shifted resonance mainly attributed to Li2/Li2a, and the most shifted resonance attributed to the Li1/L1a and the additional octahedral Li. Two resonances are also seen in the ^{31}P MAS-NMR spectra of intermediate compositions, which show increased deshielding with increasing *x*-value, but with lower asymmetry than for the Li species.

Combined X-ray and neutron diffraction analysis shows that in the intermediate compositions $x = 0.25$, 0.50 and 0.75, all exhibit disorder in the Li^+ ion sublattice. To be specific, there is partial occupancy of the Li1 and Li2 sites, with some of the ions from these sites displaced in the *c*-axis direction towards or into the neighbouring face-sharing interstitial tetrahedral sites (Li1a and Li2a, respectively). The displaced Li1a remains within the same tetrahedron throughout the compositional range while the displacement of Li2 to Li2a increases with increasing *x*-value. While two types of octahedral site are found to be occupied in the Rietveld analysis (Li3 and Li4), the total scattering analysis suggests low levels of occupancy of other octahedral sites at high *x*-values. All the compositions contain more occupied Li3 than Li4 sites, and both the octahedral Li3 and Li4 sites increase their occupancy with increasing *x*-value at roughly the same rate. Three types of defect clusters are proposed, Type I involves Li^+

ions in the Li3 site and displaced Li2a from a neighbouring Li2 site towards an empty tetrahedral site, Type II consists of an Li^+ ion in the Li4 site with a Li1 ion displaced into Li1a and a Li2 ion displaced into Li2a. Type III is a larger defect cluster involving two Type I and one Type II defects.

RMC modelling of neutron total scattering data revealed how the defect structure evolves. At low levels of substitution, the Type I and Type II defects are independent, but as *x*-increases they form a larger defect cluster involving at least one Type I defect and one Type II defect.

VT-XRD measurements show no first-order phase transitions up to 700 °C, but the thermal variation of lattice parameters reveals a change at around 250 °C, which might be attributable to a change in Li^+ distribution, i.e. a change in the defect clustering. In the absence of high temperature neutron data, the details of this transition remain somewhat speculative.

The highest lithium ion conductivity was seen in the $x = 0.75$ composition with a total conductivity of 1.83×10^{-2} S cm^{-1} at 250 °C, which shows the highest concentrations of interstitial Li^+ ions and extensive defect clustering.

Chapter 4 Structure and conductivity in the $Li_{4-2x}Ge_{1-x}Mo_xO_4$ system

4.1 Introduction

In the family of LISICON structures, in general, two types of lithium ions are involved according to the formula $Li_{3+x}MO_4$, three Li^+ ions are located in tetrahedral sites and x Li^+ ions are located in the octahedral sites, with the x-value determined by the charge of M ions. In other words, the types of M ions will determine the concentration of occupied octahedral sites. As investigated in the $Li_{3+x}Ge_xP_{1-x}O_4$ system (Chapter 3), the octahedral Li3 and Li4 sites play a key role in constructing the local defect clusters. Currently among the reported work in $Li_{3+x}MO_4$ type systems, the M species are mainly focused on the M^{4+} (M = Si, Ge, Ti) and M^{5+} (M = P, As, V) cations. W^{6+} has been reported as being incorporated into a LISICON type structure in $Li_{3.7}Ge_{0.85}W_{0.15}O_4$ [163]. This composition is part of the $Li_{4-2x}Ge_{1-x}W_xO_4$ system which is investigated in detail in Chapter 5, including the optimization of calcination conditions, the limit of solid solution, the compositional variation of conductivity and the use of Molecular Dynamics in simulating the conductivity. Doping of small amounts of Mo^{6+} into a LISICON type system has also been reported in $Li_{3.17}(P_{0.69}Ge_{0.24}Mo_{0.07})O_4$, which was synthesized by a flux method under a direct current electric field [164].

Earlier studies showed that the solid solution $Li_{3.5}Si_{0.75}Mo_{0.25}O_4$ exhibits a γ-LISICON structure in the Li_4SiO_4 -Li_2MoO_4 system and had a conductivity of ~3×10^{-7} S cm^{-1} at room temperature with the replacement mechanism of $2Li^+ + Si^{4+} \leftrightarrow Mo^{6+}$ [165]. Similarly, $Li_{3.4}Ge_{0.7}Mo_{0.3}O_4$ with the γ-LISICON structure also can be effectively formed in the Li_4GeO_4 -Li_2MoO_4 system with a reasonably high bulk conductivity of ~2.25×10^{-7} S cm^{-1} at 0 °C [149].

Based on the previous work and our systematic work on the $Li_{4-2x}Ge_{1-x}W_xO_4$ system, it can be concluded that Mo^{6+} is likely to form a LISICON type solid solution in a similar way to W^{6+} through a classical solid-state reaction. If so, then questions arise as to how extensive would this solid solution be, how does the local defect structure compare to other LISICON systems

and how does the conductivity compare to other LISICON systems? With these questions in mind, the Li_2MoO_4-Li_4GeO_4 system is investigated systematically in this chapter.

4.2 Experimental

4.2.1 Sample synthesis

Samples of composition $Li_{4-2x}Ge_{1-x}Mo_xO_4$ ($0.0 \leq x \leq 1.0$) were prepared using a classical solid-state reaction. Stoichiometric amounts of Li_2CO_3 (99%, BDH Chemicals), GeO_2 (99.999%, Aldrich Gold) and MoO_3 (99.5%, Sigma-Aldrich) were ground thoroughly in an agate mortar to form a homogenous paste with methylated spirits. After drying the paste thoroughly at 80 °C, the mixtures were heated in an alumina crucible at 650 °C for 1 h followed by calcining at temperatures between 650 and 850 °C for various times up to 24 h. Samples were slow cooled in the furnace to room temperature. Various conditions were tried to optimise the purity of the different compositions with specific details of those used to prepare the final compositions summarised in Table 4.1.

Table 4.1 Summary of preparation conditions used to prepare $Li_{4-2x}Ge_{1-x}Mo_xO_4$ samples

x	Conditions
0.1, 0.2, 0.3	650 °C for 1 h and 750 °C for 24 h
0.4	650 °C for 1 h and 650 °C/700 °C/750 °C/800 °C/850 °C/900 °C for 24 h
0.5	650 °C for 1 h and 650 °C/700 °C/725 °C/750 °C/800 °C/850 °C for 24 h
0.6	650 °C for 1 h and 750 °C for 24 h
1.0	650 °C for 25 h

The as-prepared powders were used to make pellets through spark plasma sintering (SPS) (HPD 25/1, FCT, Rauenstein, Germany). Samples were pressed into a graphite die with 10 mm diameter surrounded by carbon foil. The resulting powder was then sintered at 600 to 800 °C for 5 min at a uniaxial pressure of 60 MPa under vacuum. SPS processed samples were

subsequently annealed at 600 to 850 °C for 11-20 h to remove residual carbon arising from the carbon foil. Table 4.2 summarises the sintering conditions used for each composition.

Table 4.2 Summary of SPS sintering conditions used to prepare $Li_{4-2x}Ge_{1-x}Mo_xO_4$ pellets

x	Sintering conditions	density%
x = 0.1	750 ºC for 5 min, anneal at 750 ºC for 8 h	> 98%
x = 0.2	800 ºC for 5 min, anneal at 700 ºC for 11 h	> 99%
x = 0.3	800 ºC for 5 min, anneal at 750 ºC for 12 h	> 99%
x = 0.4	800 ºC for 5 min, anneal at 850 ºC for 20 h	> 98%
x = 0.5	600 ºC for 5 min, anneal at 600 ºC for 11 h	> 99%
x = 1.0	600 ºC for 5 min, anneal at 650 ºC for 16 h	> 95%

4.2.2 Characterization

The density of ceramics pellets was measured based on the classical Archimedes method by displacement of water. X-ray powder diffraction (XRD) was used to characterize the crystallographic structure of samples. The XRD data were collected on a PANAlytical X'Pert Pro diffractometer, equipped with an X'Celerator detector, in θ/θ geometry using Ni-filtered Cu-Kα radiation (λ = 1.5418 Å), over the 2θ range 5° to 120° in steps of 0.0334° per step, with an effective count time of 200 s per step. Elevated temperature measurements were performed using an Anton-Paar HTK 1200 high temperature camera. Data were collected in flat plate θ/θ geometry on a Pt coated sample holder. Calibration was carried out with an external LaB_6 standard. Diffraction patterns were acquired at room temperature and at 50 °C intervals from 50 °C to 750 °C, over the 2θ range 5–120° in steps of 0.033° per step, with an effective scan time of 50 s per step. The XRD data were analysed using the Rietveld method through the GSAS suite of programs [122]. The starting models were based on the structures of $Li_{3.5}Zn_{0.5}GeO_4$ [84], β-Li_3PO_4 [166] and Li_2MoO_4 [167]. The microstructure of the ceramic pellets was

examined through scanning electron microscope (SEM), using an FEI Inspect F (Hillsboro, OR).

Neutron total scattering data at room temperature were collected on the Polaris diffractometer at the ISIS Facility, Rutherford Appleton Laboratory, on back-scattering (average angle 146.72°), 90° (average angle 92.59°), intermediate-angle (average angle 52.21°), low-angle (average angle 25.99°) and very low angle (average angle 10.40°) detectors, corresponding to the approximate d-spacing ranges 0.04–2.6 Å, 0.05–4.1 Å, 0.73–7.0 Å, and 0.13–13.8 Å and 0.3–48 Å, respectively. The x = 1.0 sample was loaded in an 11 mm diameter thin walled vanadium can, located in front of the back-scattering detectors with data collections corresponding to proton beam charges of ca. 1000 μA h to allow for total scattering analysis. For room temperature measurements of x = 0.2 and 0.5, the sample was sealed in a silica tube and placed inside a thin walled vanadium can with data collections of 1000 and 500 μA h, respectively. For total scattering data correction, diffraction data were collected on an empty 11 mm diameter thin walled (0.05 mm wall thickness) vanadium can and a sealed silica tube inside a thin walled vanadium for ca. 600 μA h at room temperature. For elevated temperature measurements on x = 0.2, data were collected at 50 °C intervals from 300 °C to 700 °C with short data collections of 30 μA h carried out at the intermediate temperatures and long data collections of 1000 μA h at 700 °C. Data were summed, normalised and corrected using Gudrun [125]. The total pair correlation function $G(r)$ and the normalised total scattering structure factors $S(Q)$ were fitted by reverse Monte Carlo modelling using the program RMCProfile [127]. In each case, supercell configurations, in $P1$ symmetry, generated from the refined structures were used as starting models. For x = 0.2, a 5 × 8 × 10 supercell was used, while for x = 0.5 the supercell was 8 × 10 × 10. For the x = 0.2 composition, which showed a disordered structure, full occupancies were assumed for Li1 and Li2 and Li1a and Li2a were omitted. 10 random configurations were generated. In all cases, 10 sets of parallel calculations were performed

under periodic boundary conditions to yield satisfactory statistics on the radial distribution functions and allow for the calculation of standard deviations. The Bragg scattering data were used as a constraint on the long-range crystallinity. Pseudo-potential constraints were used for Ge-O, Mo-O and O-O as well as other Li-M long-range correlations in some cases. In the case of the $x = 0.2$ composition, a Li-O constraint was required to model the low-r Li-O distribution. This constraint constituted of an idealised $g_{LiO}(r)$ distribution, up to 1.94 Å (just before the Li-O peak apex), based on the Rietveld analysis and smoothed over 40 cycles. Soft bond valence sum constraints were applied.

For the impedance measurements, annealed ceramic pellets were first cut and polished into blocks of ca. 4 mm × 4 mm × 2 mm. Gold electrodes were sputtered by cathodic discharge. Electrical characterisation was carried out by a.c. impedance spectroscopy using a fully automated system based on a Solartron 1255 frequency response analyser in conjunction with a bespoke automatic current/voltage converter. Impedance data were collected over the frequency range 0.1 Hz to 1×10^6 Hz, in the approximate temperature range 50 to 300 °C over two cycles of heating and cooling. Fitting of impedance data was carried out using the program WFIRDARMM [159, 160].

4.3 Results and discussion

4.3.1 Solid solution formation

To explore solid solution formation in the Li_2MoO_4-Li_4GeO_4 system, the solid solution limit was first investigated. According to the formula $Li_{4-2x}Ge_{1-x}Mo_xO_4$, with increased Mo content, less lithium sites are required to compensate for the adding of positive charge. Fig.4.1 shows the XRD patterns for the $0.1 \leq x \leq 0.5$ compositions and the two end-members Li_2MoO_4 and Li_4GeO_4. As can be seen, all compositions exhibited good crystallinity. Compared to the two end-members, it can be seen that the intermediate compositions $0.1 \leq x \leq 0.5$ exhibit patterns

consistent with the γ-LISICON structure and different to the two end members. At x = 0.4 and 0.5, peaks corresponding to the end member Li_2MoO_4 are evident. Therefore, similar to the Li_2WO_4-Li_4GeO_4 system, a distinct orthorhombic structure in space group *Pnma* (No. 62) is formed between the orthorhombic Li_4GeO_4 in space group *Cmcm* (No. 63) and rhombohedral Li_2MoO_4 in space group *R*-3 (No. 148).

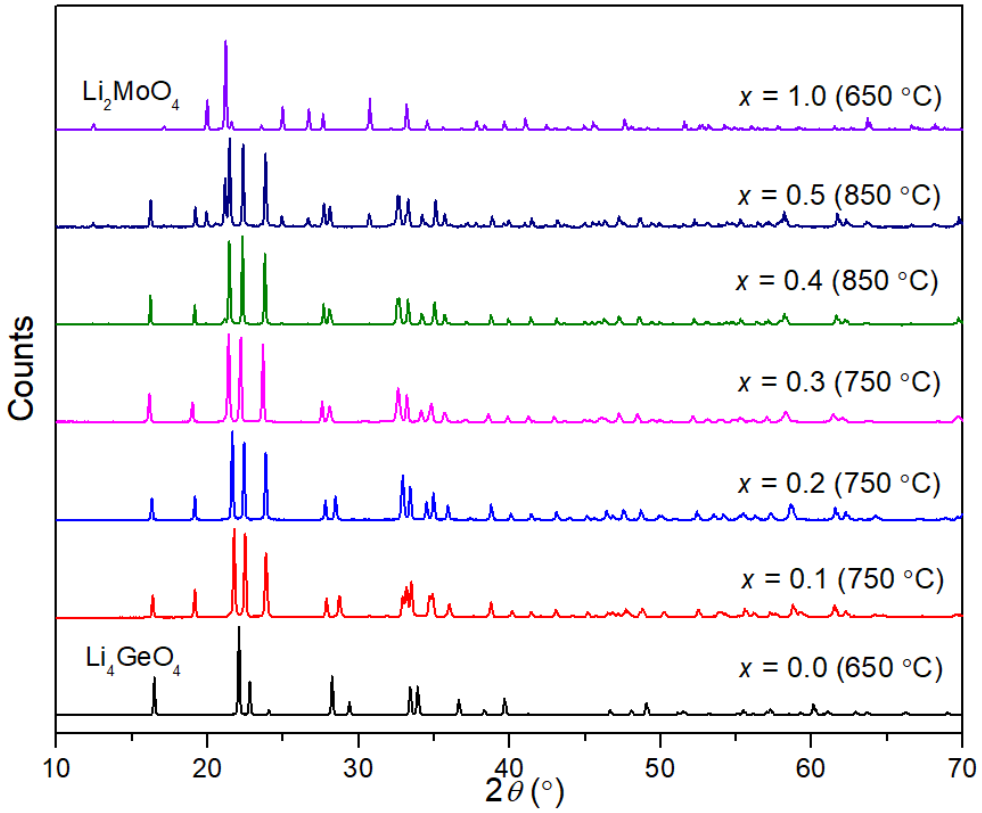

Figure 4.1 XRD patterns for selected compositions in the $Li_{4-2x}Ge_{1-x}Mo_xO_4$ system

The refined unit cell parameters for the $Li_{4-2x}Ge_{1-x}Mo_xO_4$ system are listed in Table 4.3, with the corresponding plots in Fig. 4.2. The unit cell volume in the $Li_{4-2x}Ge_{1-x}Mo_xO_4$ series shows a general linear increase with increasing x-value over $0.1 \leq x \leq 0.4$, with the unit cell volume of composition $Li_{3.2}Ge_{0.6}Mo_{0.4}O_4$ (x = 0.4) reaching 358.00(2) $Å^3$ compared to 352.42(4) $Å^3$ for $Li_{3.8}Ge_{0.9}Mo_{0.1}O_4$ (x = 0.1), an increase of around 1.6 %. This can be mainly attributed to the ionic radius of Mo^{6+} (0.41 Å) which is slightly bigger than that of Ge^{4+} (0.39 Å) when both of them are 4-coordinated [161]. This trend is reflected in the compositional variation of the *a* and *b*

axes, with a slight decrease in the *a*-axis parameter at $x = 0.30$. However, a gradual decrease in the *c*-axis with increasing *x*-value over $0.1 \leq x \leq 0.5$ is also present.

In the $Li_{4-2x}Ge_{1-x}Mo_xO_4$ system, to maintain charge balance, with increased Mo^{6+} content in the $(Li_3Ge_{1-x}Mo_xO_4)^{(1-2x)-}$ skeleton, the interstitial octahedral lithium ions are gradually eliminated to compensate for the loss of positive charge. When $x = 0.5$, the formula is $Li_3Ge_{0.5}Mo_{0.5}O_4$ and theoretically no interstitial lithium ions are present. According to the discussion in Chapter 1, the interstitial octahedral lithium ions (Li3 and Li4) can cause the tetrahedral Li1 and Li2 ions to be displaced to some extent along the *c*-axis. In other words, the less occupied the interstitial octahedral sites are, the less distortion in the Li1/Li2 tetrahedra. Therefore, the gradual decrease in *c*-axis with increasing *x*-value over $0.1 \leq x \leq 0.5$ can be attributed to the decreased distortion along the *c*-axis. The similar unit cell volumes of $Li_3Ge_{0.5}Mo_{0.5}O_4$ ($x = 0.5$) and $Li_{3.2}Ge_{0.6}Mo_{0.4}O_4$ ($x = 0.4$) and the appearance of weak peaks associated with Li_2MoO_4 in the XRD pattern for the $x = 0.4$ composition suggest that based on the conditions used the solid solution limit for the γ-phase lies between $x = 0.3$ and 0.4.

Table 4.3 Refined lattice parameters for studied compositions in the $Li_{4-2x}Ge_{1-x}Mo_xO_4$ system

composition	*a* (Å)	*b* (Å)	*c* (Å)	unit cell volume (Å^3)
$x = 0.1$	10.9278(5)	6.2458(3)	5.1635(2)	352.42(4)
$x = 0.2$	10.9419(3)	6.2973(2)	5.1506(1)	354.90(3)
$x = 0.3$	10.9323(4)	6.3374(2)	5.1458(2)	356.51(3)
$x = 0.4$	10.9638(3)	6.3660(2)	5.1293(1)	358.00(2)
$x = 0.5$	10.9746(6)	6.3674(4)	5.1236(3)	358.04(4)

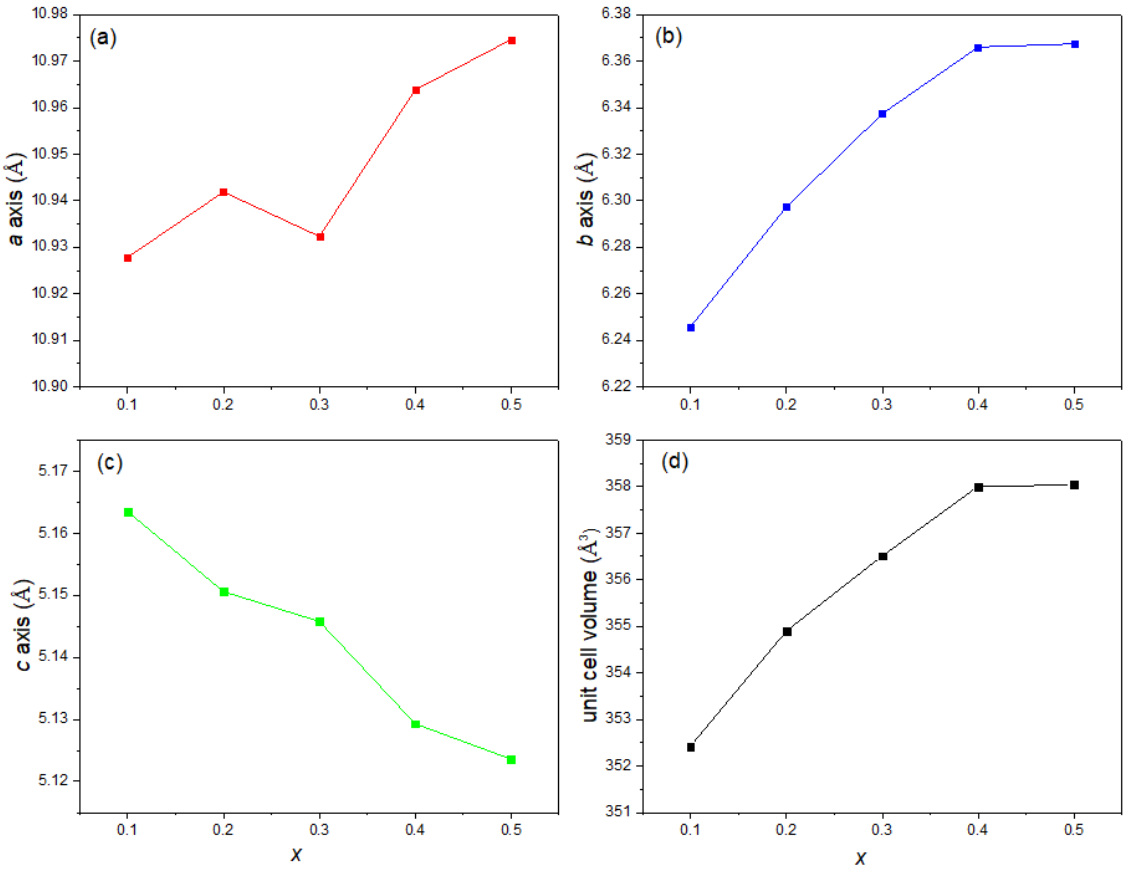

Figure 4.2 Variation of unit cell parameters (a) *a*, (b) *b*, (c) *c* and (d) unit cell volume with composition in the $Li_{4-2x}Ge_{1-x}Mo_xO_4$ system. Error bars are smaller than the symbols used.

During the synthesis, it was noted that the LISICON β-phase structure in space group $Pmn2_1$ (No. 31) appeared at different stages for these compositions. At a calcination temperature of 750 ºC, the x = 0.1, 0.2 and 0.3 compositions all yielded a pure γ-phase after 24 h. However, for the x = 0.4 composition, a mixture of β and γ phases were observed under the same conditions. Experiments on this composition at different calcination temperatures (Fig. 4.3) showed that at 650 ºC, the β phase is relatively dominant, with the ratio of γ:β phases increasing with increasing calcination temperature, until at 850 ºC, a complete transformation to the γ-phase is achieved, although accompanied by the appearance of a small amount of Li_2MoO_4. On increasing the calcination temperature further to 900 ºC, increased precipitation of Li_2MoO_4 is seen. Therefore, a calcination temperature of 850 ºC was used in the final preparation.

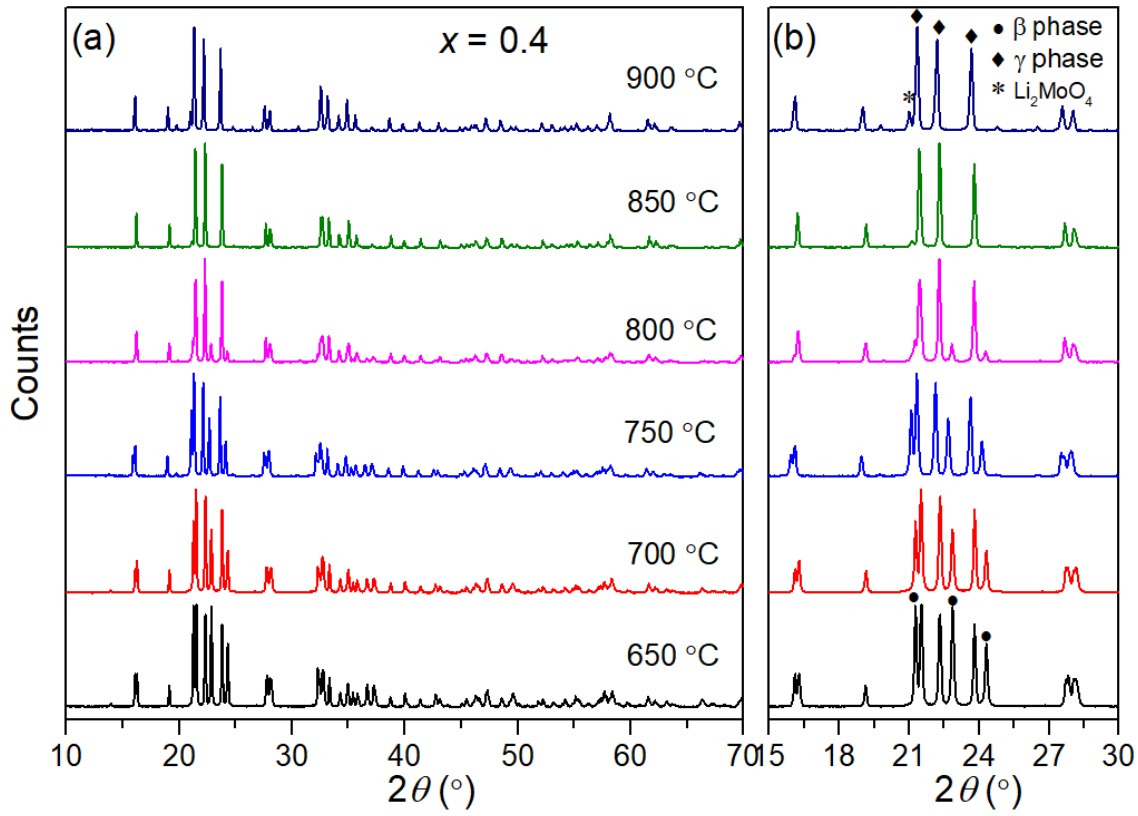

Figure 4.3 XRD patterns of the x = 0.4 composition in the $Li_{4-2x}Ge_{1-x}Mo_xO_4$ system calcined at selected temperatures for 24 h

A similar study was carried out with the x = 0.5 composition (Fig. 4.4). A pure β-phase is seen at 650 ºC and remains the dominant phase on increasing temperature up to 800 ºC. The amount of γ-phase increases over this temperature range and on increasing the temperature to 850 ºC, the γ-phase completely replaces the β-phase, but is accompanied by the appearance of a significant amount of Li_2MoO_4. The powders were found to melt at temperatures above 850 ºC.

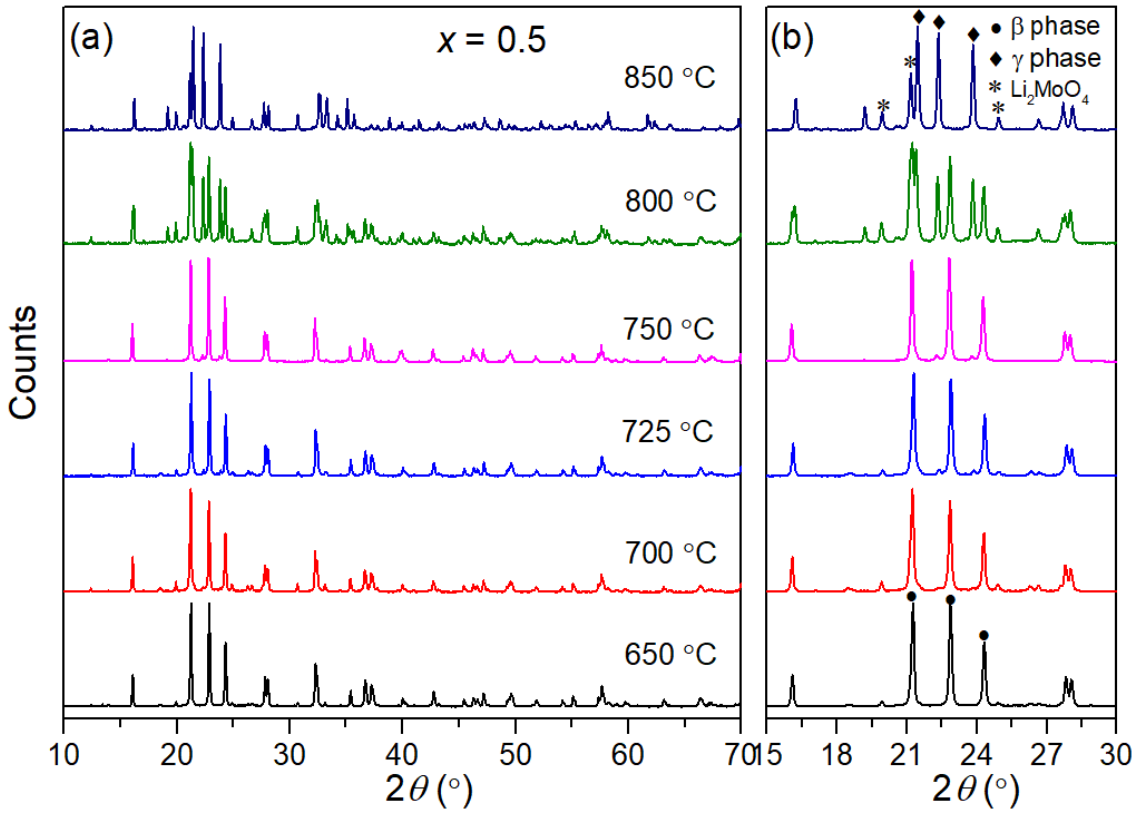

Figure 4.4 XRD patterns of the x = 0.5 composition in the $Li_{4-2x}Ge_{1-x}Mo_xO_4$ system calcined at selected temperatures for 24 h

Comparing the temperature range for the existence of the β-phase and the γ-phase for compositions of $0.1 \leq x \leq 0.5$, it can be concluded that with increased x-value in $Li_{4-2x}Ge_{1-x}Mo_xO_4$, the ratio of the β-phase to the γ-phase decreases with increasing temperature. To obtain the γ-phase in high x-value compositions, high calcination temperatures are required, but this comes at the expense of purity with the appearance of Li_2MoO_4.

To see whether the β-phase solid solution extends beyond x = 0.5, the x = 0.6 composition was synthesised. The XRD pattern of this composition is shown in Fig. 4.5. The sample shows a mixture of Li_2MoO_4 and a β-phase, presumed to be β-$Li_3Ge_{0.5}Mo_{0.5}O_4$. This is perhaps unsurprising as in order to maintain a solid solution, vacancies would need to be introduced into the tetrahedral framework, which is likely to be energetically unfavourable.

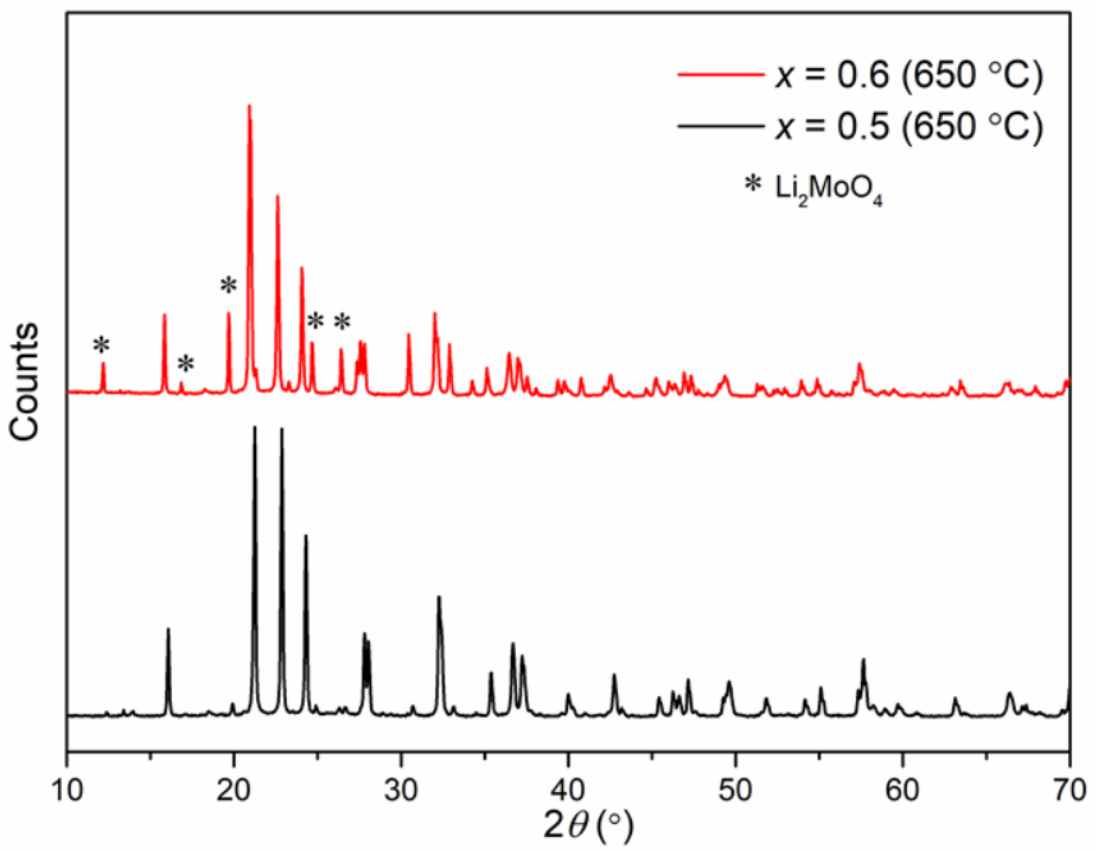

Figure 4.5 XRD patterns of the x = 0.5 and 0.6 composition in the $Li_{4-2x}Ge_{1-x}Mo_xO_4$ system synthesized under the same conditions for 24h

4.3.2 Thermal variation of structure

To check the structural thermal variation, VT-XRD was employed for x = 0.1, 0.2, 0.3, 0.4 and 0.5 compositions in the $Li_{4-2x}Ge_{1-x}Mo_xO_4$ system. The VT-XRD patterns over the temperature range 25 to 750 °C during heating and cooling are shown in Fig. 4.6 to 4.10 along with plots of the thermal variation of lattice parameters.

For the x = 0.1 composition in Fig. 4.6, the LISICON phase is preserved throughout heating and cooling. However, on heating up to 350 °C, a small amount of a second phase, $Li_6Ge_2O_7$, appears. The amount of this second phase diminishes at 750 °C, and on cooling the amount of $Li_6Ge_2O_7$ remains negligible level up to room temperature. This phase separation is evident in the lattice parameter variation on heating, which shows a discontinuity at around 250 °C on

heating, which is not seen on cooling. The thermal expansion of unit cell volume is non-linear and reveals evidence for a subtle change at around 500 °C.

For the $x = 0.2$ composition in Fig. 4.7, no obvious changes in structure are evident up to 750 °C and plots of lattice parameters are fully reproducible on heating and cooling. As with the $x = 0.1$ composition, non-linearity in the plot of thermal expansion of unit cell volume reveals evidence for a subtle change; this time at around 400 °C.

For the $x = 0.3$ composition in Fig. 4.8, similar to $x = 0.2$, no obvious changes in structure are evident up to 750 °C and the thermal expansion of unit cell volume reveals evidence for a subtle change at around 400 °C. However, in this case this temperature is associated with a small degree of hysteresis in the lattice parameters below this temperature, with the volume on cooling slightly smaller than that on heating.

For the $x = 0.4$ composition in Fig. 4.9, the γ-LISICON phase is seen throughout the heating and cooling regime. However, on heating at 600 °C the β-phase appears and the amount of this secondary phase increases up to 750 °C. On cooling the secondary β phase is maintained to room temperature. As with the $x = 0.2$ and 0.3 compositions a subtle transition is evident in the thermal expansion of unit cell volume at around 400 °C.

For the $x = 0.5$ composition in Fig. 4.10, the experiment was carried out beginning with a pure β-phase. This phase is preserved throughout heating and cooling, with no evidence of a transition to the γ-phase. As with the lower x-value compositions, a change in slope in the plot of the thermal expansion of unit cell volume is seen at around 400 °C.

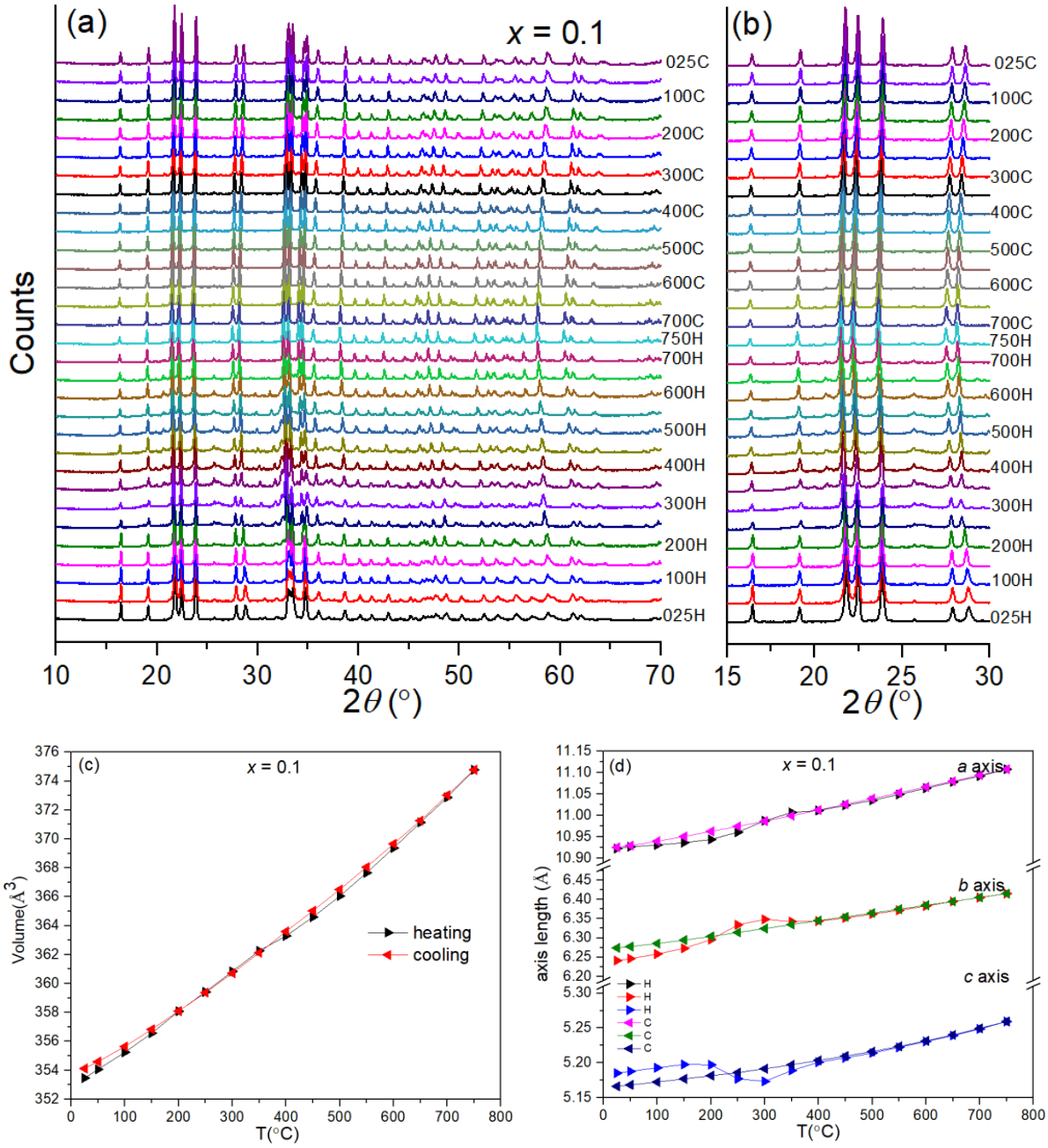

Figure 4.6 (a) VT-XRD pattern with details shown in (b), (c) and (d) refined unit cell parameters for $Li_{3.8}Ge_{0.9}Mo_{0.1}O_4$ (x = 0.1) during heating and cooling

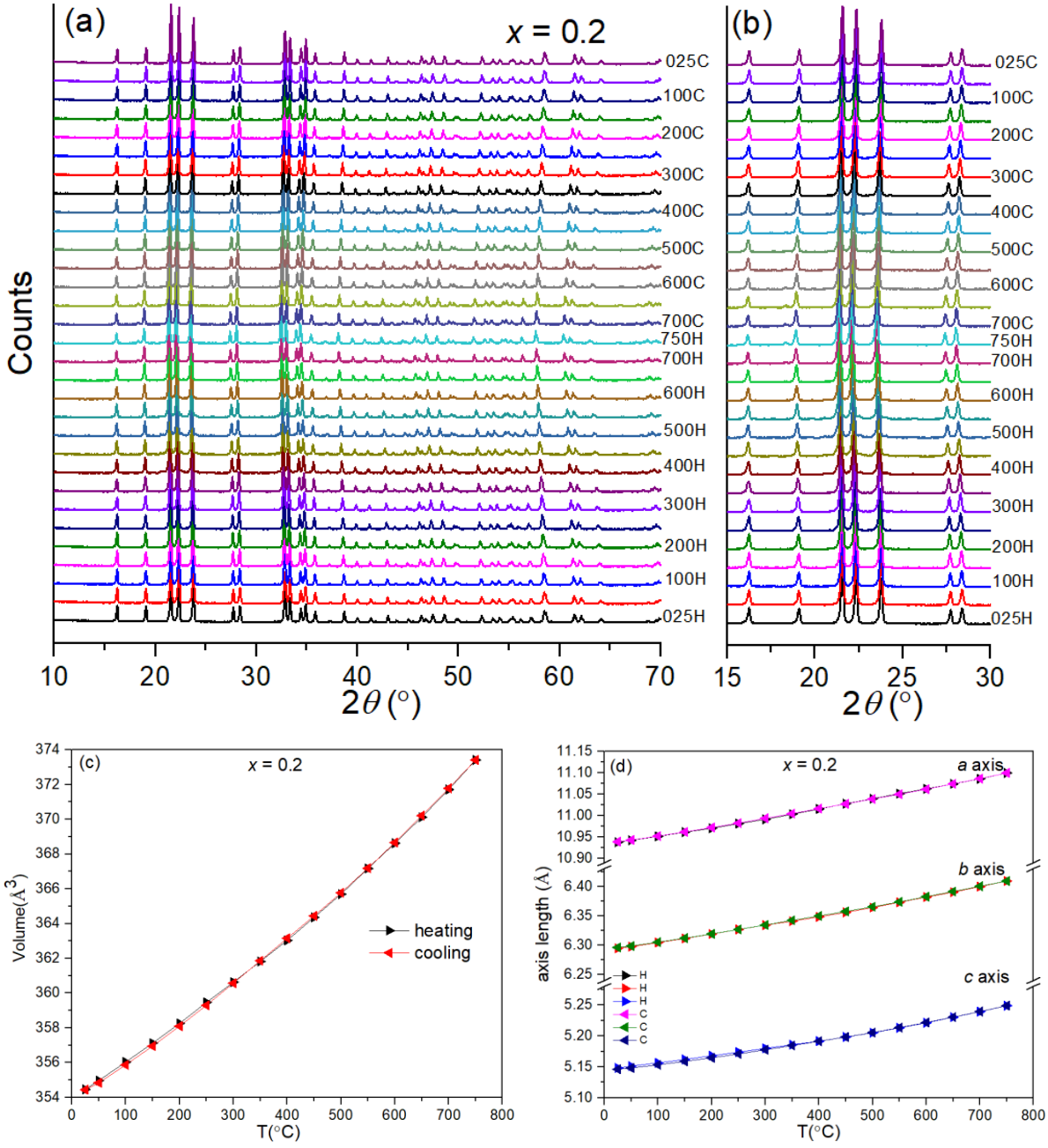

Figure 4.7 (a) VT-XRD pattern with details shown in (b), (c) and (d) refined unit cell parameters for $Li_{3.6}Ge_{0.8}Mo_{0.2}O_4$ (x = 0.2) during heating and cooling

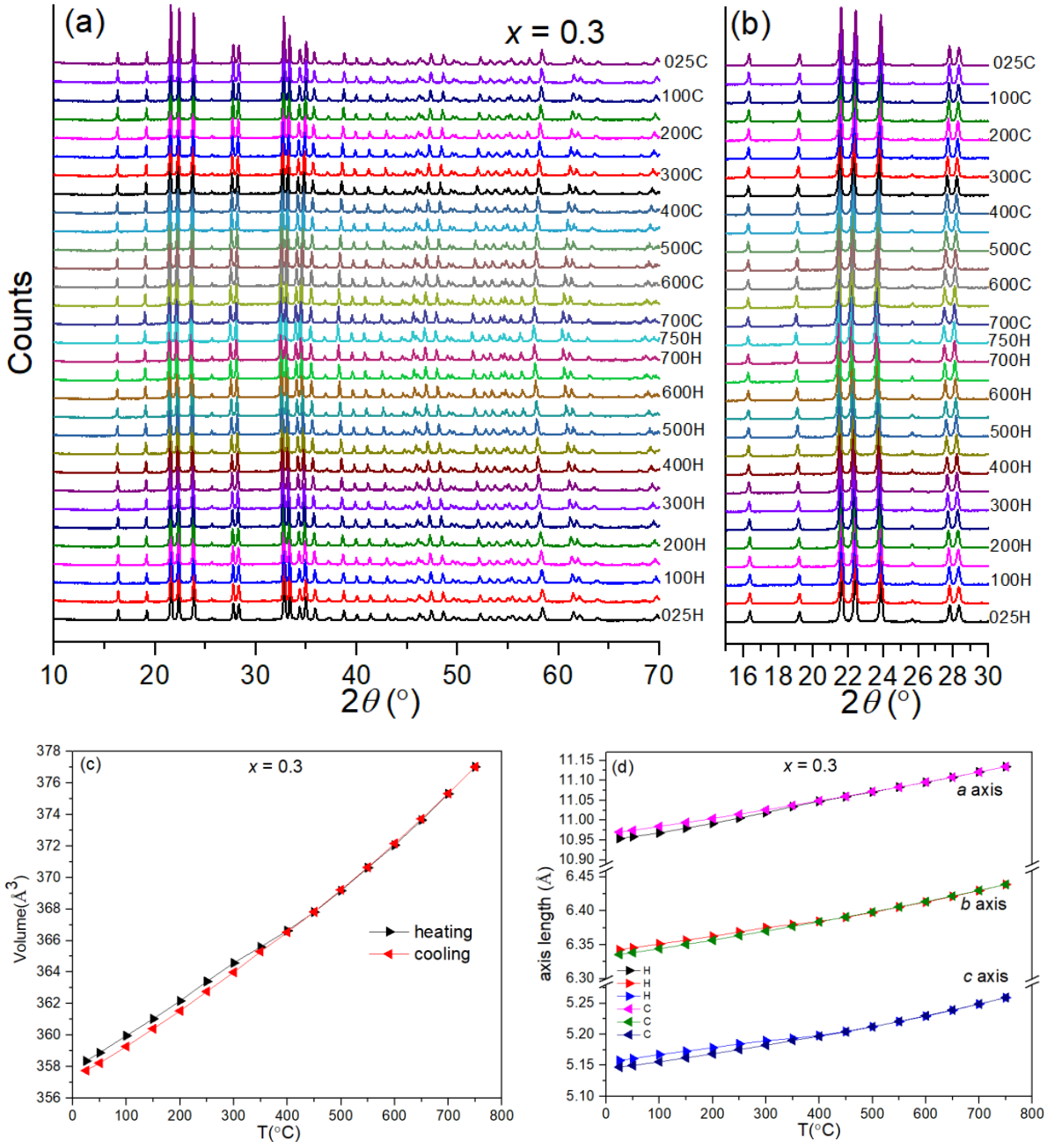

Figure 4.8 (a) VT-XRD pattern with details shown in (b), (c) and (d) refined unit cell parameters for $Li_{3.4}Ge_{0.7}Mo_{0.3}O_4$ (x = 0.3) during heating and cooling

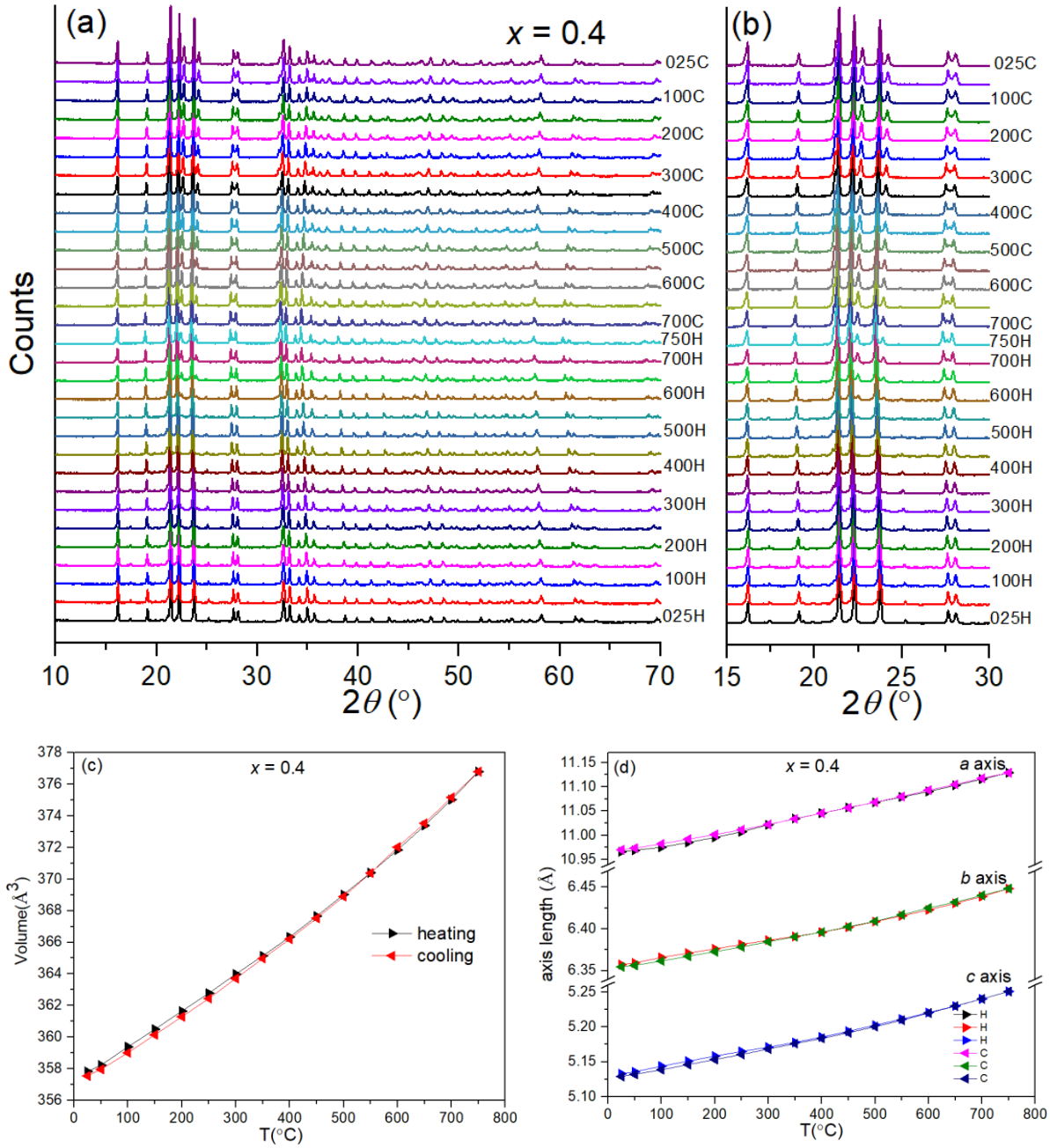

Figure 4.9 (a) VT-XRD pattern with details shown in (b), (c) and (d) refined unit cell parameters for $Li_{3.2}Ge_{0.6}Mo_{0.4}O_4$ (x = 0.4) during heating and cooling

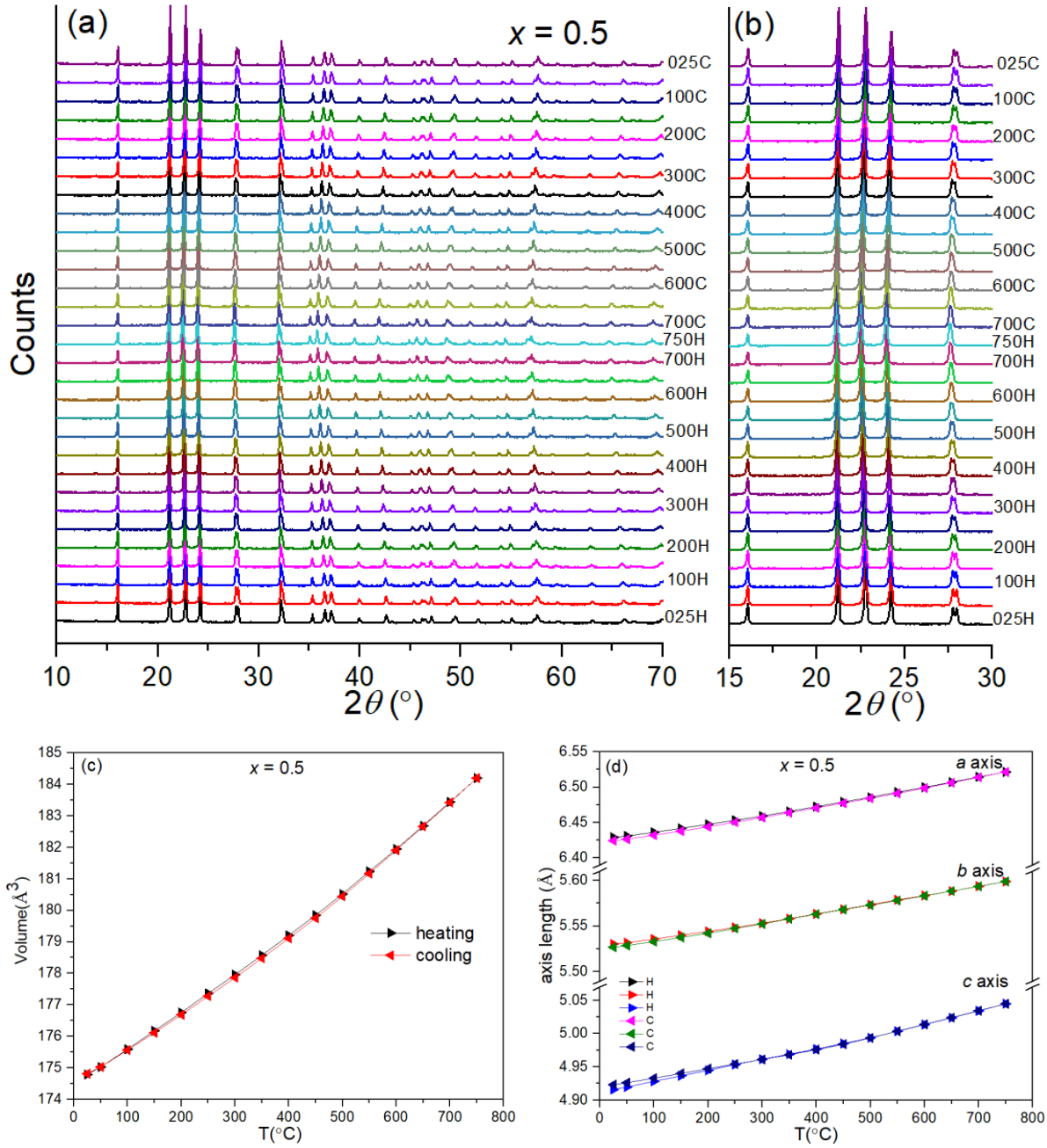

Figure 4.10 (a) VT-XRD pattern with details shown in (b), (c) and (d) refined unit cell parameters for $Li_3Ge_{0.5}Mo_{0.5}O_4$ (x = 0.5) during heating and cooling

In order to further examine the subtle changes in this system, a variable temperature neutron diffraction experiment was carried out on the x = 0.2 composition from room temperature to 700 °C. As introduced in Chapter 1, the five groups of detector banks for Polaris have different d-spacing ranges and resolution, with the back-scattering detectors having the highest

resolution and narrowest d-spacing range. To look for the appearance of weak reflections from secondary phases it is helpful to look at the lower resolution detector banks which cover the higher d-spacings, where there is less peak overlap. Fig. 4.11 shows the neutron diffraction patterns of bank 3 and bank 4 for the $x = 0.2$ composition from room temperature to 700 °C. As can be seen, weak peaks corresponding to the β-phase are present in the range 450 °C to 600 °C and disappear at 650 °C leaving the pure γ-phase. On further heating to 700 °C, weak peaks of Li_2MoO_4 become evident. However, the appearance of this phase may be due to the extended heating at 700 °C, compared to the much shorter time spent at 650 °C. Here the formation of the β-phase in the range 450 °C to 600 °C approximately corresponds to the temperature where a small change in slope is seen in the thermal expansion of unit cell volume. However, since this change is also seen in the X-ray data for the $x = 0.5$ composition, which remains in the β-phase structure throughout and it is unlikely that the appearance of small amounts of the β-phase in the $x = 0.2$ composition accounts for the observed trend in unit cell volume expansion.

In all compositions the apparent transition at around 400 °C leads to a larger volume at higher temperatures than expected from a linear extrapolation of the low temperature values. This would be consistent for example with a small reduction of Mo^{6+} to Mo^{5+}, accompanied by the creation of oxygen vacancies. However, if this was the case then one would expect this change to be most significant in the higher *x*-value compositions where the Mo concentration is highest, but similar levels of deviation are seen throughout the compositional range. Indeed, similar deviations from linearity were seen in the $Li_{3+x}Ge_xP_{1-x}O_4$ system (Chapter 3), where no change in oxidation state is likely. While, the observed transition could be associated with a change in defect structure as previously suggested for related $Li_3Zn_{0.5}GeO_4$ [84] systems. Its presence at $x = 0.5$, indicates that either this attribution is wrong or that the local structure of the β-phase, differs from the average picture obtained from the Rietveld analysis (see below).

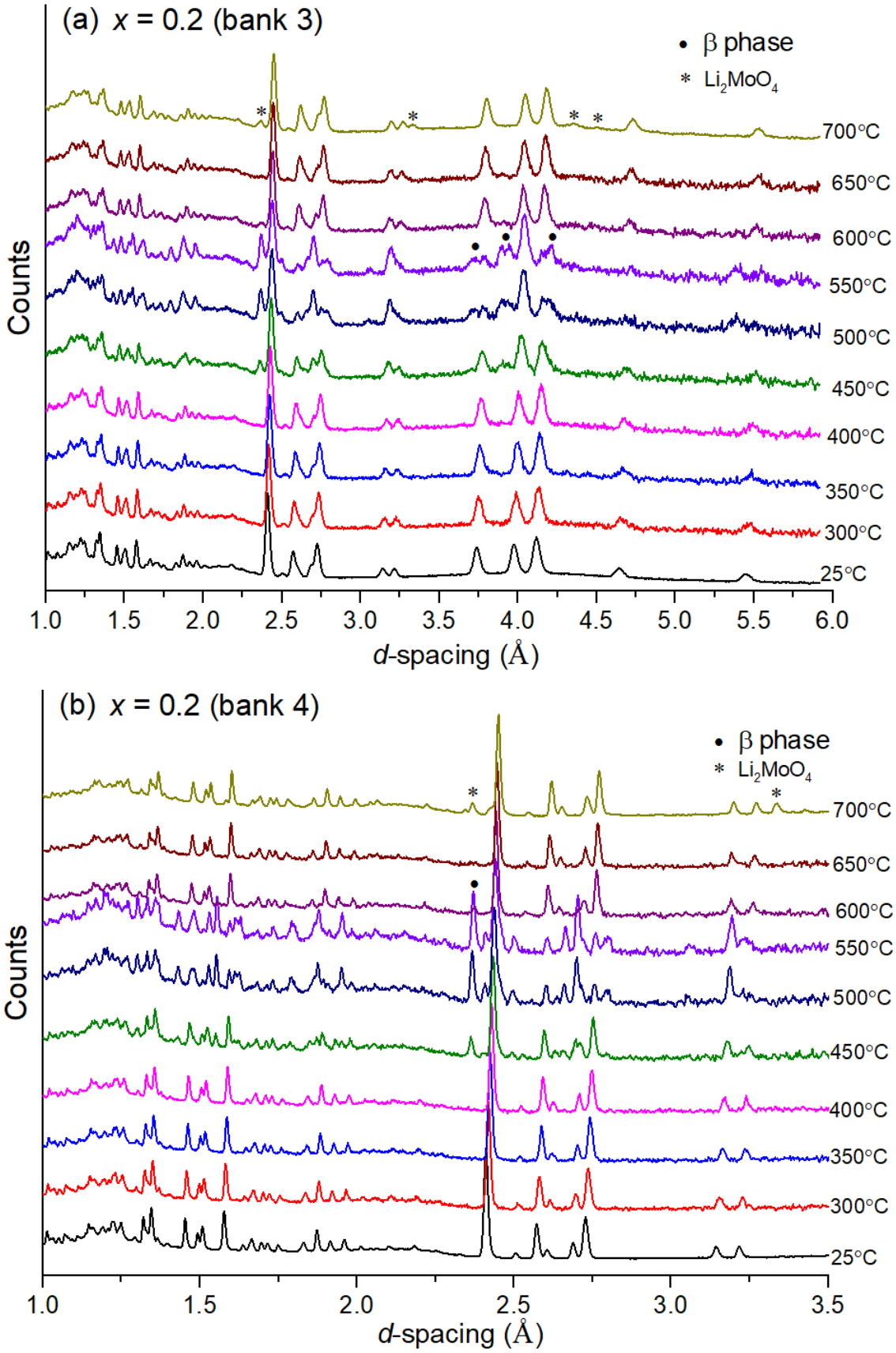

Figure 4.11 VT-neutron diffraction patterns for (a) bank 3 and (b) bank 4 for $Li_{3.6}Ge_{0.8}Mo_{0.2}O_4$ (x = 0.2) during heating

4.3.3 Pellet morphology and electrical behaviour

Pellets of the x = 0.0, 0.1, 0.2, 0.3, 0.4, 0.5 and 1.0 compositions in the $Li_{4-2x}Ge_{1-x}Mo_xO_4$ system were prepared by SPS for impedance analysis. Through using the classical Archimedes method by displacement in water, all pellets for these compositions had relative densities of over 95% theoretical density, with the relative densities of the intermediate compositions of $0.1 \leq x \leq 0.5$ over 98% (Table 4.2).

Surface and fracture SEM images for $Li_{4-2x}Ge_{1-x}Mo_xO_4$ SPS pellets after annealing are shown in Figs. 4.12 and 4.13. The images confirm good densification for all compositions, and the microstructure reveals particle aggregates of ca. 2 um in size made up of smaller crystallites around 300 nm in size for all compositions. The maintenance of small crystallite size in the SPS method, is one of the benefits of the short sintering process and avoids commonly encountered problems associated with over-sintering in conventional sintering methods over several hours.

XRD patterns of the SPS-sintered pellets after annealing in the $Li_{4-2x}Ge_{1-x}Mo_xO_4$ system are shown in Fig. 4.14. All these compositions exhibit high crystallinity and high purity. Consistent with the pristine calcined powders (Fig. 4.1), the $0.1 \leq x \leq 0.4$ compositions maintain the γ-LISICION structure, while the x = 1.0 composition maintains the rhombohedral structure. For the x = 0.5 composition, the as-prepared powder used for SPS was a pure β-phase (Fig. 4.4), and after sintering at the low temperature of 600 ºC for 5 min in SPS and annealing at 600 ºC for 11 h, this β-phase structure was maintained.

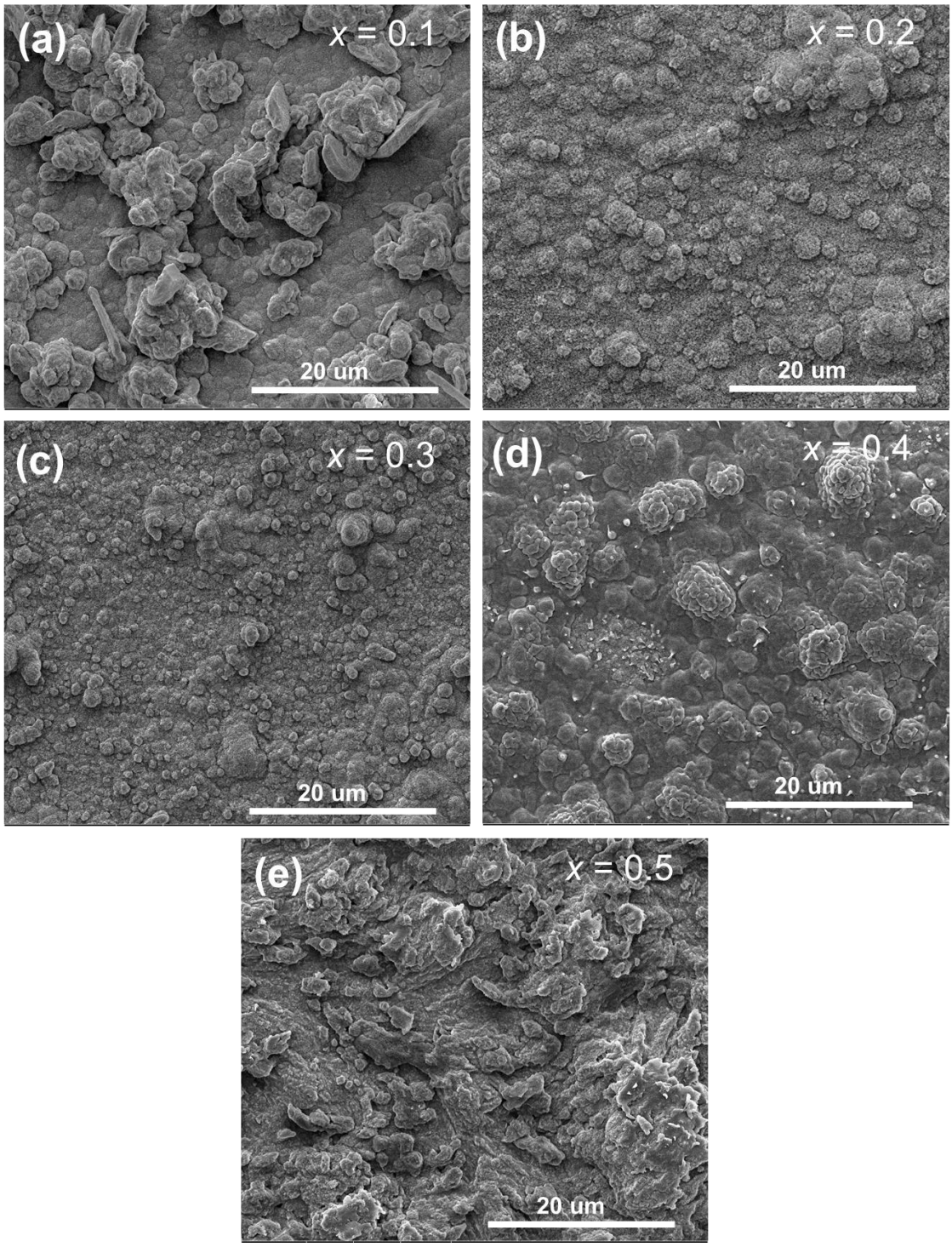

Figure 4.12 SEM surface images for SPS pellets of (a) $x = 0.1$, (b) $x = 0.2$, (c) $x = 0.3$, (d) $x = 0.4$ and (e) $x = 0.5$ compositions in the $Li_{4-2x}Ge_{1-x}Mo_xO_4$ system

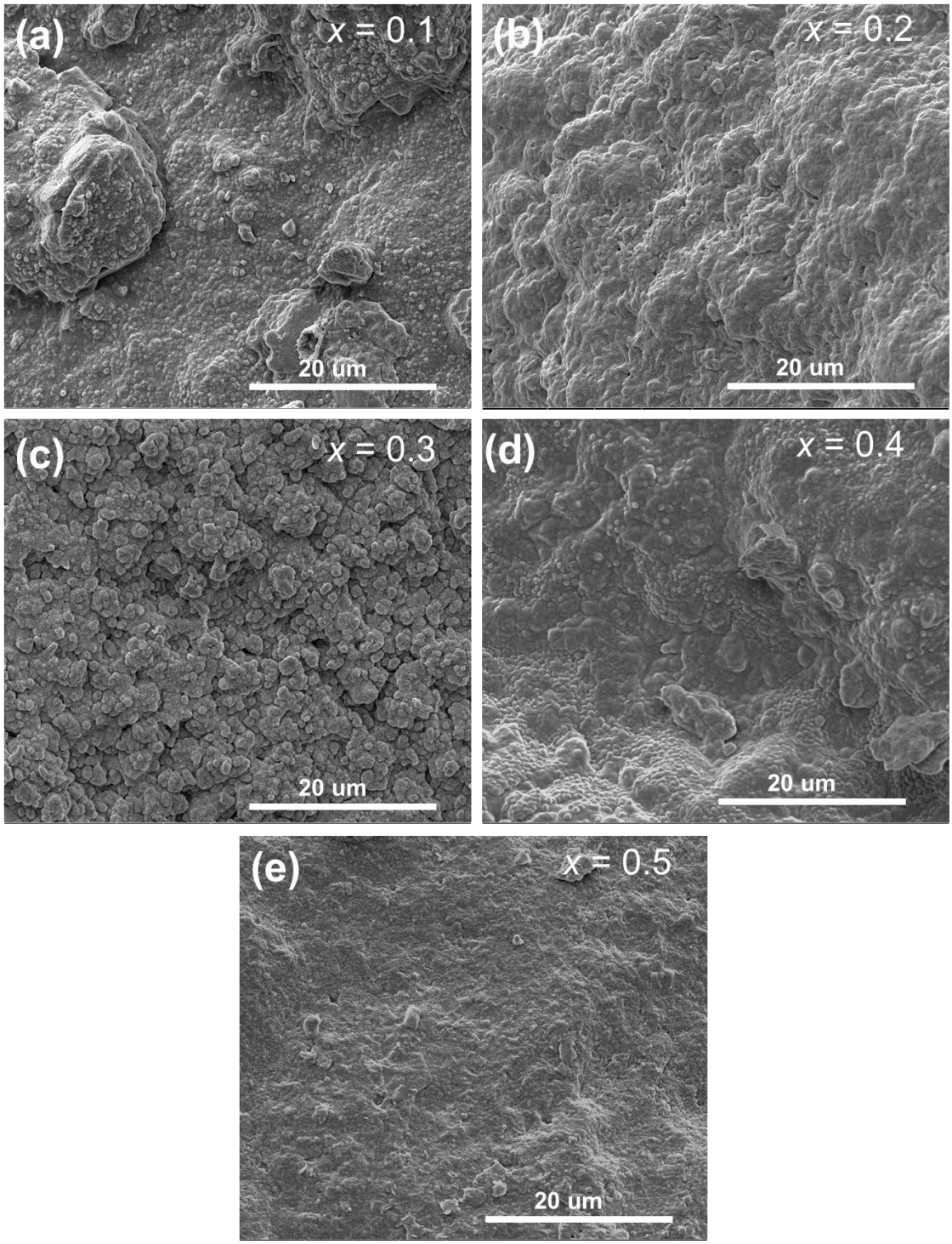

Figure 4.13 SEM fracture images for SPS pellets of (a) x = 0.1, (b) x = 0.2, (c) x = 0.3, (d) x = 0.4 and (e) x = 0.5 compositions in the $Li_{4-2x}Ge_{1-x}Mo_xO_4$ system

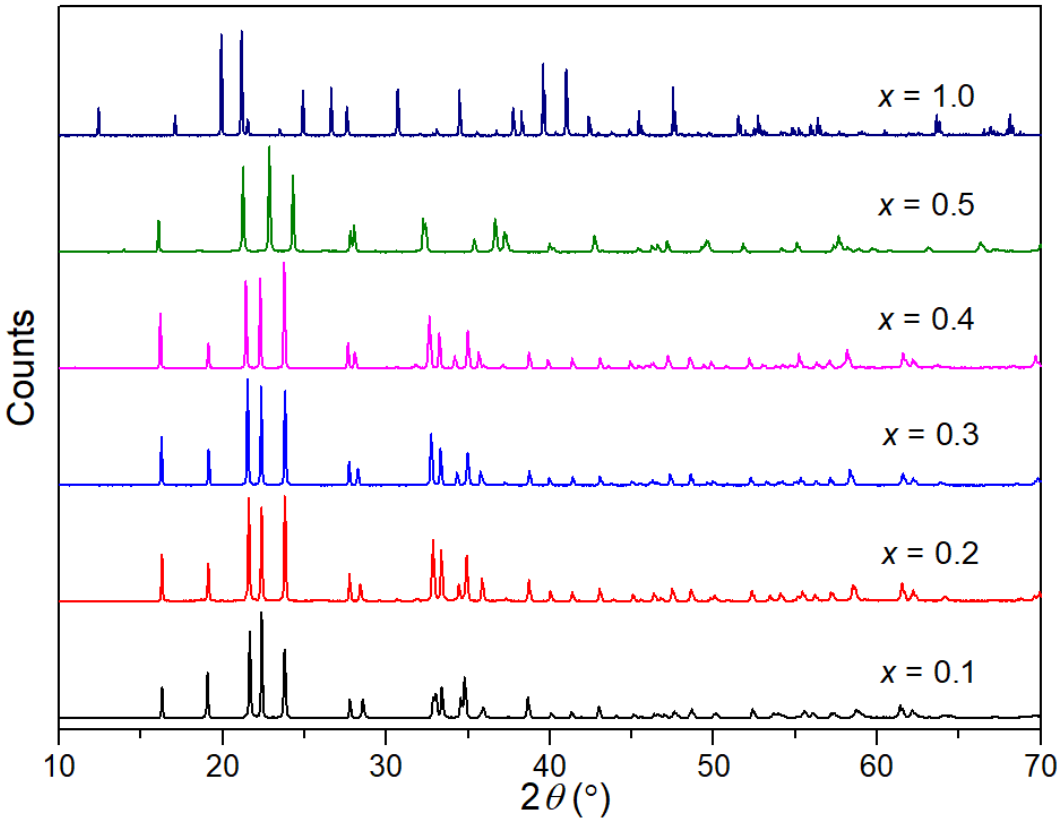

Figure 4.14 XRD patterns for SPS-sintered pellets of compositions *x* = 0.1, 0.2, 0.3, 0.4, 0.5 and 1.0 in the $Li_{4-2x}Ge_{1-x}Mo_xO_4$ system

Electrochemical impedance measurements were employed to study the electrical response of the studied compositions in the $Li_{4-2x}Ge_{1-x}Mo_xO_4$ system. Fig. 4.15 shows the Nyquist plots for $Li_{3.6}Ge_{0.8}Mo_{0.2}O_4$ at selected temperatures during the 1st heating run. As can be seen, the spectra show a capacitive semicircle at low temperatures, with a non-zero high frequency intercept with the real axis, and an inclined capacitive spike associated with the blocking electrode at low frequencies. With increasing temperature, the semicircle gets smaller and moves out of the frequency window and only the tail is observed. Interestingly for ca. 110 ºC, this semicircle increases in the 1st cooling run. A similar variation occurs in the second heating-cooling cycle. In all run cases, the high frequency intercept with the real axis was similar (Fig. 4.16).

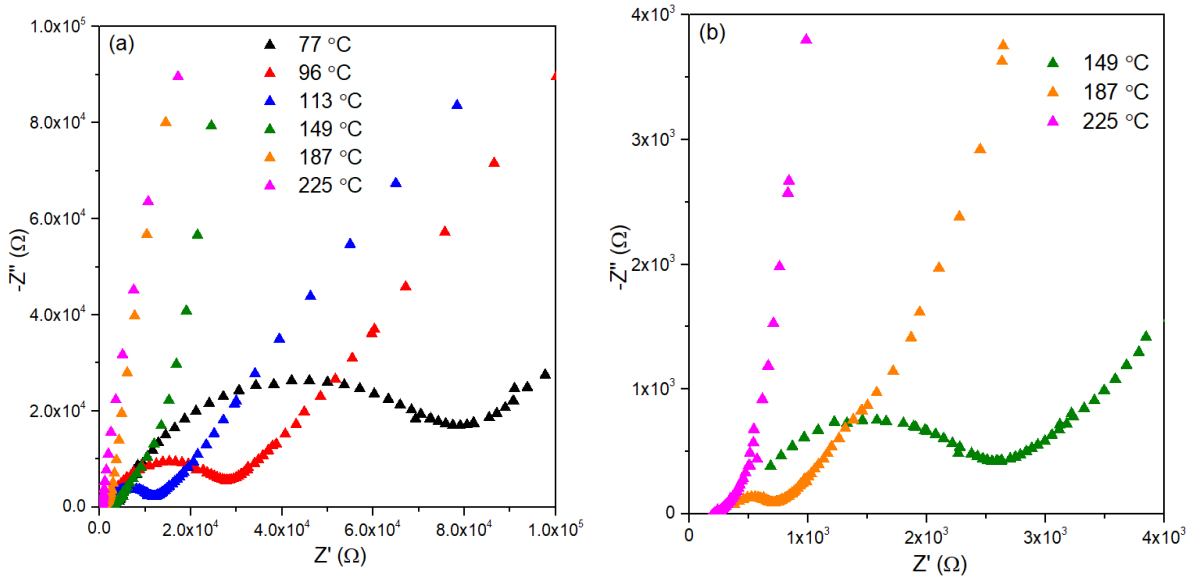

Figure 4.15 (a) Nyquist plots for $Li_{3.6}Ge_{0.8}Mo_{0.2}O_4$ with the amplification near the origin in (b) at selected temperatures during 1st heating run

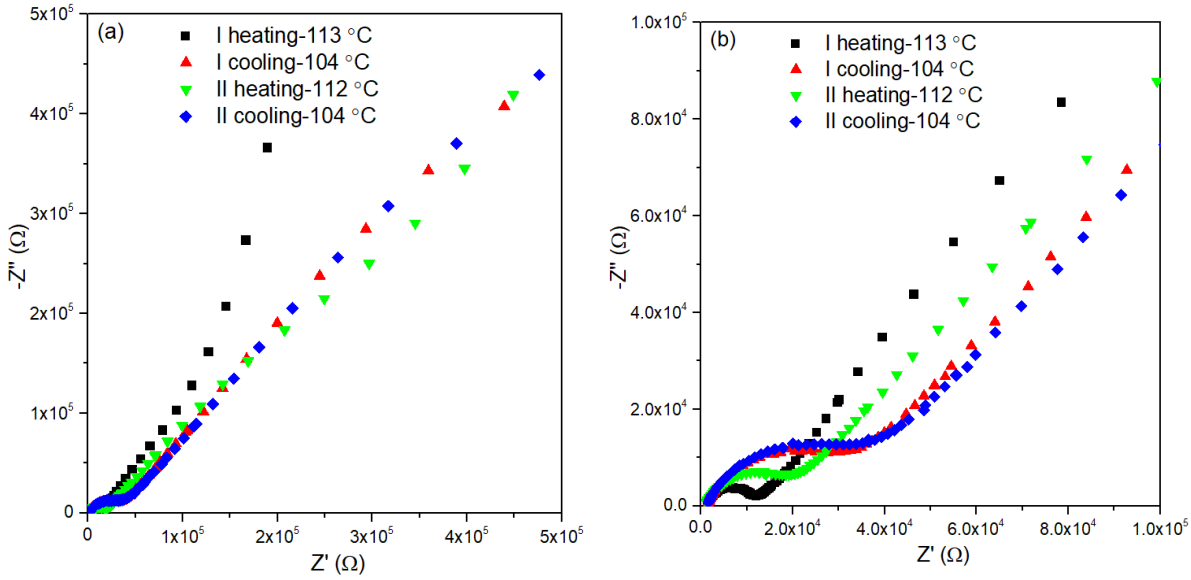

Figure 4.16 (a) Nyquist plots for $Li_{3.6}Ge_{0.8}Mo_{0.2}O_4$ at ca.110 °C with the amplification near the origin in (b) over the two heating and cooling runs

In order to understand the intrinsic electric behaviour, the optimised equivalent circuit in Fig.4.17a was used to fit the impedance spectra carefully. Fig. 4.17b and 4.17c show the fitted spectra at ca. 113 °C during the 1st heating and 2nd heating with fitted equivalent circuit

parameters summarised in Table 4.4. As can be seen in Fig. 4.17b and 4.17c, good fitting is achieved over the whole frequency range. The value of R_1 corresponds to the intercept with the real axis, P_2 and R_2 mainly contribute to the semicircle, and R_{2b}, P_{2b}, R_3, P_3 and P_4 mainly contribute to the non-linear tail. As seen in Table 4.4, the values of R_1, P_2, n_2 and R_2 were well refined with low error. Based on the empirical capacitance values and the likely responsible electrical phenomena [142], P_2 with a value in the order of 10^{-9} F and R_2 can be attributed to electrode-electrolyte processes, with R_{2b}, P_{2b}, R_3, P_3 and P_4, more closely associated with the electrode. Therefore, in a similar way to the $Li_{3+x}Ge_xP_{1-x}O_4$ system (Chapter 3), R_1 can be regarded as the total resistance of the $Li_{3.6}Ge_{0.8}Mo_{0.2}O_4$ sample. It is noteworthy that high errors in the tail related parameters were seen, which indicate that complex processes like diffusion-controlled adsorption or reaction at the electrode may occur and would require especially designed experiments to characterise these processes.

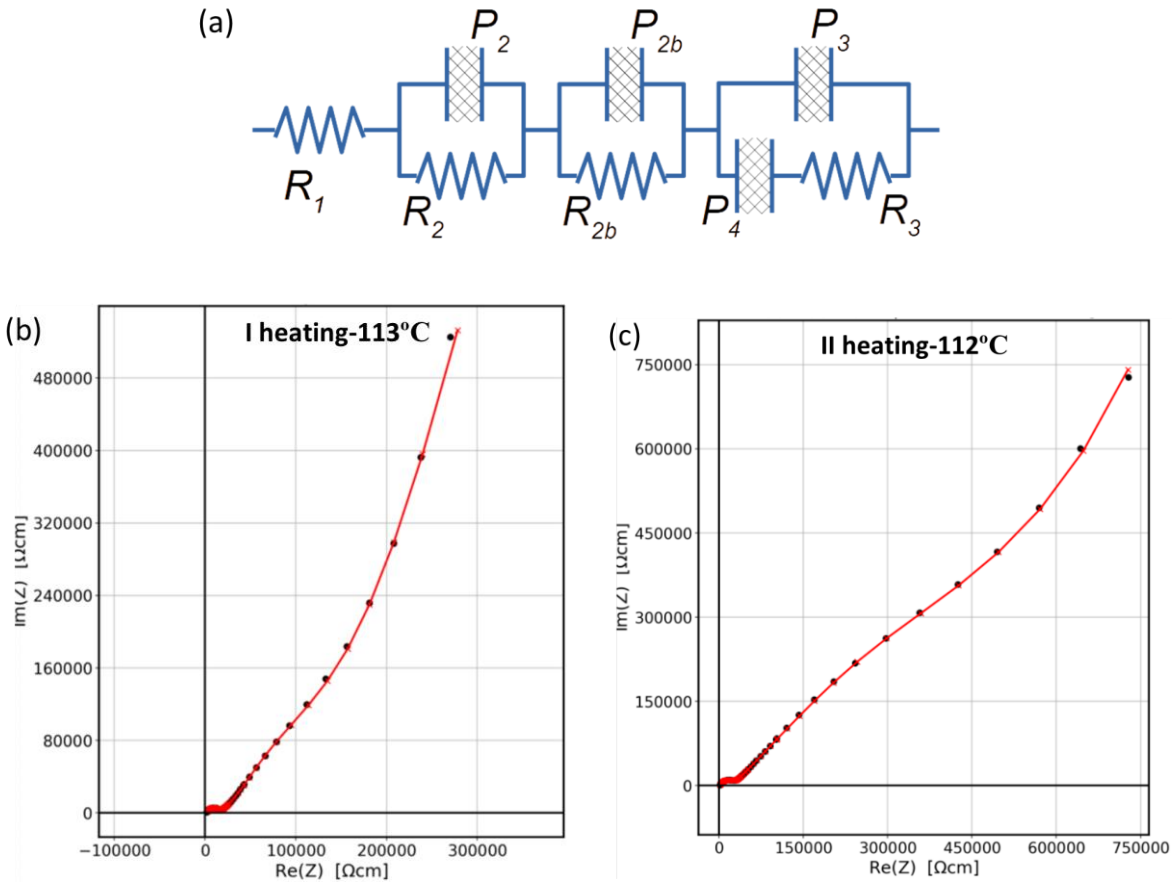

Figure 4.17 (a) equivalent circuit, (b) Experimental and simulated Nyquist plot with the amplification near the origin in (c) for $Li_{3.6}Ge_{0.8}Mo_{0.2}O_4$ at ca. 112 ºC over the 1st and 2nd heating runs

Table 4.4 Equivalent circuit parameters for for $Li_{3.6}Ge_{0.8}Mo_{0.2}O_4$ at ca. 112 ºC over the 1st and 2nd heating runs

parameters	I heating-113 ºC		II heating-112 ºC	
	value	Conf%	value	Conf%
R_1 (Ω)	1011	4.3	899	4.7
R_2 (Ω)	9276	3.4	1.6×10^{4}	5.4
P_2 (F)	2.1×10^{-9}	14.0	6.9×10^{-9}	14.9
n_2	0.16	7.7	0.23	6.3
R_{2b} (Ω)	1.4×10^{5}	368.5	9.0×10^{5}	388.6
P_{2b} (F)	6.0×10^{-6}	32.9	1.4×10^{-6}	34.9
n_{2b}	0.57	7.6	0.49	9.5
P_3 (F)	1.5×10^{-6}	43.5	1.9×10^{-6}	354.6
n_3	0.02	1237	0	-0.5
P_4 (F)	2.3×10^{-6}	44.9	2.3×10^{-6}	110.1
n_4	0.17	93.1	0.02	6699
R_3 (Ω)	1.2×10^{5}	133.9	1.6×10^{5}	246.4

Fig. 4.18 shows the Arrhenius plots of total conductivity for the selected compositions in the $Li_{4-2x}Ge_{1-x}Mo_xO_4$ system over two cycles of heating and cooling from room temperature to 300 ºC. It can be observed that all the impedance data of these compositions exhibit good repeatability except that in the cases of $x = 0.3$ and 0.5, the data for the first heating run is higher than those in subsequent cooling and heating runs. This is likely due to some form of passivation at the electrolyte/electrode interface in the first heating cycle. This issue appears most significant for the $x = 0.5$ composition. It should be noted that the VT-XRD study showed no unusual phase behaviour below 300 °C. Therefore, for subsequent discussion the data for the second heating run which showed good repeatability are used.

For all the compositions except for $x = 0.3$, a linear Arrhenius plot is seen over the entire studied temperature range. Only for the $x = 0.3$, a transition evident at around 200 °C is present. Table 4.5 summarises the conductivities at selected temperatures along with activation energies for the second heating run (for $x = 0.3$, activation energies in the low (ΔE_{LT}) and high temperature (ΔE_{HT}) regions are included). High activation energies (> 1 eV) and low conductivities are seen for the two end members Li_4GeO_4 and Li_2MoO_4. Among all the compositions, the highest conductivity and lowest activation energy are shown by the $x = 0.2$ composition with a value of conductivity at 250 °C of 5.02×10^{-3} S cm^{-1} and activation energy of 0.67 eV.

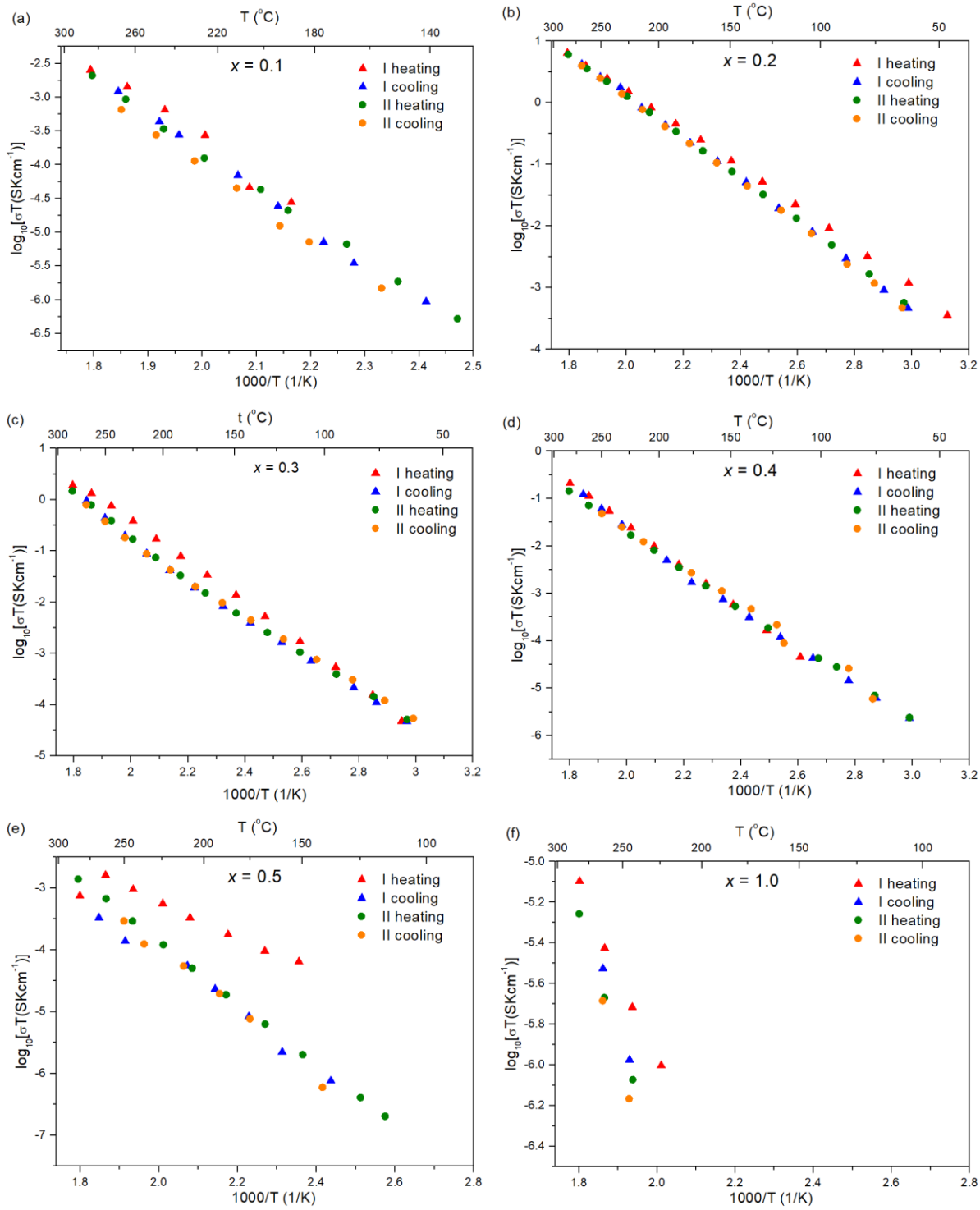

Figure 4.18 Arrhenius plots of total conductivity for x = 0.0, 0.1, 0.2, 0.3, 0.4, 0.5 and 1.0 compositions in the $Li_{4-2x}Ge_{1-x}Mo_xO_4$ system

Table 4.5 Activation energies ΔE_{LT} and ΔE_{HT} and conductivities ($\sigma_{temp°C}$) at selected temperatures for x = 0.0, 0.1, 0.2, 0.3, 0.4, 0.5 and 1.0 compositions in the $Li_{4-2x}Ge_{1-x}Mo_xO_4$ system. Data correspond to the second heating run. Estimated errors are ±1%. Values at 25°C were obtained through extrapolation.

x	ΔE_{LT} (eV)	ΔE_{HT} (eV)	$\sigma_{25°C}$ (S cm^{-1})	$\sigma_{100°C}$ (S cm^{-1})	$\sigma_{150°C}$ (S cm^{-1})	$\sigma_{250°C}$ (S cm^{-1})
0.0	1.05		/	/	/	8.08×10^{-8}
0.1	1.05		3.53×10^{-14}	1.05×10^{-10}	4.40×10^{-9}	8.79×10^{-7}
0.2	0.67		1.11×10^{-7}	1.73×10^{-5}	1.81×10^{-4}	5.02×10^{-3}
0.3	0.70	0.89	7.54×10^{-9}	1.43×10^{-6}	1.65×10^{-5}	8.83×10^{-4}
0.4	0.79		2.73×10^{-10}	1.05×10^{-7}	1.68×10^{-6}	8.55×10^{-5}
0.5	0.98		9.01×10^{-14}	1.57×10^{-10}	5.14×10^{-9}	7.20×10^{-7}
1.0	1.18		/	/	/	2.28×10^{-9}

4.3.4 Structural characterisation

4.3.4.1 Average structure analysis

To examine the lithium ion distribution and local defect structures, which determine the lithium ion conductivity in the $Li_{4-2x}Ge_{1-x}Mo_xO_4$ system, the intermediate composition x = 0.2 in the γ-phase, x = 0.5 in the β-phase and the two end-members Li_4GeO_4 and Li_2MoO_4 were selected for neutron total scattering. A combined neutron and X-ray approach was used for the Rietveld analysis for these compositions. The fitted diffraction profiles are shown in Figs. 4.19 to 4.21, with crystal and refinement parameters given in Table 4.6, refined structural parameters in Tables 4.7 to 4.9, significant contacts and angles in Table 4.10 to 4.12. Table 4.13 contains details of the Li…Li contacts and site occupancy ratios including short distances that preclude the simultaneous occupancy of sites. Since all the data for Li_4GeO_4 are shown in Chapter 3, part of them are omitted in this chapter.

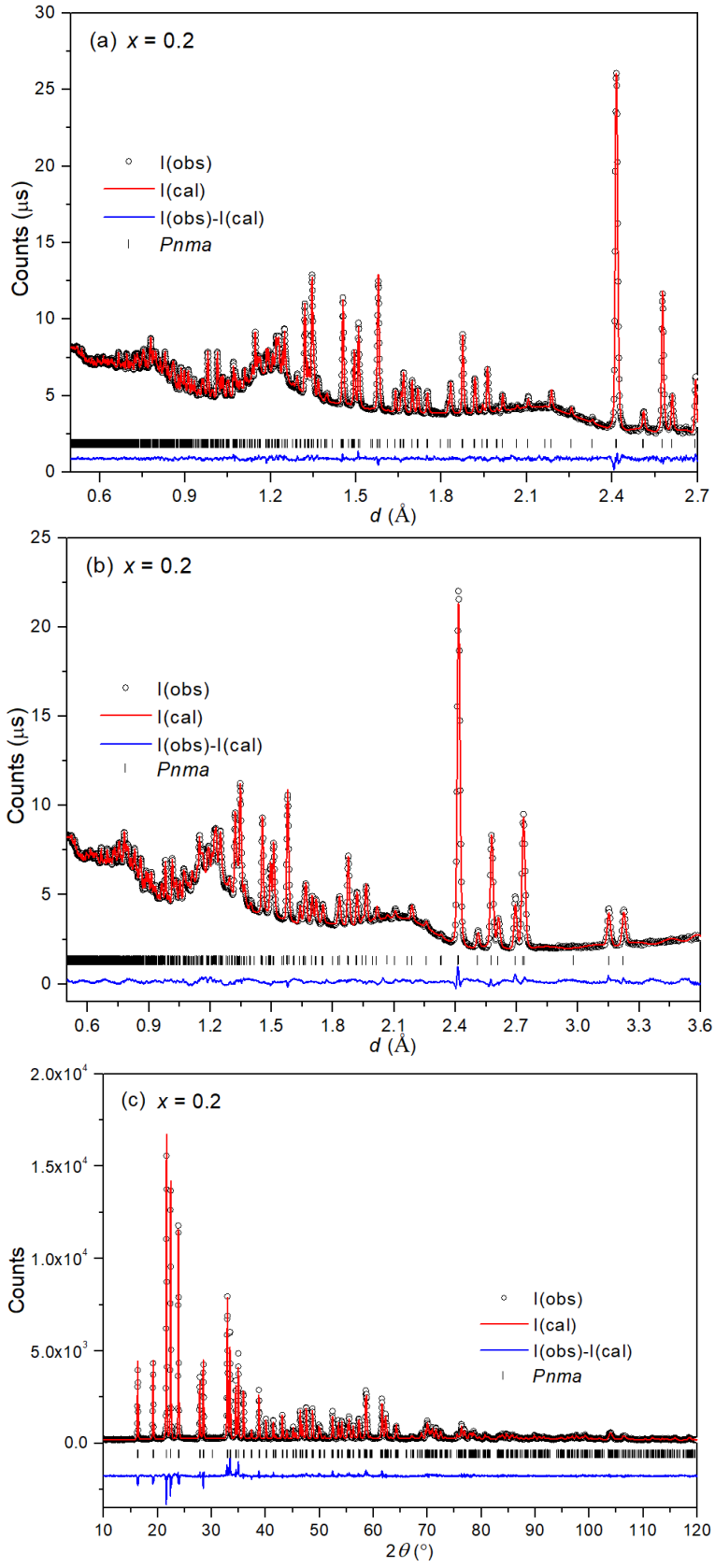

Figure 4.19 Diffraction profiles for $Li_{3.6}Ge_{0.8}Mo_{0.2}O_4$ (x = 0.2) showing (a) neutron back scattering (b) neutron 90° and (c) X-ray data, fitted by conventional Rietveld analysis. Observed (crosses), calculated (line) and difference (lower) profiles are shown, with reflection positions indicated by markers

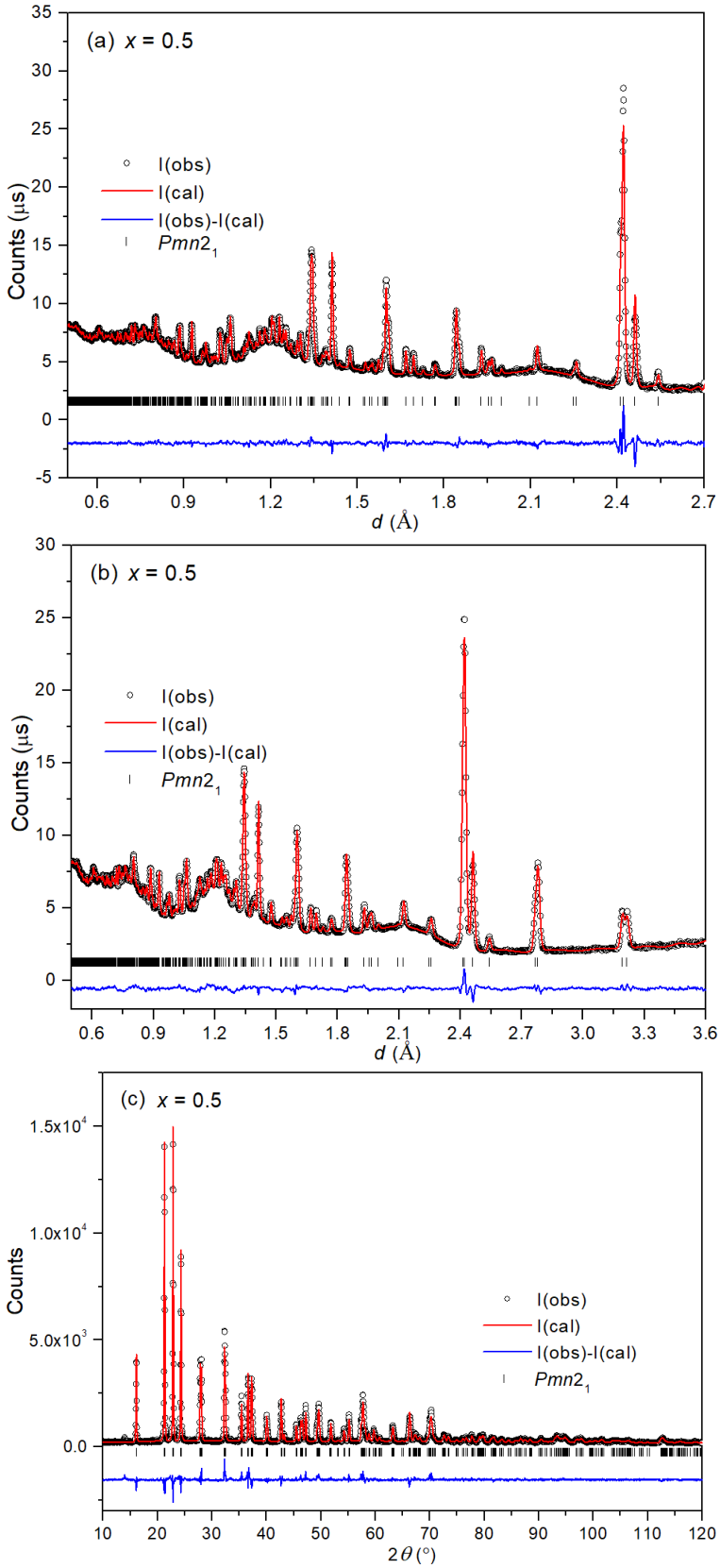

Figure 4.20 Diffraction profiles for $Li_3Ge_{0.5}Mo_{0.5}O_4$ (x = 0.5) showing (a) neutron back scattering (b) neutron 90° and (c) X-ray data, fitted by conventional Rietveld analysis. Observed (crosses), calculated (line) and difference (lower) profiles are shown, with reflection positions indicated by markers

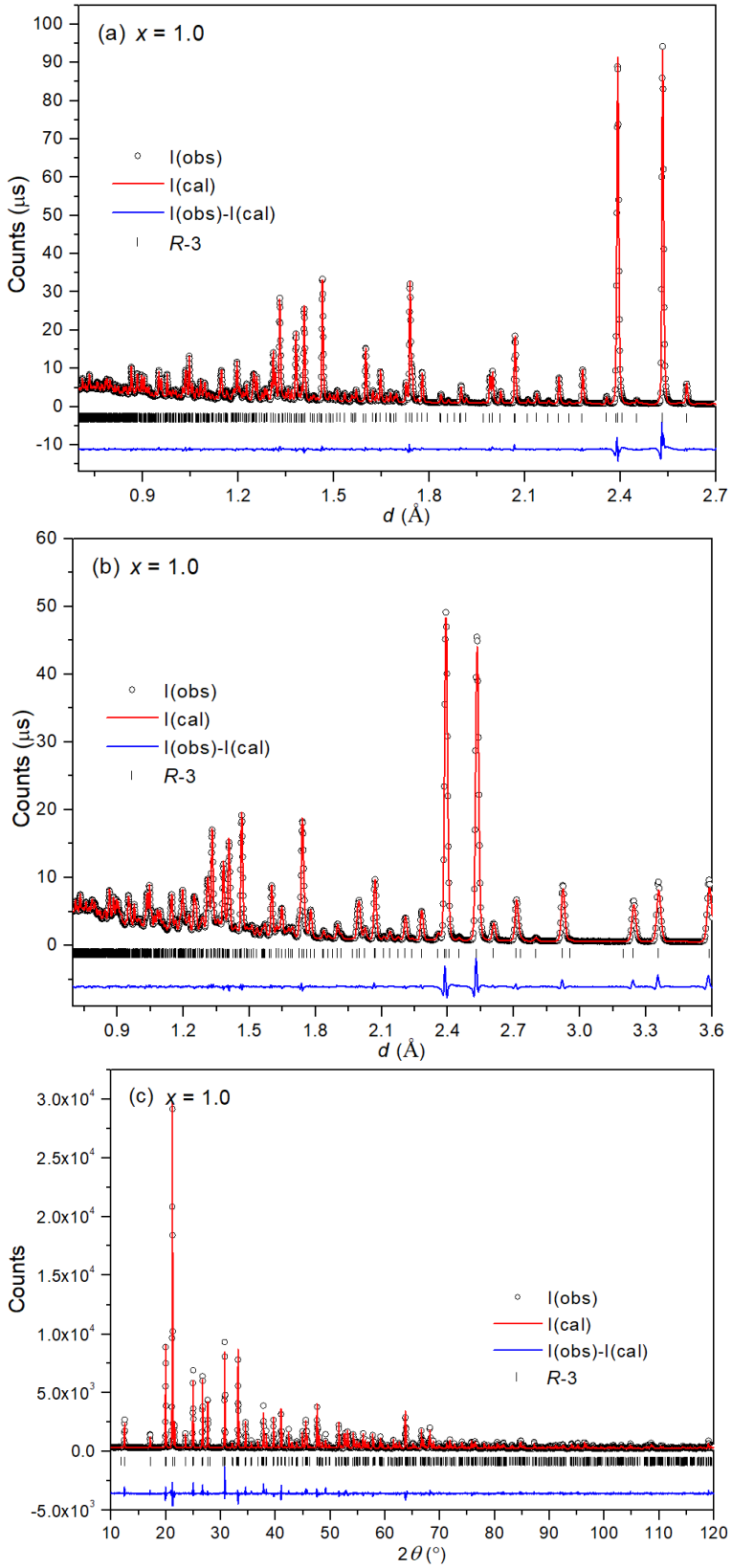

Figure 4.21 Diffraction profiles for Li_2MoO_4 (x = 1.0) showing (a) neutron back scattering (b) neutron 90° and (c) X-ray data, fitted by conventional Rietveld analysis. Observed (crosses), calculated (line) and difference (lower) profiles are shown, with reflection positions indicated by markers

Table 4.6 Crystal and refinement parameters at room temperature for compositions in the $Li_{4-2x}Ge_{1-x}Mo_xO_4$ system.

x	$x = 0.2$	$x = 0.5$	$x = 1.0$
Chemical formula	$Li_{3.6}Ge_{0.8}Mo_{0.2}O_4$	$Li_3Ge_{0.5}Mo_{0.5}O_4$	Li_2MoO_4
M_r (g mol^{-1})	166.26	169.10	173.82
Crystal system	Orthorhombic	Orthorhombic	Rhombohedral
Space group	*Pnma*	$Pmn2_1$	*R*-3
Unit cell dimensions (Å)	$a = 10.9419(3)$ $b = 6.2973(2)$ $c = 5.1506(1)$	$a = 6.4275(3)$ $b = 5.5300(2)$ $c = 4.9192(2)$	$a = 14.3425(3)$ $c = 9.5946(2)$
Volume （Å^3）	354.90(3)	174.85(2)	1709.25(8)
Z	4	2	18
Density (calculated)	3.111 g/cm^3	3.212 g/cm^3	3.040 g/cm^3
R-factors (neutron back scattering)	$R_{wp} = 0.0080$ $R_p = 0.0113$ $R_{ex} = 0.0042$ $R_F^2 = 0.0409$	$R_{wp} = 0.0117$ $R_p = 0.0179$ $R_{ex} = 0.0058$ $R_F^2 = 0.0464$	$R_{wp} = 0.0248$ $R_p = 0.0347$ $R_{ex} = 0.0059$ $R_F^2 = 0.0264$
R-factors (neutron 90º)	$R_{wp} = 0.0129$ $R_p = 0.0176$ $R_{ex} = 0.0027$ $R_F^2 = 0.0870$	$R_{wp} = 0.0159$ $R_p = 0.0188$ $R_{ex} = 0.0037$ $R_F^2 = 0.1091$	$R_{wp} = 0.0212$ $R_p = 0.0332$ $R_{ex} = 0.0032$ $R_F^2 = 0.0217$
R-factors (X-ray)	$R_{wp} = 0.0890$ $R_p = 0.0697$ $R_{ex} = 0.0462$ $R_F^2 = 0.0940$	$R_{wp} = 0.0929$ $R_p = 0.0718$ $R_{ex} = 0.0474$ $R_F^2 = 0.0918$	$R_{wp} = 0.0972$ $R_p = 0.0740$ $R_{ex} = 0.0452$ $R_F^2 = 0.1031$
Total R-factors	$R_{wp} = 0.0123$ $R_p = 0.0644$	$R_{wp} = 0.0160$ $R_p = 0.0664$	$R_{wp} = 0.0237$ $R_p = 0.0716$
χ^2	8.384	7.485	17.95
No. of variables	134	122	135
No. of profile points neutron back scattering	3483	3426	2826
neutron 90º	2058	2078	1762
X-ray	3290	3290	3440

Table 4.7 Refined structural parameters for $Li_{3.6}Ge_{0.8}Mo_{0.2}O_4$

Atom	Site	*x*	*y*	*z*	U_{iso} (Å^2)	Occ.
Li1	4*c*	0.450(2)	0.75	0.151(4)	0.0247(4)	0.33(2)
Li1a	4*c*	0.401(1)	0.75	0.212(2)	0.0247(4)	0.67(2)
Li2	8*d*	0.1616(4)	-0.0021(6)	0.3316(6)	0.0169(2)	0.812(6)
Li2a	8*d*	0.188(6)	0.181(2)	0.058(2)	0.0169(2)	0.188(6)
Li3	4*c*	0.204(2)	0.25(18)	-0.033(5)	0.105(5)	0.42(1)
Li4	4*c*	0	0	0.5	0.105(5)	0.18(1)
Ge	4*c*	0.4133(1)	0.25	0. 3355(2)	0.0117(2)	0.8
Mo	4*c*	0.4133(1)	0.25	0. 3355(2)	0.0117(2)	0.2
O1	8*d*	0. 3351(1)	0. 0216(1)	0. 2216(2)	0.0158(2)	1.0
O2	4*c*	0. 0855(2)	0.75	0. 1768(3)	0.0154(3)	1.0
O3	4*c*	0. 0643(1)	0.25	0. 2756(3)	0.0150(3)	1.0

Table 4.8 Refined structural parameters for $Li_3Ge_{0.5}Mo_{0.5}O_4$

Atom	Site	*x*	*y*	*z*	U_{iso} (Å^2)	Occ.
Li1	4*b*	0.2405(6)	0.332(1)	1.003(1)	0.0247(4)	1.0
Li2	2*a*	0.5	0.827(1)	0.968(1)	0.0169(2)	1.0
Ge	2*a*	0.0	0.8282(2)	-0.0014(0)	0.0098(2)	0.5
Mo	2*a*	0.0	0.8282(2)	-0.0014(0)	0.0098(2)	0.5
O1	4*b*	0.2286(2)	0.6772(3)	0.8899(4)	0.0148(2)	1.0
O2	2*a*	0.0	0.1386(3)	0.8940(5)	0.0130(3)	1.0
O3	2*a*	0.5	0.1714(5)	0.8564(5)	0.0200(4)	1.0

Table 4.9 Refined structural parameters for Li_2MoO_4

Atom	Site	*x*	*y*	*z*	U_{iso} (Å^2)	Occ.
Li1	18*f*	0.1372(3)	0.4526(3)	0.2488(8)	0.0159(5)	1.0
Li2	18*f*	0.3088(2)	0.8546(2)	0.5793(8)	0.0152(5)	1.0
Mo	18*f*	0.11837(5)	0.64731(5)	0.4160(2)	0.0090(2)	1.0
O1	18*f*	0.00488(7)	0.66480(9)	0.4142(3)	0.0164(2)	1.0
O2	18*f*	0.23427(7)	0.77716(7)	0.4162(2)	0.0181(2)	1.0
O3	18*f*	0.11813(9)	0.57852(8)	0.2629(2)	0.0147(2)	1.0
O4	18*f*	0.11852(8)	0.57847(7)	0.5691(2)	0.0175(2)	1.0

Table 4.10 Significant bond lengths (Å) and bond angles (°) for $Li_{3.6}Ge_{0.8}Mo_{0.2}O_4$ from conventional Rietveld analysis.

Ge/Mo-O1	1.7728(11) × 2	Li1-O1	2.156(15)× 2	Li1a-O1	1.857(5) × 2
Ge/Mo -O2	1.7582(14)	Li1-O2	1.723(18)	Li1a-O2	2.098(11)
Ge/Mo-O3	1.7497(19)	Li1-O3	1.941(19)	Li1a-O3	2.280(12)
Li2-O1	1.986(4)			Li2a-O1	1.765(18)
Li2-O1	2.0127(35)			Li2a-O1	2.191(15)
Li2-O2	1.941(4)			Li2a-O2	2.214(13)
Li2-O3	1.933(4)			Li2a-O3	1.899(17)
Li3-O1	2.415(20)				
Li3-O1	2.171(16)			Li4-O1	2.1394(11) × 2
Li3-O1	2.415(20)			Li4-O2	2.4749(11) × 2
Li3-O1	2.171(16)			Li4-O3	2.0758(10) × 2
Li3-O2	2.742(23)				
Li3-O3	2.208(24)				
Mean Ge/Mo-O	1.76(1)			Mean Li-O	2.06(7)
O1-Ge/Mo -O1	108.43(8)	O1-Li1-O1	105.0(10)	O1-Li1a-O1	134.2(7)
O1-Ge/Mo -O2	109.56(6)	O1-Li1-O2	114.6(6)	O1-Li1a-O2	111.51(29)
O1-Ge/Mo -O3	110.32(5)	O1-Li1-O3	96.8(5)	O1-Li1a-O3	95.19(33)
O1-Ge/Mo -O2	109.56(6)	O1-Li1-O2	114.6(6)	O1-Li1a-O2	111.51(29)
O1-Ge/Mo -O3	110.32(5)	O1-Li1-O3	96.8(5)	O1-Li1a-O3	95.19(33)
O2-Ge/Mo -O3	108.64(9)	O2-Li1-O3	125.7(15)	O2-Li1a-O3	96.3(5)
O1-Li2-O1	105.80(17)			O1-Li2a-O1	107.0(8)
O1-Li2-O2	110.70(18)			O1-Li2a-O2	108.1(8)
O1-Li2-O3	114.96(20)			O1-Li2a-O3	128.9(8)
O1-Li2-O2	111.62(16)			O1-Li2a-O2	81.8(5)
O1-Li2-O3	102.04(17)			O1-Li2a-O3	117.8(9)
O2-Li2-O3	111.28(20)			O2-Li2a-O3	101.8(7)

Table 4.11 Significant bond lengths (Å) and bond angles (°) for $Li_3Ge_{0.5}Mo_{0.5}O_4$ from conventional Rietveld analysis.

Ge/Mo-O1	1.7729(13)	Li1-O1	1.987(7)	Li2-O1	1.9681(34)
Ge/Mo-O1	1.7729(13)	Li1-O1	1.915(6)	Li2-O1	1.9681(34)
Ge/Mo-O2	1.7920(23)	Li1-O2	1.956(5)	Li2-O2	2.105(6)
Ge/Mo-O3	1.7600(26)	Li1-O3	2.024(5)	Li2-O3	1.984(7)
Mean Ge/Mo-O	1.77(1)			Mean Li-O	1.98(9)
O1-Ge/Mo -O1	111.97(12)	O1-Li1-O1	108.00(30)	O1-Li2-O1	124.8(4)
O1-Ge/Mo -O2	111.39(7)	O1-Li1-O2	114.75(27)	O1-Li2-O2	103.46(17)
O1-Ge/Mo -O3	107.59(8)	O1-Li1-O3	110.76(27)	O1-Li2-O3	110.46(18)
O1-Ge/Mo -O2	111.39(7)	O1-Li1-O2	109.80(31)	O1-Li2-O2	103.46(17)
O1-Ge/Mo -O3	07.59(8)	O1-Li1-O3	104.87(23)	O1-Li2-O3	110.46(18)
O2-Ge/Mo -O3	106.60(13)	O2-Li1-O3	108.21(31)	O2-Li2-O3	100.84(28)

Table 4.12 Significant bond lengths (Å) and bond angles (°) for Li_2MoO_4 from conventional Rietveld analysis.

Mo-O1	1.7667(12)	Li1-O1	1.9078(34)	Li2-O1	1.9712(30)
Mo-O2	1.7709(10)	Li1-O2	2.003(7)	Li2-O2	1.907(7)
Mo1O3	1.7683(20)	Li1-O3	1.9616(30)	Li2-O4	2.0059(34)
Mo-O4	1.7703(22)	Li1-O3	1.982(7)	Li2-O4	1.988(7)
Mean Ge/Mo-O 1.77(2)				Mean Li-O 1.97(9)	
O1-Mo-O2	107.32(5)	O1-Li1-O2	110.48(28)	O1-Li2-O2	114.68(30)
O1-Mo-O3	109.05(13)	O1-Li1-O3	108.07(15)	O1-Li2-O4	99.08(14)
O1-Mo-O4	110.20(13)	O1-Li1-O3	107.33(29)	O1-Li2-O4	104.97(27)
O2-Mo-O3	109.06(10)	O2-Li1-O3	106.30(29)	O2-Li2-O4	108.01(28)
O2-Mo-O4	108.88(10)	O2-Li1-O3	113.04(16)	O2-Li2-O4	118.40(17)
O3-Mo-O4	112.22(4)	O3-Li1-O3	111.55(27)	O4-Li2-O4	109.98(27)

Table 4.13 Li…Li inter-site contact distances (Å) and site occupancy ratios for $Li_{3.6}Ge_{0.8}Mo_{0.2}O_4$ from conventional Rietveld analysis.

Li1..Li1a	0.625(20)		
Li1..Li2	2.595(13) ×2	LI1a..Li2	2.614(8)
Li1..Li2′	2.790(19) × 2	Li1a..Li2a	2.642(21) × 2
Li1..Li3	2.35(4)	Li1a..Li3	1.748(28)
Li1..Li4	1.838(13) × 2	Li1a..Li4	2.201(9) × 2
Li2..Li2a	1.105(15)		
Li2..Li3	2.252(17)	Li2a..Li3	1.505(20)
Li2..Li3′	2.503(20)	Li2a..Li3′	2.880(23)
Li2..Li4	1.970(4)	Li2a..Li4	2.755(15)
Li3..Li4	3.60(2)	Li3..Li4′	3.64(2)
Li1a : Li3	1.60	Li2a : Li3	0.90
Li1a : Li4	3.72	Li2a : Li4	2.09
Li1a : (Li3+Li4)	1.12	Li2a : (Li3+Li4)	0.63
Li3 : Li4 2.33			

The refined structural parameters in Tables 4.8 and 4.9 and Table 3.11 confirm that the end-members Li_2MoO_4 and Li_4GeO_4, and β-$Li_3Ge_{0.5}Mo_{0.5}O_4$, all have distinct structures. All of them show full occupancy of their respective Li tetrahedral sites (Li1 and Li2) in their structures with no occupation of interstitial tetrahedral or octahedral sites. There is good agreement between the refined structural parameters for Li_2MoO_4 and those presented by Kolitsch et al.[167],

from single crystal X-ray diffraction data. β-$Li_3Ge_{0.5}Mo_{0.5}O_4$ has a unit cell volume of 174.85 $Å^3$, which is 11.5% bigger than that in the isostructural β-Li_3PO_4 (156.87 $Å^3$) [166]. This is mainly attributed to the larger ionic radius of Mo^{6+} (0.41 Å) and Ge^{4+} (0.39 Å) compared to that of P in the pentavalent state (0.17 Å) when all are 4-coordinated [161].

The intermediate composition $Li_{3.6}Ge_{0.8}Mo_{0.2}O_4$ (x = 0.2) shows disorder in the Li^+ ion sublattice. Similar to the intermediate compositions in the $Li_{3+x}Ge_xP_{1-x}O_4$ system, in $Li_{3.6}Ge_{0.8}Mo_{0.2}O_4$, there is partial occupancy of the Li1 and Li2 sites, with some ions displaced towards the neighbouring interstitial tetrahedral sites along the *c*-axis direction. To keep the thesis coherent, the lithium distribution is labelled in the same way as in Chapter 3. Fig. 4.22 illustrates the Li^+ ion positions in tetrahedral Li sites for $Li_{3.6}Ge_{0.8}Mo_{0.2}O_4$. As seen in Fig. 4.22 and Table 4.13, Li1a is displaced by a distance of 0.625 Å from Li1 although still sitting within the same tetrahedron. However, Li2a is displaced to a further distance of 1.105 Å away from Li2, putting the Li2a ions in the neighbouring tetrahedral site. It is noteworthy that the thermal parameters of Li3 and Li4 are several times higher than those for Li1/Li1a and Li2/Li2a pairs, indicating significant positional disorder in these octahedral interstitial sites.

Similar to the $Li_{3+x}Ge_xP_{1-x}O_4$ system, the displacement of the tetrahedral Li ions towards the interstitial sites is a result of the repulsive forces between Li^+ ions in the Li3 and Li4 sites and the Li^+ ions in the Li2 sites, and to a certain extent, Li1 sites. What is different is that in $Li_{3+x}Ge_xP_{1-x}O_4$ system, as the Li2-Li2a displacement increases the small Li1-Li1a displacement decreases, while in $Li_{3.6}Ge_{0.8}Mo_{0.2}O_4$, both Li2-Li2a and Li1-Li1a displacements are relatively large. The Li1a location is near the shared face between the occupied and unoccupied tetrahedra, but the distance to the furthest oxygen in the unoccupied tetrahedron (O3) is 2.927 Å, meaning it cannot be considered to be 5-coordinate.

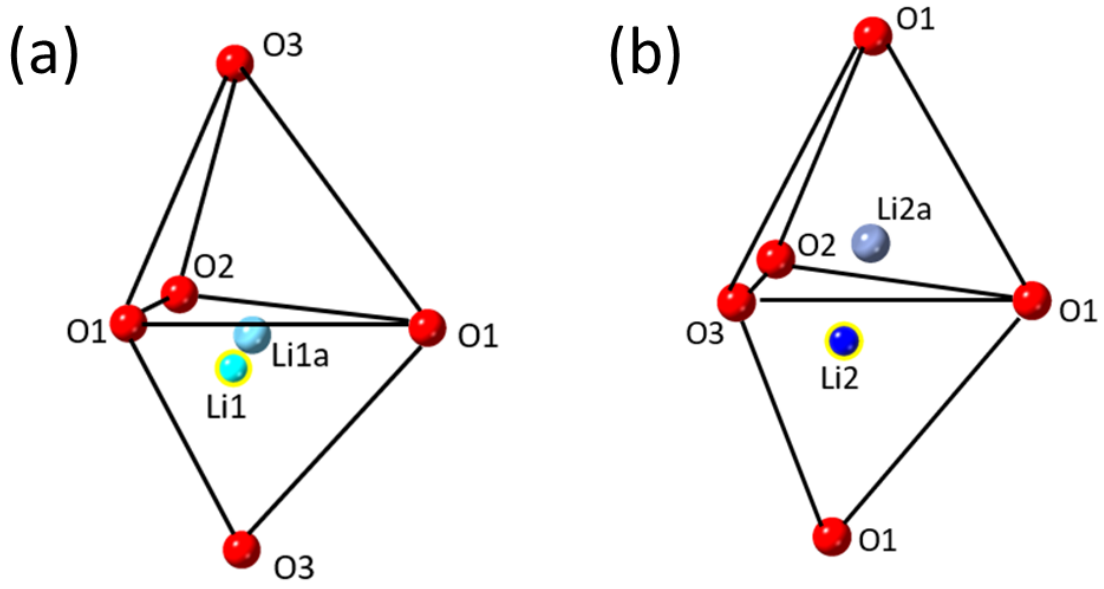

Figure 4.22 Li^+ ion positions in tetrahedral Li sites for $Li_{3.6}Ge_{0.8}Mo_{0.2}O_4$

As in the $Li_{3+x}Ge_xP_{1-x}O_4$ system, using the structural data it is possible to propose individual defects in $Li_{3.6}Ge_{0.8}Mo_{0.2}O_4$. From the inter-site ratios in Table 4.13, the Li3:Li2a ratio is approximately 1, indicating the presence of a Li^+ ion on the Li3 site causes displacement of one of the neighbouring Li2 ions (at a distance of 2.252 Å) into the Li2a site as seen in the $Li_{3+x}Ge_xP_{1-x}O_4$ system. The Li2a:Li4 ratio is approximately 2, indicating that the Li^+ ions in both the Li2 sites that face share with the Li4 site, with an Li2..Li4 distance of 1.970 Å, are displaced into the neighbouring Li2a sites. The displacement of Li1a seems to be caused by the presence of Li^+ ions in both Li3 and Li4, with the Li1a:(Li3+Li4) ratio approximating to 1. The Li3:Li4 ratio is approximately 2, suggesting clustering of these individual defects as in the $Li_{3+x}Ge_xP_{1-x}O_4$ system.

The proposed defects are summarised in Fig. 4.23. The Type I defect (Fig. 4.23a) is identical to that in the $Li_{3+x}Ge_xP_{1-x}O_4$ system, but the second defect (Fig.4.23b), designated here as Type IIa to distinguish it from that in the $Li_{3+x}Ge_xP_{1-x}O_4$ system, consists of an Li4 ion, two Li2a ions and two Li1a ions, i.e. all the face sharing Li^+ ions neighbouring the Li4 site are displaced. The 2:1 ratio of Li3:Li4 suggests clustering of the Type I and Type IIa defects. The smallest cluster

based on this ratio would involve three octahedral Li^+ ions i.e. two Type I defects with one Type IIa in the middle (Fig. 4.23c), which we designate here as Type IIIa.

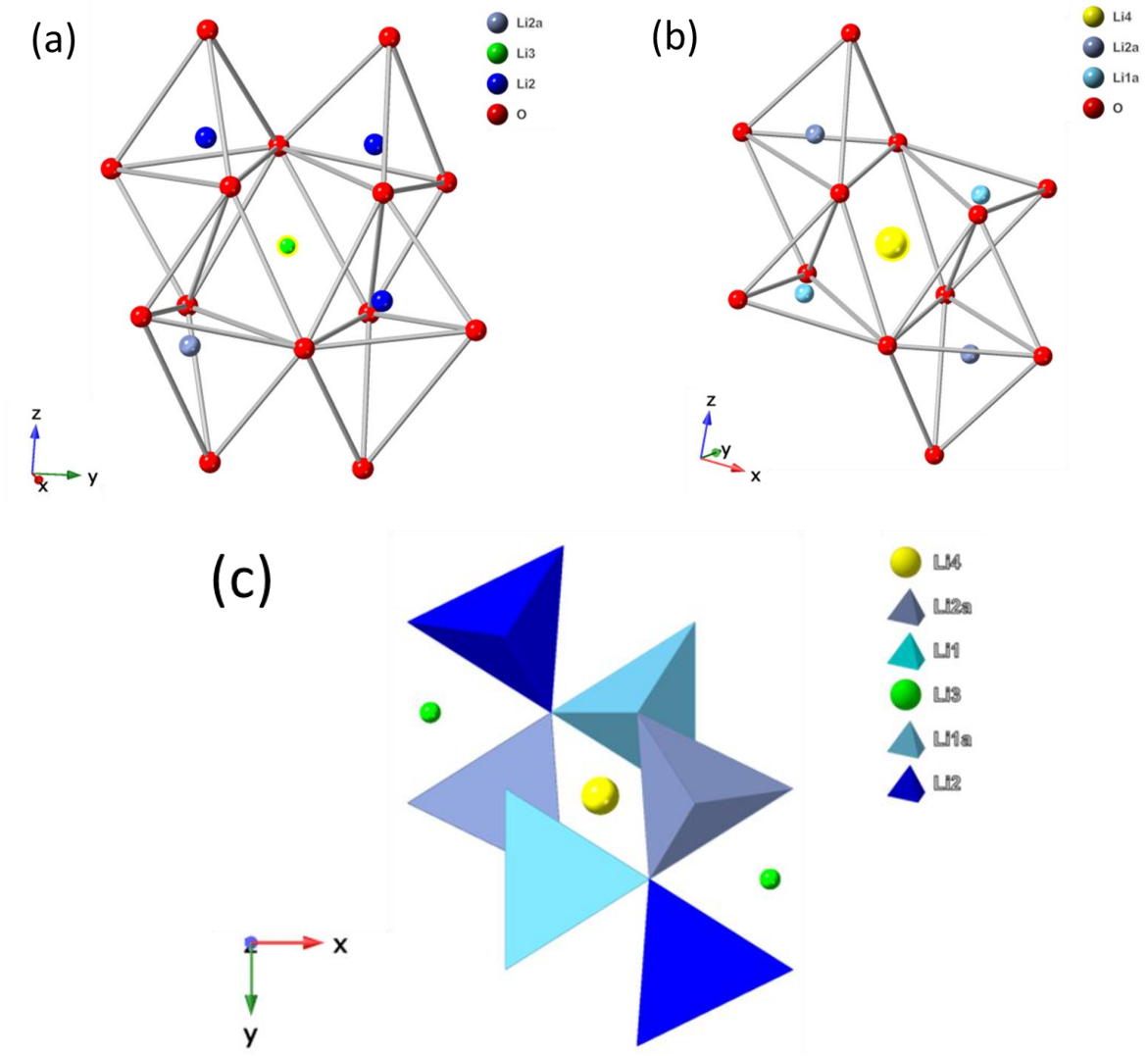

Figure 4.23 Three types of proposed defect in $Li_{3.6}Ge_{0.8}Mo_{0.2}O_4$: (a) Type I, (b) Type IIa and (c) Type IIIa defect clusters

4.3.4.2 Neutron total scattering

Although the average structure of the intermediate composition x = 0.2, β-$Li_3Ge_{0.5}Mo_{0.5}O_4$ and the two end-members Li_4GeO_4 and Li_2MoO_4 can be well identified through Rietveld analysis, the proposed defects in the x = 0.2 composition are simply derived from looking at inter-site contacts and site occupancy ratios. Further analysis of the diffuse neutron scattering

through total scattering methods allows for direct physical evidence of defect clustering to be probed. RMC simulations were carried out to fit the functions $S(Q)$ and $G(r)$ with the Bragg scattering used as a constraint.

Fig.4.24 shows the total pair correlation functions $G(r)$ for the studied compositions along with calculated patterns derived from the initial configurations based on the refined structures, but assuming full occupancy of Li1 and Li2 and excluding Li1a and Li2a. These calculated profiles were obtained through 40 cycles of smoothing of the corresponding individual pair correlations of the primary idealised configuration and summing them based on the neutron scattering coefficients. Since the primary idealised configuration-derived $G(r)$ represents the highly ordered crystalline structure and the experimental $G(r)$ illustrates the actual structure including the short-rang and long-range order, the difference between the primary model-derived $G(r)$ and experimental $G(r)$ is a measure of the disorder of the system.

As can be seen in Fig. 4.24, for the experimental $G(r)$, similar overall distributions can be observed for $x = 0.2$ and $x = 0.5$ since the space group $Pmn2_1$ for $x = 0.5$ is a subgroup of the space group *Pnma* for $x = 0.2$, while the experimental distributions for $x = 0.0$ and 1.0, are noticeably different, reflecting the change in structure for Li_4GeO_4 and Li_2MoO_4. The primary idealised configuration-derived $G(r)$ exhibits good accordance with the experimental $G(r)$ for $x = 0.0$ and 1.0 both over the short range (Fig. 4.24b) and the long range (Fig. 1a), reflecting their highly ordered crystalline structures (Tables 3.11 and 4.9). For the intermediate compositions $x = 0.2$ and β-$Li_3Ge_{0.5}Mo_{0.5}O_4$ ($x = 0.5$), the primary idealised configuration-derived $G(r)$ exhibits good agreement with the experimental data over the long range (3.6 Å and beyond); for the short range of 1.3-3.6 Å, the deviation from the experimental $G(r)$ indicates underlying local disorder. In the case of the $x = 0.5$ composition this is somewhat unexpected since the average structure shows no evidence of disorder. However, this would be

consistent with the proposal that the subtle transition at around 400 °C seen in the lattice parameter evolution is associated with changes in the defect structure.

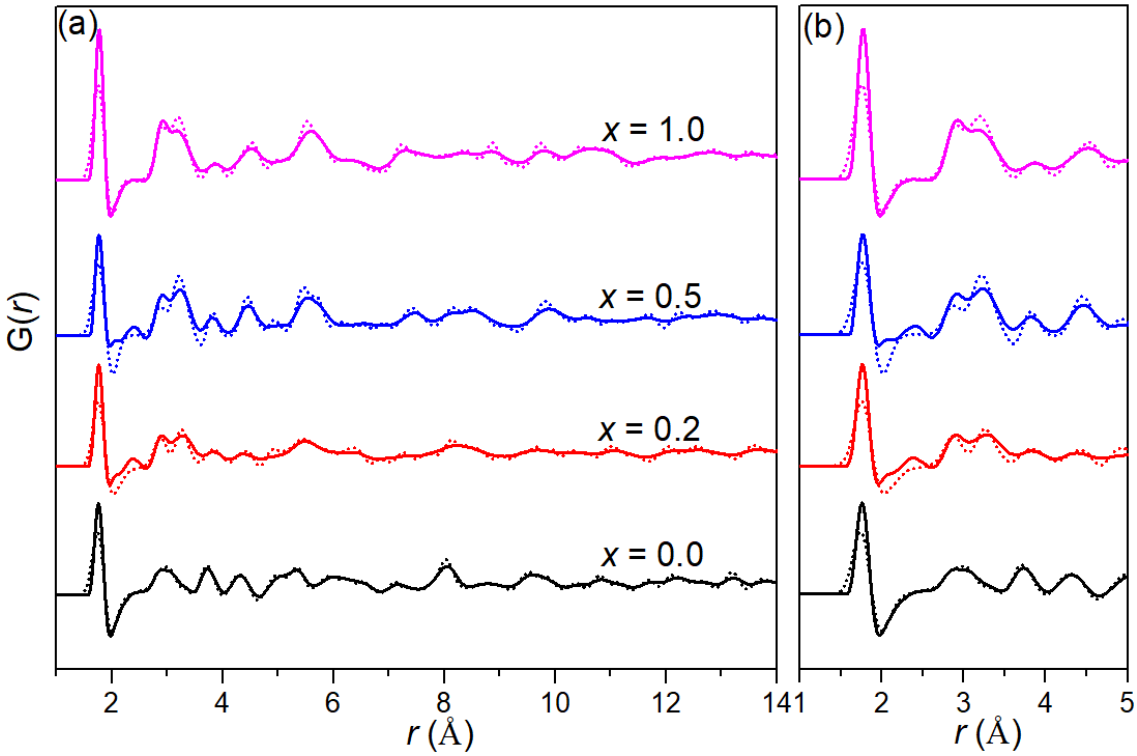

Figure 4.24 (a) Experimental (solid line) and primary idealised configuration-derived (dotted line) G(*r*) profiles for compositions in $Li_{4-2x}Ge_{1-x}Mo_xO_4$ system with short range correlations shown in (b)

To ensure adequate statistics in the individual pair correlations, 10 parallel sets of RMC calculations were performed over 7 days. For the intermediate composition, $x = 0.2$, the initial configurations had random distributions of Li3 and Li4 sites, with Ge and Mo randomly distributed on their shared site. For β-$Li_3Ge_{0.5}Mo_{0.5}O_4$, 10 different initial configurations were used each with a random distribution of Ge and Mo. Calculations were also performed for Li_4GeO_4 and Li_2MoO_4, but since there was no randomness in the initial configuration, a single configuration was used for each of the 10 parallel calculations, but each calculation was started at a different time to ensure different random seeds were used. Fig. 4.25 to Fig. 4.27 show the final fitted *G*(*r*) and *S*(*Q*) profiles for these calculations.

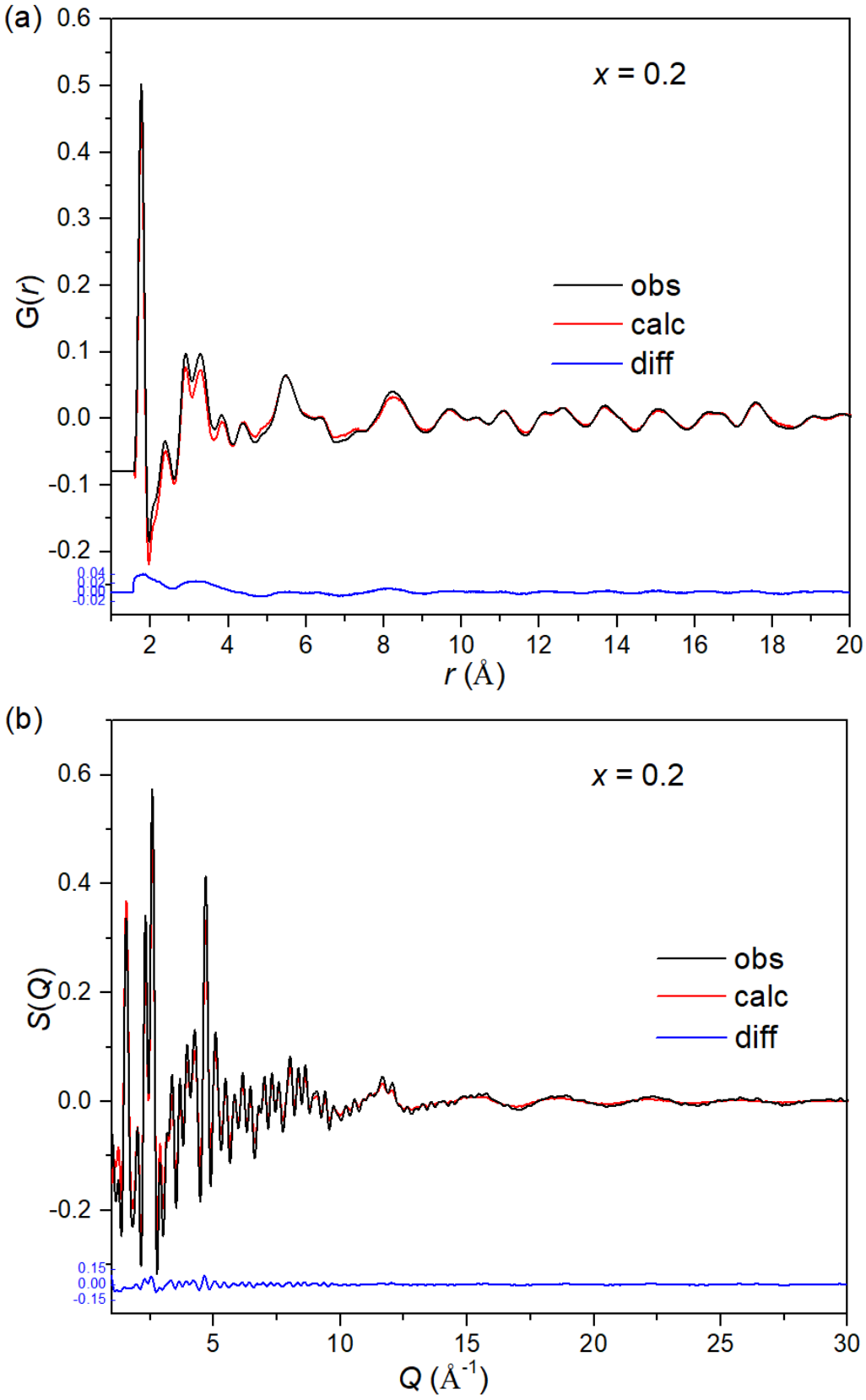

Figure 4.25 (a)fitted total pair correlation functions, *G*(*r*) and (b) fitted normalised total scattering structure factor, *S*(*Q*) for $Li_{3.6}Ge_{0.8}Mo_{0.2}O_4$ (x = 0.2) in $Li_{4-2x}Ge_{1-x}Mo_xO_4$ system

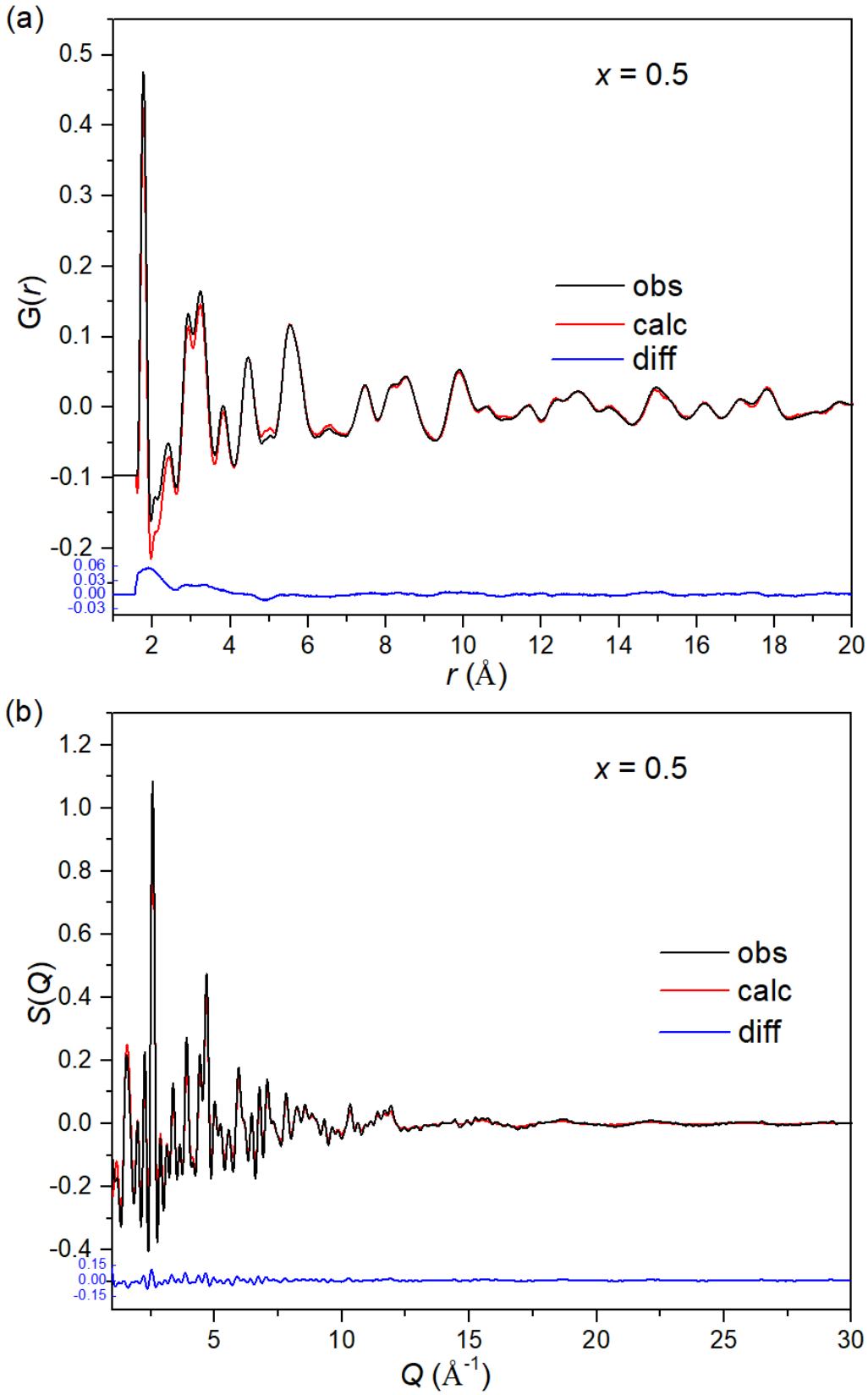

Figure 4.26 (a)fitted total pair correlation functions, *G*(*r*) and (b) fitted normalised total scattering structure factor, *S*(*Q*) for β-$Li_3Ge_{0.5}Mo_{0.5}O_4$ (*x* = 0.5) in $Li_{4-2x}Ge_{1-x}Mo_xO_4$ system

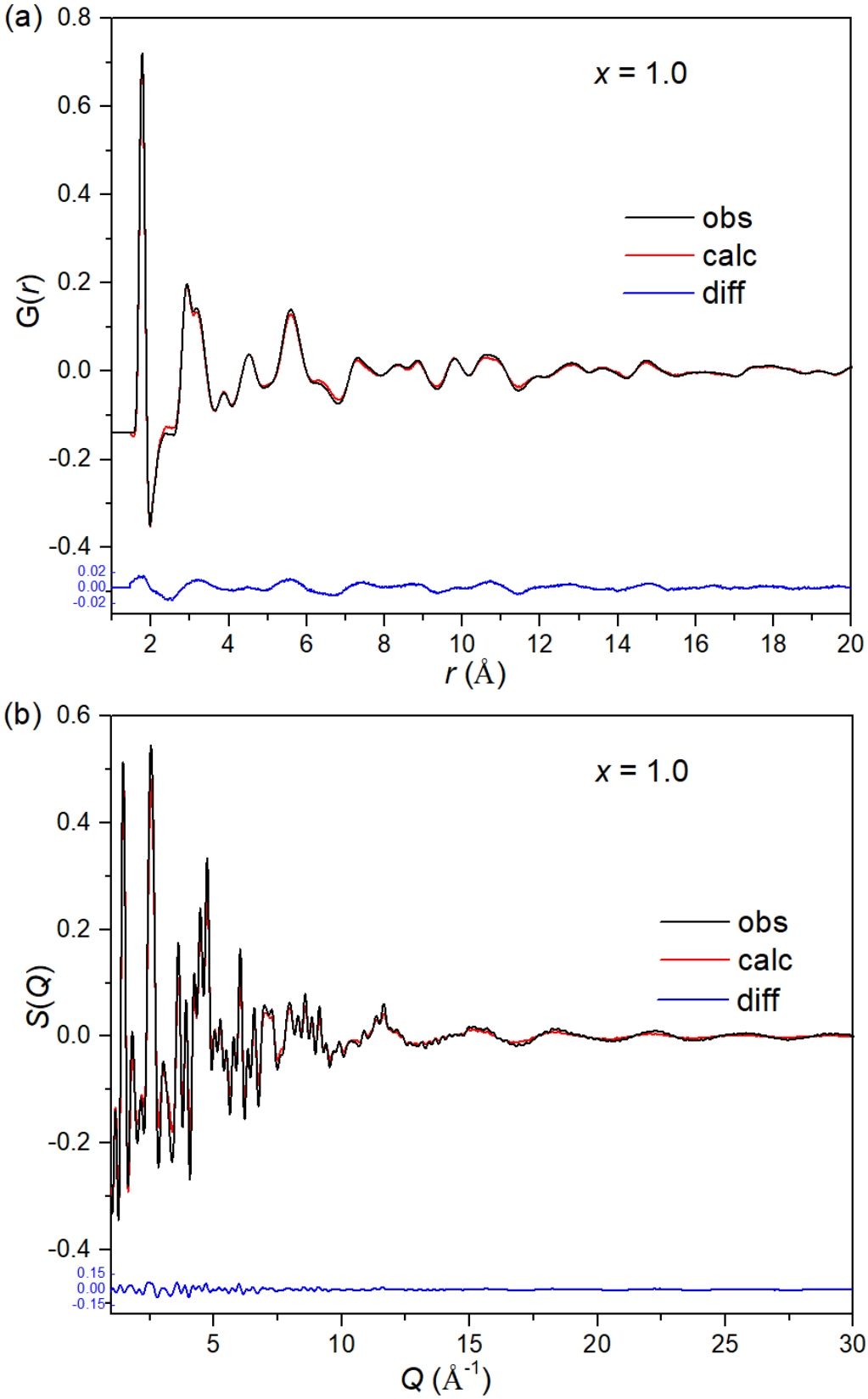

Figure 4.27 (a)fitted total pair correlation functions, *G*(*r*) and (b) fitted normalised total scattering structure factor, *S*(*Q*) for Li_2MoO_4 (*x* = 1.0) in $Li_{4-2x}Ge_{1-x}Mo_xO_4$ system

While the fits to both the $S(Q)$ and $G(r)$ data for the $x = 1.0$ composition are good, the fits to $G(r)$ profiles for $x = 0.5$ and 0.2 are less so, despite good fits to their $S(Q)$ data. In the case of the $x = 0.5$ data this may be due to the fact that the counting time for data collection was about half that in the other data collections, leading to poorer statistics. In both cases the main differences occur due to the modelling of the Li-O correlations. These correlations lead to negative peaks in the $G(r)$ profiles, the shortest at about 1.9 Å, where the largest differences occur. Despite these issues, the RMC method does appear to generally reproduce the experimental profiles and some information may be extracted from these fits.

Fig. 4.28 shows the individual pair correlations $g_{ij}(r)$ derived from the RMC configurations, with coordination numbers and modal and mean contacts given in Tables 4.14 to 4.16. The $g_{OO}(r)$ correlations are dominated by two peaks at around 2.9 and 3.2 Å, as expected from the average structures. However, all three compositions show a weaker peak at around 2.3 to 2.4 Å suggesting some local distortion in the cation polyhedron, a feature not seen in the average structure. The Ge-O and Mo-O correlations, are very similar with a modal distance of approximately 1.77 Å in all cases, indicating that fits cannot distinguish between the Ge^{4+} and Mo^{6+} cations in their shared tetrahedral site. The value is however in good agreement with the average values obtained in the Rietveld analysis. As mentioned above the Ge^{4+} and Mo^{6+} cations have very similar ionic radii of 0.39 and 0.41 Å in 4-coordinate geometry [161] and therefore similar bond lengths are expected for these cations. For the Li-O correlations, mean distances of approximately 2.26, 2.02 and 2.17 Å are observed for $x = 0.2$, 0.5 and 1.0 compositions, respectively. However, the mean values differ considerably from the mean distances from the Rietveld analysis (2.06, 1.98 and 1.97 Å for $x = 0.2$, 0.5 and 1.0 compositions, respectively) except for $x = 0.5$, although the trend is the same. For the reasons discussed above these distances should be interpreted cautiously. The Ge/Mo-Ge/Mo correlations are as expected from the average structures for $x = 0.2$ and 0.5. The $g_{MoMo}(r)$ profile for the $x = 1.0$

configuration is somewhat broadened and less well defined than expected considering the quality of the fit. The small spike seen at around 3.5 Å is due to the build-up of atoms in the model at the minimum distance value set in the calculations. The Li-Ge/Mo correlations all show asymmetry in the first correlation peak most noticeably in the $x = 0.2$ composition where a clear second maximum is seen at around 3.5 Å. This feature is again not directly evident from the average structure from the Rietveld analysis. The $g_{\text{Li-Li}}(r)$ profiles differ considerably for $x = 0.2$ compared to the two other compositions. In the $x = 0.2$ composition, the main correlation is shifted to a much lower value of around 2.5 Å compared to values of ca. 3 Å in the $x = 0.5$ and 1.0 compositions. While some short Li-Li correlations would be expected due to the presence of interstitial Li^+ ions and the resulting defect structure, one would still expect the vast majority of Li-Li contacts to be in the order of 3 Å, but despite the broadness of the correlation, this does not appear to be reflected in the RMC derived model for the $x = 0.2$ composition. The spike in the $g_{\text{Li-Li}}(r)$ profile for $x = 0.2$ at around 2.2 Å is due to the build-up of atoms at the minimum distance as discussed above for the $g_{\text{MoMo}}(r)$ profile for the $x = 1.0$ composition.

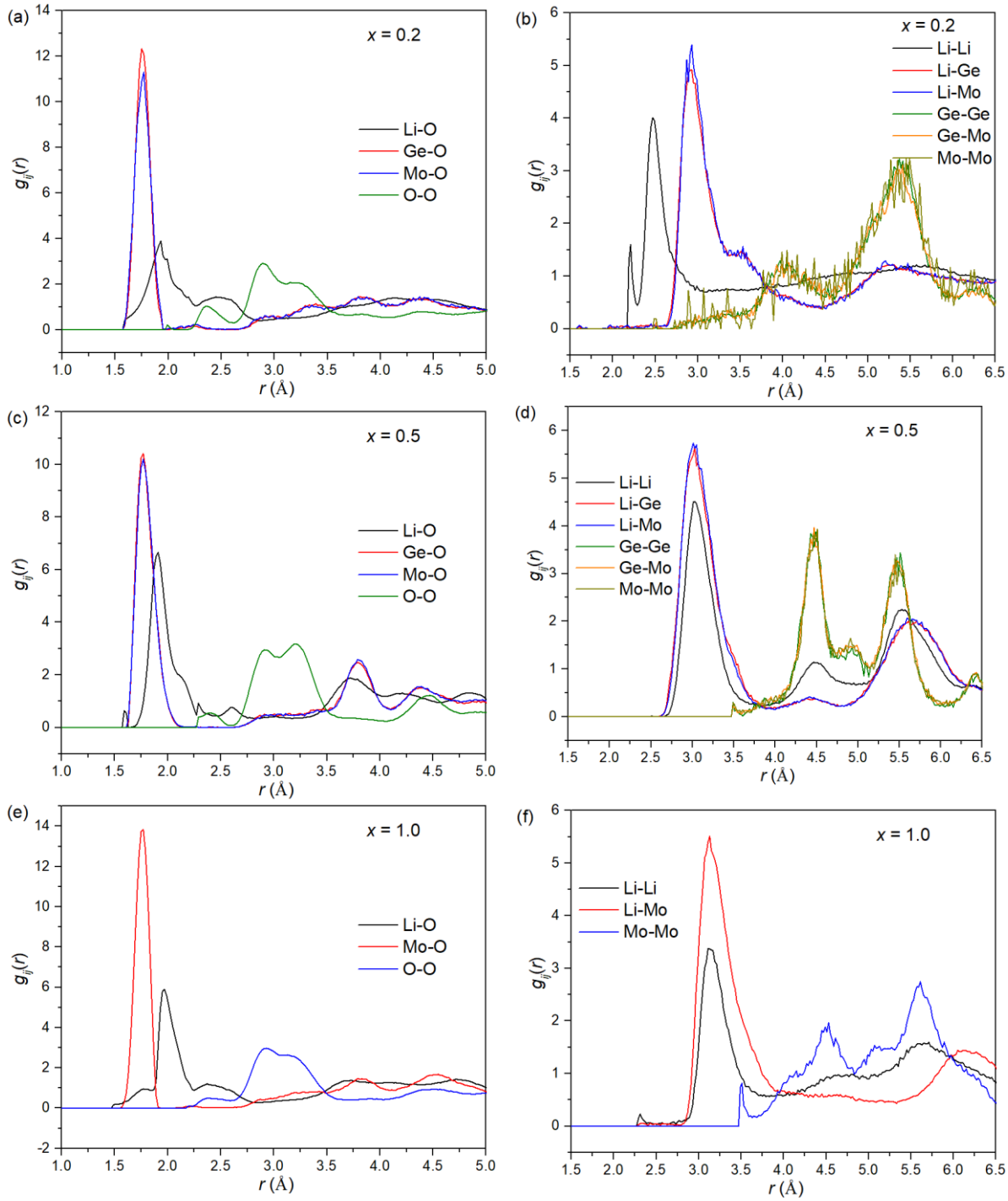

Figure 4.28 (left) $g_{MO}(r)$ and $g_{OO}(r)$, (right) $g_{MM}(r)$ pair correlation functions for (a, b) x = 0.2, (c, d) x = 0.5 and (e, f) x = 1.0 compositions in $Li_{4-2x}Ge_{1-x}Mo_xO_4$ system

Tables 4.14 to 4.16 summarise the coordination numbers (CN), modal distances and mean distances for the individual pair correlations in x = 0.2, 0.5 and 1.0. The oxygen coordination numbers for Ge and Mo approximate to 4 in the x = 0.2 composition, consistent with the tetrahedral geometry for these atoms. The weighted average of the mean Ge/Mo-O distances of 1.77 Å is almost identical to the value of 1.76 Å derived from the Rietveld analysis. In contrast, the Li coordination number to oxygen is around 5.6, far greater than the theoretical value based on the formula of 4.3 (i.e. $0.83 \times 4 + 0.17 \times 6$). At the same time, the mean Li-O distance of 2.26 Å is much higher than the corresponding weighted average values from the Rietveld analysis of 2.06 Å and the modal value of 1.89 Å. Examination of the $g_{\mathrm{LiO}}(r)$ profile in Fig. 4.28 shows it to be very broad, with a second broad correlation at around 2.5 Å. The two peaks can be approximately attributed to the tetrahedrally and octahedrally coordinated Li^+ ions, respectively, however, their relative intensities suggest more Li with higher coordination than would be predicted, as confirmed by the coordination number.

Table 4.14 Summary of the coordination numbers (CN), modal and mean bond distances from the RMC analysis of x = 0.2 composition in $Li_{4-2x}Ge_{1-x}Mo_xO_4$ system. Estimated standard deviations between the 10 parallel calculations are given in parentheses.

central atom	bonded atom	CN	Modal distance (Å)	Mean distance (Å)	Cut off (Å)
Li	Li	7.026(7)	2.706(18)	2.782(1)	3.50
Li	Ge	3.552(7)	2.900(5)	3.326(2)	4.40
Li	Mo	0.900(2)	2.904(11)	3.334(5)	4.40
Li	O	5.582(8)	1.892(3)	2.259(1)	3.00
Ge	Li	15.984(33)	2.900(5)	3.330(2)	4.40
Ge	Ge	1.952(18)	3.93(14)	4.033(6)	4.60
Ge	Mo	0.493(5)	4.07(20)	4.053(13)	4.60
Ge	O	3.729(7)	1.811(2)	1.7732(4)	2.00
Mo	Li	16.192(36)	2.904(11)	3.327(7)	4.40
Mo	Ge	1.973(20)	4.07(20)	4.037(11)	4.60
Mo	Mo	0.505(36)	3.7(1.1)	4.048(36)	4.60
Mo	O	3.635(24)	1.801(8)	1.774(2)	2.00
O	Li	5.023(7)	1.892(3)	2.257(1)	3.00
O	Ge	0.746(1)	1.811(2)	1.7755(4)	2.00
O	Mo	0.182(1)	1.801(8)	1.777(2)	2.00
O	O	12.636(9)	2.841(7)	3.192(1)	4.00

Table 4.15 Summary of the coordination numbers (CN), modal and mean bond distances from the RMC analysis of x = 0.5 composition in $Li_{4-2x}Ge_{1-x}Mo_xO_4$ system. Estimated standard deviations between the 10 parallel calculations are given in parentheses.

central atom	bonded atom	CN	Modal distance (Å)	Mean distance (Å)	Cut off (Å)
Li	Li	8.152(13)	3.032(10)	3.154(1)	3.80
Li	Ge	1.986(4)	3.010(19)	3.156(2)	3.80
Li	Mo	1.985(3)	3.015(15)	3.151(2)	3.80
Li	O	4.173(10)	1.853(4)	2.018(2)	2.50
Ge	Li	11.917(23)	3.010(19)	3.157(1)	3.80
Ge	Ge	2.369(22)	4.490(21)	4.445(10)	4.80
Ge	Mo	2.422(22)	4.477(31)	4.442(5)	4.80
Ge	O	3.972(8)	1.873(6)	1.817(1)	2.50
Mo	Li	11.913(18)	3.015(15)	3.152(1)	3.80
Mo	Ge	2.422(22)	4.477(31)	4.441(6)	4.80
Mo	Mo	2.343(35)	4.42(13)	4.443(10)	4.80
Mo	O	3.952(10)	1.880(5)	1.819(2)	2.50
O	Li	3.130(7)	1.853(4)	2.016(2)	2.50
O	Ge	0.497(1)	1.873(6)	1.818(1)	2.50
O	Mo	0.494(1)	1.880(5)	1.820(2)	2.50
O	O	12.416(20)	3.256(6)	3.172(2)	4.00

Table 4.16 Summary of the coordination numbers (CN), modal and mean bond distances from the RMC analysis of x = 1.0 composition in $Li_{4-2x}Ge_{1-x}Mo_xO_4$ system. Estimated standard deviations between the 10 parallel calculations are given in parentheses.

central atom	bonded atom	CN	Modal distance (Å)	Mean distance (Å)	Cut off (Å)
Li	Li	4.858(19)	3.132(7)	3.334(3)	4.00
Li	Mo	4.200(9)	3.117(9)	3.329(1)	4.00
Li	O	4.654(7)	2.185(10)	2.173(2)	2.85
Mo	Li	8.400(18)	3.117(9)	3.336(1)	4.00
Mo	Mo	3.393(25)	4.47(15)	4.375(4)	4.83
Mo	O	3.685(4)	1.826(2)	1.7685(2)	2.00
O	Li	2.327(3)	2.185(10)	2.160(2)	2.85
O	Mo	0.921(1)	1.826(2)	1.7720(2)	2.00
O	O	10.235(14)	2.878(7)	3.099(1)	3.70

Based on the above results, it was concluded that the RMC calculations for the x = 0.2 composition fail to accurately model the Li^+ ion distribution and further analysis was postponed until a better fit or new data were obtained.

4.4 Conclusions

The solid solution limit was first investigated in the Li_2MoO_4-Li_4GeO_4 ($Li_{4-2x}Ge_{1-x}Mo_xO_4$) system, it was found that pure LISICON type structures can be formed in the range of $0.1 \leq x \leq 0.5$ with a relatively low synthesis temperature in the range of 650 to 850 ºC, and the relative amounts of the β-phase and γ-phase change with temperature especially for the x = 0.4 and x = 0.5 compositions.

Rietveld analysis of combined neutron and X-ray diffraction data for the x = 0.2 composition revealed a γ-phase structure with two interstitial octahedral sites (Li3 and Li4) and displacement of ions in both tetrahedral sites. Two basic types of defect were found associated with the interstitial octahedral sites Li3 and Li4. The Type I defect is identical to that in the $Li_{3+x}Ge_xP_{1-x}O_4$ system, and involves Li^+ ions in the Li3 site and a displacement of one of the Li2 ions from

a face sharing site into the Li2a position. Thus, this defect consists of two interstitials (one octahedral and one tetrahedral) and a tetrahedral vacancy. The second type of defect, Type IIa, is slightly different to the Type II defect identified in the $Li_{3+x}Ge_xP_{1-x}O_4$ system and consists of an Li4 ion, two displaced Li2a ions and two displaced Li1a ions. Since the Li1a positions is located in the same tetrahedron as Li1, this tetrahedron cannot be considered to be vacant and the defect can be described as being made up of three interstitial Li^+ ions (2 tetrahedral and one octahedral), two tetrahedral vacancies, and two slightly displaced tetrahedral Li^+ ions. The structural evidence suggests possible clustering of these two individual defects in a 2:1 ratio. The Type IIIa defect cluster represents the simplest model, consisting of two Type I and one Type IIa.

For the $x = 0.2$ composition, the failure of RMC calculations to accurately model the Li^+ ion distribution might be due to the use of natural Li in the starting materials which includes ^6Li and ^7Li at the same time. For ^6Li, it has a much higher absorption cross section of 940 barns than that of ^7Li (0.045 barns) giving natural Li an absorption cross section of 70.5 barn [116]. The high absorption cross section of natural Li makes the collected Li-related signal less prominent, making analysis more difficult. Use of a pure ^7Li sample as used in $Li_{3+x}Ge_xP_{1-x}O_4$ would aid the analysis, but would require new data to be collected.

Further work based on the current data could utilise a more realistic starting model including the displaced Li1a and Li2a positions, although technically it is difficult to produce a random supercell configuration based on this model. Other approaches could involve constraints separating out octahedral and tetrahedral Li in the model, although attractive, this approach needs to be considered carefully since it introduces a preconceived bias into the model.

In the $Li_{4-2x}Ge_{1-x}Mo_xO_4$ system, the highest conductivity and lowest activation energy are seen in the $x = 0.2$ composition with a value of conductivity at 250 °C of 5.02×10^{-3} S cm^{-1} and activation energy of 0.67 eV.

Chapter 5 Structure and conductivity in the $Li_{4-2x}Ge_{1-x}W_xO_4$ system

5.1 Introduction

Among the LISICON-type oxides, $Li_{3+x}M_yN_{1-y}O_4$, the valence difference between the cation pairs of M and N is usually one, such as $Li_{3+x}Si_xP_{1-x}O_4$, $Li_{3+x}Ge_xP_{1-x}O_4$ and $Li_{3+x}Ge_xV_{1-x}O_4$; other types are seldom reported. In 2003, Burmakin et al. reported that $Li_{3.70}Ge_{0.85}W_{0.15}O_4$ was isostructural with $Li_{3.75}Ge_{0.75}V_{0.25}O_4$, exhibiting an ionic conductivity of 0.06 $mS\cdot cm^{-1}$ at 25 ℃ and 10 $mS\cdot cm^{-1}$ at 200 ℃, making it among the best LISICON conductors [163]. However, details of the synthesis conditions required to produce pristine powders and sintered pellets were not reported. In earlier work by these authors on the $Li_{4-2x}Ge_{1-x}W_xO_4$ system, a γ-type phase was seen in the compositional range $0.10 \leq x \leq 0.20$, with phase mixtures seen at lower and higher x-value compositions [168]. Conductivity was reported to reach a maximum and activation energy a minimum (*ca*. 0.41 eV) at $x = 0.15$. These authors attributed this to optimum bottleneck size in the $x = 0.15$ composition. Details of the Li^+ ion distribution were investigated by neutron diffraction [163]. It was found that the Li^+ ion distribution varied with temperature (Table 5.1).

Table 5.1 Refined structural parameters of $Li_{3.70}Ge_{0.85}W_{0.15}O_4$ at 25 °C and 600 °C [163]

Space group		*Pnma*				
Temp.		**25 °C**				
Atom	Position	*x*	*y*	*z*	Temp. factor	Population
Li1	4*c*	0.092(3)	0.250	0.668(7)	0.59(8)	0.61(3)
Li1a	4*c*	0.084(6)	0.250	0.868(8)	0.59(8)	0.39(3)
Li2	8*d*	0.168(2)	-0.024(3)	0.325(4)	1.13(9)	1.40(4)
Li2a	8*d*	0.168(4)	0.052(7)	0.116(8)	1.13(9)	0.60(4)
Li3	4*c*	0.285(9)	0.250	-0.038(6)	0.67(9)	0.16(2)
Li4	8*d*	0.039(4)	0.440(7)	0.384(7)	0.67(9)	0.54(2)
Ge	4*c*	0.4157(5)	0.250	0.345(1)	---	0.850
V	4*c*	0.4157(5)	0.250	0.345(1)	---	0.150
O1	8*d*	0.3353(5)	0.0215(8)	0.2217(8)	---	2.0
O2	4*c*	0.4138(6)	0.250	0.670(1)	---	1.0
O3	4*c*	0.0623(7)	0.250	0.259(1)	---	1.0
Unit cell parameters		a = 10.938(1) Å, b = 6.274(1) Å, c = 5.1609(6) Å, V = 354.18(7) Å^3				
Temp.		**600 °C**				
Atom	Position	*x*	*y*	*z*	Temp. factor	Population
Li1	4*c*	0.110(8)	0.250	0.667(9)	0.59(8)	0.51(5)
Li1a	4*c*	0.096(8)	0.250	0.873(8)	0.59(8)	0.49(5)
Li2	8*d*	0.167(4)	-0.031(6)	0.327(6)	1.13(9)	1.04(6)
Li2a	8*d*	0.169(6)	0.041(7)	0.124(8)	1.13(9)	0.96(6)
Li3	4*c*	0.190(9)	0.250	-0.022(7)	0.67(9)	0.36(2)
Li4	8*d*	0.041(6)	0.485(9)	0.421(8)	0.67(9)	0.34(2)
Ge	4*c*	0.4156(5)	0.250	0.345(1)	---	0.850
V	4*c*	0.4156(5)	0.250	0.345(1)	---	0.150
O1	8*d*	0.3352(6)	0.0226(11)	0.232(1)	---	2.0
O2	4*c*	0.4136(7)	0.250	0.671(1)	---	1.0
O3	4*c*	0.0601(6)	0.250	0.257(1)	---	1.0
Unit cell parameters		a = 11.052(1) Å, b = 6.345(1) Å, c = 5.244(1) Å, V = 367.71(7) Å^3				

The thermal variation of interstitial Li^+ ion distribution would be consistent with changes in defect clustering, as proposed by Abrahams and Bruce in $Li_{3.5}Ge_{0.5}V_{0.5}O_4$ [85]. Despite the work carried out by Burmakin et al., there are still questions regarding the optimum synthesis and sintering conditions. Considering that the LISICON structure is readily preserved in other systems over large compositional ranges, why is the solid solution limit only $x = 0.20$ in this system? The theoretical limit would be around $x = 0.50$, ($Li_3Ge_{0.5}W_{0.5}O_4$) i.e. when all the octahedral sites were vacant. Could optimisation of the synthesis conditions allow the solid solution limit be extended? Could higher conductivities be attained by improved sintering? The exceptionally high conductivity of this system merits further study through a systematic investigation.

5.2 Experimental

5.2.1 Sample synthesis

Samples of general formula $Li_{4-2x}Ge_{1-x}W_xO_4$ (x = 0.05, 0.10, 0.15, 0.20, 0.25, 0.30, 0.40, 0.50, 0.60 and 1.0), were prepared by solid-state reaction. Stoichiometric amounts of Li_2CO_3 (99%, BDH), GeO_2 (99.999%, Aldrich) and WO_3 (99.8%, Alfa Aesar) were ground thoroughly in an agate mortar to form a homogenous paste with methylated spirits. After drying at 80 °C, the mixtures were heated in an alumina crucible at 650 °C for 1 h followed by calcining at temperatures between 650 and 1050 °C for various times up to 24 h. Samples were slow cooled in the furnace to room temperature. In some cases, regrinding and reheating several times was required in order to complete the reactions. Details of the specific heating regimes used are summarised in Table 5.2.

Table 5.2 Summary of Heating regimes used to prepare $Li_{4-2x}Ge_{1-x}W_xO_4$ samples

x value in $Li_{4-2x}Ge_{1-x}W_xO_4$	Heating regimes
$x = 0.05$	650 ºC for 1 h, 1000 ºC for 3 h
$x = 0.05$	650 ºC for 1 h, 1000 ºC for 6 h
$x = 0.05$	650 ºC for 1 h, 1000 ºC for 24 h
$x = 0.05$	650 ºC for 1 h, 1050 ºC for 6 h
$x = 0.10$	650 ºC for 1 h, 1000 ºC for 5 h, reground and reheated at 1000 ºC for 2.5 h, reground and reheated at 1000 ºC for 6 h
$x = 0.15$	650 ºC for 1 h, 1000 ºC for 5 h, reground and reheated at 1000 ºC for 2.5 h
$x = 0.20$	650 ºC for 1 h, 700 ºC for 24 h
$x = 0.20$	650 ºC for 1 h, 850 ºC for 24 h
$x = 0.20$	650 ºC for 1 h, 950 ºC for 6 h
$x = 0.20$	650 ºC for 1 h, 950 ºC for 24 h
$x = 0.20$	650 ºC for 1 h, 1000 ºC for 5 h
$x = 0.25$	650 ºC for 1 h, 1000 ºC for 5 h
$x = 0.30$	650 ºC for 1 h, 1000 ºC for 5 h
$x = 0.40$	650 ºC for 1 h, 900 ºC for 6 h
$x = 0.40$	650 ºC for 1 h, 1000 ºC for 6 h
$x = 0.50$	650 ºC for 1 h, 900 ºC for 6 h
$x = 0.50$	650 ºC for 1 h, 1000 ºC for 6 h
$x = 0.60$	650 ºC for 1 h, 900 ºC for 6 h
$x = 0.60$	650 ºC for 1 h, 1000 ºC for 6 h
$x = 1.0$	650 ºC for 1 h, 650 ºC for 24 h
$x = 1.0$	650 ºC for 1 h, 700 ºC for 24 h
$x = 1.0$	650 ºC for 1 h, 750 ºC for 24 h
$x = 1.0$	650 ºC for 1 h, 890 ºC for 16 h

The as-prepared powders were made into pellets using spark plasma sintering (SPS) (HPD 25/1, FCT, Rauenstein, Germany). Samples were pressed into a graphite die with 10 mm diameter surrounded by carbon foil. The resulting powder was then calcined at 800 to 950 °C

for 5 min at a uniaxial pressure of 60 MPa under vacuum. SPS processed samples were subsequently annealed at 850 °C for 13 h to remove residual carbon arising from the carbon foil.

5.2.2 Characterization

The density of ceramics pellets was measured based on the classical Archimedes method by displacement of water. X-ray powder diffraction (XRD) was used to characterize the crystallographic structure of samples. The XRD data were collected on a PANAlytical X'Pert Pro diffractometer, equipped with an X'Celerator detector, in θ/θ geometry using Ni-filtered Cu-Kα radiation (λ = 1.5418 Å), over the 2θ range 5° to 70° or 120° in steps of 0.0334° per step, with an effective count time of 200 s per step. The XRD data were analyzed using the Rietveld method with the GSAS suite of programs [122]. The starting models were based on the structures of $Li_{3.5}Zn_{0.5}GeO_4$ [84], Li_2WO_4 [169] and Li_4WO_5 [170]. The microstructure of the ceramic pellets was examined through scanning electron microscopy (SEM), using a FEI Inspect F (Hillsboro, OR) equipped with energy-dispersive X-ray spectroscopy (EDS).

For the impedance measurements, annealed ceramic pellets were first cut and polished into blocks of ca. 4 mm × 4 mm × 2 mm. Gold electrodes were sputtered by cathodic discharge. Electrical characterisation was carried out by a.c. impedance spectroscopy using a fully automated system based on a Solartron 1255 frequency response analyser in conjunction with a bespoke automatic current/voltage converter. Impedance data were collected over the frequency range 0.1 Hz to 1 × 10^6 Hz, in the approximate temperature range 50 to 300 °C. Fitting of impedance data was carried out using the program WFIRDARMM [159, 160].

Molecular dynamics (MD) simulations were perfomed to model the ion diffusion in $Li_{3.7}Ge_{0.85}W_{0.15}O_4$ using DL_POLY 4.09 [171]. A time step of 0.5 fs for MD runs of up to 0.5 ns

with a supercell containing 13920 ions was employed. Simulations were carried out at several temperatures (50 −300 °C).

5.3 Results and discussion

5.3.1 Synthesis condition exploration and structure refinement

Based on the successful synthesis of $x = 0.20$ in literature [168], the $x = 0.20$ composition was first selected to explore suitable synthesis conditions for the $Li_{4-2x}Ge_{1-x}W_xO_4$ system. Table 5.3 lists the calcination temperatures that were used in experiments to optimise the synthesis of the $x = 0.20$ composition and the corresponding reaction products. The corresponding XRD patterns are shown in Fig. 5.1.

Table 5.3 Synthesis conditions and corresponding reaction products for $x = 0.20$ composition in $Li_{4-2x}Ge_{1-x}W_xO_4$

Symbol	Final synthesis conditions	reaction products
A	700 ºC for 24h	Li_4WO_5 and Li_4GeO_4
B	850 ºC for 24h	Li_4WO_5 (major), LISICON solid solution (minor)
C	950 ºC for 6h	LISICON solid solution, Li_4WO_5, Li_2GeO_3
D	950 ºC for 24h	LISICON solid solution, Li_4WO_5, Li_2GeO_3
E	1000 ºC for 5h	LISICON solid solution (major), Li_4WO_5 (minor)

As can be seen in Fig. 5.1, when the calcination temperature is about 700 ºC, the starting material WO_3 reacts directly with Li_2O, which is the decomposition product of Li_2CO_3, at low temperatures (less than 600 ºC) to produce Li_4WO_5. Similarly, at these temperatures Li_4GeO_4 is formed through reaction of Li_2O and GeO_2. On increasing the temperature to 850 ºC, small amounts of a LISICON structured product are observed. This suggested that a higher temperature was required to complete the reaction. Raising the temperature to 950 ºC for

calcination time up to 24 h failed to yield pure products with samples always containing significant levels of Li_4WO_5 and Li_2GeO_3. As can be seen in Fig. 5.1, calcination at 1000 ºC for 5 h yielded an almost perfect LISICON XRD pattern, with good crystallinity, although a small amount of residual Li_4WO_5 was still present (2%). These experiments were used to guide the choice of synthesis conditions for the other compositions in the $Li_{4-2x}Ge_{1-x}W_xO_4$ system.

An orthorhombic LISICON structured solid solution, different from the structures of the end members, rhombohedral Li_2WO_4 and orthorhombic Li_4GeO_4, is observed in the $Li_{4-2x}Ge_{1-x}W_xO_4$ system. It is interesting that even under the "optimum" conditions some residual Li_4WO_5 remains. Based on the XRD results at 850 °C and 950 °C, which show significant amounts of Li_2GeO_3 and Li_4WO_5, it is clear that lithia volatilization represents a significant problem in the synthesis of compositions in the $Li_{4-2x}Ge_{1-x}W_xO_4$ system and that shorter reaction times at higher temperatures may be preferable to longer times at lower temperatures.

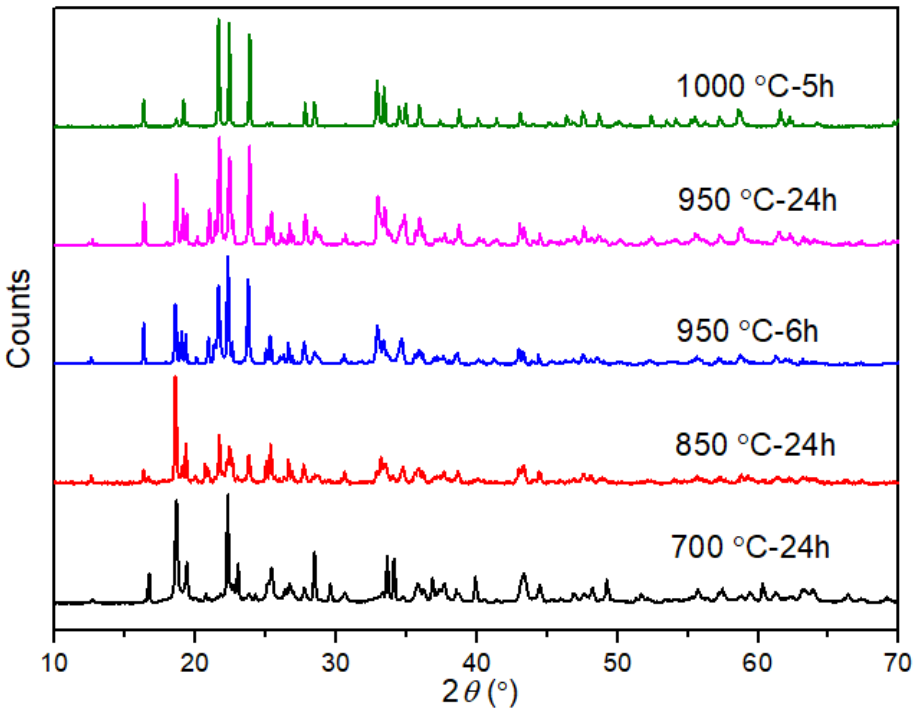

Figure 5.1 XRD patterns for x = 0.20 composition in the $Li_{4-2x}Ge_{1-x}W_xO_4$ system under different synthesis conditions

Fig. 5.2 shows the XRD patterns for the x = 0.05 composition prepared under different conditions. Based on the best synthesis conditions for the x = 0.20 composition, calcination at 1000 ºC for 3 h was used as a starting point for exploring the conditions required for this composition. As seen in Fig. 5.2a, a LISICON-type solid solution can be effectively synthesized under these conditions. However, a non-negligible amount of the end member Li_4GeO_4 is also present. Through prolonging the calcination time from 6 h to 24 h, the amount of Li_4GeO_4 decreased, but the new impurities Li_2GeO_3 and $Li_6Ge_2O_7$ became evident, with $Li_6Ge_2O_7$ becoming relatively dominant under the harsher conditions of calcination at 1050 ºC for 6 h. The appearance of these lithium germanate phases is consistent with lithia loss. Since no evidence of a residual lithium tungstate phase was seen it is likely that the LISICON phase produced is richer in W and poorer in Ge than would be inferred from the starting composition. This is consistent with the lower end of the solid solution lying above x = 0.05, as previously proposed by Burmakin et al. [168].

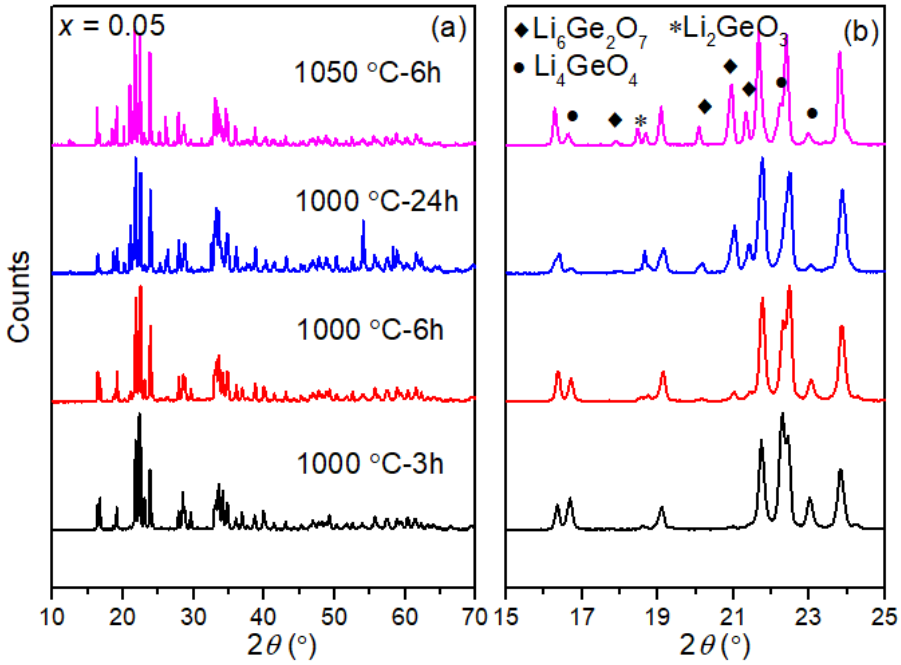

Figure 5.2 XRD patterns of the x = 0.05 composition synthesized under various conditions

Fig.5.3 shows the XRD patterns for selected compositions in the range of $0.10 \leq x \leq 0.40$ in the $Li_{4-2x}Ge_{1-x}W_xO_4$ system, all of which were calcined at 1000 ºC for several hours. As in the analogous molybdate system, with increasing W content, less lithium sites are required to compensate for the adding of positive charge. From the XRD patterns for the compositions (x = 0.10, 0.15, 0.20, 0.25, 0.30 and 0.40), it can be seen that a LISICON structured phase is formed in the range of $0.10 \leq x \leq 0.40$. However, in all these compositions, the impurity Li_4WO_5 is evident and increases with increasing x-value, especially for x = 0.30 and x = 0.40 compositions.

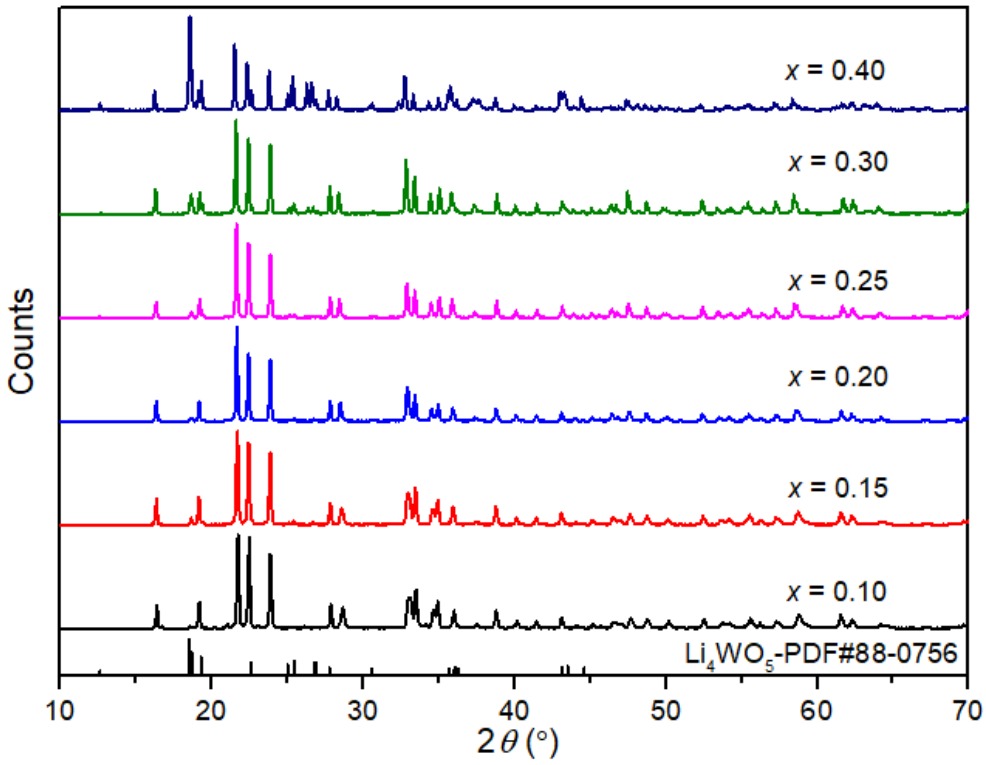

Figure 5.3 XRD patterns for x = 0.10, 0.15, 0.20, 0.25, 0.30 and 0.40 compositions of $Li_{4-2x}Ge_{1-x}W_xO_4$. All were calcined at 1000 ºC for several hours

The structures of the compositions $0.10 \leq x \leq 0.40$ were refined and crystal and refinement parameters are summarised in Table 5.4 and presented graphically in Fig. 5.4. The a and b axes increase while the c-axis decreases with increasing W content. With increasing x-value, the unit

cell volume, *V*, generally increases and is consistent with the replacement of smaller Ge^{4+} ions by larger W^{6+} ions (r = 0.39 and 0.42 Å, respectively in 4-fold coordination [161]). The variation in unit cell volume shows a sharp rise in the range of $0.10 \leq x \leq 0.25$, but levels off in the range of $0.25 \leq x \leq 0.40$. Combined with the increasing levels of Li_4WO_5 evident in the XRD patterns (Fig. 5.3), it can be concluded that the solid solution limit lies around x = 0.25 in the $Li_{4-2x}Ge_{1-x}W_xO_4$ system. This is somewhat higher than that observed by Burmakin et al. [168].

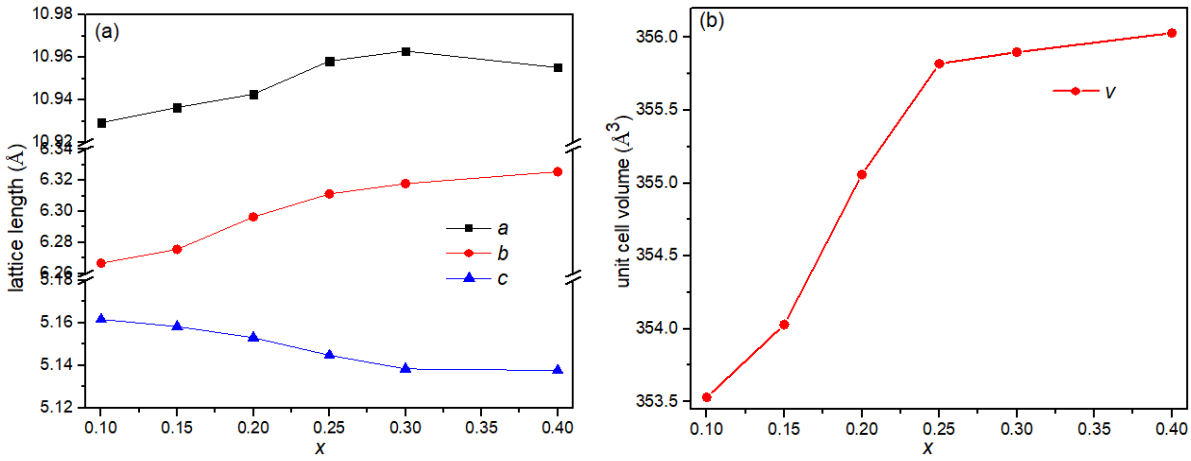

Figure 5.4 Compositional variation of (a) lattice parameters and (b) unit cell volume in the $Li_{4-2x}Ge_{1-x}W_xO_4$ system.

Table 5.4 Crystal and refinement parameters for $Li_{4-2x}Ge_{1-x}W_xO_4$

Chemical formula	$Li_{3.8}Ge_{0.9}W_{0.1}O_4$	$Li_{3.7}Ge_{0.85}W_{0.15}O_4$	$Li_{3.6}Ge_{0.8}W_{0.2}O_4$	$Li_{3.5}Ge_{0.85}W_{0.25}O_4$	$Li_{3.4}Ge_{0.7}W_{0.3}O_4$	$Li_{3.2}Ge_{0.6}W_{0.4}O_4$
Crystal system	Orthorhombic	Orthorhombic	Orthorhombic	Orthorhombic	Orthorhombic	Orthorhombic
Space group	*Pnma*	*Pnma*	*Pnma*	*Pnma*	*Pnma*	*Pnma*
Unit cell dimensions (Å)	*a* = 10.9293(8) *b* = 6.2667(4) *c* = 5.1617(3)	*a* = 10.9365(8) *b* = 6.2756(4) *c* = 5.1583(5)	*a* = 10.9427(6) *b* = 6.2965(3) *c* = 5.1531(2)	*a* = 10.9583(5) *b* = 6.3113(3) *c* = 5.1448(2)	*a* = 10.9630(5) *b* = 6.3179(3) *c* = 5.1384(3)	ɑ = 10.9552(8) *b* = 6.3256(4) *c* = 5.1377(3)
Volume (Å^3)	353.53(6)	354.03(6)	355.06(4)	355.82(4)	355.90(4)	356.03(4)
Z	4	4	4	4	4	4
Density (calculated)	3.271 g/cm^3	3.357 g/cm^3	3.439 g/cm^3	3.522 g/cm^3	3.613 g/cm^3	3.806 g/cm^3
Weight fraction of Li_4WO_5 phase	NA	1.9%	1.2%	2.3%	7.8%	47.8%
R-factors[a]	R_{wp} = 0.1253 R_p = 0.0919 R_{ex} = 0.0420 R_F^2 = 0.1028	R_{wp} =0.1297 R_p =0.0979 R_{ex} = 0.0409 R_F^2 =0.1128	R_{wp} = 0.1197 R_p = 0.0924 R_{ex} = 0.0411 R_F^2 = 0.1144	R_{wp} = 0.1235 R_p = 0.0961 R_{ex} = 0.0453 R_F^2 = 0.1051	R_{wp} = 0.1452 R_p = 0.1115 R_{ex} = 0.0446 R_F^2 = 0.1653	R_{wp} = 0.1753 R_p = 0.1225 R_{ex} = 0.0445 R_F^2 = 0.1838
No. of variables	32	42	43	44	42	60
No. of profile points used	3290	1794	1794	1794	1794	3290

Fig. 5.5 shows the fitted diffraction profiles for the x = 0.15 and 0.40 compositions. For the x = 0.15 composition, the LISICION phase (space group *Pnma*) shows good crystallinity, with only a small amount of Li_4WO_5 as a secondary phase. In contrast, the monoclinic Li_4WO_5 becomes the dominant phase in the x = 0.40 composition, with a LISICON secondary phase probably corresponding to x = 0.25, the solid solution limit.

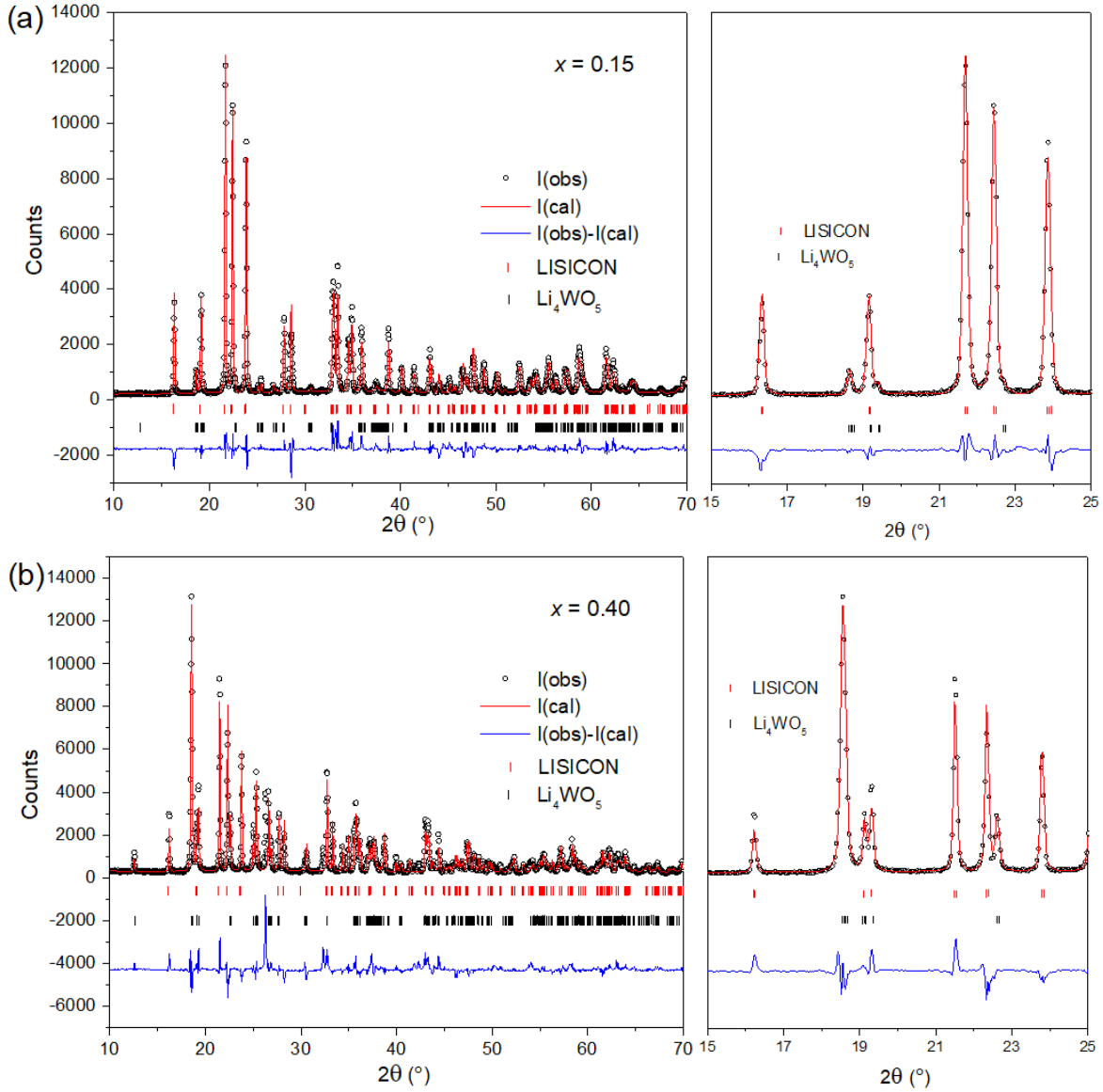

Figure 5.5 Fitted diffraction profiles for (a) x = 0.15 and (b) x = 0.40 compositions in $Li_{4-2x}Ge_{1-x}W_xO_4$, showing observed (◦ symbols), calculated (red line) and difference (blue line) profiles. Reflection positions are indicated by markers.

In the xLi$_2$WO$_4$ – (1-x) Li$_4$GeO$_4$ system, the products for compositions $x \geq 0.40$ (x = 0.40, 0.50 and 0.60) were explored. A temperature of 1000 ºC was initially selected as the calcination temperature, based on the fact it worked well for other compositions ($0.10 \leq x \leq 0.40$). It was found that when the calcination temperature is 1000 ºC, the products of x = 0.50 and 0.60 had fused together and were extremely difficult to scrape out of the Al$_2$O$_3$ crucible, suggesting partial melting had occurred. When a lower calcination temperature of 900 ºC was used for 6 h, the powder morphology was maintained with appropriate flowability. The XRD patterns for compositions $x \geq 0.40$ (x = 0.40, 0.50 and 0.60) prepared in this way are shown in Fig. 5.6. The patterns show only Li$_4$WO$_5$ and Li$_2$GeO$_3$, with no evidence of a LISCION phase, including in the pattern for x = 0.40, which showed significant amounts of a LISICON phase at higher temperatures (Fig. 5.5b). The phenomenon is consistent with Fig. 5.1, where the solid solution was observed after calcination at 950 ºC, but not lower temperatures.

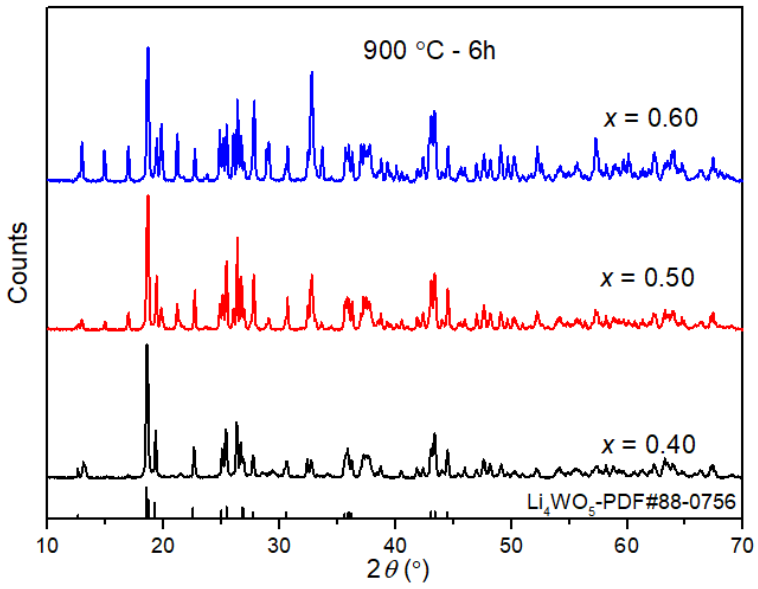

Figure 5.6 XRD patterns for x = 0.40, 0.50 and 0.60 compositions in Li$_{4-2x}$Ge$_{1-x}$W$_x$O$_4$, calcined at 900 ºC for 6h.

5.3.2 Pellet morphology and EDS

Pellets of the x = 0.10, 0.15, 0.20, 0.25 and 0.30 compositions in the $Li_{4-2x}Ge_{1-x}W_xO_4$ system, were prepared by SPS. All pellets for these compositions had relative densities of over 96% theoretical density measured using the classical Archimedes method by displacement in water. SEM images for $Li_{4-2x}Ge_{1-x}W_xO_4$ pellets after polishing and thermal etching (1000 °C for 20 min) are shown in Figs. 5.7 to 5.11. The images confirm good densification, and the microstructure revealed a similar particle size of around 200 to 300 nm (Figs. 5.7d-5.11d) for all compositions, similar to that of the calcined powders before SPS. The maintenance of particle size in SPS, is one of the benefits of the process and avoids commonly encountered problems associated with over-sintering in conventional sintering processes over several hours. Additionally, it is noted that with increasing x-value, the presence of additional particles on the surface of the dense pellet matrix is observed, which are supposed to be a second phase (Figs. 5.7b-11b). Throughout the compositions x = 0.15, 0.20, 0.25 and 0.30, the particle size of the second phase is around 1 to 3 um. Element maps from EDS and XRD methods were employed to check the phase information of the second phase.

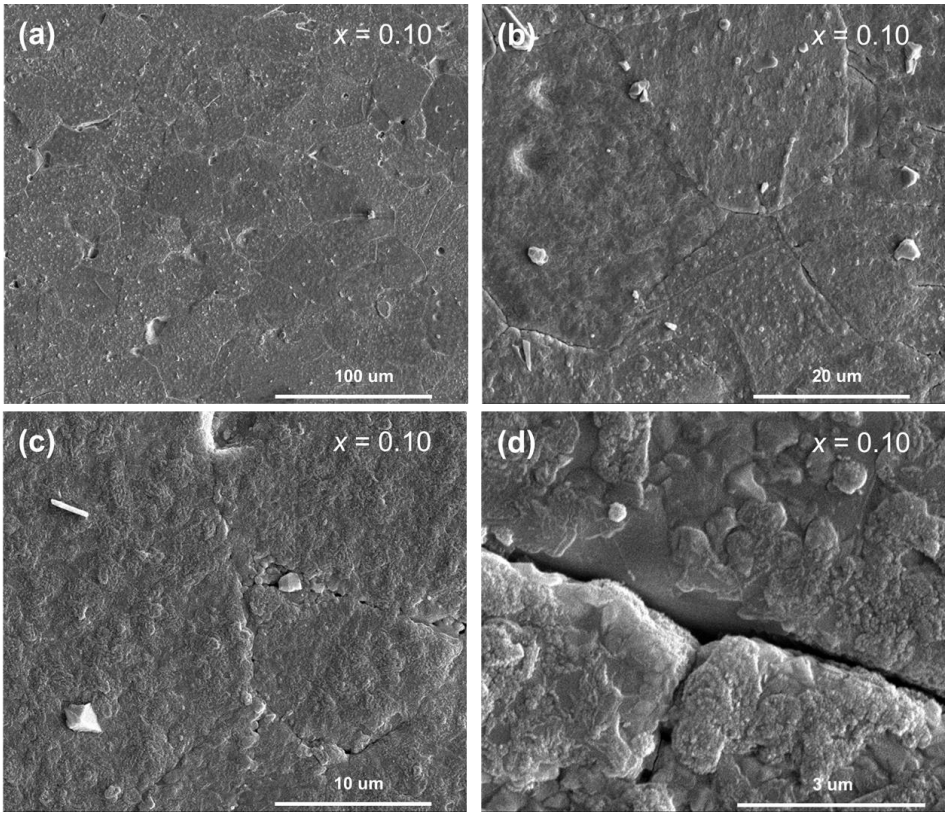

Figure 5.7 SEM images for the SPS pellet of $x = 0.10$ composition in $Li_{4-2x}Ge_{1-x}W_xO_4$

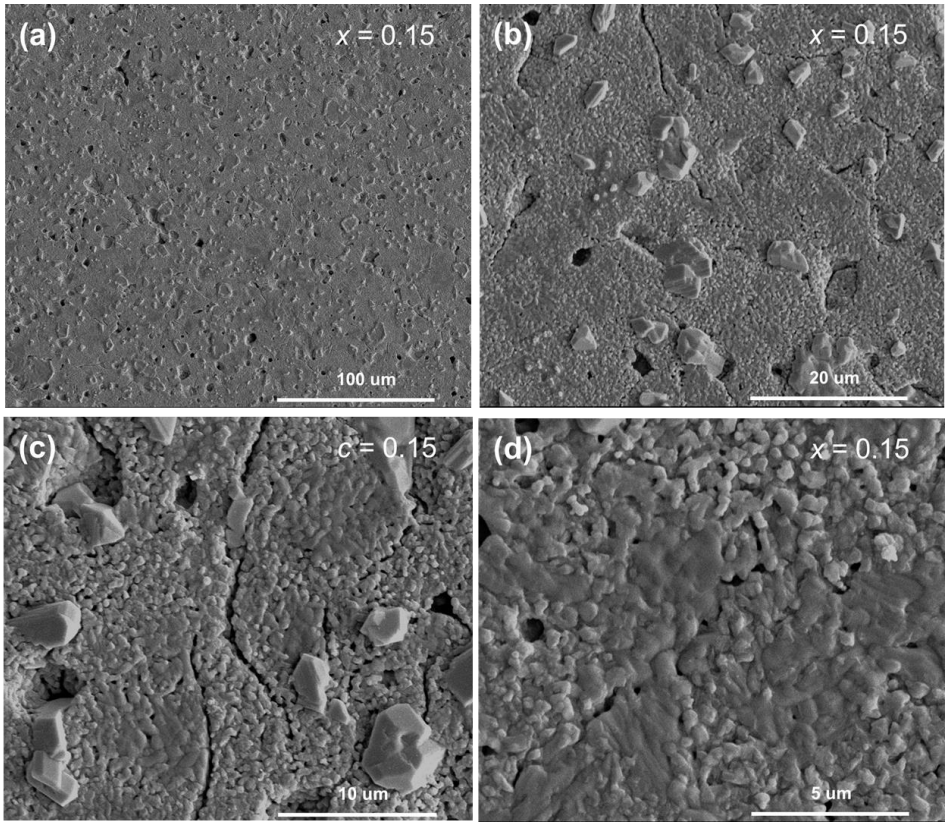

Figure 5.8 SEM images for the SPS pellet of $x = 0.15$ composition in $Li_{4-2x}Ge_{1-x}W_xO_4$

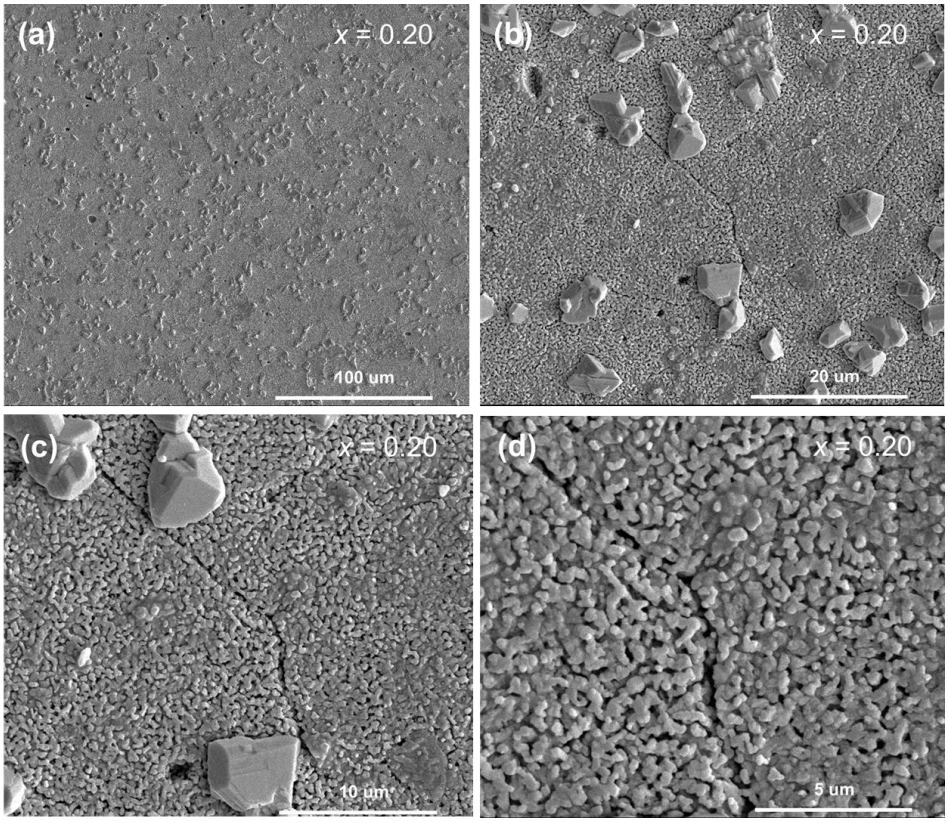

Figure 5.9 SEM images for the SPS pellet of $x = 0.20$ composition in $Li_{4-2x}Ge_{1-x}W_xO_4$

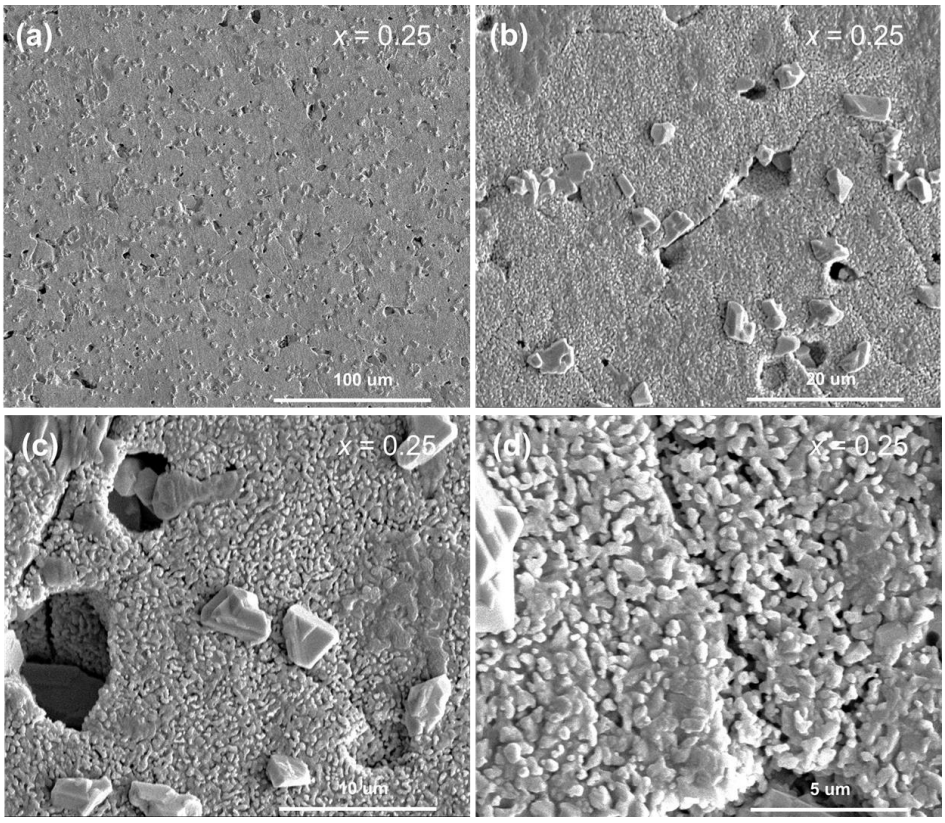

Figure 5.10 SEM images for the SPS pellet of $x = 0.25$ composition in $Li_{4-2x}Ge_{1-x}W_xO_4$

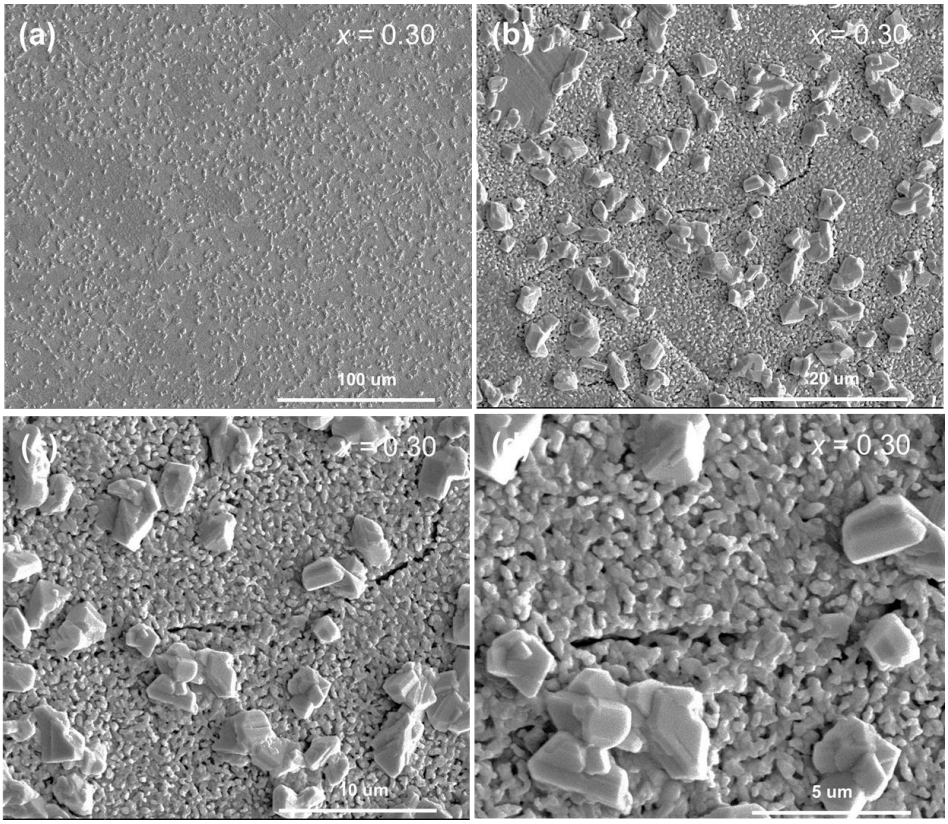

Figure 5.11 SEM images for the SPS pellet of x = 0.30 composition in $Li_{4-2x}Ge_{1-x}W_xO_4$

Element maps and the corresponding energy spectra of two distinct regions (the smooth matrix area and the surface particles) for each composition are shown in Figs. 5.12 and 5.13. From Fig. 5.12, the element maps of W, Ge and O confirm a uniform cation and anion distribution within the matrix throughout the whole series. Additionally, the energy spectra reveal W to be dominant compared to Ge in the surface particles, consistent with these particles being predominantly a lithium tungstate species. Table 5.5 summarises the elemental analysis from the matrix and surface particles of the studied compositions and confirms that the W:Ge ratio is much higher in the surface particles than in the matrix. It is notable that the W:Ge ratio of the matrix is generally higher (apart from x = 0.15) than the theoretical ratio. Along with the appearance of W rich surface particles, this suggests that the thermal etching may cause some diffusion of W^{6+} near to the surface eventually leading to the formation of the W-rich secondary phase.

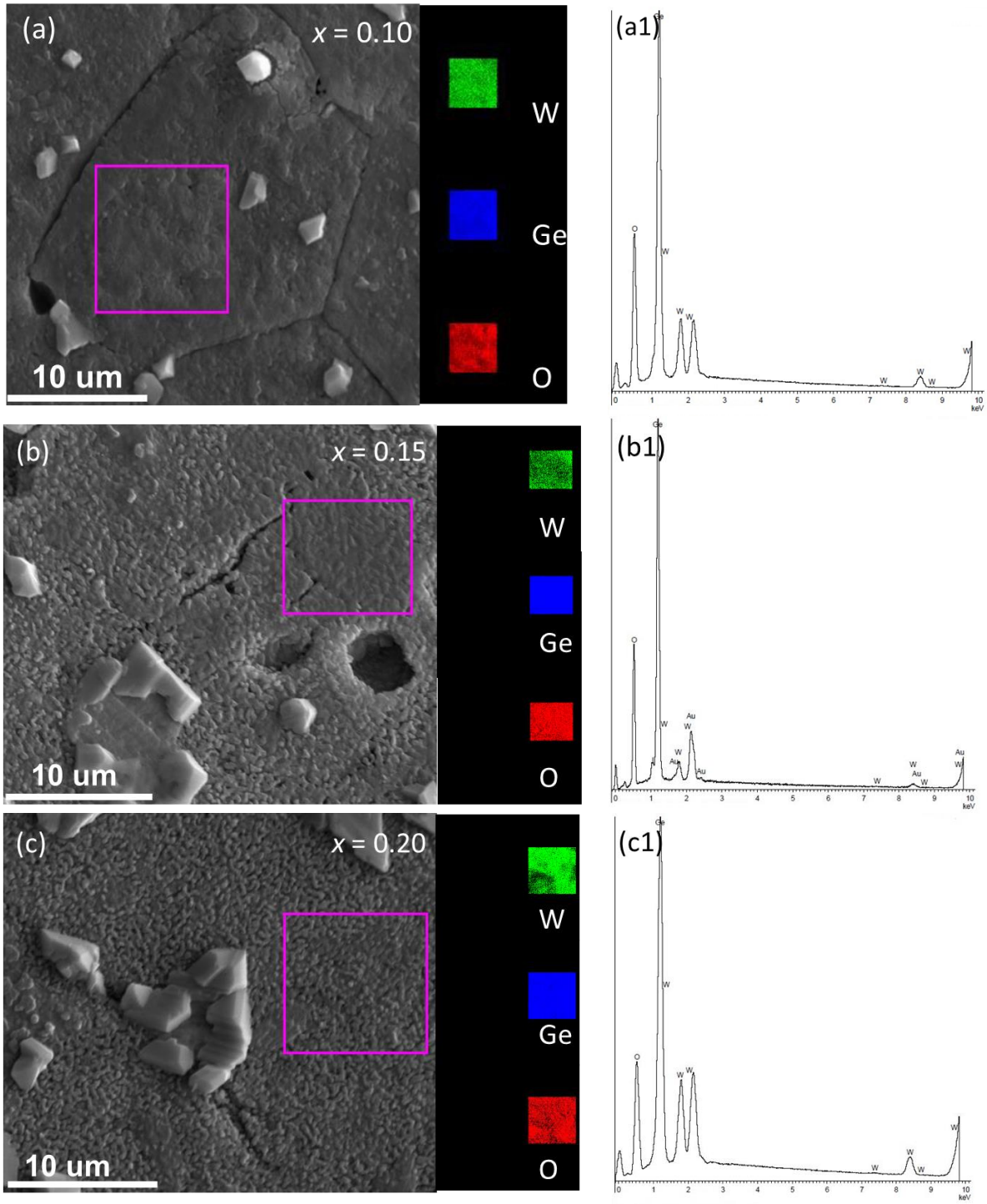

Figure 5.12 continued on next page

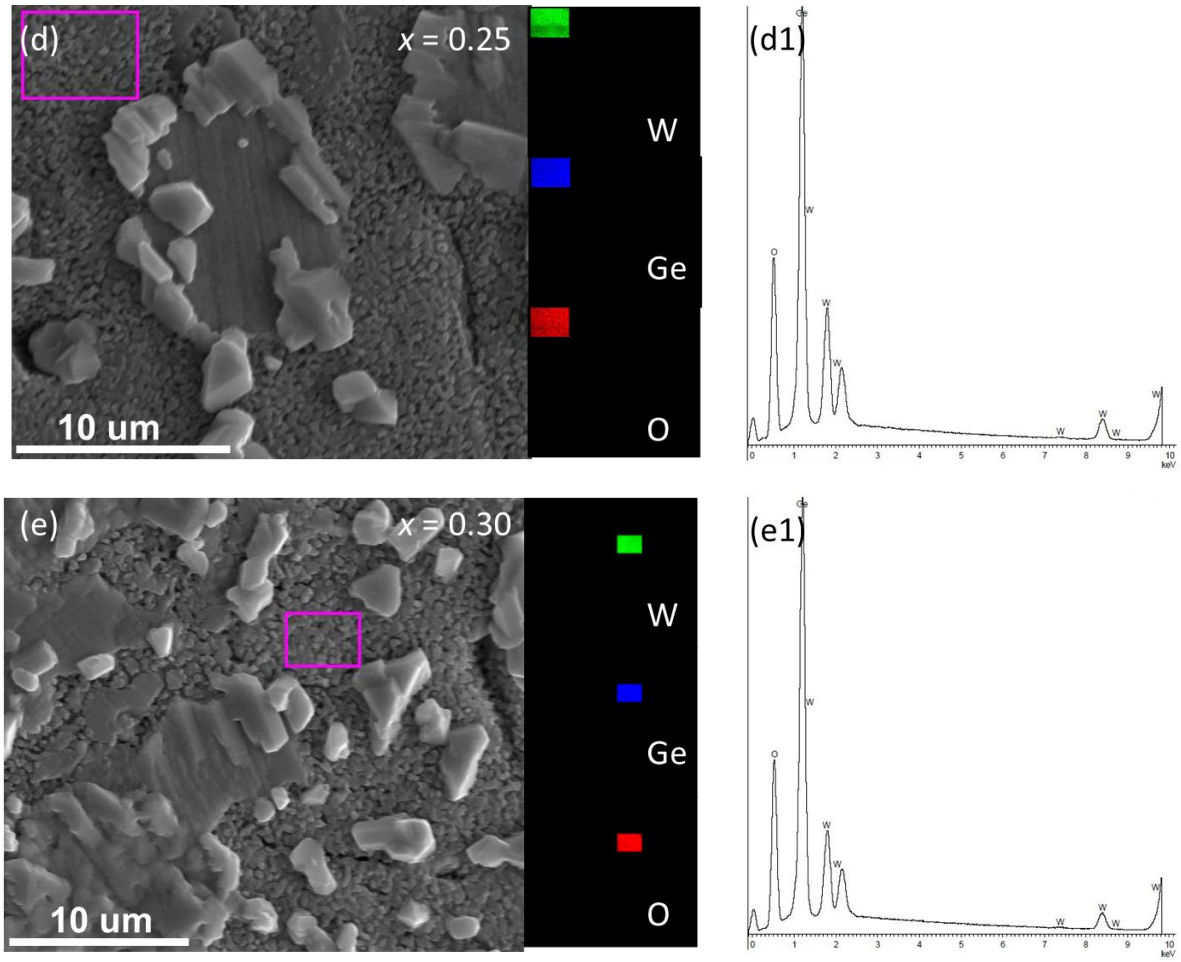

Figure 5.12 SEM images used for EDS analysis and corresponding element mapping of selected regions (W (green), Ge (blue), O (red)) for (a) x = 0.10, (b) x = 0.15, (c) x = 0.20, (d) x = 0.25 and (e) x = 0.30 compositions in $Li_{4-2x}Ge_{1-x}W_xO_4$ along with the corresponding energy spectra (right) of the selected regions.

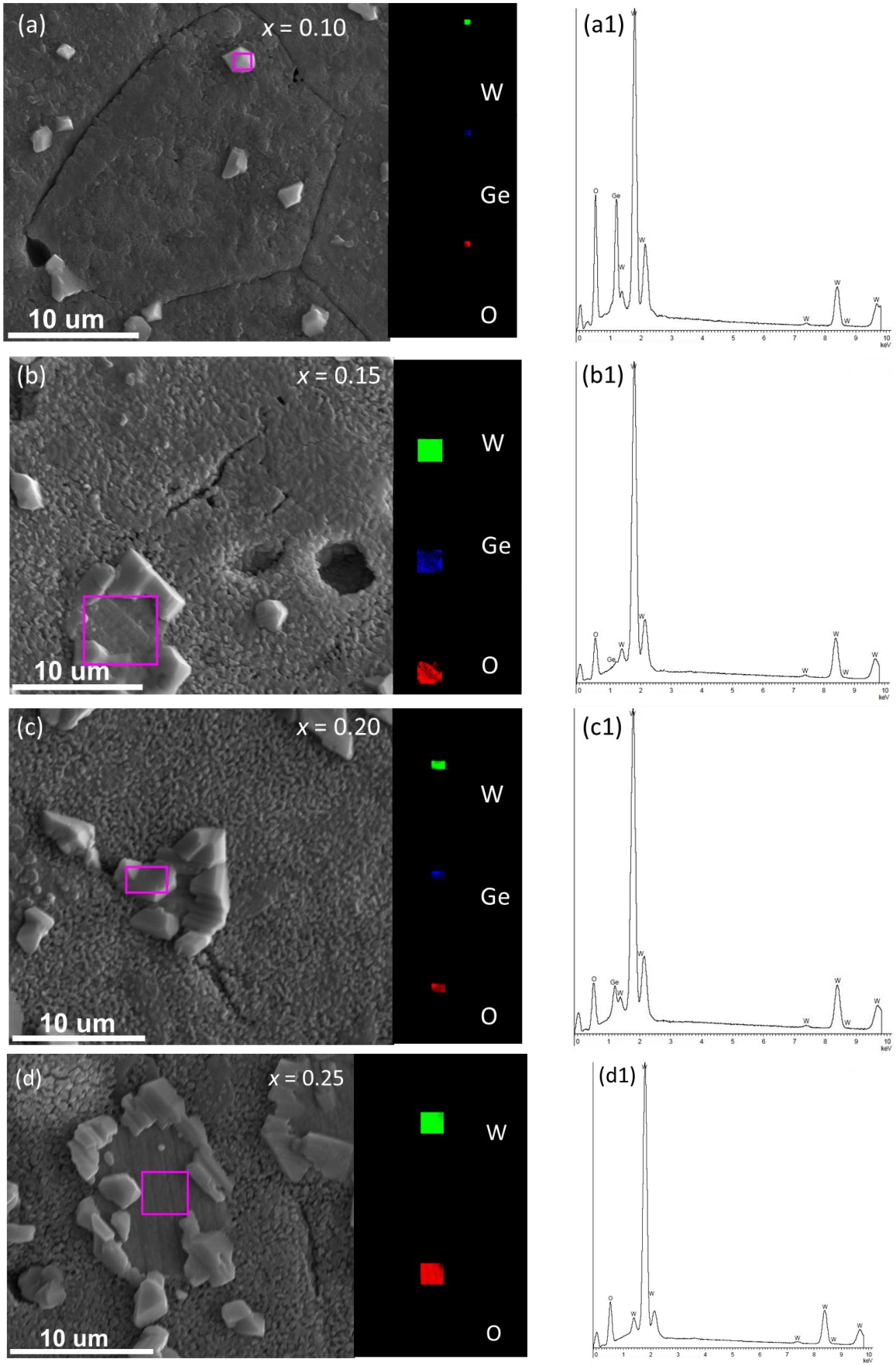

Figure 5.13 continued on next page

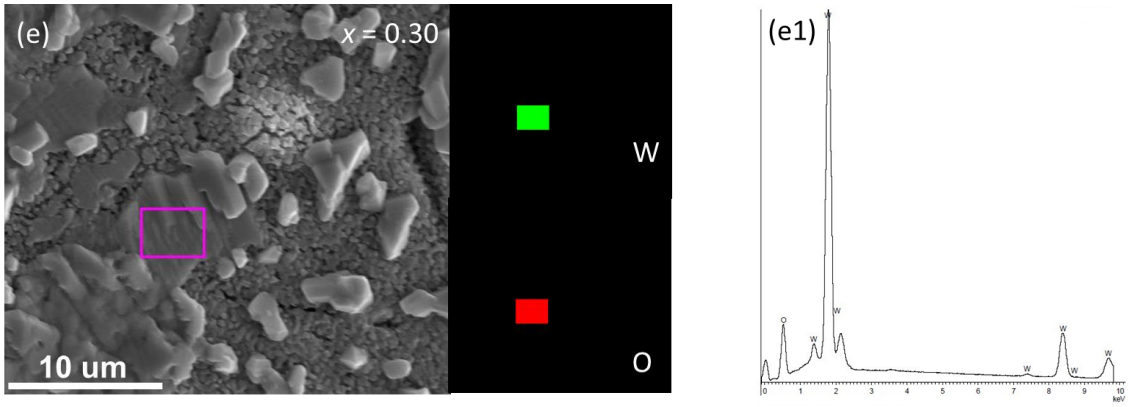

Figure 5.13 SEM images used for EDS analysis and corresponding element mapping of selected regions (W (green), Ge (blue), O (red)) for (a) x = 0.10, (b) x = 0.15, (c) x = 0.20, (d) x = 0.25 and (e) x = 0.30 compositions in $Li_{4-2x}Ge_{1-x}W_xO_4$, along with the corresponding energy spectra of the selected regions.

Table 5.5 W/Ge elemental atomic ratio from EDS analysis of $Li_{4-2x}Ge_{1-x}W_xO_4$ at surface particles (site 1) and matrix (site 2)

x value	W	Ge	W : Ge (actual)	W : Ge (theorical)
0.10 (site 1)	11.21	1.46	7.68	NA
0.10 (site 2)	3.08	7.9	0.39	0.11
0.15 (site 1)	22.44	1.65	13.6	NA
0.15 (site 2)	1.34	8.38	0.16	0.18
0.20 (site 1)	20.56	2.36	8.71	NA
0.20 (site 2)	4.71	9.48	0.50	0.25
0.25 (site 1)	---	---	---	---
0.25 (site 2)	4.31	6.21	0.69	0.33
0.30 (site 1)	---	---	---	---
0.30 (site 2)	3.66	6.71	0.55	0.43

XRD patterns of the SPS-sintered pellets are shown in Fig. 5.14. All compositions maintain strong LISICION diffraction peaks with good crystallinity, consistent with the pristine calcined powders (Fig. 5.3), but with greater proportions of the second phase Li_4WO_5. This is most noticeable in the x = 0.10 compositions, which might be related to its relatively low SPS-sintering temperature (800 ºC). Based on the above SEM images and the EDS results (Figs.

5.12 and 5.13), it can be deduced that the W-rich surface particles are Li_4WO_5. The precipitated Li_4WO_5 crystallites grow quickly in size and adhere to the surface of the LISICON matrix.

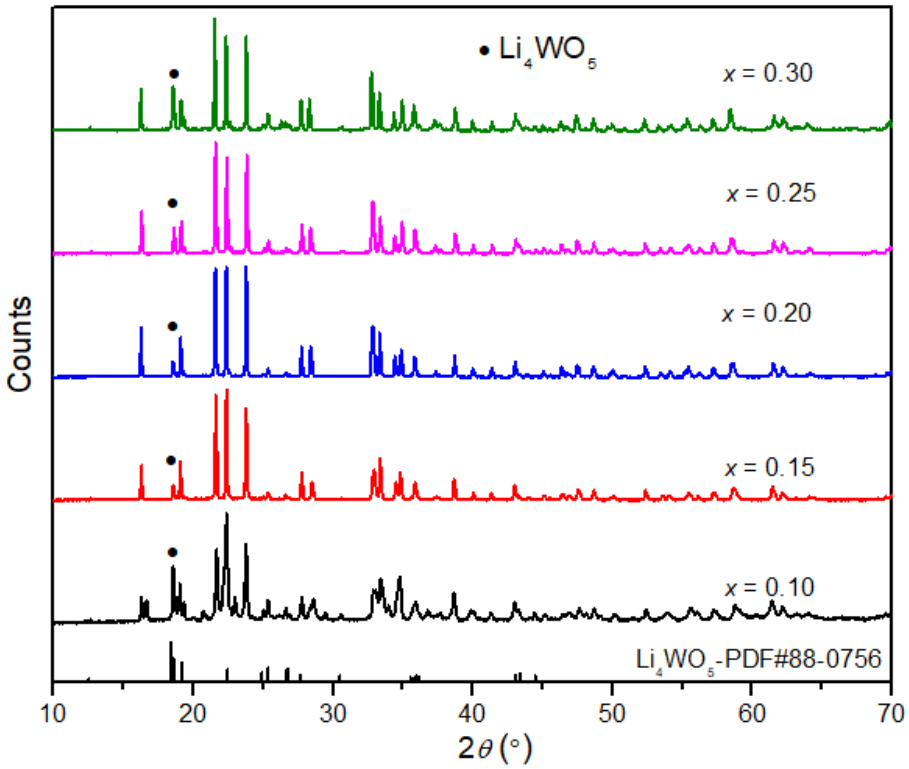

Figure 5.14 XRD patterns for SPS-sintered pellets of x = 0.10, 0.15, 0.20, 0.25 and 0.30 in $Li_{4-2x}Ge_{1-x}W_xO_4$

5.3.3 Electrical behaviour

Electrochemical impedance measurements were employed to study the electrical response of the studied compositions in $Li_{4-2x}Ge_{1-x}W_xO_4$ system. Fig. 5.15 shows the Nyquist plots for $Li_{3.7}Ge_{0.85}W_{0.15}O_4$ at selected temperatures during the 1st heating run. The spectra at low temperatures show a capacitive semicircle, with a non-zero high frequency intercept with the real axis. At low frequencies an inclined capacitive spike is observed associated with the blocking electrode. At higher temperatures the semicircle moves out of the frequency window and only the tail is observed. Interestingly this semicircle increases significantly in the

following cooling run and is stabilized around the same level during the subsequent cycles of 2nd heating and cooling (Fig. 5.16).

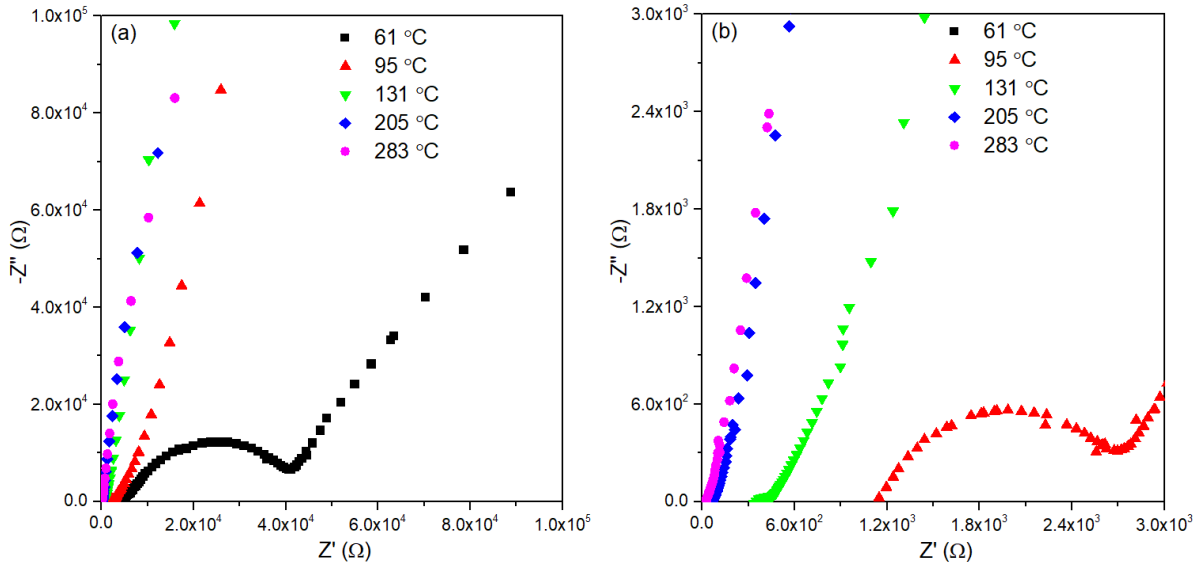

Figure 5.15 (a) Nyquist plots for $Li_{3.7}Ge_{0.85}W_{0.15}O_4$ with the (b) magnification near the origin at selected temperatures during the 1st heating run

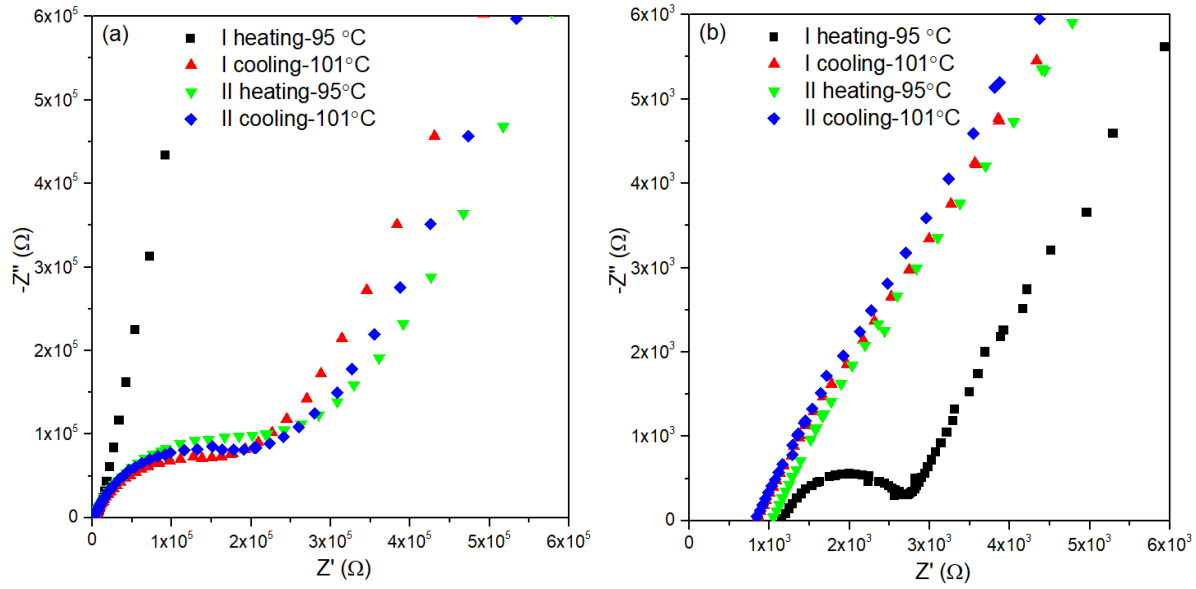

Figure 5.16 (a) Nyquist plots for $Li_{3.7}Ge_{0.85}W_{0.15}O_4$ at ca.100 °C with (b) magnification near the origin for two heating and cooling runs

To understand the underlying reasons for this variation in electrical behaviour, careful fitting of the impedance spectra to an equivalent circuit was carried out. Fig. 5.17 shows the model fitting for 95 ºC during the 1st heating based on the proposed equivalent circuit as inset in Fig. 5.17. Table 5.6 summaries the fitted equivalent circuit parameters for the spectra at ca.100 ºC during the two runs (for I cooling, II heating and II cooling). It can be seen that all the fittings exhibit low error level, indicating that the selected simplified equivalent circuit reasonably models the electrical response. The semicircle related constant phase element 1 (CPE1) has a capacitance of 10^{-8} F throughout the two runs and lies between the ranges normally associated with grain boundary and surface layer response. For the semicircle associated resistance *R*2, a dramatic increase from 1438 Ω in the 1st heating to 10^{-5} Ω in subsequent runs is observed. This evolution with runs suggests that the greatly enlarged semicircle is primarily caused by the surface layer response. The capacitance of CPE2 is in the order of 10^{-6} F throughout and is attributed to the electrical response from the electrolyte-gold electrode interface.

In summary, the semicircle and the following tail in the impedance spectra are associated with the response from the electrolyte surface layer and the electrolyte-gold electrode interface rather than from the bulk electrolyte itself and that the total electrolyte resistance corresponds to the high frequency intercept of this semicircle with the real axis.

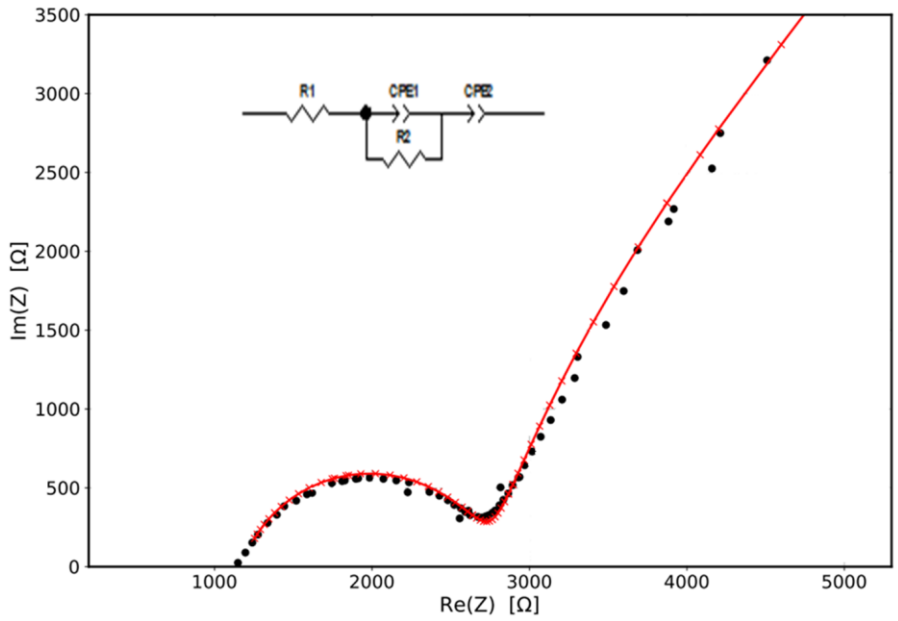

Figure 5.17 Experimental Nyquist plot and best simulation fit based on the inset equivalent circuit for $Li_{3.7}Ge_{0.85}W_{0.15}O_4$ on 1st heating at ca. 95 ºC

Table 5.6 Equivalent circuit parameters for $Li_{3.7}Ge_{0.85}W_{0.15}O_4$ at ca.100 ºC during heating and cooling runs

	I heating	I cooling	II heating	II cooling
R1 (Ω)	1206	823	1066	816
Conf%	1.1	1.8	4.1	1.6
R2 (Ω)	1438	2.1×10^5	3.0×10^5	2.4×10^5
Conf%	1.6	2.8	8.9	2.8
CPE1-P (F)	1.23×10^{-8}	9.6×10^{-8}	9.8×10^{-8}	6.8×10^{-8}
Conf%	14.7	3.1	6.9	3.2
CPE1-n	0.17	0.32	0.33	0.29
Conf%	7.0	1.0	2.4	1.2
CPE2-P (F)	4.1×10^{-6}	1.4×10^{-6}	1.4×10^{-6}	1.4×10^{-6}
Conf%	6.1	2.0	7.9	2.1
CPE2-n	0.32	0.30	0.29	0.31
Conf%	2.7	5.1	2.3	5.1

Fig. 5.18 shows the Arrhenius plots of total conductivity for compositions of $0.10 \leq x \leq 0.30$ in $Li_{4-2x}Ge_{1-x}W_xO_4$ over two cycles of heating and cooling from room temperature to 300 ºC. It can be observed that during the two cycles, all compositions exhibit good reversibility and repeatability. Two linear regions are seen for all compositions over the studied temperature range, although the transition temperature between the two regions varies slightly with composition (x = 0.10, ca. 135 °C; x = 0.15 and 0.20, ca. 170 °C; x = 0.25 and 0.30, ca. 155 °C). The high-temperature region possesses a lower activation energy than the low-temperature region.

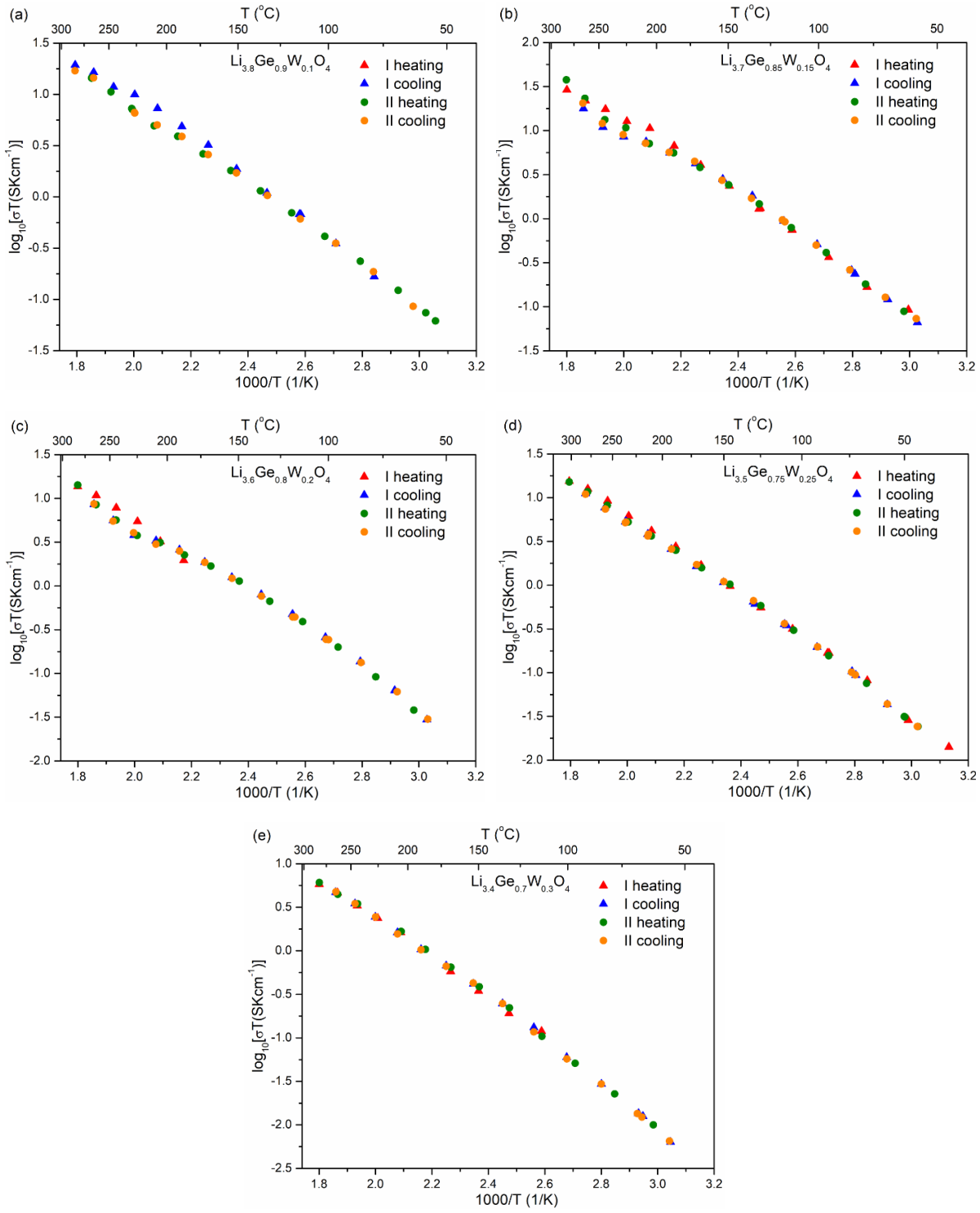

Figure 5.18 Arrhenius plots of total conductivity for x = 0.10, 0.15, 0.20, 0.25 and 0.30 compositions in the $Li_{4-2x}Ge_{1-x}W_xO_4$ system.

Table 5.7 summarises conductivities at selected temperatures along with activation energies in the low (ΔE_{LT}) and high temperature (ΔE_{HT}) regions for the second cooling run. Fig 5.19 is a graphical illustration of the compositional variation of ΔE_{LT} and ΔE_{HT}. It can be seen that with increasing *x*-value, both the low-temperature and high-temperature activation energies exhibit a general increasing trend from $x = 0.10$ to $x = 0.30$, with a local maximum at $x = 0.15$. The difference between ΔE_{LT} and ΔE_{HT} ranges from 0.05 to 0.09 eV. Since $x = 0.25$ represents the solid solution limit and the $x = 0.30$ composition includes significant amounts of Li_4WO_5, the activation energy for the $x = 0.30$ composition (($\Delta E_{LT} = 0.43$ eV, ($\Delta E_{HT} = 0.52$ eV) is higher than that for the $0.10 \leqslant x \leqslant 0.25$ compositions due to the high resistance of the second phase, Li_4WO_5.

Table 5.7 ΔE_{LT} and ΔE_{HT} and conductivities ($\sigma_{temp°C}$) at selected temperatures for $x = 0.10$, 0.15, 0.20, 0.25 and 0.30 compositions in the $Li_{4-2x}Ge_{1-x}W_xO_4$ system. Data correspond to the second cooling run. Estimated errors are ±5%.

x	ΔE_{LT} (eV)	ΔE_{HT} (eV)	$\sigma_{25°C}$ (S cm^{-1})	$\sigma_{100°C}$ (S cm^{-1})	$\sigma_{150°C}$ (S cm^{-1})	$\sigma_{250°C}$ (S cm^{-1})
0.10	0.408	0.359	5.29×10^{-5}	1.03×10^{-3}	3.78×10^{-3}	2.01×10^{-2}
0.15	0.461	0.382	4.32×10^{-5}	1.27×10^{-3}	6.08×10^{-3}	3.12×10^{-2}
0.20	0.446	0.373	2.26×10^{-5}	5.98×10^{-4}	2.73×10^{-3}	1.31×10^{-2}
0.25	0.484	0.408	1.06×10^{-5}	3.76×10^{-4}	1.97×10^{-3}	1.92×10^{-2}
0.30	0.518	0.428	3.44×10^{-6}	1.58×10^{-4}	9.34×10^{-4}	6.97×10^{-3}

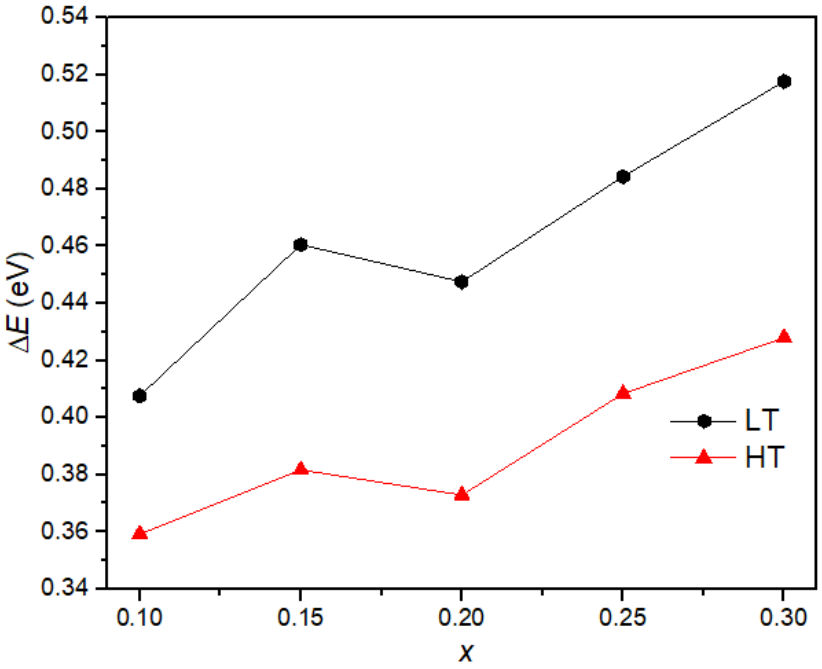

Figure 5.19 Compositional variation of activation energies at low-temperature (LT), and high-temperature (HT) in the $Li_{4-2x}Ge_{1-x}W_xO_4$ system

The compositional variation of total conductivities at selected temperatures for the $Li_{4-2x}Ge_{1-x}W_xO_4$ system is shown in Fig. 5.20. At room temperature, the x = 0.10 composition exhibits the highest conductivity of 5.29×10^{-5} S cm^{-1} and gradually decreases to 1.06×10^{-5} S cm^{-1} at x = 0.25. The low conductivity of 3.44×10^{-5} S cm^{-1} at x = 0.30 is due to the high resistance of the second phase, Li_4WO_5. At elevated temperatures, it is the intermediate composition x = 0.15 which shows the highest conductivity with values of $\sigma_{100°C} = 1.27 \times 10^{-3}$ S cm^{-1}, $\sigma_{150°C} = 6.08 \times 10^{-3}$ S cm^{-1} and $\sigma_{250°C} = 3.12 \times 10^{-2}$ S cm^{-1}. It is noteworthy that among the reported work for binary LISICON oxides, $Li_{4-2x}Ge_{1-x}W_xO_4$ system shows the best ionic conductivity.

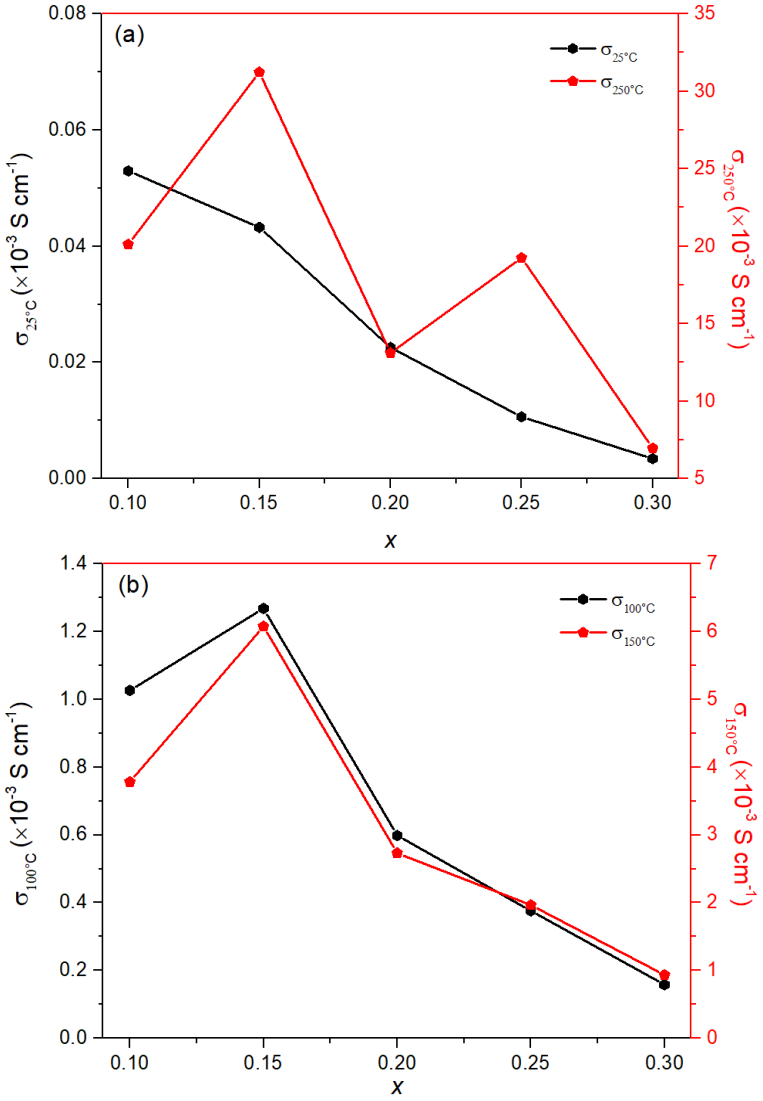

Figure 5.20 Compositional variation of conductivity at 25 ºC, 100 ºC, 150 ºC and 250 ºC in $Li_{4-2x}Ge_{1-x}W_xO_4$

5.3.4 Molecular dynamics simulations

Two starting models were used for Molecular Dynamics simulations of $Li_{3.7}Ge_{0.85}W_{0.15}O_4$. Model 1 started with full occupancy of the Li1 and Li2 sites and no occupancy of Li1a and Li2a sites. Model 2 had the initial Li distribution reported in reference [1], with Li1, Li1a, Li2 and Li2a sites partially occupied. Little difference is seen in the final results and unless stated otherwise the results reported below refer to Model 2.

Figs. 5.21 and 5.22 show the partial pair distributions of Li-Li and Li-O pairs from the final configurations of the MD simulations at different temperatures. It can be seen that the 1st peak

for Li-Li and Li-O pairs are 2.90 Å and 1.94 Å, respectively. With higher temperature, the first peak of Li-Li and Li-O pairs broadens to around 0.7 Å in width, indicating a greater range of Li-Li and Li-O distances with increasing temperature and is consistent with greater lithium ion mobility at high temperatures.

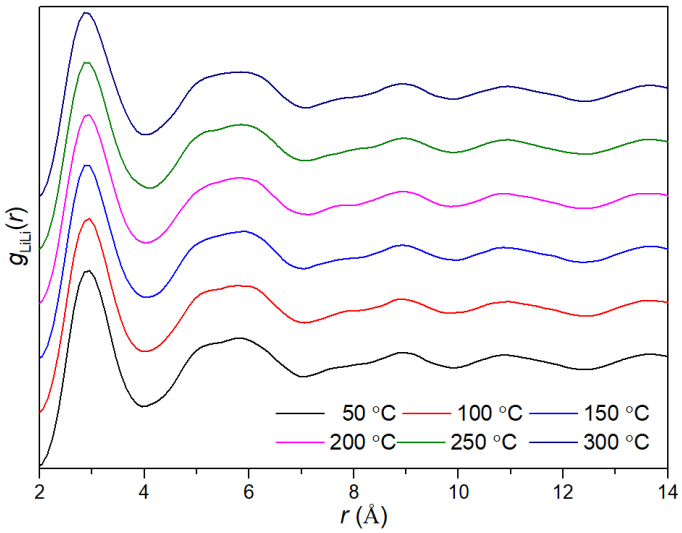

Figure 5.21 Li-Li partial pair distributions $g_{LiLi}(r)$ at selected temperatures from MD simulations of $Li_{3.7}Ge_{0.85}W_{0.15}O_4$

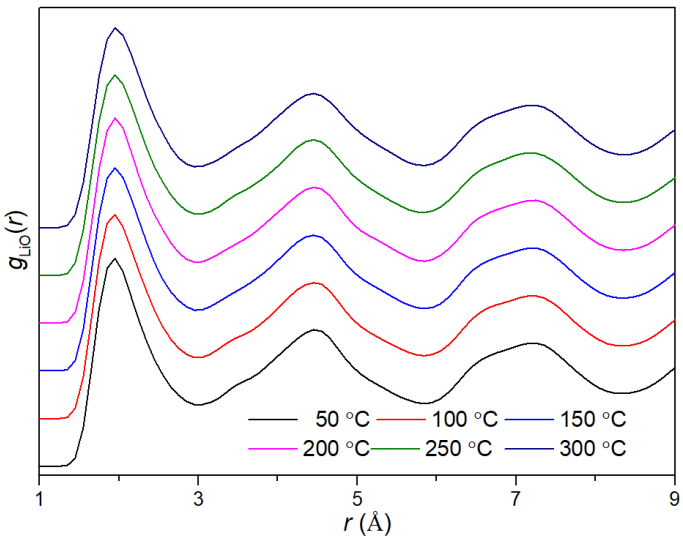

Figure 5.22 Li-O partial pair distributions $g_{LiO}(r)$ at selected temperatures from MD simulations of $Li_{3.7}Ge_{0.85}W_{0.15}O_4$

Table. 5.8 shows the coordination numbers (CN) and the 1st peak positions for the selected Li-Li, Li-O, Ge-O and W-O pairs. Coordination shell cut off values were determined from the individual pair correlation functions. It can be seen that the W^{6+} and Ge^{4+} are 4-coordinate to the O^{2-} anions and Li^{+} is higher than 4 due to the existence of partial Li^{+} occupancy in octahedral sites. The modal distances (i.e. the first peak position) in the relevant $g_{ij}(r)$ profile are around 1.92, 1.67 and 1.95 Å for Li-O, Ge-O and W-O, respectively. Compared with respective values of 1.97, 1.77 and 1.80 Å for Li-O, Ge-O and W-O based on the sum of the ionic radii [161] assuming the anions to be in 4-coordinate geometry, the simulations appear to overestimate the W-O distance significantly, but show good agreement for Li-O. There is little variation in coordination number and M-O distance with temperature.

Table 5.8 Summary of coordination numbers (CN), 1st peak positions and cutoff values for selected Li-Li, Li-O, Ge-O and W-O pairs from MD simulations of $Li_{3.7}Ge_{0.85}W_{0.15}O_4$ at selected temperatures

Selected pairs		50 ºC	100 ºC	150 ºC	200 ºC	250 ºC	300 ºC
Li-Li	CN	8.32	8.34	8.34	8.34	8.38	8.33
	1st peak (Å)	2.94	2.94	2.93	2.93	2.84	2.84
	Cutoff (Å)	4.00					
Li-O	CN	4.28	4.28	4.27	4.28	4.28	4.29
	1st peak (Å)	1.92	1.92	1.92	1.93	1.92	1.92
	Cutoff (Å)	3.06					
Ge-O	CN	4	4	4	4	4	4
	1st peak (Å)	1.67	1.67	1.67	1.67	1.67	1.67
	Cutoff (Å)	2.80					
W-O	CN	3.99	3.98	3.99	3.99	3.98	3.98
	1st peak (Å)	1.95	1.96	1.95	1.95	1.96	1.94
	Cutoff (Å)	2.80					

Fig. 5.23 illustrates the angular distribution functions (ADFs) for O-Li-O, O-Ge-O and O-W-O. It can be seen that the angle distribution is broader for O-Li-O than for O-Ge-O and O-W-O, and both O-Ge-O and O-W-O exhibit a predominant bond angle of 109.5 º though O-W-

O shows slight distribution asymmetry and a much broader angle distribution than O-Ge-O. These indicate that all the Ge^{4+} and W^{6+} cations are located in the center of the O_4 tetrahedra, though the WO_4 tetrahedra are slightly distorted. Unlike Ge^{4+} and W^{6+} cations, the O-Li-O bond angle exhibits a predominant distribution around 99.7 º and a partial distribution around 68 º, indicating that the skeletal LiO_4 tetrahedra are greatly distorted and the additional interstitial Li^+ ions are located in a distorted pentahedron. It is likely that these interstitial Li^+ ions and skeletal Li^+ ions work together through an interstitialcy mechanism to yield the high conductivity with low activation energy observed in this system.

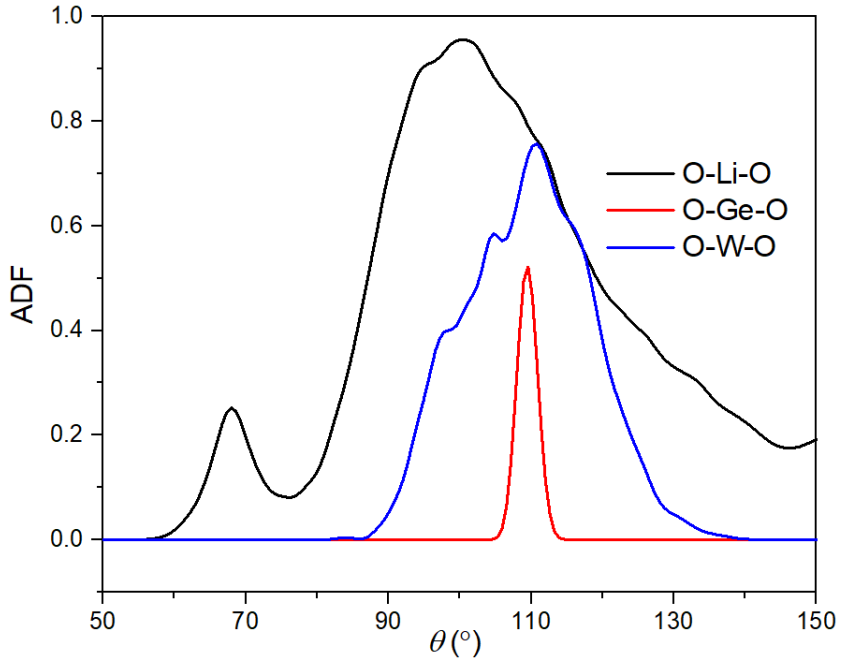

Figure 5.23 ADFs for O-Li-O, O-Ge-O and O-W-O from MD simulations of $Li_{3.7}Ge_{0.85}W_{0.15}O_4$ at 50 ºC

The simulated conductivity data based on the MD simulations are shown in Fig. 5.24. Comparing the results from the two models, it can be seen that apart from a small difference at 150 °C, the models achieve consitent results. At high temperature, the simulated conductivity is about an order of magnitute higher than the experimental value, with this difference increasing with decreasing temperature, due to the difference in the simulated and observed

activation energies. The simulated conductivity has an activation energy of 0.22 eV and is much lower than that observed. This difference in conductivity and activation energy may be attributed to the fact that the simulated data have no grain boundary contribution and reflect the situtation in the single crystal rather than the bulk ceramic.

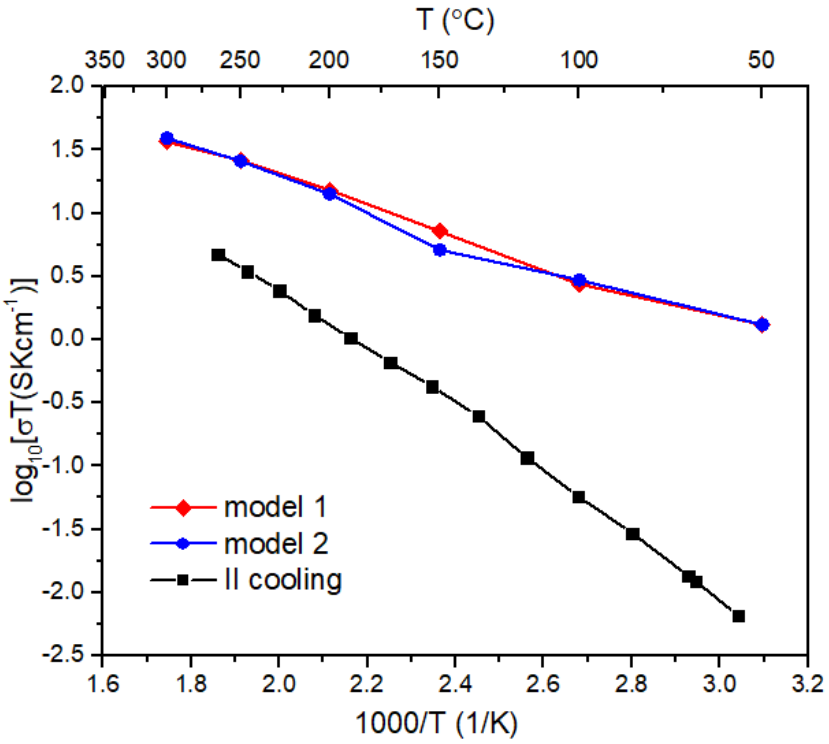

Figure 5.24 Simulated and experimental conductivity for $Li_{3.7}Ge_{0.85}W_{0.15}O_4$

5.3.5 Li_4WO_5 and Li_2WO_4

Li_2WO_4, the end-member in the $Li_{4-2x}Ge_{1-x}W_xO_4$ system and the related Li_4WO_5 phase are both seen in XRD data of this system. Both can be used as low-temperature firing microwave dielectric ceramics [172, 173], indicating their low ionic and electronic conducting nature. It is reported that the conductivity of Li_2WO_4 at 300 ºC is 2.18 $\times 10^{-7}$ S cm^{-1} with an activation energy of 0.94 eV [174]. Dissanayake et al. reported that a solid solution can be formed between β-Li_2SO_4 and Li_2WO_4 [175]. In this system, two conductivity maxima appeared for the eutectic 66% β-Li_2SO_4 – 34% Li_2WO_4 composition ($\sigma_{400\,°C}$ = 4.9 $\times 10^{-5}$ S cm^{-1}) and 30% β-Li_2SO_4 – 70%Li_2WO_4 ($\sigma_{400\,°C}$ = 1.0 $\times 10^{-4}$ S cm^{-1}), both are significantly higher than the two end members

β-Li_2SO_4 ($\sigma_{400\,°C}$ = 1.8 ×10^{-6} S cm^{-1}) and Li_2WO_4 ($\sigma_{400\,°C}$ = 6.0 ×10^{-6} S cm^{-1}). The phase diagram for Li_2WO_4 indicates it has a solid-liquid phase transition at 738 ºC [174, 175].

Here we explored the synthesis of Li_2WO_4 and Li_4WO_5, the XRD results of which are shown in Fig. 5.25. Rhombohedral Li_2WO_4 [169] can be synthesized and exhibits good crystallinity with high purity over a wide temperature range from 650 ºC to 750 ºC (Fig. 5.25). Based on the structure refinement results, a calcination temperature of 700 ºC for 24 h, appears the optimum. The fitted X-ray diffraction profile for the sample calcined at 700 °C is shown in Fig. 5.26a, with structure and refinement parameters shown in Tables 5.9 and 5.10. Li_2WO_4 is rhombohedral in space group *R*-3 (No. 148), with cell parameters *a* = 14.3638(1) Å and *c* = 9.6044(1) Å.

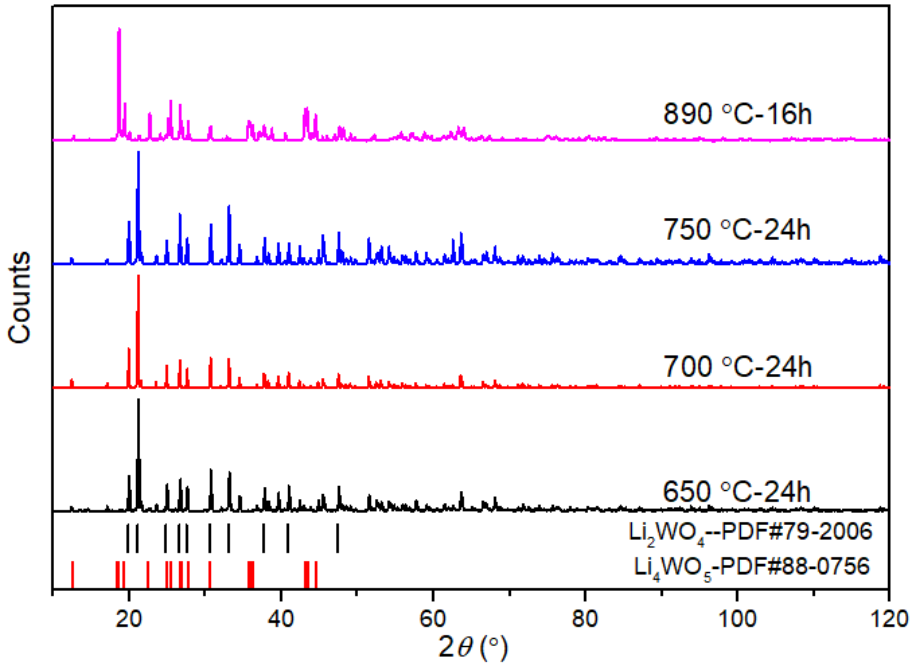

Figure 5.25 XRD patterns for the lithium ortho-tungstates at different temperatures

According to Xiao's report [176], a single rock salt structured Li_4WO_5 can be obtained using a calcination temperature of 870-910 ºC. An intermediate temperature of 890 ºC was selected to check the formation of Li_4WO_5, with the sample heated for 16 h at this temperature (Fig. 5.25). The fitted X-ray diffraction profile based on the model in paper [170] is shown in Fig. 5.26b, with

structure and refinement parameters shown in Tables 5.9 and 5.10. It is evident that at this temperature triclinic Li_4WO_5 is readily formed, impurities of rhombohedral Li_2WO_4 and unknown compounds are also seen. Considering that the reported melting point for Li_2WO_4 is 738 ºC [174, 175], the coexistence of Li_2WO_4 with Li_4WO_5 indicates the melting point of Li_2WO_4 should be higher than 890 ºC.

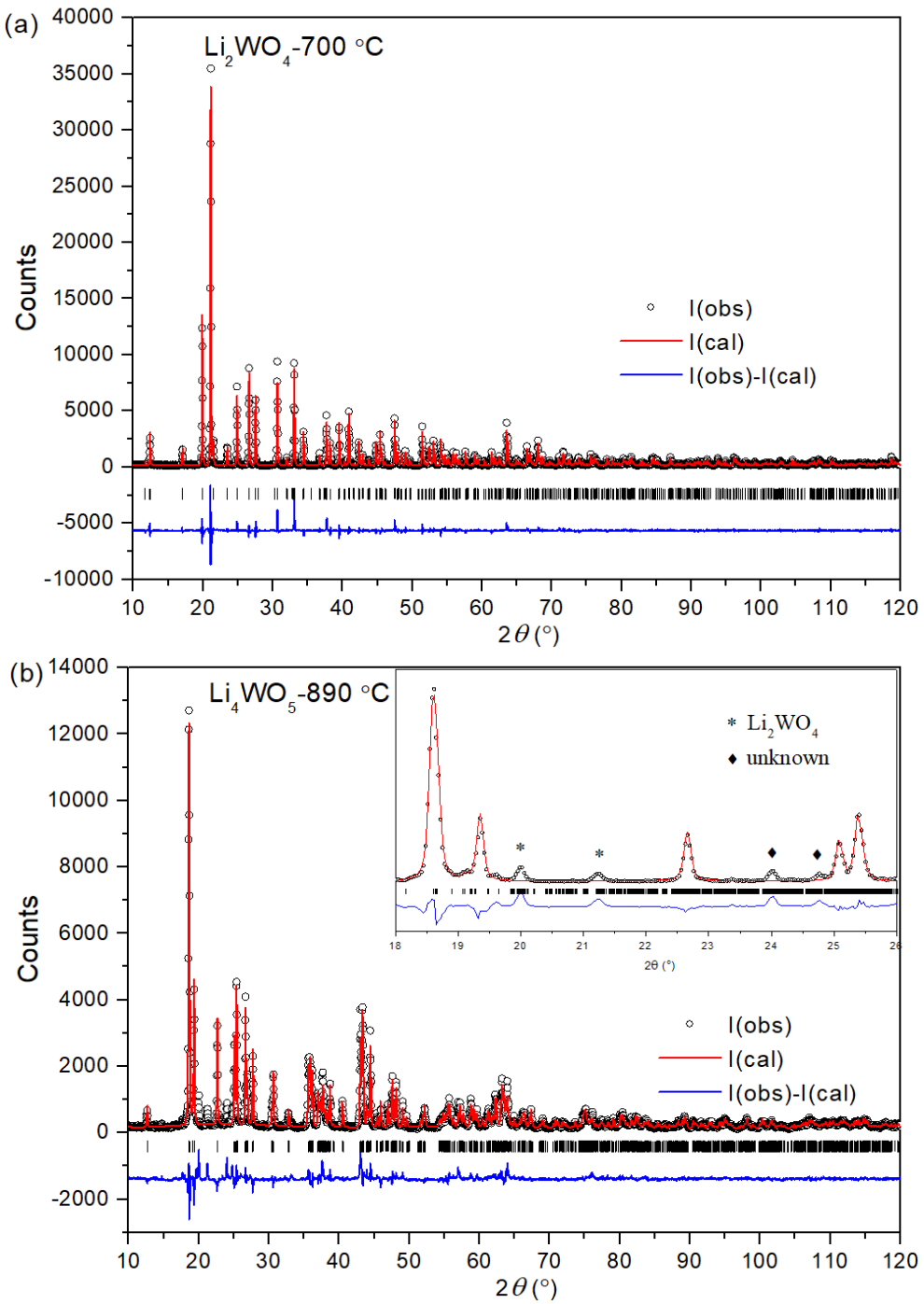

Figure 5.26 Fitted diffraction profiles for lithium ortho-tungstates at different temperatures, showing observed (◦ symbols), caluclated (red line) and difference (blue line) profiles. Reflection positions are indicated by markers.

Table 5.9 Crystal and refinement parameters for Li_2WO_4 and Li_4WO_5

Chemical formula	Li_2WO_4	Li_4WO_5
Crystal system	Rhombohedral	Triclinic
Space group	*R*-3	*P*-1
Unit cell dimensions （Å）	a = 14.3638(1) c = 9.6044(1)	a = 5.1259(2) α = 101.573(2)º b = 7.7480(3) β = 101.507(2)º c = 5.0839(2) γ = 108.519(2)º
Volume （$Å^3$）	1716.09(3)	179.87(1)
Z	18	4
Density (calculated)	4.559 g/cm^3	5.384 g/cm^3
R-factors[o]	R_{wp} = 0.1272 R_p = 0.0982 R_{ex} = 0.0474 R_F^2 = 0.0763	R_{wp} =0.1408 R_p =0.1025 R_{ex} = 0.0515 R_F^2 =0.1134
No. of variables	39	41
No. of profile points used	3440	3440

Table 5.10 Refined structural parameters for Li_2WO_4 and Li_4WO_5. Estimated standard deviations are given in parentheses.

	Atom	Site	x	y	z	Occ.	Uiso ($Å^2$)
Li_2WO_4	Li (1)	18*f*	0.117223	0.352771	0.551901	1	0.75(19)
	Li (2)	18*f*	0.186496	0.678564	0.665834	1	0.75(19)
	W	18*f*	0.1172(1)	0.6460(1)	0.4149(3)	1	0.0030(4)
	O (1)	18*f*	0.0004(17)	0.668(2)	0.434(4)	1	0.002
	O (2)	18*f*	0.241(1)	0.782(1)	0.431(3)	1	0.002
	O (3)	18*f*	0.130(2)	0.577(2)	0.239(3)	1	0.002
	O (4)	18*f*	0.125(1)	0.577(2)	0.563(3)	1	0.002
Li_4WO_5	Li(1)	1*c*	0.0	0.5	0.0	1	0.01360
	Li(2)	1*b*	0.0	0.0	0.5	1	0.01640
	Li(3)	2*i*	0.41270	0.90800	0.22540	1	0.01480
	Li(4)	2*i*	0.59540	0.60580	0.27740	1	0.01170
	Li(5)	2*i*	0.81020	0.30200	0.42590	1	0.01760
	W	2*i*	0.2182(5)	0.2164(4)	0.1065(5)	1	0.00032
	O (1)	2*i*	0.605(5)	0.356(3)	0.026(5)	1	0.00032
	O (2)	2*i*	0.790(5)	0.031(4)	0.132(5)	1	0.00032
	O (3)	2*i*	0.994(5)	0.742(3)	0.240(5)	1	0.00032
	O (4)	2*i*	0.195(5)	0.445(4)	0.369(6)	1	0.00032
	O (5)	2*i*	0.386(5)	0.164(3)	0.481(5)	1	0.00032

Fig.5.27 illustrates the crystal structure of rhombohedral Li_2WO_4. Rhombohedral Li_2WO_4 consists of a three-dimensional network of corner-linked LiO_4 and WO_4 tetrahedra. Open channels along the 3-fold axis are present based on these atomic arrangements. Within this structure, there are no mobile Li^+ ions, therefore extremely low conductivity is observed.

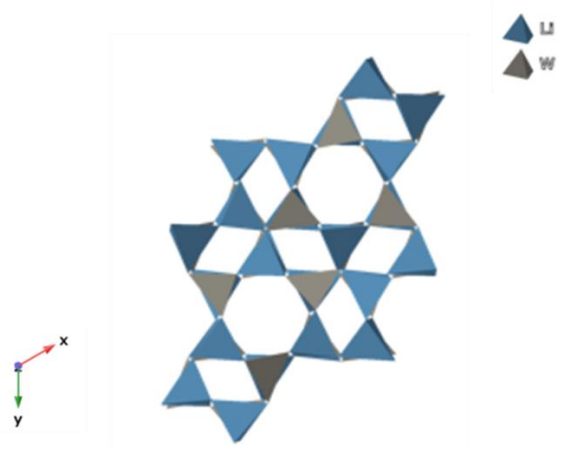

Figure 5.27 Crystal structure of Li_2WO_4

Fig.5.28 illustrates the crystal structure for monoclinic Li_4WO_5. The structure is that of an ordered rocksalt with Li^+ and W^{6+} cations in edge sharing octahedral sites. There are no interstitial Li^+ ions or vacancies and therefore it exhibits extremely low conductivity.

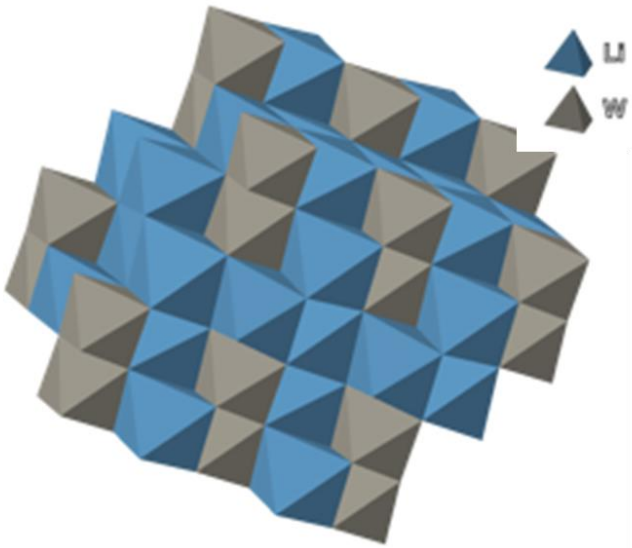

Figure 5.28 Crystal structure of Li_4WO_5

5.4 Conclusions

The solid solution limit in the LISICON-based solid electrolyte $Li_{4-2x}Ge_{1-x}W_xO_4$ was examined and found to be $0.10 \leq x \leq 0.25$ with an optimum calcination temperature of 1000 ºC. Above this range Li_4WO_5 is preferentially formed. Compared with the $Li_{4-2x}Ge_{1-x}Mo_xO_4$ system, the effective solid solution range in $Li_{4-2x}Ge_{1-x}W_xO_4$ system is much narrower and the optimum calcination temperature is quite high.

Through employing the SPS method, dense pellets with relative densities of over 96% theoretical density were achieved. It is noteworthy that a second phase with macro-sized particles appears on the pellet matrix surface and its amount increases with increasing *x*-value. Through elemental mapping and EDS analysis, this has been shown to be a W-rich phase and confirmed by post XRD analysis to be Li_4WO_5. Its appearance is attributed to the thermal etching process used, with rapid growth of Li_4WO_5 crystallites which adhere to the surface of the LISICON matrix.

Impedance spectroscopy measurements showed that $Li_{4-2x}Ge_{1-x}W_xO_4$ ($0.1 \leq x \leq 0.3$) compositions exhibited fast lithium ion conductivity, with the $x = 0.10$ composition showing the highest room temperature conductivity ($\sigma_{25°C} = 5.29 \times 10^{-5}$ S cm^{-1}) and the $x = 0.15$ composition showing the best high temperature conductivity ($\sigma_{250°C} = 3.12 \times 10^{-2}$ S cm^{-1}). It should be noted that the electrical response from electrolyte-gold electrode interface varied on thermal cycling and specialised experimental designs would be needed to probe the complex behaviour at this interface.

MD simulation was used to model the lithium ion conductivity in the $x = 0.15$ composition. The simulated conductivity values are higher than those observed at least partly due to the additional grain boundary resistance in the experimental measurements. On the whole the MD simulations resulted in reasonable structural parameters, with some overestimation of the W-

O bond length. The resulting Li-Li partial pair distribution function was subsequently used as a constraint for RMC calculations on the related $Li_{3+x}Ge_xP_{1-x}O_4$ system (see Chapter 3).

Chapter 6 Conclusions and future work

6.1 Conclusions

In this thesis, three LISICON-structure based systems were investigated systematically, to be specific, the $Li_{3+x}Ge_xP_{1-x}O_4$, $Li_{4-2x}Ge_{1-x}Mo_xO_4$ and $Li_{4-2x}Ge_{1-x}W_xO_4$ systems.

In the (1-*x*) Li_3PO_4- *x*$Li_4Ge_4O_4$ system, it was found that a solid solution can be formed in the compositional range of $0.00 \leq x \leq 0.90$ experimentally which is basically isostructural with the end member γ-Li_3PO_4 in space group *Pnma* (No. 62), but with interstitial lithium ions introduced. Due to the larger ionic radius of Ge^{4+} (0.39 Å) compared to that of P in the pentavalent state (0.17 Å) and extra introduced lithium ions in the LISICON structure, the unit cell parameters including *a*, *b*, *c* axis and unit cell volume exhibit a general increase with increasing *x*-value. Further studies were carried out for the intermediate compositions *x* = 0.25, 0.50 and 0.75 and the two end-members γ-Li_3PO_4 and Li_4GeO_4. An apparent single ^{7}Li NMR signal centred at around 0 ppm can be seen in the ^{7}Li MAS-NMR spectra, which was actually made up of two separate resonances through modelling of the centre band resonance. For the intermediate compositions of *x* = 0.25, 0.50 and 0.75, with increased *x*-value the less shifted resonance shifts to high field and is mainly attributed to the framework tetrahedral lithium signal (Li1/Li1a), and the additional octahedral Li mainly contributes to the second resonance. In ^{31}P MAS-NMR spectra, an isotropic resonance is seen at around 10 ppm. With increasing *x*-value, an increased broadening of the line shapes can be seen, which represents various chemical environments.

A combined X-ray and neutron diffraction study showed the intermediate compositions exhibit disorder within the Li^+ ion sublattice, which is associated with the defect structure. Three types of defect clusters are proposed, Type I involves Li^+ ions in one of the octahedral sites, Li3, and a displaced Li (Li2a) from a neighbouring tetrahedral Li (Li2) site towards an empty tetrahedral site. Type II consists of Li^+ in another tetrahedral site (Li4) with two types

of displaced tetrahedral Li ions; Li1 is displaced into Li1a and Li2 is displaced into Li2a. Type III is a larger defect cluster involving two Type I and one Type II defects. RMC modelling of the neutron total scattering data further reveals how the defect cluster evolves with *x*-value. The results show independent Type I and Type II defects are seen at low levels of substitution, with larger defect clusters, involving at least one Type I defect and one Type II defect at higher *x*-values. The highest lithium ion conductivity was seen in the $x = 0.75$ composition, with a total conductivity of 1.83×10^{-2} S cm^{-1} at 250 °C. For this composition defect clustering even at low temperatures is predicted to be significant.

In the Li_2MoO_4-Li_4GeO_4 ($Li_{4-2x}Ge_{1-x}Mo_xO_4$) system, it is found that pure LISICON type structures can be formed in the range of $0.1 \leq x \leq 0.5$ with a relatively low synthesis temperature in the range 650 to 850 ºC, while the β-phase of $x = 0.5$ composition represents the theoretical limit where no interstitial cations are present in the LISICON structure. Furthermore, the relative amounts of the β-phase and γ-phase change with temperature especially for the $x = 0.4$ and $x = 0.5$ compositions. In the γ-phase range, the unit cell parameters including the *a* and *b* axes and unit cell volume exhibit a general increase with increasing *x*-value due to the slighter bigger ionic radius of Mo^{6+} (0.41 Å) compared to that of Ge^{4+} (0.39 Å), while a gradual decrease in the *c*-axis due to the decreased lithium concentration.

For the intermediate composition, $x = 0.2$ in the γ-phase $Li_{4-2x}Ge_{1-x}Mo_xO_4$ system, three types of defects are proposed to co-exist. The Type I defect is essentially the same as that seen in the $Li_{3+x}Ge_xP_{1-x}O_4$ system and involves Li^+ ions in the Li3 site and one displaced Li2a. The Type IIa defect consists of an Li4 ion, two displaced Li2a ions and two displaced Li1a ions. The larger Type IIIa defect is essentially a combination of two Type I defects with one Type IIa in the middle. As in the $Li_{3+x}Ge_xP_{1-x}O_4$ system, the existence of a subtle second order transition is evident in the thermal variation of lattice parameters at around 400 °C. This transition might be attributed to changes in defect structure as in $Li_3Zn_{0.5}GeO_4$ [84]. Interestingly, the presence of

such a transition in the $x = 0.5$ β-composition, where no interstitial Li^+ ions are thought to be present suggests that the average structure obtained from Rietveld analysis may not give a true picture of the local structure, particularly at elevated temperatures. Indeed, attempts to model the room temperature total neutron scattering data for the $x = 0.5$ composition based on the average structure model, showed significant differences in the total radial distribution function, mainly associated with the Li ion distribution.

The failure of RMC calculations to model the Li^+ ion distribution in the $x = 0.5$ and $x = 0.2$ compositions in the $Li_{4-2x}Ge_{1-x}Mo_xO_4$ system point to the limitations of the method. Modelling the relatively weak diffuse scattering of Li even using neutron data is challenging. Additionally, the relative structural complexity of the orthorhombic LISICON structures, compared to previous studies on high symmetry cubic and rhombohedral phases make the present studies amongst the most challenging studies ever undertaken using the RMC method. Further improvement in experimental design and model optimization is proposed.

The highest conductivity and lowest activation energy in the $Li_{4-2x}Ge_{1-x}Mo_xO_4$ system were seen in the $x = 0.2$ composition, with a value of total conductivity at 250 °C of 5.02×10^{-3} S cm^{-1} and activation energy of 0.67 eV.

The compositions, $Li_{3.75}Ge_{0.75}P_{0.25}O_4$ and $Li_{3.6}Ge_{0.8}Mo_{0.2}O_4$, both exhibit the highest conductivity in their respective solid solution systems. According to the combined X-ray and neutron data, for both of them, there exists big defect clusters, at least including one octahedral Li3, one octahedral Li4 and the displaced Li^+ ions: Li2a displaced from the Li2 site and Li1a displaced from the Li1 site, although the extent of displacement varies between $Li_{3.75}Ge_{0.75}P_{0.25}O_4$ and $Li_{3.6}Ge_{0.8}Mo_{0.2}O_4$. Large defect clusters reported in $Li_3Zn_{0.5}GeO_4$ and $Li_{3.5}Ge_{0.5}V_{0.5}O_4$ [86] were proposed to undergo an interstitialcy mechanism for lithium ion conduction, as shown in Fig. 1.19 (Chapter 1). That is to say, the clusters exchange places with the neighouring stoichiometric regions within the structural framework when the lithium ions

migrate. This mechanism is also well supported by the estimated energy barriers for lithium ion motion in work by Simonov et al. [151], where large energy barriers need to be overcome if only a simple insterstital hopping mechanism is considered innvolving the octahedral Li3 and Li4 ions, but dramatically decreased energy barriers occur for an interstitialcy mechanism involving the synergistic motion of the interstitial Li1a, Li2a, Li3, Li4 ions and the structural Li1 and Li2 ions. Based on this, it can be proposed here that for $Li_{3.75}Ge_{0.75}P_{0.25}O_4$ and $Li_{3.6}Ge_{0.8}Mo_{0.2}O_4$, it is likely that ionic motion also proceeds through an interstitialcy mechanism involving the large defect clusters, though the specific synergistic motions vary since the dispacement effect from Li3 and Li4 vary.

Similar to the $Li_{4-2x}Ge_{1-x}Mo_xO_4$ system, the solid solution limit in the Li_4GeO_4-Li_2WO_4 system was first studied. It was found that a γ-LISICON type solid solution, $Li_{4-2x}Ge_{1-x}W_xO_4$, was formed between Li_4GeO_4 and Li_2WO_4 and the effective solid solution range was $0.10 \leq x \leq 0.25$ with an optimum calcination temperature of 1000 ºC. Compared to its analogue, $Li_{4-2x}Ge_{1-x}Mo_xO_4$, $Li_{4-2x}Ge_{1-x}W_xO_4$ exhibits a narrow solid solution range and requires high calcination temperatures. Dense pellets with relative densities of over 96% theoretical density were achieved through employing the SPS method. The $x = 0.10$ composition showed the highest room temperature conductivity ($\sigma_{25°C} = 5.29 \times 10^{-5}$ S cm^{-1}) and the $x = 0.15$ composition shows the best high temperature conductivity ($\sigma_{250°C} = 3.12 \times 10^{-2}$ S cm^{-1}). Interfacial phenomena occur at the electrolyte-gold electrode interface during thermal cycling, leading to a variation in electrical response. Improvements in experimental design including performing experiments under different atmospheres are needed to probe the complex behaviour. Based on the published neutron data, MD simulations were used to model the lithium ion conductivity in the $x = 0.15$ composition. The simulated conductivity values are at least one order of magnitude higher than those observed, which is partly due to the unresolved grain boundary

resistance in the experimental measurements, indicating further improvement can be obtained through optimizing the sintering conditions.

6.2 Future work

Based on the current work, we believe that the enhancement in the ionic conductivity of LISICON oxides can boost their potential applications greatly based on their properties of low cost and high stability in air. The existence of defect clusters, their concentration and size are critical in determining the extent of ionic conductivity. Further detailed work is required in probing the defect clusters, particularly at elevated temperatures and especially for LISICONs with good conductivity.

Isolating the bulk conductivity is helpful in understanding the intrinsic property of lithium ion conduction in LISICON oxides. Future studies could focus on growing single crystals or very dense ceramics where grain boundary resistances would be eliminated or minimised and to do more research based on the high-quality single crystals.

During the study of $Li_{4-2x}Ge_{1-x}Mo_xO_4$ system, the preliminary results showed that pellets of the intermediate $x = 0.4$ composition with high ratios of the β-phase to the γ-phase exhibited better conductivity than pellets with low ratios. It would therefore be interesting to examine pure β-phase with interstitial Li present. This would allow for a more direct comparison of the local structures in β and γ phases.

Despite their chemical similarities and the almost identical ionic radii of Mo^{6+} and W^{6+} ($rMo^{6+} = 0.41$ Å, $rW^{6+} = 0.42$ Å for the ions in 4 coordinate geometry [161]), the $Li_{4-2x}Ge_{1-x}W_xO_4$ system exhibits a higher conductivity than $Li_{4-2x}Ge_{1-x}Mo_xO_4$ system. The exact reasons for this are unclear and a future detailed neutron diffraction study to assess the structural differences could shed some light on possible reasons for the difference in conductivity.

Lists of Figures and Tables

7.1 Lists of Figures

7.2 Lists of Tables

References

1. J. C. Li, C. Ma, M. F. Chi, C. D. Liang and N. J. Dudney, *Advanced Energy Materials*, 2015, **5**.
2. M. S. Whittingham, *Science*, 1976, **192**, 1126-1127.
3. D. W. Murphy, J. Broadhead and B. C. H. Steele, *Materials for Advanced Batteries*, PLENUM PRESS· NEW YORK AND LONDON, 1980.
4. J. B. Goodenough and K. S. Park, *J Am Chem Soc*, 2013, **135**, 1167-1176.
5. A. Yamada, S. C. Chung and K. Hinokuma, *Journal of The Electrochemical Society*, 2001, **148**, A224-A229.
6. G. Li, H. Azuma and M. Tohda, *Electrochemical and Solid-State Letters*, 2002, **5**, A135-A137.
7. H. Huang, S. C. Yin, T. Kerr, N. Taylor and L. F. Nazar, *Advanced Materials*, 2002, **14**, 1525-1528.
8. D. K. Kim, P. Muralidharan, H. W. Lee, R. Ruffo, Y. Yang, C. K. Chan, H. Peng, R. A. Huggins and Y. Cui, *Nano Lett*, 2008, **8**, 3948-3952.
9. J. H. Kim, S. T. Myung, C. S. Yoon, S. G. Kang and Y. K. Sun, *Chemistry of Materials*, 2004, **16**, 906-914.
10. H. Wang, *Journal of The Electrochemical Society*, 1999, **146**, 473-480.
11. M. V. Reddy, G. V. Subba Rao and B. V. R. Chowdari, *The Journal of Physical Chemistry C*, 2007, **111**, 11712-11720.
12. J. M. Tarascon and M. Armand, *Nature*, 2001, **414**, 359-367.
13. M. Wakihara, *Materials Science and Engineering: R: Reports*, 2001, **33**, 109-134.
14. L. Ji, Z. Lin, M. Alcoutlabi and X. Zhang, *Energy & Environmental Science*, 2011, **4**, 2682-2699.
15. G. E. Blomgren, *Journal of Power Sources*, 1999, **81-82**, 112-118.

16. K. Xu, *Chem Rev*, 2004, **104**, 4303-4417.

17. J. Zhang, X. Zang, H. Wen, T. Dong, J. Chai, Y. Li, B. Chen, J. Zhao, S. Dong, J. Ma, L. Yue, Z. Liu, X. Guo, G. Cui and L. Chen, *Journal of Materials Chemistry A*, 2017, **5**, 4940-4948.

18. I. A. T. Association., 2016.

19. J. Bates, *Solid State Ionics*, 2000, **135**, 33-45.

20. Y. Liu, P. He and H. Zhou, *Advanced Energy Materials*, 2018, **8**, 1701602-n/a.

21. L. Z. Long, S. J. Wang, M. Xiao and Y. Z. Meng, *Journal of Materials Chemistry A*, 2016, **4**, 10038-10069.

22. J. W. Fergus, *Journal of Power Sources*, 2010, **195**, 4554-4569.

23. L.-Z. Fan, X.-L. Wang, F. Long and X. Wang, *Solid State Ionics*, 2008, **179**, 1772-1775.

24. T. Itoh, K. Hirai, T. Uno and M. Kubo, *Ionics*, 2007, **14**, 1-6.

25. C. Zhu, H. Cheng and Y. Yang, *Journal of The Electrochemical Society*, 2008, **155**, A569.

26. H. M. J. C. Pitawala, M. A. K. L. Dissanayake, V. A. Seneviratne, B. E. Mellander and I. Albinson, *Journal of Solid State Electrochemistry*, 2008, **12**, 783-789.

27. M. Zhu, J. X. Wu, Y. Wang, M. M. Song, L. Long, S. H. Siyal, X. P. Yang and G. Sui, *Journal of Energy Chemistry*, 2019, **37**, 126-142.

28. I. Abrahams, E. Hadzifejzovic and J. R. Dygas, *Dalton Trans*, 2004, DOI: 10.1039/b401582g, 3129-3136.

29. S. R. Elliott, *Physics of amorphous materials*, Longman, 1983.

30. J. Fu, *Solid State Ionics*, 1997, **96**, 195-200.

31. I. Abrahams, *Solid State Ionics*, 2000, **134**, 249-257.

32. A. Hayashi and M. Tatsumisago, *Electronic Materials Letters*, 2012, **8**, 199-207.

33. R. G. Pearson, *Journal of Chemical Education*, 1968, **45**, 581.

34. T. J. Salami, S. H. Imanieh, J. G. Lawrence and I. Martin, *Materials Letters*, 2019, **254**, 294-296.

35. X. Zhang, *Journal of Power Sources*, 2002, **112**, 209-215.

36. J. C. Bachman, S. Muy, A. Grimaud, H. H. Chang, N. Pour, S. F. Lux, O. Paschos, F. Maglia, S. Lupart, P. Lamp, L. Giordano and Y. Shao-Horn, *Chemical Reviews*, 2016, **116**, 140-162.

37. H. J. Deiseroth, S. T. Kong, H. Eckert, J. Vannahme, C. Reiner, T. Zaiss and M. Schlosser, *Angew Chem Int Ed Engl*, 2008, **47**, 755-758.

38. N. Kamaya, K. Homma, Y. Yamakawa, M. Hirayama, R. Kanno, M. Yonemura, T. Kamiyama, Y. Kato, S. Hama, K. Kawamoto and A. Mitsui, *Nat Mater*, 2011, **10**, 682-686.

39. M. Park, X. Zhang, M. Chung, G. B. Less and A. M. Sastry, *Journal of Power Sources*, 2010, **195**, 7904-7929.

40. A. R. West, *Solid state chemistry and its applications*, John Wiley & Sons, Ltd, Chichester, West Sussex, Second, student;2nd, student; edn., 2014.

41. D. B. McWhan, S. J. Allen, J. P. Remeika and P. D. Dernier, *Physical Review Letters*, 1975, **35**, 953-956.

42. Y. Yung-Fang Yu and J. T. Kummer, *Journal of Inorganic and Nuclear Chemistry*, 1967, **29**, 2453-2475.

43. J. B. Goodenough, H. Y. P. Hong and J. A. Kafalas, *Materials Research Bulletin*, 1976, **11**, 203-220.

44. H. Y. P. Hong, *Materials Research Bulletin*, 1976, **11**, 173-182.

45. G. F. Ortiz, M. C. López, P. Lavela, C. Vidal-Abarca and J. L. Tirado, *Solid State Ionics*, 2014, **262**, 573-577.

46. M. Subramanian, R. Subramanian and A. Clearfield, *Solid State Ionics*, 1986, **18-19**, 562-569.

47. A. Kubanska, L. Castro, L. Tortet, O. Schäf, M. Dollé and R. Bouchet, *Solid State Ionics*, 2014, **266**, 44-50.

48. V. Thangadurai, A. K. Shukla and J. Gopalakrishnan, *Journal of Materials Chemistry*, 1999, **9**, 739-741.

49. M. Catti, *Solid State Ionics*, 1999, **123**, 173-180.

50. J. A. S. Oh, L. He, A. Plewa, M. Morita, Y. Zhao, T. Sakamoto, X. Song, W. Zhai, K. Zeng and L. Lu, *ACS Applied Materials & Interfaces*, 2019, **11**, 40125-40133.

51. F. Zheng, M. Kotobuki, S. Song, M. O. Lai and L. Lu, *Journal of Power Sources*, 2018, **389**, 198-213.

52. F. Sudreau, D. Petit and J. P. Boilot, *Journal of Solid State Chemistry*, 1989, **83**, 78-90.

53. V. Thangadurai and W. Weppner, *Ionics*, 2006, **12**, 81-92.

54. H. Aono, *Journal of The Electrochemical Society*, 1990, **137**, 1023-1027.

55. H. Aono, *Journal of The Electrochemical Society*, 1989, **136**, 590-591.

56. C. Cao, Z.-B. Li, X.-L. Wang, X.-B. Zhao and W.-Q. Han, *Frontiers in Energy Research*, 2014, **2**.

57. W. Xiao, J. Wang, L. Fan, J. Zhang and X. Li, *Energy Storage Materials*, 2019, **19**, 379-400.

58. Y. A. Abramov, V. G. Tsirelson, V. E. Zavodnik, S. A. Ivanov and Brown I. D., *Acta Crystallographica Section B*, 1995, **51**, 942-951.

59. A. G. Belous, G. N. Novitskaya, S. V. Polyanetskaya and Y. I. Gornikov, *Inorganic Materials*, 1987, **23**, 412-415.

60. S. Stramare, V. Thangadurai and W. Weppner, *Chemistry of Materials*, 2003, **15**, 3974-3990.

61. H. Kawai, *Journal of The Electrochemical Society*, 1994, **141**, L78-L79.

62. J. A. Dawson, P. Canepa, T. Famprikis, C. Masquelier and M. S. Islam, *Journal of the American Chemical Society*, 2018, **140**, 362-368.

63. Y. Zhao and L. L. Daemen, *J Am Chem Soc*, 2012, **134**, 15042-15047.

64. V. Thangadurai, H. Kaack and W. J. F. Weppner, *Journal of the American Ceramic Society*, 2003, **86**, 437-440.

65. V. Thangadurai, S. Adams and W. Weppner, *Chemistry of Materials*, 2004, **16**, 2998-3006.

66. V. Thangadurai and W. Weppner, *Journal of Power Sources*, 2005, **142**, 339-344.

67. V. Thangadurai and W. Weppner, *Advanced Functional Materials*, 2005, **15**, 107-112.

68. V. Thangadurai and W. Weppner, *Journal of the American Ceramic Society*, 2005, **88**, 411-418.

69. J. Awaka, A. Takashima, K. Kataoka, N. Kijima, Y. Idemoto and J. Akimoto, *Chemistry Letters*, 2011, **40**, 60-62.

70. J. Awaka, N. Kijima, H. Hayakawa and J. Akimoto, *Journal of Solid State Chemistry*, 2009, **182**, 2046-2052.

71. F. Chen, J. Li, Z. Huang, Y. Yang, Q. Shen and L. Zhang, *The Journal of Physical Chemistry C*, 2018, **122**, 1963-1972.

72. V. Thangadurai, S. Narayanan and D. Pinzaru, *Chemical Society Reviews*, 2014, **43**, 4714-4727.

73. C. Bernuy-Lopez, W. Manalastas, J. M. Lopez del Amo, A. Aguadero, F. Aguesse and J. A. Kilner, *Chemistry of Materials*, 2014, **26**, 3610-3617.

74. J. R. Rea, D. L. Foster, P. R. Mallory and I. Co, *Materials Research Bulletin*, 1979, **14**, 841-846.

75. B. A. Boukamp and R. A. Huggins, *Physics Letters A*, 1976, **58**, 231-233.

76. M. Matsuo, T. Sato, Y. Miura, H. Oguchi, Y. Zhou, H. Maekawa, H. Takamura and S.-i. Orimo, *Chemistry of Materials*, 2010, **22**, 2702-2704.

77. H. D. Lutz, W. Schmidt and H. Haeuseler, *Journal of Physics and Chemistry of Solids*, 1981, **42**, 287-289.

78. P. G. Bruce and A. R. West, *Materials Research Bulletin*, 1980, **15**, 379-385.

79. H. Y. P. Hong, *Materials Research Bulletin*, 1978, **13**, 117-124.

80. I. Abrahams, P. G. Bruce, A. R. West and W. I. F. David, *Journal of Solid State Chemistry*, 1988, **75**, 390-396.

81. I. Abrahams, P. G. Bruce, W. I. F. David and A. R. West, *Acta Crystallographica Section B Structural Science*, 1989, **45**, 457-462.

82. W. H. Baur, *Materials Research Bulletin*, 1981, **16**, 339-345.

83. A. R. West and P. G. Bruce, *Acta Crystallographica Section B*, 1982, **38**, 1891-1896.

84. P. G. Bruce, I. Abrahams and A. R. West, *Solid State Ionics*, 1990, **40-41**, 293-299.

85. I. Abrahams and P. G. Bruce, *Acta Crystallographica Section B Structural Science*, 1991, **47**, 696-701.

86. P. G. Bruce and I. Abrahams, *Journal of Solid State Chemistry*, 1991, **95**, 74-82.

87. J. Kuwano and A. R. West, *Materials Research Bulletin*, 1980, **15**, 1661-1667.

88. A. Khorassani and A. West, *Solid State Ionics*, 1982, **7**, 1-8.

89. A. Khorassani and A. R. West, *Journal of Solid State Chemistry*, 1984, **53**, 369-375.

90. *Journal*, 1975, **141**, 422.

91. Y. A. Du and N. A. W. Holzwarth, *Physical Review B*, 2007, **76**, 174302.

92. L. D. Prayogi, M. Faisal, E. Kartini, W. Honggowiranto and Supardi, *AIP Conference Proceedings*, 2016, **1710**, 030047.

93. Y. Deng, C. Eames, J.-N. Chotard, F. Lalère, V. Seznec, S. Emge, O. Pecher, C. P. Grey, C. Masquelier and M. S. Islam, *Journal of the American Chemical Society*, 2015, **137**, 9136-9145.

94. D. Tranqui, R. D. Shannon, H. Y. Chen, S. Iijima and W. H. Baur, *Acta Crystallographica Section B Structural Crystallography and Crystal Chemistry*, 1979, **35**, 2479-2487.

95. Y. W. Hu, *Journal of The Electrochemical Society*, 1977, **124**, 1240-1242.

96. Y. Deng, C. Eames, B. Fleutot, R. David, J.-N. Chotard, E. Suard, C. Masquelier and M. S. Islam, *ACS Applied Materials & Interfaces*, 2017, **9**, 7050-7058.

97. A. R. West, *Journal of Applied Electrochemistry*, 1973, **3**, 327-335.

98. I. M. Hodge, M. D. Ingram and A. R. West, *Journal of the American Ceramic Society*, 1976, **59**, 360-366.

99. R. Kanno and M. Murayama, *Journal of The Electrochemical Society*, 2001, **148**, A742-A746.

100. M. Murayama, *Journal of Solid State Chemistry*, 2002, **168**, 140-148.

101. L. Zhang, L. Cheng, J. Cabana, G. Chen, M. M. Doeff and T. J. Richardson, *Solid State Ionics*, 2013, **231**, 109-115.

102. P. Bron, S. Johansson, K. Zick, J. Schmedt auf der Gunne, S. Dehnen and B. Roling, *J Am Chem Soc*, 2013, **135**, 15694-15697.

103. J. M. Whiteley, J. H. Woo, E. Y. Hu, K. W. Nam and S. H. Lee, *Journal of the Electrochemical Society*, 2014, **161**, A1812-A1817.

104. M. N. Rahaman, *sintering of ceramics*, Taylor & Francis Group, LLC, 2007.

105. Fine Ceramics Use Highly Purified Raw Materials, https://global.kyocera.com/fcworld/first/production.html, (accessed Febrary 10th, 2020).

106. I. W. Chen and X. H. Wang, *Nature*, 2000, **404**, 168.

107. S. D. Antolovich and H. Conrad, *Materials and Manufacturing Processes*, 2004, **19**, 587-610.

108. R. Raj, M. Cologna, J. S. C. Francis and D. J. Green, *Journal of the American Ceramic Society*, 2011, **94**, 1941-1965.

109. O. Guillon, J. Gonzalez-Julian, B. Dargatz, T. Kessel, G. Schierning, J. Räthel and M. Herrmann, *Advanced Engineering Materials*, 2014, **16**, 830-849.

110. D. I. Yushin, A. V. Smirnov, N. W. Solis Pinargote, P. Y. Peretyagin and R. Torrecillas San Millan, *Materials Science Forum*, 2015, **834**, 41-50.

111. Electromagnetic radiation, https://en.wikipedia.org/wiki/Electromagnetic_radiation, (accessed July 11th, 2020).

112. X-ray reflection in accordance with Bragg's Law, https://serc.carleton.edu/research_education/geochemsheets/BraggsLaw.html, (accessed Febrary 15th, 2020).

113. D. Chateigner, PhD, Université de Caen Normandie and Université de Liège, 2014.

114. *Neutron Applications in Materials for Energy*, Springer International Publishing, Switzerland, 2015.

115. J. R. D. Copley, *The Fundamentals of Neutron Powder Diffraction*, National Institute of Standards and Technology, WASHINGTON, 2001.

116. V. F. Sears, *Neutron News*, 1992, **3**, 26-37.

117. L. Wang, PhD, Queen Mary University of London 2020.

118. *Neutron Applications in Earth, Energy and Environmental Sciences*, Springer Science+Business Media, New York, 2009.

119. Neutron Source, https://mlz-garching.de/englisch/neutron-research/neutron-source.html, (accessed August 10th, 2020).

120. I. A. S. T. Norberg, R. I. Smith, S. G. Eriksson, L. C. Chapon and S. Hull, Poster, Rutherford Appleton Laboratory, Oxford, 2009.

121. H. M. Rietveld, *Journal of Applied Crystallography*, 1969, **2**, 65-71.

122. *A. C. Larson, R. B. Von Dreele, Los Alamos National Laboratory Report, No. LAUR-86–748*, 1987.

123. I. Abrahams, personal communication.

124. D. A. Keen, *Journal of Applied Crystallography*, 2001, **34**, 172-177.

125. A. K. Soper, *Journal*, 2012.

126. R. L. McGreevy and L. Pusztai, *Molecular Simulation*, 1988, **1**, 359-367.

127. M. D. Matt Tucker, Andrew Goodwin, Anthony Phillips, David Keen, Helen Playford, Wojciech A. Slawinski, Igor Levin, Victor Krayzman, Maksim Eremenko, Yuanpeng Zhang, *Journal*, 2019.

128. A. Nanakoudis, What is SEM? Scanning Electron Microscopy Explained, https://www.thermofisher.com/blog/microscopy/what-is-sem-scanning-electron-microscopy-explained/, (accessed June 5th, 2020).

129. E. Jensen, Example: Mechanism of Scanning electron microscopy, https://texample.net/tikz/examples/scanning-electron-microscopy/, (accessed June 5th, 2020).

130. C. A. Fyfe, *Solid State NMR for Chemists*, C.F.C. Press, P.O. Box 1720, Ontario, 1983.

131. M. J. Duer, *Solid-State NMR Spectroscopy Principles and Applications*, Blackwell Science Ltd, 2002.

132. U. Haeberlen, *High Resolution NMR in Solids Selective Averaging*, Academic Press, 1976.

133. J. Herzfeld and A. E. Berger, *The Journal of Chemical Physics*, 1980, **73**, 6021-6030.

134. M. Mehring, *Principles of High Resolution NMR in Solids*, Springer-Verlag, Berlin, 2nd revised edition edn., 1983.

135. R. N. C. Jones, A. R. H.; Miller, F. A.; Elyashévich, M. A.; Förster, T.; Hadni, A.; Morino, and N. F. Y.; Sheppard, E.; Lippincott, E. R.; Lord, R. C.; Nagakura, S.; Plivá, J.; Sir Thompson, H.; Turner, D. W.; Herzberg, G.; Urbanski, T, *Journal*, 1972, **29**, 625.

136. E. R. Andrew, A. Bradbury and R. G. Eades, *Nature*, 1958, **182**, 1659-1659.

137. I. J. Lowe, *Physical Review Letters*, 1959, **2**, 285-287.

138. M. M. O. Fernanda, L. R. A. Menezes, L. M. Dutra, M. F. C. Santos and S. A. A. Barison, in *eMagRes*, 2017, DOI: 10.1002/9780470034590.emrstm1536, pp. 325-342.

139. G. Facey, Magic Angle Spinning, http://u-of-o-nmr-facility.blogspot.com/2007/11/magic-angle-spinning.html, (accessed Apirl 15th, 2020).

140. O. Heaviside, *Electrical papers*, New York and London : Macmillan and co., 1894.

141. J. J. Biendicho and A. R. West, *Solid State Ionics*, 2012, **226**, 41-52.

142. J. T. S. Irvine, D. C. Sinclair and A. R. West, *Advanced Materials*, 1990, **2**, 132-138.

143. E. J. Abram, D. C. Sinclair and A. R. West, *Journal of Electroceramics*, 2003, **10**, 165-177.

144. L. Popovi, B. Manoun, D. de Waal, M. K. Nieuwoudt and J. D. Comins, *Journal of Raman Spectroscopy*, 2003, **34**, 77-83.

145. C. Keffer, A. D. Mighell, F. Mauer, H. E. Swanson and S. Block, *Inorganic Chemistry*, 1967, **6**, 119-125.

146. B. Wang, B. C. Chakoumakos, B. C. Sales, B. S. Kwak and J. B. Bates, *Journal of Solid State Chemistry*, 1995, **115**, 313-323.

147. R. Hofmann and R. Hoppe, *Zeitschrift für anorganische und allgemeine Chemie*, 1987, **555**, 118-128.

148. J. Kamphorst and E. Hellstrom, *Solid State Ionics*, 1980, **1**, 187-197.

149. A. Rodger, Kuwano, J., West, A. R., *Solid State Ionics*, 1985, **15**, 185-198.

150. A. K. Ivanov-Shitz and V. V. Kireev, *Crystallography Reports*, 2003, **48**, 112-115.

151. M. K. Rabadanov, A. Pietraszko, V. V. Kireev, A. K. Ivanov-Schitz and V. I. Simonov, *Crystallography Reports*, 2003, **48**, 744-749.

152. S. Muy, J. C. Bachman, H.-H. Chang, L. Giordano, F. Maglia, S. Lupart, P. Lamp, W. G. Zeier and Y. Shao-Horn, *Chemistry of Materials*, 2018, **30**, 5573-5582.

153. G. Zhao, K. Suzuki, M. Yonemura, M. Hirayama and R. Kanno, *ACS Applied Energy Materials*, 2019, **2**, 6608-6615.

154. U. V. S. Yakubovich O. V., *Kristallografiya*, 1997, **42**, 301-308.

155. D. Massiot, F. Fayon, M. Capron, I. King, S. Le Calvé, B. Alonso, J.-O. Durand, B. Bujoli, Z. Gan and G. Hoatson, *Magnetic Resonance in Chemistry*, 2002, **40**, 70-76.

156. I. Abrahams, *NMRLSS – Program for least squares fitting of solid state MAS NMR spectra*, 2004.

157. K. Eichele, *HBA — Herzfeld-Berger Analysis (user manual)*, 2015.

158. U. Haeberlen, *High Resolution NMR in Solids Selective Averaging*, 1976.

159. J. R. Dygas and M. W. Breiter, *Electrochimica Acta*, 1996, **41**, 993-1001.

160. J. R. Dygas and M. W. Breiter, *Electrochimica Acta*, 1999, **44**, 4163-4174.

161. R. D. Shannon, *Acta Crystallographica Section A*, 1976, **32**, 751-767.

162. P. Hartmann, J. Vogel and B. Schnabel, *Journal of Non-Crystalline Solids*, 1994, **176**, 157-163.

163. E. I. Burmakin, V. I. Voronin and G. S. Shekhtman, *Russian Journal of Electrochemistry*, 2003, **39**, 1124-1129.

164. D. A. Ksenofontov, N. V. Zubkova, D. Y. Pushcharovsky, L. N. Dem'yanets, U. Kolitsch, E. Tillmanns and A. K. Ivanov-Shits, *Crystallography Reports*, 2006, **51**, 391-394.

165. J. Kuwano, M. Nagamine, M. Higuchi and K. M., *Denki Kagaku* 1981, **49**, 667.

166. N. I. P. Ayu, E. Kartini, L. D. Prayogi, M. Faisal and Supardi, *Ionics*, 2016, **22**, 1051-1057.

167. U. Kolitsch, *Zeitschrift für Kristallographie - Crystalline Materials*, 2001, **216**, 449-454.

168. E. I. a. A. Burmakin, V.N., *Elektrokhimiya*, 1987, **23**, 1124-1127.

169. J.-S. Kim, J.-H. Choi, B.-M. Jeong and H.-J. Kang, *J. Korean Ceram. Soc*, 2006, **43**, 10-10.

170. R. Hoffmann and R. Hoppe, *Zeitschrift für anorganische und allgemeine Chemie*, 1989, **573**, 157-169.

171. I. T. Todorov, W. Smith, K. Trachenko and M. T. Dove, *Journal of Materials Chemistry*, 2006, **16**, 1911-1918.

172. J. Li, L. Fang, H. Luo, J. Khaliq, Y. Tang and C. Li, *Journal of the European Ceramic Society*, 2016, **36**, 243-246.

173. D. Zhou, C. A. Randall, L.-X. Pang, H. Wang, J. Guo, G.-Q. Zhang, X.-G. Wu, L. Shui and X. Yao, *Journal of the American Ceramic Society*, 2011, **94**, 348-350.

174. M. A. K. L. Dissanayake, *Solid State Ionics*, 1988, **27**, 109-111.

175. M. A. K. L. Dissanayake, M. A. Careem, P. W. S. K. Bandaranayake, R. P. Gunawardane and C. N. Wijesekara, *Solid State Ionics*, 1990, **40-41**, 23-26.

176. K. Xiao, C. Li, H. Xiang and L. Fang, *Journal of Materials Science: Materials in Electronics*, 2018, **29**, 6397-6402.